

Translucent load-bearing GFRP envelopes for daylighting and solar cell integration in building construction

THÈSE N° 6405 (2014)

PRÉSENTÉE LE 7 NOVEMBRE 2014

À LA FACULTÉ DE L'ENVIRONNEMENT NATUREL, ARCHITECTURAL ET CONSTRUIT
LABORATOIRE DE CONSTRUCTION EN COMPOSITES
PROGRAMME DOCTORAL EN GÉNIE CIVIL ET ENVIRONNEMENT

ÉCOLE POLYTECHNIQUE FÉDÉRALE DE LAUSANNE

POUR L'OBTENTION DU GRADE DE DOCTEUR ÈS SCIENCES

PAR

Carlos PASCUAL AGULLO

acceptée sur proposition du jury:

Prof. K. Beyer, présidente du jury
Prof. T. Keller, Dr J. de Castro San Roman Fest, directeurs de thèse
Prof. J. Knippers, rapporteur
Prof. J. Ramôa Correia, rapporteur
Dr F. Vigliotti, rapporteur



ÉCOLE POLYTECHNIQUE
FÉDÉRALE DE LAUSANNE

Suisse
2014

Preface

Glass fiber-reinforced polymer (GFRP) composites allow the creation of multifunctional building systems that cannot be realized using traditional materials. The low thermal conductivity of lightweight GFRP composites in particular permits the integration of structural and building physics functions into single building components. This allows a merging of load-bearing structure and building envelope and therefore leads to a significant reduction in the number of building components, which can be prefabricated under controlled conditions, thus enabling rapid construction and improved quality compared to multilayered on-site production. Low-energy standards can be easily met while lightweight construction is maintained.

A further function integration step is based on the optional translucency and transparency of GFRP composites, which also allows the integration of solar cells into load-bearing GFRP skins – therefore adding architectural and energy supply functions to the multifunctional GFRP components.

The aim of this thesis is thus to investigate the relationships between the optical and mechanical properties of transparent/translucent GFRP skins and define material specifications for structural skylights for daylighting of buildings and solar cell encapsulation into GFRP skins of load-bearing sandwich structures.

I would like to acknowledge the support for this research provided by EPFL Middle East (financial support), the EPFL Solar Energy and Building Physics Laboratory LESO-PB (optical measurements and knowhow), Flexcell and Solaronix (for providing the flexible and DSC cells and knowhow) and Scobalit AG (for providing the GFRP materials).

Prof. Dr. Thomas Keller

Acknowledgments

This project has been conducted during four years of research at the Composite Construction Laboratory under the supervision of Prof. Thomas Keller and Dr. Julia de Castro. It is first to them that I want to express all my gratitude. Thank you Prof. Keller for the opportunity you gave me to join your team and work in such a motivating and interdisciplinary research environment. Your guidance, advice and careful revisions have undoubtedly improved the quality of this work. Thanks also to Dr. Julia de Castro for your many contributions to this research, your confidence in my work, your friendship and the time you devoted to supporting me.

I want to sincerely thank the thesis defense committee composed of the jury members Dr. Franco Vigliotti (EPFL Middle East), Prof. João Ramôa Correia (Técnico Lisboa) and Prof. Jan Knippers (Universität Stuttgart) and the president of the jury Prof. Katrin Beyer (EPFL). Your comments, interest in the project and feedback have been really appreciated. I remember with great pleasure the times that I met you during my doctoral studies and I was extremely pleased to welcome you for my thesis defense.

I wish to thank all the partners of this research. First, thanks to EPFL Middle East for the financial support and encouragement during these last years. I also sincerely appreciate the contribution of Flexcell and Solaronix, the companies that provided the solar cells, equipment and a friendly environment for this project. The contribution of Scobalit in providing materials for the fabrication of composite laminates is also acknowledged. Finally I would like to express my sincere gratitude to the Solar Energy and Building Physics Laboratory (EPFL), particularly to Dr. Andreas Schueler, for an intense and productive collaboration in this work.

I cannot imagine myself performing this research outside the EPFL environment. I was fortunate enough to meet many talented and friendly people here, including undergraduate students, PhD students, scientists and technicians, who contributed many ideas to this research. I would like to thank all my friends from the Civil Engineering Institute and particularly Dr. Anastasios P. Vassilopoulos for sharing with me your knowledge of composites, my office mates Behzad and Kyriaki and my colleagues Ehsan, Wei, Haifeng and Sonia for your sincere friendship every day at CCLAB. Many thanks also to Margaret Howett for all the efforts correcting the English text of my thesis. Thanks also to the brilliant students Alain Pillonel for helping me in the experimental work and Max Florean for making the computerized drawings used in this thesis and in the presentations and conferences associated with it.

Life in Lausanne has been an amazing personal experience shared with unforgettable friends. Thanks to all of you, and especially my deepest gratitude to my family for your extraordinary support and care throughout all these years.

Abstract

This project investigates the light transmittance of load-bearing glass fiber-reinforced polymer (GFRP) laminates with a view to two architectural applications: the daylighting of buildings through load-bearing translucent GFRP envelopes and encapsulation of solar cells into the GFRP building skins of sandwich structures. The total and diffuse visible light transmittances of the laminates were experimentally investigated using a spectrophotometer coupled to an integrating sphere. The refractive indices of polymeric resin and glass fibers were also investigated and numerical ray-tracing simulations were performed to demonstrate the experimentally observed wavelength dependency of light diffusion. The total transmittance and translucency of GFRP laminates were analytically modeled as a function of the reinforcement weight, fiber architecture and fiber volume fraction. Goniophotometric experiments – performed to investigate the directional light scattering of laminates reinforced with different fiber architectures – were demonstrated as an effective method to predict the fiber architecture of translucent GFRP laminates. The optical properties of the laminates, i.e. the total and diffuse transmittances and directionality of light diffusion, were correlated with the experimentally investigated mechanical properties, i.e. the directional tensile strength and E-modulus.

The experimental work demonstrated that structural skylights could be designed with GFRP laminates exhibiting a translucency of 0.9 and total light transmittance of 0.5 – minimum values recommended for daylighting of buildings through translucent envelopes – and that solar cells could be encapsulated in load-bearing GFRP laminates with a total light transmittance of around 0.83. A case study was performed using the GFRP/polyurethane sandwich roof of the Novartis Campus Main Gate Building to demonstrate the basic feasibility of integrating skylights and solar cells into the external translucent skin of optimized sandwich structures.

Finally, the encapsulation of transparent and colored dye solar cells in translucent GFRP laminates has been explored. Prototype solar panels have been fabricated and a significant weight reduction, increase in structural strength and around 10% reduction of electrical efficiency compared to traditional solar panels with glass encapsulants were achieved.

Keywords

Glass fiber-reinforced polymer, sandwich structure, multifunctional structure, light transmittance, refractive index, daylit building, solar cell encapsulation

Résumé

Ce projet étudie la transmittance de lumière de laminés structuraux en polymères renforcés par des fibres de verre (GFRP) en vue de deux applications architecturales: l'éclairage naturel de bâtiments à travers des enveloppes translucides et structurales en GFRP et l'encapsulation de cellules solaires dans les laminés en GFRP de structures sandwich pour les bâtiments. Les transmittances totale et diffuse des laminés ont été étudiées expérimentalement dans le domaine visible en utilisant un spectrophotomètre connecté à une sphère intégrante. Les indices de réfraction de la résine polymérique et des fibres de verre ont été aussi investigués expérimentalement et des simulations numériques de tracé de rayons ont été réalisées afin de démontrer l'observation expérimentale qui indiquait une dépendance de la diffusion de la lumière par rapport à longueur d'onde. La transmittance totale et la translucidité des laminés GFRP ont été modélisées analytiquement en fonction du taux de renforcement, l'architecture des fibres et la fraction volumique de fibres. Des expériences de goniophotométrie – réalisés pour investiguer les propriétés directionnelles de la diffusion de la lumière de laminés renforcés avec différentes architectures de fibres – ont montré leur efficacité pour prédire l'architecture de fibres de laminés translucides en GFRP. Les propriétés optiques des laminés, i.e. transmittance totale et diffuse et propriétés directionnelles de la diffusion de la lumière, ont été corrélées avec les propriétés mécaniques investiguées expérimentalement, i.e. résistance à la traction et module élastique dans différentes directions.

Le travail expérimental a montré que des lanterneaux structuraux pourraient être construits avec des laminés en GFRP présentant une translucidité de 0.9 et une transmittance totale de 0.5 – valeurs minimales recommandées pour l'éclairage naturel de bâtiments à travers des enveloppes translucides – et que des cellules solaires pourraient être encapsulées dans des laminés en GFRP présentant une transmittance totale autour de 0.83. Une étude de cas a été réalisée en utilisant la toiture sandwich en GFRP/polyuréthane du Novartis Campus Main Gate Building afin de démontrer la faisabilité d'intégrer des lanterneaux et des cellules solaires dans le laminé externe et translucide de structures sandwich optimisées.

Finalement, l'encapsulation de cellules solaires à colorant et transparentes dans des laminés en GFRP a été investiguée. Des prototypes de panneaux solaires ont été fabriqués et une réduction significative du poids, une augmentation de la résistance mécanique et une réduction de l'efficacité électrique d'environ 10% en comparaison avec les panneaux solaires traditionnels présentant des encapsulants en verre ont été obtenues.

Mots clés

Polymères renforcés par des fibres de verre, structure en sandwich, structure multifonctionnelle, transmittance de lumière, indice de réfraction, éclairage naturel de bâtiments, encapsulation de cellules solaires

Contents

Preface	i
Acknowledgments	iii
Abstract	v
Résumé	vi
List of Figures	xi
List of Tables	xv
1 Introduction	1
1.1. Context and motivation	1
1.2. Objectives.....	3
1.3. Methodology	4
1.4. Thesis organization	4
1.5. References	6
2 Total light transmittance of GFRP laminates	7
2.1. Introduction	7
2.2. Experimental procedure	9
2.2.1. Overview	9
2.2.2. Materials.....	9
2.2.3. Specimen fabrication	10
2.2.4. Experimental set-up.....	12
2.3. Experimental results and discussion	14
2.3.1. Spectrophotometric experiments	14
2.3.2. Solar radiation flash experiments	16
2.3.3. Comparison of experimental results	16
2.4. Modeling of light transmittance	17
2.4.1. Model based on spectrophotometric results	17
2.4.2. Model based on short circuit current measurements	19
2.4.3. Modeling of mean value of visible total light transmittance.....	20
2.4.4. Application of existing model	21
2.4.5. Application to generate spectral transmittance curves.....	21
2.5. Conclusions	22

2.6. References	23
3 Diffuse light transmittance of GFRP laminates	25
3.1. Introduction	25
3.2. Experimental procedure	27
3.2.1. Overview	27
3.2.2. Materials.....	27
3.2.3. Specimen fabrication	27
3.2.4. Spectrophotometric set-up	28
3.3. Spectrophotometric results	30
3.4. Analysis of spectrophotometric results.....	34
3.4.1. Overview	34
3.4.2. Characterization of polyester resin refractive index	34
3.4.3. Characterization of E-glass fiber refractive index	36
3.4.4. Ray-tracing simulation of GFRP spectral light transmittance.....	37
3.5. Analytical modeling of GFRP translucency	40
3.5.1. Model for 555-nm wavelength depending on reinforcement weight	40
3.5.2. Model for visible spectrum depending on reinforcement weight	43
3.5.3. Model for 555-nm wavelength depending on total transmittance	44
3.6. Evaluation of applications	45
3.7. Conclusions	45
3.8. References	46
4 Optomechanical investigation of GFRP laminates	49
4.1. Introduction	49
4.2. Theoretical background of light scattering in GFRP laminates	50
4.2.1. Directional scattering by UD aligned fibers	50
4.2.2. Single and multiple light scattering	51
4.3. Experimental procedure	51
4.3.1. Materials.....	51
4.3.2. Specimen fabrication	52
4.3.3. Goniophotometric experiments.....	54
4.3.4. Tensile experiments.....	55
4.4. Experimental results	57
4.4.1. Goniophotometric results.....	57
4.4.2. Tensile results	60
4.5. Analytical modeling of tensile properties of GFRP laminates.....	63
4.5.1. Overview	63
4.5.2. Optically-based model of fiber volume fraction	63
4.5.3. Optically-based model of directional fiber volume fraction	65
4.5.4. Strength and E-modulus of translucent GFRP laminates	66
4.6. Evaluation of applications	68
4.7. Conclusions	69
4.8. References	69

5	Integration of dye solar cells in GFRP laminates	73
5.1.	Introduction	73
5.2.	Experimental procedure	75
5.2.1.	Overview	75
5.2.2.	Materials.....	75
5.2.3.	Fabrication	76
5.2.4.	Experiments.....	81
5.3	Experimental results.....	82
5.3.1.	Electrical results for panels	82
5.3.2.	Optical results for GFRP specimens and PMMA substrate	83
5.3.3.	Thermal cycle results for panels.....	84
5.4.	Modeling.....	86
5.4.1.	Overview	86
5.4.2.	Analytical modeling of total light transmittance.....	86
5.4.3.	Analytical modeling of solar panel efficiency	87
5.4.4.	Numerical modeling of thermal experiments.....	88
5.5.	Discussion.....	92
5.6.	Conclusions	93
5.7.	References	94
6	Conclusions and future work	97
6.1.	Conclusions	97
6.1.1.	Scientific conclusions	97
6.1.2.	Applications for building construction.....	98
6.1.3.	Materials and fabrication methods.....	98
6.1.4.	Measurements of light transmittance.....	99
6.2.	Original contributions	99
6.3.	Recommendations for future work.....	100
A	Laminates and PV modules	101
B	Optical microscopy	115
C	Spectrophotometric results	119
D	Solar radiation results	139
E	Immersion liquids and refractive indices	143
F	Goniophotometric results	147
G	Results of tensile experiments	159
	Curriculum Vitae	175

List of Figures

Figure 1.1.	<i>Lightweight GFRP skylight (a) during installation and (b) exhibiting high translucency and large dimensions.</i>	1
Figure 1.2.	<i>Translucent GFRP roof of "Les Echanges" pavilion (a) after and (b) during construction (Lausanne, 1964).</i>	1
Figure 1.3.	<i>GFRP facade of Polymer Engineering Center from (a) front view at night and (b) lateral view (Melbourne, 2001).</i>	2
Figure 1.4.	<i>Flexible amorphous-silicon PV cells (a) non-encapsulated and (b) encapsulated in the top skin of a GFRP/polyurethane sandwich structure.</i>	2
Figure 1.5.	<i>SwissTech Convention Center with (a) DSC glass panels fixed to facade and (b) view of panels from interior daylight hall (Lausanne, 2014).</i>	3
Figure 2.1.	<i>Bending experiment on a GFRP/PUR sandwich structure with encapsulated a-Si PV cells.</i>	7
Figure 2.2.	<i>Spectral response of Flexcell a-Si PV cells and spectral luminous efficiency function for photopic vision²⁶.</i>	10
Figure 2.3.	<i>Hand lay-up encapsulation of three serial-connected a-Si PV cells in GFRP.</i>	11
Figure 2.4.	<i>Dimensions (mm) and components of PV modules with a-Si PV cells (not to scale).</i>	11
Figure 2.5.	<i>Integrating sphere with GFRP specimen located in port A for total light transmittance experiment.</i>	13
Figure 2.6.	<i>Schematic representation of integrating sphere set-up (top view, dimensions in mm).</i>	13
Figure 2.7.	<i>Hemispherical solar spectral irradiance of 1000 W/m² and AM1.5 (a: wavelength range of visible light, b: wavelength range of solar response of a-Si PV cells).</i>	13
Figure 2.8.	<i>Spectral transmittance of unidirectional specimens at different reinforcement weights and transmittance and reflectance of 1-mm-thick resin specimen.</i>	14
Figure 2.9.	<i>Spectral transmittance of unidirectional specimens at different volume fractions.</i>	15
Figure 2.10.	<i>Spectral transmittance of unidirectional and cross-ply specimens.</i>	15
Figure 2.11.	<i>Spectral transmittance of hand lay-up and vacuum specimens with $w = 820 \text{ g/m}^2$.</i>	15
Figure 2.12.	<i>Transmittance measurements at 555-nm wavelength, from solar radiation flash experiments and analytical model (UD specimens).</i>	16
Figure 2.13.	<i>Loss of transmittance, $L_{555}(w)$, at 555 nm.</i>	19
Figure 2.14.	<i>Comparison of modeling results according to Iba et al.^{11,12} and equation (2.11) for UD laminates.</i>	21
Figure 2.15.	<i>Spectral curve of loss parameter, $L(w_1)$, for UD laminates without vacuum bag ($w_1 = 410 \text{ g/m}^2$).</i>	22

Figure 2.16.	<i>Measured and predicted spectral transmittance for $w = 820 \text{ g/m}^2$ and $w = 3280 \text{ g/m}^2$.</i>	22
Figure 3.1.	<i>Schematic representation of integrating sphere set-up for diffuse transmittance experiments (top view, dimensions in mm).</i>	29
Figure 3.2.	<i>Spectral total and diffuse transmittance of specimen 820UD-L with different roving orientations (0°, 45° and 90°) at entrance port A of integrating sphere.</i>	30
Figure 3.3.	<i>Plane of major light diffusion inside integrating sphere for specimen 820UD-L with rovings oriented at 90° with respect to horizontal plane.</i>	30
Figure 3.4.	<i>Spectral diffuse transmittance of unidirectional specimens at different reinforcement weights.</i>	31
Figure 3.5.	<i>Bluish appearance of specimens (a) 820UD-L and (b) 1640UD-L when illuminated with white light.</i>	31
Figure 3.6.	<i>Spectral diffuse transmittance of specimens 1230UD and 1640UD at different volume fractions.</i>	32
Figure 3.7.	<i>Spectral diffuse transmittance of unidirectional and cross-ply specimens ($w = 1230 \text{ g/m}^2$) at different volume fractions.</i>	32
Figure 3.8.	<i>Spectral total and diffuse transmittance measured with integrating sphere set-up of unidirectional specimens with 15- and 30- (*) minute gel times.</i>	33
Figure 3.9.	<i>Detailed view of specimen (a) 1640 UD-L (15-min gel time) and (b) 1640 UD-L* (30-min gel time) with text behind the specimens.</i>	33
Figure 3.10.	<i>Spectral total and diffuse transmittance of three polyester specimens.</i>	34
Figure 3.11.	<i>Spectral total reflectance and absorptance of three polyester specimens.</i>	34
Figure 3.12.	<i>Refractive indices of E-glass fiber, n_f, and polyester resin, n_r, and attenuation coefficient, α_r, of polyester resin.</i>	35
Figure 3.13.	<i>Through-thickness optical microscopy image of specimen 1640UD-L* (A: rovings, $12.8 \mu\text{m}$ diameter, B: yarns, $8.9 \mu\text{m}$ diameter).</i>	38
Figure 3.14.	<i>Ray-tracing geometrical model (a) of a 2.6-mm-thick GFRP laminate with $w = 1640 \text{ g/m}^2$ ($R = \text{resin}$, $F = \text{fiber layer}$), and (b) partial representation of light rays (units in μm).</i>	38
Figure 3.15.	<i>Diffuse transmittance simulated by ray-tracing model, experimental results for specimen 1640UD-L* and refractive index mismatch between resin and fibers.</i>	39
Figure 3.16.	<i>Total transmittance and total reflectance simulated by ray-tracing model and total transmittance experimental results for specimen 1640UD-L*.</i>	39
Figure 3.17.	<i>Exponential model of translucency at 555 nm as function of equivalent reinforcement weight w_{eq} of UD and CP laminates (for gel time of 15 min).</i>	41
Figure 3.18.	<i>Linear model of translucency at 555 nm as function of equivalent reinforcement weight $w_{eq} < 2000 \text{ g/m}^2$ of UD and CP laminates for short and long (*) gel times.</i>	42
Figure 3.19.	<i>Models of total and diffuse transmittance as function of reinforcement weight of UD and CP laminates, considering $w = w_{eq}$.</i>	43
Figure 3.20.	<i>Models of translucency as function of total transmittance at 555 nm and experimental results.</i>	44
Figure 4.1.	<i>Goniophotometric specimens indicating (a) orientation of 0°- and 90°-directions, (b) major planes of light diffusion when illuminated by a concentrated beam and (c) detailed view of light scattering around the forward direction (laminate 1230CP-L).</i>	54
Figure 4.2.	<i>Goniophotometric set-up (a) view of sensor and specimen, (b) lateral view and (c) top view.</i>	56

Figure 4.3.	<i>Scattering diagram of reference measurement (without specimen).</i>	57
Figure 4.4.	<i>Tensile experiment on GFRP specimen with strain gage located in center.</i>	57
Figure 4.5.	<i>Scattering diagrams of UD-L specimens with $410 \leq w \leq 1640$ g/m² in 0°-direction and UD-L specimen with $w = 410$ g/m² in 90°-direction (representation in logarithmic scale).</i>	59
Figure 4.6.	<i>Scattering diagrams of specimens 410UD-L in 0°- and 90°-directions and specimen 820UD-L in 0°-direction.</i>	59
Figure 4.7.	<i>Scattering diagrams of UD specimens in 0°-direction at different fiber volume fractions.</i>	59
Figure 4.8.	<i>Experimental results of scattered radiation ratio, R_{scat}, as function of average fiber volume fraction of gonio- and spectrophotometric specimens and model predictions according to equation (4.13).</i>	60
Figure 4.9.	<i>Scattering diagrams of specimens 1640CP-L in 0°- and 90°-directions.</i>	60
Figure 4.10.	<i>Load-strain curves for UD-L and UD-H specimens loaded in 0°-direction.</i>	62
Figure 4.11.	<i>Load-strain curves of 1640CP-L and 1640CP-H specimens loaded in 0°- and 90°-directions.</i>	62
Figure 4.12.	<i>Load-strain curves of UD-L and UD-H specimens loaded in 90°-direction.</i>	62
Figure 4.13.	<i>Failure modes of specimen (a) 1640UD-L exhibiting more transparency than specimen (b) 1640UD-H.</i>	63
Figure 4.14.	<i>Experimental results of translucency at 555 nm as function of equivalent reinforcement weight and modeling predictions according to equation (4.8).</i>	65
Figure 4.15.	<i>Directional fiber volume fraction, $f_{i, mod}$, from equation (4.17) compared to average directional volume fraction, f_i, from gonio- and spectrophotometric results (dotted line indicates a model that would exhibit perfect accuracy).</i>	66
Figure 4.16.	<i>Directional strength as function of directional fiber volume fraction, mechanical model predictions according to equation (4.18) and model resulting when considering $f_i = f_{i, mod}$.</i>	67
Figure 4.17.	<i>Directional E-modulus as function of directional fiber volume fraction, model predictions according to the ROM, predictions of mechanical model from equation (4.22) and model resulting when considering $f_i = f_{i, mod}$.</i>	68
Figure 4.18.	<i>(a) Novartis Campus Main Gate Building, Basel, (b) roof top view, (c) roof cross section and (d) concept for integrating PV cells and skylights.</i>	69
Figure 5.1.	<i>(a) Exploded view of dye solar cell and (b) module formed by eleven cells between two electrically conductive glass substrates.</i>	74
Figure 5.2.	<i>Fabrication of (a-d) functional DSC module on glass substrates and (e-h) dummy module with PMMA substrates.</i>	77
Figure 5.3.	<i>(a) Module showing 4-mm lateral shift of glass substrates and (b) reference group of three DSC modules connected in parallel.</i>	77
Figure 5.4.	<i>Geometry and components of solar panels (not to scale).</i>	78
Figure 5.5.	<i>Fabrication of (a) Glass-Polyester panel by hand lamination and (b) Glass-Silane panel by infusion.</i>	79
Figure 5.6.	<i>Fabrication of Glass-Silicone panel.</i>	80
Figure 5.7.	<i>PMMA and GFRP specimens for optical experiments with text behind the specimens.</i>	80
Figure 5.8.	<i>Glass-Silane panel (a) out of solar simulator and (b) being introduced into solar simulator.</i>	81

Figure 5.9.	<i>Integrating sphere (a) set-up with port B closed for total transmittance experiment and (b) detailed view through open port B (diffuse transmittance experiment).</i>	82
Figure 5.10.	<i>(a) Six-hour thermal cycle with extreme temperatures at 60 °C and -20 °C and (b) Glass-Silane panel subjected to thermal cycles in RUMED incubator.</i>	82
Figure 5.11.	<i>I-V and P-V curves of reference group of three modules together with those of (a) Glass-Silane panel and (b) Glass-Silicone panel.</i>	83
Figure 5.12.	<i>Spectral total and diffuse transmittance of GFRP and PMMA specimens.</i>	84
Figure 5.13.	<i>Glass-Polyester panel exhibiting after one thermal cycle (a) large delaminated surfaces and (b) large amount of cracks in pure polyester bands around modules (dotted lines indicate cracks and delaminations on rear side of module).</i>	85
Figure 5.14.	<i>Glass-Silane panel exhibiting no cracks after five thermal cycles and (a) few delaminations and (b) loss of electrolyte in delaminated surface (photographs correspond to opposite sides of panel).</i>	85
Figure 5.15.	<i>PMMA(-) panel exhibiting (a) high translucency and blue light diffusion and (b-c) no delaminations on module surface after 50 thermal cycles (photographs taken under different conditions of illumination).</i>	86
Figure 5.16.	<i>Glass-Silicone exhibiting after one thermal cycle (a) no cracks and no delaminations (bottom outer encapsulant side), and (b) cracks in adhesive polyester layer and milky cloudiness over DSC modules (top outer encapsulant side).</i>	86
Figure 5.17.	<i>Shear stresses (a-b) τ_{xy} and τ_{yz} on modules of Glass-Silane panel and (c-d) τ_{xy} on modules of PMMA(-) panel from numerical simulation at $\Delta T = -40$ °C.</i>	91
Figure 5.18.	<i>First principal stress σ_1 (tensile) for unreinforced volumes of polyester resin in (a) Glass-Polyester panel and (b) Glass-Silicone panel from numerical simulation at $\Delta T = -40$ °C.</i>	91
Figure 5.19.	<i>Conceptual through-thickness design of translucent sandwich structure integrating solar energy production and detailed views of external skin with (b) DSC acrylic (PMMA) modules and (c) DSC glass modules.</i>	93

List of Tables

Table 1.1.	<i>Summary of thesis content indicating experimental techniques, modeled parameters, appendices and papers associated with four main chapters.</i>	5
Table 2.1.	<i>Fiber volume fraction and thickness of fabricated GFRP specimens.</i>	11
Table 2.2.	<i>Short circuit currents for PV modules with different fiber architecture of upper encapsulants.</i>	12
Table 2.3.	<i>Calibration parameter, $L_{555}(w_i)$, as function of reinforcement architecture and fabrication process.</i>	19
Table 2.4.	<i>Mean values of light transmittance for specimen 410UD-L and corresponding PV module.</i>	20
Table 2.5.	<i>Mean values of light transmittance for specimen 820UD-L and corresponding PV module.</i>	20
Table 3.1.	<i>Fiber volume fraction and thickness of fabricated GFRP specimens.</i>	28
Table 3.2.	<i>Main oxide components of E-glass fibers and their concentration in weight (w_i) according to ASTM D578/D578M-05,²² molar mass (M_i), concentration in mole (c_i) according to equation (3.12), and refractive index at 588 nm ($n_{588,i}$) and principal dispersion (D_i) from Bach and Neuroth¹⁷.</i>	36
Table 3.3.	<i>Diffuse and total transmittance (average) measurements at 555 nm, total transmittance according to model developed by Pascual et al.¹⁰ given in equation (3.22), estimation of entrance loss of integrating sphere, experimental translucency at 555 nm according to equation (3.17) and equivalent reinforcement weight from equation (3.18).</i>	41
Table 3.4.	<i>Parameter a and R-square factor for exponential translucency model.</i>	41
Table 3.5.	<i>Slope b and R-square factor for linear translucency model, for $w_{eq} < 2000$ g/m².</i>	42
Table 3.6.	<i>Translucency at 430 nm, 555 nm and in visible range of specimens 410UD-L and 820UD-L.</i>	44
Table 4.1.	<i>Total and directional reinforcement weights, directional reinforcement weight fractions and ratio of reinforcement weight of unidirectional (UD) and cross-ply (CP) laminates.</i>	53
Table 4.2.	<i>Fiber volume fraction and thickness of unidirectional (UD) GFRP specimens for goniophotometric, tensile and spectrophotometric experiments.</i>	53
Table 4.3.	<i>Fiber volume fraction and thickness of cross-ply (CP) GFRP specimens for tensile, goniophotometric and spectrophotometric experiments.</i>	53
Table 4.4.	<i>Ratio of reinforcement weights (R_w), ratio of ultimate loads (R_F) and ratio of scattered radiation (R_{scat}) for unidirectional (UD) and cross-ply (CP) laminates.</i>	60
Table 4.5.	<i>Experimental ultimate loads of unidirectional (UD) and cross-ply (CP) tensile specimens. Note: shaded background indicates specimens loaded in 90°-direction.</i>	61
Table 4.6.	<i>Total transmittance and translucency at 555 nm, fiber volume fraction modeled by equation (4.12) and reinforcement weight fractions modeled by equation (4.16) of UD and CP laminates.</i>	63

Table 4.7.	<i>Parameters of translucency and total transmittance models according to equations (4.8) and (4.10).</i>	64
Table 5.1.	<i>Mechanical properties, thermal expansion coefficient and density considered for glass fibers and polyester resin used in this research.</i>	76
Table 5.2.	<i>In-plane dimensions a, b and c (see Figure 5.4(a)) and total thickness d of fabricated panels.</i>	78
Table 5.3.	<i>Fabrication process, fiber volume fraction and through-thickness components of the four fabricated solar panels.</i>	79
Table 5.4.	<i>Thickness, fiber volume fraction and total transmittance at 535-nm wavelength of the four GFRP specimens.</i>	81
Table 5.5.	<i>Electrical properties of electrically functional solar panels and reference group of three DSC modules.</i>	83
Table 5.6.	<i>Number of thermal cycles performed on fabricated panels, delaminated surfaces and crack locations.</i>	85
Table 5.7.	<i>Material properties of substrates, sealants and unreinforced encapsulants (all isotropic) and reinforced encapsulants (orthotropic) considered for numerical simulations.</i>	89

1 Introduction

1.1. Context and motivation

Translucent building envelopes diffuse daylight into working and living spaces, reducing the need for artificial lighting and therefore building energy consumption, and the glare produced by bright sunlight. For this purpose glass fiber-reinforced polymer (GFRP) laminates began to be explored in Switzerland during the 1950s for building skylights due to their light weight, impact resistance and load-bearing capacity compared to glass components. The easy forming of GFRP into complex forms allowed the designing of structurally efficient double curvature GFRP skylights of 5.5-m span and only 4-mm thickness for the daylighting of low-rise buildings (see Figure 1.1).¹ Later, for the Swiss National Exhibition of 1964 in Lausanne, a 7780-m² daylit pavilion was constructed with a translucent roof made of 3-mm thickness GFRP hyperbolic paraboloids (see Figure 1.2).² However the poor weatherability and low fire resistance of resins used at that time limited the widespread use of translucent GFRP building envelopes.

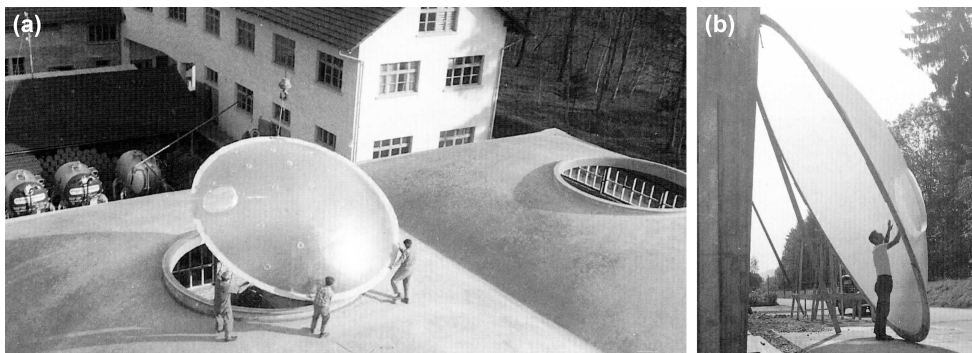


Figure 1.1. Lightweight GFRP skylight (a) during installation and (b) exhibiting high translucency and large dimensions.¹

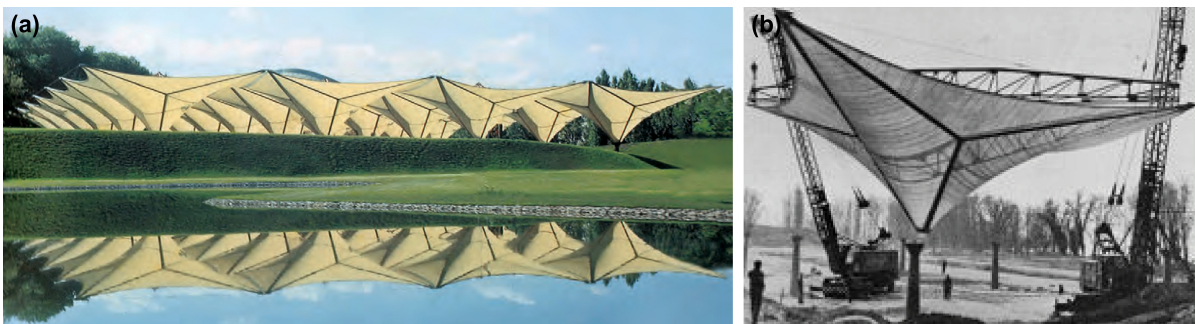


Figure 1.2. Translucent GFRP roof of "Les Echanges" pavilion (a) after and (b) during construction (Lausanne, 1964).²

Now the long-term stability of resins has been improved – resins can be stabilized against ultraviolet (UV) radiation – and they can also exhibit fire retardant properties combined with low thermal conductivity and high light transmittance.^{3,4} Iconic buildings are designed with translucent GFRP facades providing daylight during the day and transforming the building into a shining and architecturally expressive object at night. These lighting effects are shown in Figure 1.3 for the 75-m-long facade of the Polymer Engineering Center in Melbourne using corrugated and UV-stabilized GFRP laminates with light transmittance of 0.38 as cladding material.⁵ However, translucent applications of GFRP laminates are nowadays limited to secondary loading components.



Figure 1.3. GFRP facade of Polymer Engineering Center from (a) front view at night and (b) lateral view (Melbourne, 2001).

Since the early 1980s, high light transmittance GFRP laminates have been considered as a low-cost alternative for replacing glass components in solar energy applications for building construction.^{6,7} In 2009, Keller et al.⁸ validated the mechanical and thermal feasibility of encapsulating flexible amorphous-silicon photovoltaic (PV) cells in the external translucent GFRP skin of lightweight and curved sandwich structures, thus integrating structural, architectural and energy production functions into single components (see Figure 1.4). This multifunctional sandwich constitutes an important step towards the full integration of PV cells in load-bearing components. Furthermore, the foam core of the sandwich structure could be locally removed – or replaced by translucent aerogel insulation – thereby creating GFRP skylights completely integrated into the load-bearing structure.⁹

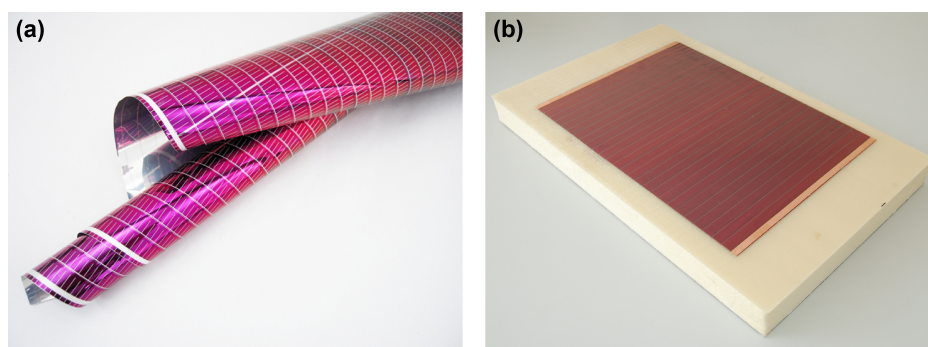


Figure 1.4. Flexible amorphous-silicon PV cells (a) non-encapsulated and (b) encapsulated in the top skin of a GFRP/polyurethane sandwich structure.

Transparent and colored dye solar cells (DSC) offer the possibility of integrating solar energy production into the transparent envelopes of daylight buildings. Unlike traditional silicone cells, active layers of DSC are protected by waterproof substrates and their electrical efficiency is stable in warm conditions –

therefore constituting a promising source of energy for hot and humid tropical climates. The encapsulation of these cells into a silicone layer between two laminated glasses – as adopted in the facade of the SwissTech Convention Center (see Figure 1.5) – is structurally inefficient and heavy and comprises risks associated with overhead glazing due to the brittleness and generally low structural capacity of glass. Instead, the encapsulation of DSC modules in translucent GFRP laminates would offer potential for developing lightweight composite components integrating load-bearing resistance together with architectural (daylighting) and energy production functions. However no optomechanical research has yet correlated the optical and mechanical properties of GFRP laminates as required for designing optimized composite structures. Moreover, no feasibility study of encapsulating DSC modules in GFRP laminates for envelopes of daylit buildings has been performed.

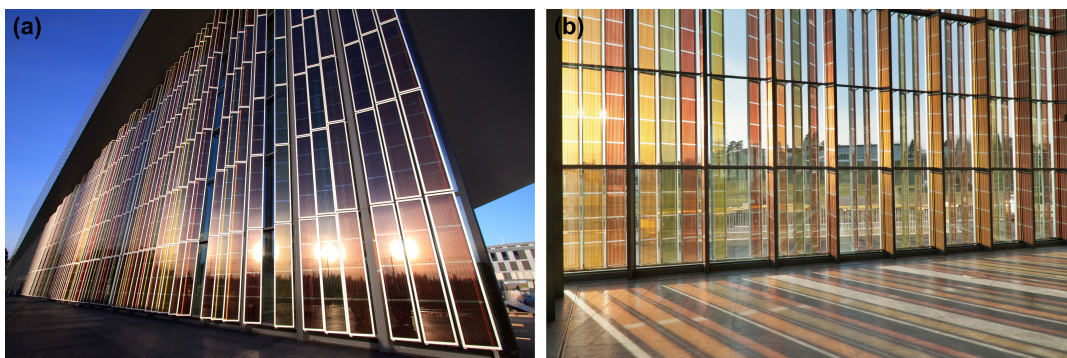


Figure 1.5. SwissTech Convention Center with (a) DSC glass panels fixed to facade and (b) view of panels from interior daylit hall (Lausanne, 2014).

1.2. Objectives

The aims of this research are: 1) the investigation of optimum GFRP laminates in terms of optical and mechanical performances adapted for the load-bearing envelopes of daylit buildings and encapsulation of solar cells, and 2) the development of composite components combining daylighting and solar energy production functions. In order to achieve this, the following objectives were defined:

- Investigate the total light transmittance of GFRP laminates and model it as function of fiber architecture, fiber volume fraction, reinforcement weight and resin gel time in order to study the optical feasibility of integrating PV cells in structural GFRP encapsulants.
- Investigate the diffuse light transmittance of GFRP laminates and model the translucency (the ratio between diffuse and total transmittance) as function of fiber architecture, fiber volume fraction, reinforcement weight and resin gel time in order to study the optical feasibility of designing GFRP translucent skylights for daylit buildings.
- Develop an optically-based model of the directional fiber volume fraction, and therefore of the tensile strength and E-modulus, of GFRP laminates based on the total and diffuse transmittance and directional light scattering of the composite in order to determine optimum laminates in terms of optical and mechanical performances.
- Investigate the feasibility of manufacturing translucent solar panels composed of DSC modules encapsulated in GFRP laminates and study the electrical efficiency and thermal behavior of these panels.

1.3. Methodology

The methodology used to attain the objectives of this research is as follows:

- Experimental investigation of the total light transmittance of GFRP laminates using an integrating sphere coupled to a spectrophotometer.
- Validation of total light transmittance experiments by experimental measurements of short circuit currents generated by PV cells encapsulated in GFRP laminates and exposed to simulated solar radiation.
- Experimental investigation of the diffuse light transmittance of GFRP laminates using an integrating sphere coupled to a spectrophotometer.
- Investigation of the refractive indices of resin (by spectrophotometry) and glass fibers (by chemical composition and fiber fabrication process).
- Numerical simulations of total and diffuse light transmittance by numerical ray-tracing analyses.
- Experimental investigation of the directional light scattering of GFRP laminates by goniophotometry.
- Experimental investigation of the directional tensile strength and E-modulus of GFRP laminates under static loads.
- Investigation of infusion as a fabrication method of solar panels comprising DSC modules encapsulated in GFRP laminates.
- Experimental investigation of the electrical efficiency of GFRP/DSC solar panels subjected to simulated solar radiation.
- Experimental investigation of the performance of GFRP encapsulants under cyclic thermal loads.

1.4. Thesis organization

The research presented in this thesis is divided into four main chapters in order to address the four objectives defined in Section 1.2 and an additional chapter summarizing the conclusions of the research. The general organization of the thesis is shown in Table 1.1.

The following is a summary of the chapter contents:

- Chapter 2: The total light transmittance of GFRP laminates is experimentally investigated by spectrophotometry. The results are validated by short circuit currents of PV cells encapsulated in GFRP laminates and exposed to solar radiation. An analytical model of total light transmittance is developed and the optical feasibility of encapsulating PV cells in GFRP laminates is demonstrated.
- Chapter 3: The diffuse light transmittance of GFRP laminates and the refractive index of the resin are experimentally investigated by spectrophotometry. The refractive index of the glass fiber is analytically modeled based on the refractive indices of its oxide components. Numerical ray-tracing analyses are performed to demonstrate that refractive index mismatches between resin and fibers are responsible for the light diffusion of GFRP laminates. An analytical model of translucency, i.e. ratio between diffuse and total transmittance, is developed and the optical feasibility of designing GFRP skylights for daylight buildings is demonstrated.
- Chapter 4: An optically-based model of directional fiber volume fraction, and therefore of tensile strength and E-modulus, is developed based on the total and diffuse transmittance and directional

light scattering of the composite. Goniophotometry is investigated as an effective technique for evaluating the fiber architecture of highly transparent laminates. Optimum laminates in terms of optical and mechanical performance were investigated for skylight construction and PV cell encapsulation. A real GFRP/polyurethane sandwich structure is selected as a design example.¹⁰

- Chapter 5: The feasibility of fabricating translucent solar panels – constituted of DSC modules encapsulated in GFRP laminates – by infusion is investigated. The electrical efficiency of the solar panels is experimentally evaluated and analytically modeled. The panels are also subjected to thermal cycles and the thermal stresses are numerically investigated. Conceptual designs for multifunctional composite components integrating solar energy production and daylighting functions for building envelopes are proposed.
- Chapter 6: The conclusions from the experimental, analytical and numerical investigations of the research are summarized. Suggestions for future research are also formulated.

Table 1.1. Summary of thesis content indicating experimental techniques, modeled parameters, appendices and papers associated with four main chapters.

Main chapters	Experimental techniques	Modeled parameters		Appendices	Papers
		Analytically	Numerically		
2. Total light transmittance of GFRP laminates	Spectrophotometry Simulated solar radiation	Total light transmittance	-	A, B, C, D	1
3. Diffuse light transmittance of GFRP laminates	Spectrophotometry	Translucency	Total and diffuse transmittance (by ray-tracing simulations)	A, B, C, E	2
4. Optomechanical investigation of GFRP laminates	Spectrophotometry Goniophotometry Tensile experiments	Directional fiber volume fraction	-	A, B, C, F, G	3
5. Integration of DSC in GFRP laminates	Spectrophotometry Simulated solar radiation Thermal cycle experiments	Efficiency of solar panels	Thermal stresses (by finite element models)	-	4

The following seven appendices present further details concerning the main chapters of the thesis (see Table 1.1):

- Appendix A: Laminates and PV modules
- Appendix B: Optical microscopy
- Appendix C: Spectrophotometric results
- Appendix D: Solar radiation results
- Appendix E: Immersion liquids and refractive indices
- Appendix F: Goniophotometric results
- Appendix G: Results of tensile experiments

The results of this thesis have been included in four journal papers – three of them submitted (of which, two were accepted) and one in progress. The four papers are listed below and correspond to the four main chapters of this thesis (see Table 1.1):

1. Pascual C, de Castro J, Schueler A, Vassilopoulos AP and Keller T. Total light transmittance of glass fiber-reinforced polymer laminates for multifunctional load-bearing structures. Accepted for publication in *J Compos Mater* 2013; DOI: 10.1177/0021998313511653.

2. Pascual C, de Castro J, Kostro A, Schueler A, Vassilopoulos AP and Keller T. Diffuse light transmittance of glass fiber-reinforced polymer laminates for multifunctional load-bearing structures. Accepted for publication in *J Compos Mater* 2013; DOI: 10.1177/0021998313511655.
3. Pascual C, de Castro J, Kostro A, Schueler A, Vassilopoulos AP and Keller T. Optomechanical investigation of glass fiber-reinforced polymer laminates for multifunctional load-bearing structures. Submitted to *J Compos Mater* in June 2014.
4. Pascual C, de Castro J and Keller T. Integration of dye solar cells in load-bearing translucent glass fiber-reinforced polymer laminates. In progress.

1.5. References

1. Chilton J. Heinz Isler – The Engineer's Contribution to Contemporary Architecture. London: Thomas Telford, 2000.
2. Knippers J, Cremers J, Gabler M, et al. *Construction Manual for Polymers + Membranes*. Basel: Birkhäuser, 2011.
3. Zhang C, Huang JY, Liu SM et al. The synthesis and properties of a reactive flame-retardant unsaturated polyester resin from a phosphorus-containing diacid. *Polym Adv Technol* 2011; 22:1768-1777.
4. Ampelite company. Product information at: http://50.28.34.130/~trials/media/SL_Fire_Retardant_Brochure.pdf (accessed 6 May 2014).
5. Engelsmann S, Spalding V, Peters S. *Plastics in Architecture and Construction*. Basel: Birkhäuser, 2010.
6. Blaga, A. Use of plastics in solar energy applications. *Sol Energy* 1978; 21(4):331-378.
7. Sawai H, Toshikawa H, Shibata A, et al. The development of a low cost photovoltaic module using FRP molded encapsulation. In: *Proceedings of the 16th IEEE Photovoltaic Specialists Conference*, San Diego, USA, 28 September 1982, pp.932-937. Piscataway, NJ: IEEE.
8. Keller T, Vassilopoulos AP and Manshadi BD. Thermomechanical behavior of multifunctional GFRP sandwich structures with encapsulated photovoltaic cells. *J Compos Constr* 2010; 14(4):470-478.
9. Keller T. Towards Structural Forms for Composite Fibre Materials. *SEI* 1999; 9(4):297-300.
10. Keller T, Haas C and Vallée T. Structural concept, design, and experimental verification of a glass fiber-reinforced polymer sandwich roof structure. *J Compos Constr* 2008; 12(4):454-468.

2 Total light transmittance of GFRP laminates

2.1. Introduction

Nowadays glass fiber-reinforced polymer (GFRP) materials are increasingly used in building construction for the design of multifunctional structures. These composite materials allow the integration of structural functions, building physics functions (mainly thermal insulation) and architectural functions (complex forms and color) in single large-scale building components.¹ GFRP materials also allow the fabrication of translucent structural components with high degree of transparency when optically aligned resins and glass fibers are used,^{2,3} i.e. their refractive indices are identical. Moreover, amorphous silicon (a-Si) flexible photovoltaic (PV) solar cells can be encapsulated in the GFRP skins of freeform building envelopes, integrating electric energy production in lightweight and low-cost structures. Reducing the cost of the encapsulation process of PV cells has been a main issue since the early age of photovoltaic energy and for this purpose systems using GFRP composites can constitute a valuable option.⁴

The integration of PV cells in multifunctional composite elements has begun to be explored recently for high-tech applications in aerospace.^{5,6} However, in such cases, FRP composites are used as mechanical support for the PV cells and not as the top encapsulant of the cells. For building applications, recent research has explored the thermal and mechanical feasibility of encapsulating PV cells in the translucent skin of structural GFRP/PUR (polyurethane) sandwich structures, as shown in Figure 2.1.⁷ However, no optical investigation of the light transmittance through structural GFRP encapsulants was performed in this study. For traditional encapsulants of a-Si PV cells, that is, cells covered with a thin layer of ethylene vinyl acetate adhesive and front sheets of glass or fluoropolymers, transmittance ranges from 0.89 to 0.95 were reported by Samuels et al.⁸

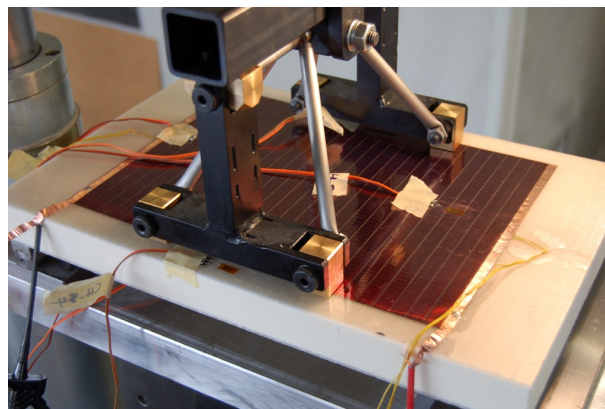


Figure 2.1. Bending experiment on a GFRP/PUR sandwich structure with encapsulated a-Si PV cells.

The light transmittance depends on the energy loss of a beam of light during propagation from one medium to another through a laminate. This loss has three components: reflected light in the interfaces between the external mediums and the laminate and scattered and absorbed light inside the laminate.^{9,10} The reflection of light is the return of radiant energy caused by an interface between mediums with different refractive indices. The scattering of light corresponds to the energy emanating from the beam of light due to the presence of material obstacles in the rectilinear light propagation. Scattered and non-scattered waves may interfere due to a difference in their phases. As a consequence of the superposition of these waves, the energy of the original beam may be reduced. Finally, absorption is the conversion of radiant energy to a different form of energy by interaction with matter. The three types of energy loss - and therefore light transmittance - are wavelength-dependent properties.

Iba et al.^{11,12} proposed a theoretical model for the light transmittance prediction in the direction perpendicular to fiber axis of unidirectional (UD) fiber-reinforced composites. Transmittance T of a laminate is calculated according to equation (2.1):

$$T = T_m \cdot T_c \quad (2.1)$$

where T_m is the transmittance of a sample of resin at the considered wavelength, and T_c is the normalized transmittance of the composite laminate in the bulk given by equation (2.2):

$$T_c = \left(1 - 2 \cdot Q_{ext} \cdot \sqrt{\frac{f}{\pi}} \right)^{\frac{d}{R_f} \sqrt{\frac{f}{\pi}}} \quad (2.2)$$

where Q_{ext} is an extinction function that depends on the fiber radius, R_f , the spectral mismatch of refractive indices, Δn , between resin and fiber in the composite, and the wavelength, λ , of light. The other parameters of this model are the thickness, d , of the specimen and the fiber volume fraction, f . The model considers that energy is removed by reflection in the laminate surfaces (considered in the term T_m) and by forward light scattering (interference) due to fibers inside the composite (considered in the term T_c).

As observed experimentally, and modeled by equation (2.2), light scattering occurs already for a very small Δn and therefore the refractive indices of resin and fibers must be very precisely known. However, in the field of GFRP composites for architectural construction, refractive indices are generally known with an accuracy of around ± 0.01 , which is significantly lower than the accuracy of ± 0.0001 required by the model of equation (2.2).¹¹ Moreover, refractive indices generally depend on the strain level and may also be affected by the fabrication process due to thermally induced strains.^{13,14} The model also does not consider air inclusions and voids, which behave as scattering particles reflecting and deviating light rays and therefore decrease transmittance. The amount of non-wet fibers (fibers not completely immersed in the resin but surrounded by an air pocket) is the most important factor reducing transmittance if the refractive indices of fiber and resin match closely.¹⁵ Finally, load-bearing GFRP components are in most cases cross-ply reinforced laminates and thus the model, since it is developed for UD reinforcement, is not adapted.

To overcome these limitations, a new analytical model for the total light transmittance prediction of UD and cross-ply hand lay-up GFRP laminates illuminated at near normal incidence is developed. This model is employed for the light transmittance investigation of GFRP laminates used as translucent load-bearing structures and encapsulants of solar cells. In the first application, the percentage of visible light transmitted through GFRP laminates surrounded by air is investigated. In the second application, where

the GFRP laminate is in contact with air on one side and laminated onto a solar cell on the other, the percentage of solar irradiance transmitted through the laminate and reaching the surface of a-Si PV cells is studied.

2.2. Experimental procedure

2.2.1. Overview

Polyester resin and E-glass fibers of similar refractive indices were selected for the fabrication of the laminates. The total light transmittance of these laminates, surrounded by air, was investigated by spectrophotometry using an integrating sphere to collect the light transmitted after scattering inside the laminates. Furthermore, a-Si PV cells were encapsulated into GFRP laminates. These PV modules were subjected to standardized artificial sunlight and the short circuit currents were measured. Based on the principles of photovoltaic energy conversion, the percentage of solar irradiance transmitted through the laminates and reaching the PV cells was investigated.

2.2.2. Materials

Unidirectional E-glass fabrics from Tissa (Oberkulm, Switzerland) with reinforcement weight, w , of 410 g/m² were used for the laminate reinforcement. Longitudinal rovings constituted 78% of the reinforcement weight, 17% of the weight corresponded to twisted longitudinal yarns and 5% to transversal yarns. Rovings (reference code ACF407-600) were manufactured by Taiwan Glass Industry Corporation (Taipei, Taiwan). The measured fiber diameter was 12.8 ± 1.3 μm . Yarns (reference code EC9-68-620) were manufactured by AGY (Aiken, United States). The measured fiber diameter was 8.9 ± 0.8 μm . The refractive index of the E-glass fibers, n_f , ranged between 1.55 and 1.56 according to Dunkers et al.¹⁶ and Kinsella et al.¹⁷

Polylite 420-181 unsaturated polyester resin, manufactured by Reichhold Inc. (Durham, United States), was selected. This orthophthalic polyester resin, designed for translucent GFRP components, has a refractive index, n_r , adjusted to match the refractive index of E-glass mats according to manufacturer's data sheet. The resin is UV-stabilized by a BASF Tinuvin® additive, absorbing the UV radiation below 380 nm. The resin also has low viscosity (330-360 mPa·s) making it suitable for hand lay-up lamination. Butanox M-60 organic peroxide from AkzoNobel (Amsterdam, Netherlands) was the catalyst used to initiate the polymerization reaction.

Thin-film flexible a-Si PV cells, manufactured by Flexcell (Yverdon-les-Bains, Switzerland),¹⁸ were used for the fabrication of PV modules. The PV cells were cut from a 482-mm-wide roll of interconnected cells, which were produced by a roll-to-roll manufacturing process with final annealing at 150 °C. The structure of the PV cells comprised four different layers of a total thickness of approximately 50 μm . The bottom layer was a polyethylenephthalate (PEN) substrate used as support for the deposition of the three active layers. The materials composing these active layers were: aluminum (the bottom metallic contact of the PV cell), amorphous silicon (the semiconductor material of the PV cell) and indium tin oxide (ITO, the antireflective conductive top layer of the PV cell). These PV cells are sensitive to light wavelengths from 300 nm to 800 nm. The spectral response, $SR(\lambda)$, of the cells is shown in Figure 2.2 and was obtained from the external quantum efficiency data, $EQE(\lambda)$, given by Flexcell, as described by Patra

and Maskell¹⁹. The data obtained for wavelengths, λ , of 350 nm to 800 nm was linearly extrapolated to 300 nm.

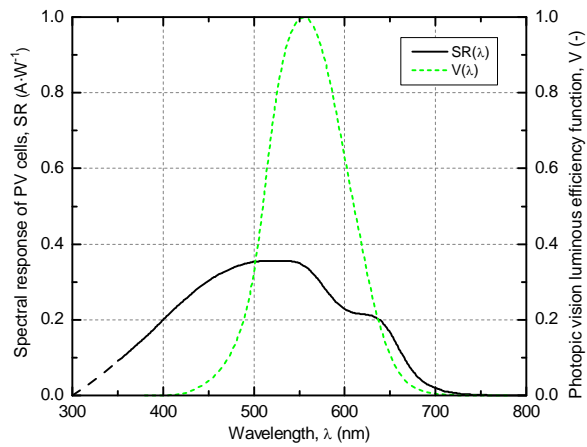


Figure 2.2. Spectral response of Flexcell a-Si PV cells and spectral luminous efficiency function for photopic vision²⁶.

2.2.3. Specimen fabrication

GFRP specimens. Unidirectional (UD) and cross-ply (CP) GFRP laminates with reinforcement weights, w , between 410 and 3280 g/m² (from one to eight layers of E-glass fabrics) were fabricated by a hand lay-up process at room temperature (23±2 °C). The volume of catalyst mixed with the resin corresponded to 1% of the resin weight. The laminates were cured for 24 h under the same temperature, either as they were produced or assisted by a vacuum bag, and were then postcured for another 24 h at 60 °C to obtain fully cured specimens. The former laminates are denominated "hand lay-up" and the latter "vacuum" in the following. Laminates were manufactured with three different fiber volume fractions: series L with low (0.24±0.03), series M with intermediate (0.32±0.02) and series H with high (0.42±0.01) fiber volume fraction.

Eight UD specimens (reinforcement weight, w , from 410 to 3280 g/m²) and four CP symmetric specimens (of 1230 and 1640 g/m²) were cut from the hand lay-up laminates (one specimen per laminate). Furthermore, one UD and one CP specimen (of 820 g/m²) were cut from the laminates fabricated by the vacuum process. Specimens were labeled according to their reinforcement weight, fiber architecture and fiber volume fraction, e.g. 1640CP-L refers to the specimen reinforced with $w = 1640$ g/m² of E-glass fibers, with cross-ply fiber architecture and low fiber volume fraction. The nominal specimen dimensions were 120x175 mm² for specimens with $w \leq 820$ g/m² and 90x90 mm² for the other specimens. Fiber volume fraction and thickness of all GFRP specimens are given in Table 2.1.

In addition, one pure resin specimen (60x60x1 mm³) was fabricated and cured without vacuum bag using the same procedure as for the other specimens.

PV modules. Seven PV modules with three serial-connected PV cells in each module were fabricated by hand lay-up at room temperature (23±2 °C), as shown in Figure 2.3. The PV cells were cut from a roll of interconnected cells and two metallic electric connectors (supplied by Flexcell) were incorporated as the positive and negative terminals for each group of cells. Additionally, a reference non-encapsulated PV module with three serial-connected bare cells was fabricated.

The dimensions and through-thickness components of the PV modules are shown in Figure 2.4. The PV modules consisted of three different components: a rectangular glass pane support ($300 \times 250 \times 10 \text{ mm}^3$), three connected a-Si PV cells ($150 \times 50 \text{ mm}^2$) and the GFRP encapsulant. One UD layer of E-glass was laminated onto the glass support and the thin PV cells were placed in the wet resin on top of this layer. The upper GFRP encapsulant, also fabricated using 1% of catalyst, was laminated over the PV cells. The fiber architecture and reinforcement weight of the upper encapsulant differed for each module according to Table 2.2 (from 410 to 3280 g/m² in UD and CP architecture). The fiber volume fraction of the GFRP encapsulation could not be controlled during fabrication. Since postcuring at elevated temperature could not be applied in order to avoid the risk of damaging the electronic connectors, the PV modules were cured at room temperature ($23 \pm 2 \text{ }^\circ\text{C}$) for seven days to obtain full cure.

Table 2.1. Fiber volume fraction and thickness of fabricated GFRP specimens.

Series	Property	Unidirectional specimens					Cross-ply specimens		
		410UD	820UD	1230UD	1640UD	3280UD	820CP	1230CP	1640CP
L	Vol. fraction (-)	0.21	0.23	0.24	0.29	-	-	0.22	0.25
	Thickness (mm)	0.8 ± 0.13	1.4 ± 0.09	2.0 ± 0.13	2.2 ± 0.10	-	-	2.1 ± 0.07	2.6 ± 0.21
M	Vol. fraction (-)	-	0.31*	0.33	-	0.34	0.30*	-	-
	Thickness (mm)	-	1.0* ± 0.04	1.4 ± 0.06	-	3.8 ± 0.09	1.1* ± 0.04	-	-
H	Vol. fraction (-)	-	-	0.41	0.43	-	-	0.40	0.41
	Thickness (mm)	-	-	1.2 ± 0.07	1.5 ± 0.06	-	-	1.2 ± 0.03	1.5 ± 0.02

* specimens fabricated by the vacuum process.

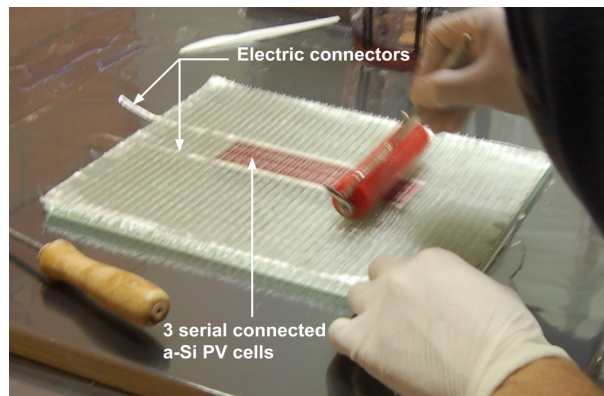


Figure 2.3. Hand lay-up encapsulation of three serial-connected a-Si PV cells in GFRP.

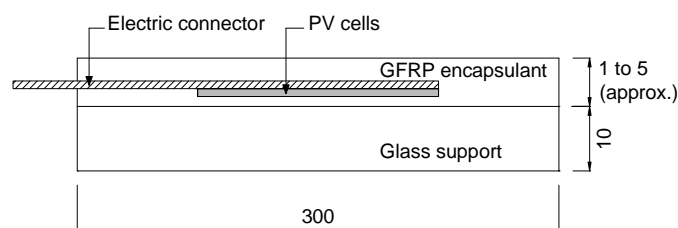


Figure 2.4. Dimensions (mm) and components of PV modules with a-Si PV cells (not to scale).

Table 2.2. Short circuit currents for PV modules with different fiber architecture of upper encapsulants.

PV cells upper encapsulant	I_{sc} (mA)	$T_{PV\ exp}$ (-)
none	187	1
410UD	164	0.88
820UD	155	0.83
1230UD	152	0.81
1640UD	140	0.75
3280UD	118	0.63
1230CP	-	-
1640CP	136	0.73

2.2.4. Experimental set-up

Spectrophotometry. The hemispherical spectral total light transmittance, T_t , of the fourteen GFRP specimens was investigated by spectrophotometry with a 152-mm-diameter integrating sphere as shown in Figure 2.5. The measurements were performed using a halogen light source (Osram 64642 HLX, 150 W, 24 V, Xenophot®), an integrating sphere (LOT RT-060-SF) and a spectrophotometer (Oriel, model 77400, MultiSpec 125™, type 1/8m) measuring from 400 to 800 nm and connected to a computer equipped with InstaSpec™ II software for signal analysis. The set-up is schematically shown in Figure 2.6. Optical lenses and a 1-mm diaphragm were used to collimate a beam of light from the source. The beam was reflected in a plane mirror and then passed through a 5-mm-diameter diaphragm. Specimens were located at the entrance port A and crossed by the beam of light at nearly normal incidence (81°). The specimens were oriented with the reinforcement rovings forming an approximate angle of 45° with the horizontal plane (see Figure 2.5). Port B of the sphere remained closed. The light passing through the specimen was reflected and uniformly scattered by the sphere's white interior (barium sulfate) coating. Incoming light from point C entered the spectrophotometer where it was split into components of different wavelengths by a diffraction grating. A detector head consisting of photodiode arrays connected to InstaSpec™ II software allowed the amount of light reaching the detector to be computed. Transmittance was the result of a relative measurement with and without specimen on the entrance port A. For each specimen, four measurements at different locations of the specimen were performed and, in the following, the average spectral curves will be presented.

The total hemispherical spectral light transmittance, T_t , and reflectance, R , of the 1-mm-thick resin specimen (without fibers) was also investigated. For the total reflectance experiment the specimen was located at port B, with port A kept open.

Solar radiation flash. The percentage of solar irradiance reaching the surface of a-Si PV cells encapsulated in GFRP material was investigated, subjecting the fabricated PV modules to a standardized radiation flash of 1000 W/m² and measuring the generated short circuit current. The flasher reproduced the terrestrial reference hemispherical solar spectral irradiance, $E(\lambda)$, according to ASTM G173-03 for an air mass value (AM) of 1.5.²⁰ This spectral distribution of radiation, shown in Figure 2.7, is the common reference for evaluating spectrally selective PV solar cells. The experiments were performed at ambient temperature between 19 °C and 20 °C.

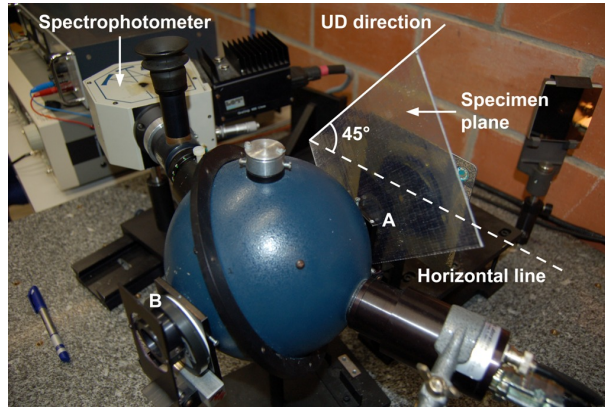


Figure 2.5. Integrating sphere with GFRP specimen located in port A for total light transmittance experiment.

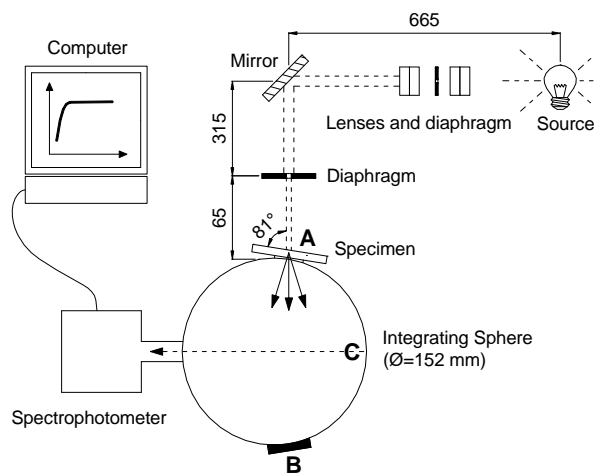


Figure 2.6. Schematic representation of integrating sphere set-up (top view, dimensions in mm).

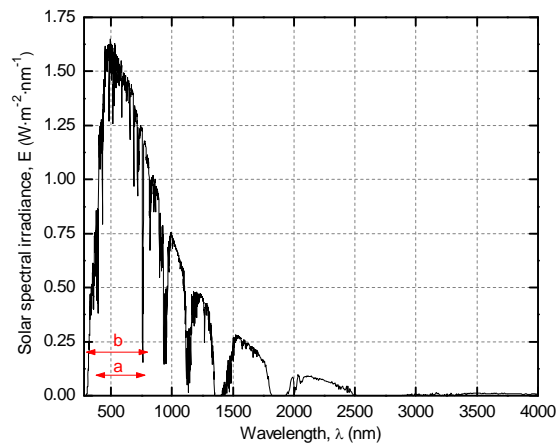


Figure 2.7. Hemispherical solar spectral irradiance of 1000 W/m² and AM1.5 (a: wavelength range of visible light, b: wavelength range of solar response of a-Si PV cells).²⁰

2.3. Experimental results and discussion

2.3.1. Spectrophotometric experiments

The measured spectral light transmittance curves of the UD specimens are shown in Figure 2.8. Light transmittance decreased when the reinforcement weight was increased. However, for the same reinforcement weight, the fiber volume fraction had no influence on the light transmittance, as shown in Figure 2.9. The transmittance of UD and CP specimens is compared in Figure 2.10. For the hand lay-up fabrication, the transmittance of CP specimens was approximately 4% lower than that of UD specimens. This difference was less than 1% for specimens fabricated by the vacuum process. However, GFRP specimen transmittances obtained with the vacuum fabrication process were approximately 5% lower than those achieved by the hand lay-up process (see Figure 2.11).

The transmittance and reflectance results of the polyester resin specimen are also shown in Figure 2.8. Light absorption in the resin started at 430-nm wavelength and increased linearly until 400 nm. Using another spectrophotometer (Perkin Elmer Lambda 2), measuring regular transmittance from 190 nm to 1100 nm, showed that transmittance disappeared completely at 380 nm, from which point the light was absorbed by the UV additive. The spectral transmittance curves of the resin and GFRP specimens were therefore linearly extrapolated to zero at 380 nm, as shown in Figure 2.8.

The experimental total transmittance results at wavelengths of 555 nm and 700 nm, $T_{t,555 \text{ exp}}$ and $T_{t,700 \text{ exp}}$, of the pure resin, UD-L and 3280UD-M specimens are shown in Figure 2.12. The 555-nm wavelength approximately corresponds to the maximum spectral response of the PV cells (see Figure 2.2) and the maximum solar spectral irradiance (see Figure 2.7). At 700 nm, the maximum values of total transmittance were observed (see Figures 2.8 to 2.11), which, however, were only 0.02 on average higher than at 555 nm. The standard deviations of the four measurements per specimen at each wavelength were small: ± 0.02 for specimen 3280UD-M and ± 0.01 for the UD-L specimens, indicating good reproducibility and accuracy of the measurements.

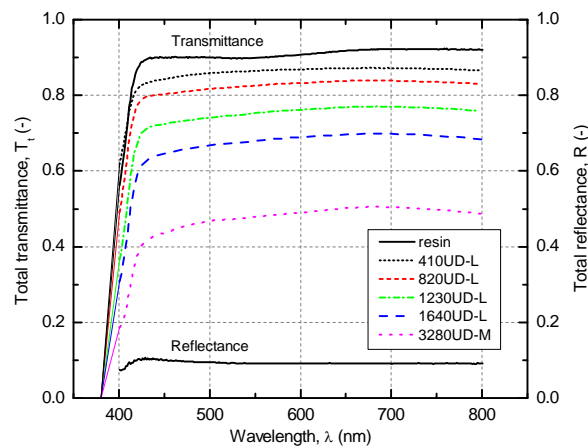


Figure 2.8. Spectral transmittance of unidirectional specimens at different reinforcement weights and transmittance and reflectance of 1-mm-thick resin specimen.

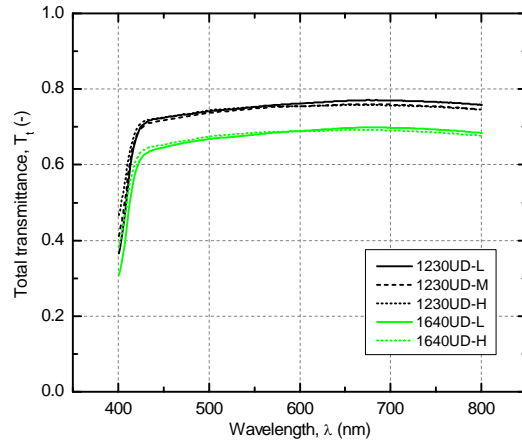


Figure 2.9. Spectral transmittance of unidirectional specimens at different volume fractions.

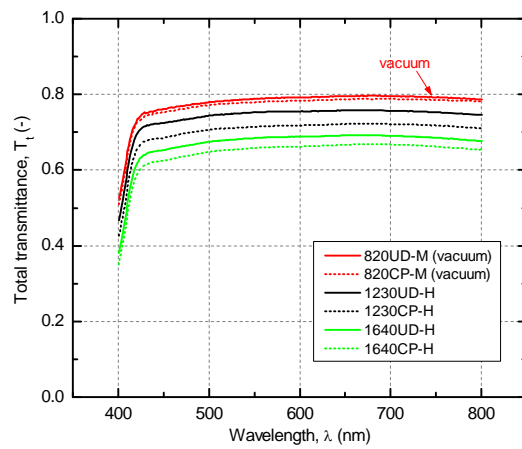


Figure 2.10. Spectral transmittance of unidirectional and cross-ply specimens.

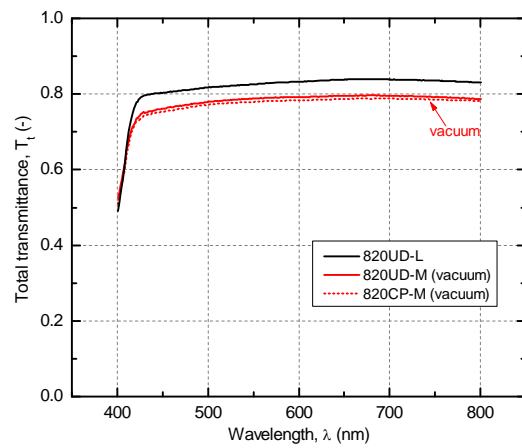


Figure 2.11. Spectral transmittance of hand lay-up and vacuum specimens with $w = 820 \text{ g/m}^2$.

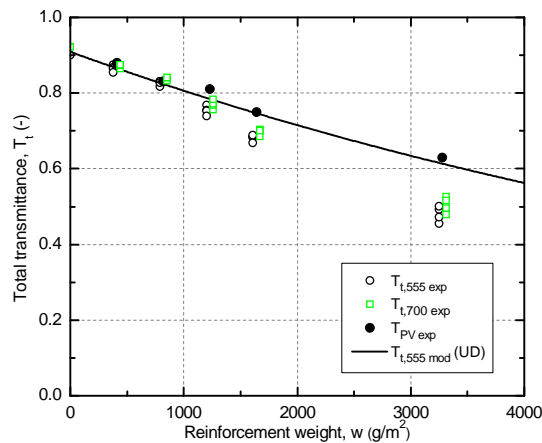


Figure 2.12. Transmittance measurements at 555-nm wavelength, from solar radiation flash experiments and analytical model (UD specimens).

2.3.2. Solar radiation flash experiments

The short circuit current, I_{sc} , of a solar cell is directly proportional to the irradiance reaching the surface of the cell.²¹ An experimental value of the light transmittance, $T_{PV exp}$, of the encapsulation system was therefore defined as the ratio between the I_{sc} generated by the encapsulated cells and the I_{sc} generated by the bare cells. The results are shown in Table 2.2 and Figure 2.12. The PV cells with the 1230CP upper encapsulant did not generate any current during the experiment and it was concluded that these cells were damaged during the encapsulation process.

2.3.3. Comparison of experimental results

The light transmittance results obtained from spectrophotometric experiments at 555-nm wavelength, $T_{t,555 exp}$, and solar radiation flash experiments, $T_{PV exp}$, are compared in Figure 2.12. Both sets of results show that light transmittance significantly decreased when reinforcement weight increased. However, for $w > 820 \text{ g/m}^2$, $T_{t,555 exp}$ decreased much faster than $T_{PV exp}$. It was concluded that in the spectrophotometric measurements, for $w > 820 \text{ g/m}^2$, not all of the scattered light inside the specimen passed through port A of the integrating sphere. The results obtained from the integrating sphere are therefore reliable only for low scattering specimens and the $T_{t,555 exp}$ results for $w > 820 \text{ g/m}^2$ were discarded in the following study.

In an ideal laminate with perfectly matching refractive indices and without any air inclusions, the transmittance should be independent on the reinforcement weight and architecture. The observed dependence of the transmittance on the reinforcement weight and, to a lesser extent, on the reinforcement architecture (UD or CP) and fabrication process may be attributed to three effects: 1) Even a small mismatch of the refractive indices of fibers and resin reduces transmittance; this reduction increases with increasing reinforcement weight (but remains independent of the volume fraction). 2) Hand lamination cannot prevent the inclusion of some air pores, which represent a "material" (air) with a different refractive index. Locations sensitive to such voids are, in particular, crossings of fibers in CP laminates, which explains the slightly lower transmittance of CP compared to UD laminates. This hypothesis is supported by the lower UD-CP transmittance difference of vacuum specimens. 3) Slightly higher curing temperatures inside the vacuum bag may have reduced fiber impregnation time and accelerated resin

shrinkage and thus increased the formation of non-wet fibers or microcracks, which explains the slightly lower transmittance of vacuum compared to hand lay-up laminates.

As shown in Table 2.2, encapsulant 820UD had a transmittance $T_{PV\,exp} = 0.83$, which is between 7% and 13% lower than that of traditional encapsulations.⁸ The Archinsolar project showed that a 10% loss in efficiency, and therefore a 10% loss of transmittance, is well accepted for architecturally well integrated PV modules.²² The slightly lower efficiency of the encapsulation of PV cells into multifunctional GFRP elements with load-bearing capacity presented here thus seems acceptable.

2.4. Modeling of light transmittance

2.4.1. Model based on spectrophotometric measurements

A new theoretical model to predict light transmittance through GFRP laminates can be established if the following points are assumed:

- incident radiant flux, P_0 , and transmitted radiant flux, P , are normal to the surfaces of the laminate,
- multiple reflections inside the laminate are disregarded,
- a loss of transmittance, $L(w)$, occurs inside the laminate, which depends on the reinforcement weight, w , reinforcement architecture and fabrication process.

According to ASTM E772-11,²³ transmittance, T , is defined as the ratio of the transmitted radiant flux, P , to the incident flux, P_0 :

$$T = \frac{P}{P_0} \quad (2.3)$$

Reflectance is defined in ASTM E772-11 as the ratio of the reflected radiant flux to the incident flux.²³ The transmitted radiant flux, P , is therefore:

$$P = (1 - r_{in}) \cdot (1 - r_{out}) \cdot (1 - L(w)) \cdot P_0 \quad (2.4)$$

where r_{in} and r_{out} are the reflectance of the first and second air/resin interfaces. For an incident flux normal to the laminate surface and considering Fresnel Equations,⁹ reflectance is calculated as:

$$r_{in} = \left(\frac{n_r - n_a}{n_r + n_a} \right)^2 \quad (2.5)$$

$$r_{out} = \left(\frac{n_a - n_r}{n_r + n_a} \right)^2 \quad (2.6)$$

where n_r is the refractive index of resin and n_a is the refractive index of air. Thus:

$$r_{in} = r_{out} = r \quad (2.7)$$

where r is the reflectance of an air/resin interface, leads to:

$$T = (1 - r)^2 \cdot (1 - L(w)) \quad (2.8)$$

Assuming that multiple reflections are disregarded, a total reflectance of $R = 2r$ results for a pure resin laminate. Disregarding second order terms, the transmittance model is given by:

$$T = (1 - R) \cdot (1 - L(w)) \quad (2.9)$$

where transmittance, T , is spectrally defined since R and $L(w)$ are wavelength dependent. The total reflectance, R , is shown in Figure 2.8. To specify the total loss, $L(w)$, the loss at one specific weight, $L(w_1)$, (e.g. for one fiber layer) must be known or measured. If a GFRP laminate with reinforcement weight $w > w_1$ is sliced in w/w_1 layers with constant reinforcement weight, w_1 , in each layer, the total loss is:

$$L(w) = 1 - \left(1 - L(w_1)\right)^{\frac{w}{w_1}} \quad (2.10)$$

where $L(w_1)$ is denominated "calibration parameter" in the following.

At 555-nm wavelength $R = 0.091$ and therefore, according to equation (2.9), the model for total light transmittance is given by:

$$T_{t,555 \text{ mod}} = 0.909 \cdot (1 - L_{555}(w)) \quad (2.11)$$

where $L_{555}(w)$ is the loss of transmittance of GFRP at 555 nm and is calibrated in the following for UD and CP laminates at $w_1 = 410 \text{ g/m}^2$. For UD laminates assuming $T_{t,555 \text{ mod}} = 0.865$ (average of four 410UD-L measurements) and $w = w_1$, the solution of equation (2.11) for the calibration parameter at 555 nm is $L_{555}(w_1) = 0.048$. According to equation (2.10) the loss of transmittance at 555-nm wavelength for UD laminates is therefore given by:

$$L_{555UD}(w) = 1 - 0.952^{\frac{w}{410}} \quad (2.12)$$

The transmittance model, $T_{t,555 \text{ mod}}$, is shown in Figure 2.12 and the loss of transmittance, L_{555UD} , in Figure 2.13. The model agrees well with the measured transmittance, $T_{PV \text{ exp}}$.

Concerning the CP laminates, no reliable spectrophotometric measurement for $w \leq 820 \text{ g/m}^2$ was available. Taking into account, however, that the transmittance of specimen 1640CP-L was 4% lower than that of 1640UD-L and a similar reduction (3%) was measured on the PV modules (1640CP compared to 1640UD, see Table 2.2), the model $T_{t,555 \text{ mod}}$ of equation (2.11) was applied for a UD laminate with $w = 1640 \text{ g/m}^2$ and the result was reduced by 4% to $T_{t,555 \text{ mod}} = 0.717$. Therefore, the solution of equation (2.11) for the loss of transmittance of CP laminates at $w = 1640 \text{ g/m}^2$ is $L_{555}(w) = 0.211$. Substituting these values into equation (2.10), $L_{555}(w_1) = 0.058$ results for $w_1 = 410 \text{ g/m}^2$. The loss of transmittance at 555-nm wavelength for CP laminates is therefore given by:

$$L_{555CP}(w) = 1 - 0.942^{\frac{w}{410}} \quad (2.13)$$

The L_{555CP} curve is also shown in Figure 2.13. As discussed above, the CP laminate losses are higher than the UD losses, which is attributed to the hand lay-up method.

The loss of transmittance, $L_{555}(w)$, is also calibrated at $\lambda = 555 \text{ nm}$ for laminates fabricated by the vacuum process. The calibration parameter $L_{555}(w_1)$ is calculated from the average measurements performed on specimens 820UD-M and 820CP-M (see Figure 2.10). The values of the calibration parameter $L_{555}(w_1)$ are summarized in Table 2.3 for different reinforcement architectures and fabrication

processes. The L_{555UD} and L_{555CP} curves for vacuum fabrication are shown in Figure 2.13. As already discussed, the UD-CP vacuum laminate losses are higher than the UD-CP hand lay-up laminate losses.

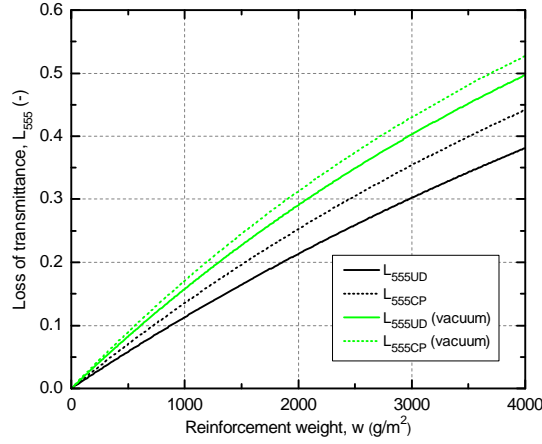


Figure 2.13. Loss of transmittance, $L_{555}(w)$, at 555 nm.

Table 2.3. Calibration parameter, $L_{555}(w_1)$, as function of reinforcement architecture and fabrication process.

	$L_{555}(w_1)$ for $w_1 = 410 \text{ g/m}^2$ (-)	
	Hand lay-up fabrication	Vacuum fabrication
UD laminate	0.048	0.068
CP laminate	0.058	0.074

2.4.2. Model based on short circuit current measurements

For an encapsulated PV cell, sensitive to light wavelengths in the band from λ_1 to λ_2 , the transmittance of the encapsulant can be determined according to Samuels et al.⁸ as follows:

$$T_{PV\ mod} = \frac{I_{sc\ encaps.\ cell}}{I_{sc\ bare\ cell}} = \frac{A \cdot \int_{\lambda_1}^{\lambda_2} SR(\lambda) \cdot T_t(\lambda) \cdot E(\lambda) \cdot d\lambda}{A \cdot \int_{\lambda_1}^{\lambda_2} SR(\lambda) \cdot E(\lambda) \cdot d\lambda} \quad (2.14)$$

where A is the area of the PV cell (m^2), $SR(\lambda)$ is the spectral response of the PV cell ($\text{A} \cdot \text{W}^{-1}$) (see Figure 2.2), $T_t(\lambda)$ is the spectral total transmittance of the PV cell upper encapsulant (-) and $E(\lambda)$ is the solar spectral irradiance ($\text{W} \cdot \text{m}^{-2} \cdot \text{nm}^{-1}$) (see Figure 2.7). The numerator of equation (2.14) corresponds to the short circuit current of the encapsulated PV cell and the denominator is the short circuit current of the bare PV cell. The limits of the integrals of equation (2.14) are $\lambda_1 = 300 \text{ nm}$ and $\lambda_2 = 800 \text{ nm}$, and correspond to the spectral range of the PV cell (see Figure 2.2).

Equation (2.14) was evaluated for the four spectrophotometric measurements performed on specimens 410UD-L and 820UD-L; the results are shown in Tables 2.4 and 2.5 (columns $T_{PV\ mod}$). For encapsulant 410UD-L, $T_{PV\ mod}$ was 7% lower than $T_{PV\ exp}$ and for encapsulant 820UD-L this difference was 6%. Good agreement existed therefore between the transmittance measurements of the PV modules and the predictions. The small discrepancies may be attributed to two effects: 1) In the $T_{PV\ exp}$ measurements the back reflectance, r_{out} , was very small due to the presence of the antireflective ITO layer of the

encapsulated cell. Considering a refractive index of 1.90 for ITO and 1.56 for the resin, the reflectance in this interface would result in $r_{out} \approx 0.01$ according to equation (2.6).²⁴ The transmittance spectrums, $T_t(\lambda)$, used for the calculation of $T_{PV\ mod}$, however, were obtained from the integrating sphere where the specimens had air/resin interfaces on both sides with $r_{out} \approx 0.045$ (half the value of the total reflectance R in Figure 2.8). 2) The transmittance spectrums obtained with the integrating sphere set-up, and used in equation (2.14), may be slightly underestimated due to a small amount of light scattered by the specimen outside the sphere at its entrance port.

Furthermore, the values of $T_{PV\ mod}$ are just 6% lower than the transmittance at 555 nm, $T_{t,555\ exp}$ (see Tables 2.4 and 2.5). As this difference is similar to that between $T_{PV\ mod}$ and $T_{PV\ exp}$, the model $T_{t,555\ mod}$ of equation (2.11) can also be used to predict $T_{PV\ exp}$ and therefore the percentage of solar irradiance reaching a-Si PV cells encapsulated in GFRP.

Table 2.4. Mean values of light transmittance for specimen 410UD-L and corresponding PV module.

Wavelengths	300 – 800 nm		380 – 780 nm	555 nm
	$T_{PV\ mod}$ (-)	$T_{PV\ exp}$ (-)	$T_{t,vis}$ (-)	$T_{t,555\ exp}$ (-)
Measurement 1	0.83	-	0.87	0.87
Measurement 2	0.82	-	0.87	0.87
Measurement 3	0.82	-	0.86	0.86
Measurement 4	0.81	-	0.86	0.86
PV module	-	0.88	-	-
Mean	0.82±0.01	0.88	0.87±0.01	0.87±0.01

Table 2.5. Mean values of light transmittance for specimen 820UD-L and corresponding PV module.

Wavelengths	300 – 800 nm		380 – 780 nm	555 nm
	$T_{PV\ mod}$ (-)	$T_{PV\ exp}$ (-)	$T_{t,vis}$ (-)	$T_{t,555\ exp}$ (-)
Measurement 1	0.79	-	0.83	0.83
Measurement 2	0.78	-	0.83	0.83
Measurement 3	0.77	-	0.82	0.82
Measurement 4	0.78	-	0.83	0.83
PV module	-	0.83	-	-
Mean	0.78±0.01	0.83	0.83±0.01	0.83±0.01

2.4.3. Modeling of mean value of visible total light transmittance

For architectural applications, the GFRP visible total light transmittance, $T_{t,vis}$, is of particular interest since it allows the creation of translucent structures. Based on ASTM E1175-87,²⁵ the mean value of visible total transmittance for a given material is:

$$T_{t,vis} = \frac{\int_{380}^{780} V(\lambda) \cdot T_t(\lambda) \cdot E(\lambda) \cdot d\lambda}{\int_{380}^{780} V(\lambda) \cdot E(\lambda) \cdot d\lambda} \quad (2.15)$$

where $V(\lambda)$ is the spectral luminous efficiency function for photopic vision, representing the efficiency of an electromagnetic radiation of wavelength λ in producing a visual sensation on the human eye (see Figure 2.2).²⁶ The limits of the integrals in equation (2.15) correspond to the limit wavelengths of the visual range of spectral sensitivity, i.e. from 380 to 780 nm. The resulting mean values $T_{t,vis}$ for specimens

410UD-L and 820UD-L are given in Tables 2.4 and 2.5 and were identical to the transmittance at 555 nm due to the maxima of functions $E(\lambda)$ and $V(\lambda)$ in the region of this wavelength (see Figures 2.2 and 2.7). Therefore the visible light transmittance of UD and CP laminates is given by:

$$T_{t,vis} = T_{t,555\ mod} \quad (2.16)$$

where model $T_{t,555\ mod}$ is defined in equation (2.11).

2.4.4. Application of existing model

The model proposed by Iba et al.^{11,12} (equations (2.1) and (2.2)) was applied at $\lambda = 555$ nm to the UD specimens of Table 2.1, assuming different mismatches of refractive index $\Delta n = 0.001, 0.0005, 0.0001$ between resin and glass fibers. Furthermore, $R_f = 6.4 \mu\text{m}$ and $T_m = 1 - R = 0.909$ were assumed. The results, shown together with model $T_{t,555\ mod}$ in Figure 2.14, are very sensitive to even small mismatches in the refractive indices. Assuming a perfect agreement of the indices results in a constant transmittance, independent of reinforcement weight, as discussed above. The applicability of this model, however, requires very accurate measurements of the refractive indices of the material components.

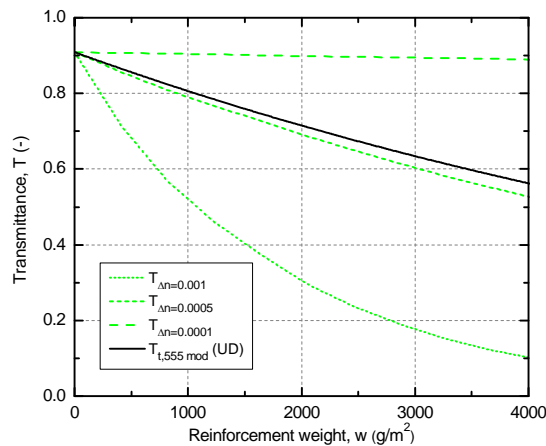


Figure 2.14. Comparison of modeling results according to Iba et al.^{11,12} and equation (2.11) for UD laminates.

2.4.5. Application to generate spectral transmittance curves

The transmittance model of equation (2.9) is wavelength dependent and can be used to predict light transmittance, $T(\lambda)$, at any wavelength. Considering the spectral reflectance curve of the resin (see Figure 2.8) and selecting the spectral transmittance curve of specimen 410UD-L as reference, the calibration parameter $L(w_i)$ was calculated for the wavelengths in the band of 400 to 800 nm (see Figure 2.15) and linearly extrapolated to one at 380 nm, from which point the light was absorbed by the UV additive. Based on this result, the spectral transmittance curves of two UD hand lay-up GFRP specimens with reinforcement weights of 820 and 3280 g/m^2 were predicted. The predicted and experimental curves are compared in Figure 2.16 and agree well for $w = 820 \text{ g/m}^2$. For $w = 3280 \text{ g/m}^2$, however, the predicted transmittance is higher than the measured one. As discussed above, this difference is due to losses of scattered light at the entrance port of the integrating sphere. Based on equation (2.15),

the predicted curves were integrated and the results matched well with the visible light transmittance predictions from equation (2.16), thereby showing the consistency of the developed analytical model.

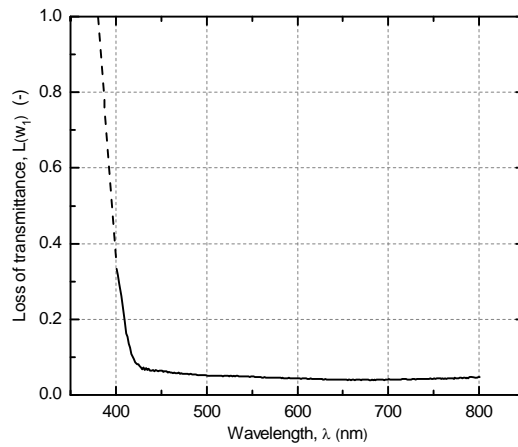


Figure 2.15. Spectral curve of loss parameter, $L(w_1)$, for UD laminates without vacuum bag ($w_1 = 410 \text{ g/m}^2$).

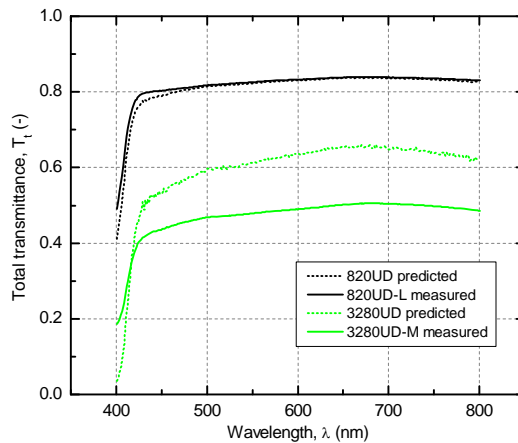


Figure 2.16. Measured and predicted spectral transmittance for $w = 820 \text{ g/m}^2$ and $w = 3280 \text{ g/m}^2$.

2.5. Conclusions

The total light transmittance of GFRP laminates for building construction applications was measured and analytically modeled. The following conclusions were drawn:

1. A model for predicting the wavelength-dependent spectral light transmittance of GFRP laminates is proposed, whose predictions compare well with the experimental results. To calibrate the model for other materials, the spectral reflectance curve of a 1-mm-thick pure resin specimen and the spectral transmittance curve of a GFRP laminate are required.
2. The most important parameter affecting the light transmittance of GFRP is the fiber reinforcement weight of the laminate, the transmittance increases with decreasing weight. The fiber volume fraction (for a constant fiber reinforcement weight) has no influence on light transmittance.
3. Small-diameter integrating sphere measurements are reliable for low scattering laminates only. Measurements based on the short circuit current generation of encapsulated PV cells lead to more accurate values of GFRP light transmittance, particularly for thicker laminates.

4. The solar irradiance in the band of 300-800 nm, reaching a-Si PV cells encapsulated in GFRP, is reduced by approximately 10% compared to traditional encapsulating systems if a structurally significant reinforcement weight of 820 g/m² is used for the covering layer. This drawback, however, can be compensated by the possible integration of PV cells into multifunctional load-bearing components, opening up new possibilities in architectural design.

2.6. References

1. Keller T, Haas C and Vallée T. Structural concept, design, and experimental verification of a glass fiber-reinforced polymer sandwich roof structure. *J Compos Constr* 2008; 12(4):454-468.
2. Keller T, de Castro J and Schollmayer M. Adhesively bonded and translucent glass fiber reinforced polymer sandwich girders. *J Compos Constr* 2004; 8(5):461-470.
3. ASTM Standard E284-12, 2012. *Standard Terminology of Appearance*. West Conshohocken, PA: American Society for Testing and Materials, August 2012.
4. Sawai H, Toshikawa H, Shibata A, et al. The development of a low cost photovoltaic module using FRP molded encapsulation. In: *Proceedings of the 16th IEEE Photovoltaic Specialists Conference*, San Diego, USA, 28 September 1982, pp.932-937. Piscataway, NJ: IEEE.
5. Rion J. *Ultra-light photovoltaic composite sandwich structures*. PhD thesis, Ecole Polytechnique Fédérale de Lausanne, Switzerland, 2008.
6. Maung KJ, Hahn HT and Ju YS. Multifunctional integration of thin-film silicon solar cells on carbon-fiber-reinforced epoxy composites. *Sol Energy* 2010; 84(3):450-458.
7. Keller T, Vassilopoulos AP and Manshadi BD. Thermomechanical behavior of multifunctional GFRP sandwich structures with encapsulated photovoltaic cells. *J Compos Constr* 2010; 14(4):470-478.
8. Samuels SL, Glassmaker NJ, Andrews GA, et al. Teflon® FEP frontsheets for photovoltaic modules: improved optics leading to higher module efficiency. In: *Proceedings of the 35th IEEE Photovoltaic Specialists Conference*, Honolulu, USA, 20-25 June 2010, pp.2788-2790. Piscataway, NJ: IEEE.
9. Hecht E. *Optics*, 4th ed. San Francisco: Addison Wesley, 2002.
10. van de Hulst HC. *Light scattering by small particles*. New York: Dover Publications, 1981.
11. Iba H and Kagawa Y. Light transmittance of continuous fibre-reinforced composites: analysis, model experiment and parametric study. *Philos Mag B* 1998; 78(1):37-52.
12. Iba H, Naganuma T, Matsumura K, et al. Fabrication of transparent continuous oxynitride glass fiber-reinforced glass matrix composite. *J Mat Sci* 1999; 34(23):5701-5705.
13. Kim KS, Kollár L and Springer GS. A model for embedded fiber optic Fabry-Perot temperature and strain sensors. *J Compos Mater* 1993; 27(17):1618-1662.
14. Kagawa Y, Iba H, Tanaka M, et al. Fabrication and optical/thermal properties of glass particle-epoxy optically transparent composites. *Acta Mater* 1998; 46(1):265-271.
15. Lin H, Day DE, Weaver KD, et al. Temperature and wavelength dependent transmission of optically transparent glass fiber poly(methyl methacrylate) composites. *J Mat Sci* 1994; 29(19):5193-5198.
16. Dunkers JP, Parnas RS, Zimba CG, et al. Optical coherence tomography of glass reinforced polymer composites. *Compos Part A* 1999; 30(2):139-145.

17. Kinsella M, Murray D, Crane D, et al. Mechanical properties of polymeric composites reinforced with high strength glass fibers. In: *Proceedings of the 33rd International SAMPE Technical Conference*, Seattle, USA, 5-8 November 2001, pp.1644-1657. Covina, CA: SAMPE.
18. Pagliario M, Palmisano G and Ciriminna R. *Flexible Solar cells*. Weinheim: Wiley-VCH, 2008.
19. Patra JC and Maskell DL. Modeling of multi-junction solar cells for estimation of EQE under influence of charged particles using artificial neural networks. *Renew Energy* 2012; 44:7-16.
20. ASTM Standard G173-03, 2008. *Standard Tables for Reference Solar Spectral Irradiances: Direct Normal and Hemispherical on 37° tilted Surface*. West Conshohocken, PA: American Society for Testing and Materials, October 2008.
21. Markvart T (ed). *Solar electricity*, 2nd ed. Chichester: John Wiley & Sons, 2000.
22. Péliisset S, Joly M, Chapuis V, et al. Efficiency of silicon thin-film photovoltaic modules with a front coloured glass. In: *Proceedings of CISBAT International Conference*, Lausanne, Switzerland, 14-16 September 2011, pp.37-42. Lausanne: LESO-PB.
23. ASTM Standard E772-11, 2011. *Standard Terminology of Solar Energy Conversion*. West Conshohocken, PA: American Society for Testing and Materials, November 2011.
24. Sathiaraj TS. Effect of annealing on the structural, optical and electrical properties of ITO films by RF sputtering under low vacuum level. *Microelectron J* 2008; 39(12):1444-1451.
25. ASTM Standard E1175-87, 2009. *Standard Test method for Determining Solar or Photopic Reflectance, Transmittance and Absorptance of Materials Using a Large Diameter Integrating Sphere*. West Conshohocken, PA: American Society for Testing and Materials, June 2009.
26. CIE 1932. In: *Report of activities and proceedings of the Commission Internationale de l'Eclairage*, Cambridge, United Kingdom, 14-19 September 1931, pp.25-26. Cambridge: Cambridge University Press.

3 Diffuse light transmittance of GFRP laminates

3.1. Introduction

Today, iconic building projects creating lighting effects on their facades are constructed using polymer materials. The visual perception of the building facade changes according to the illumination conditions, thus increasing the architectural expression of the building. For this purpose, load-bearing glass fiber-reinforced polymer (GFRP) laminates offering high total light transmittance are increasingly used due to their low cost, light weight and impact resistance compared to traditional glass facade components.^{1,2}

The total light transmittance, T_t , of a laminate crossed by a beam of light comprises two components: the regular transmittance, T_r , related to the amount of light crossing the specimen in the same direction as the incident beam, and the diffuse transmittance, T_d , related to the light crossing the specimen with a change in the direction. The proportions of T_r and T_d with respect to the total transmittance define the transparency (T_r/T_t) and translucency (T_d/T_t) of the laminate, the latter being referred to as haze when given in terms of a percentage.³ Both components are wavelength-dependent.

A transparent glazing transmitting bright light, such as sunlight, into a room can create visual discomfort due to an inappropriate distribution of luminance, designated glare, that reduces the ability to perceive details,³ i.e. on a blackboard or computer screen. Recent research carried out in schools has demonstrated that student performance increased with the amount of daylight in classrooms and especially with the amount of diffuse daylight transmitted through the building skin.⁴ These findings led to new strategies in the design of daylit schools using translucent and curved glazing components.⁵ Another study characterizing the lighting conditions in museums revealed the disadvantages of direct sunlight illumination: direct light damages the integrity of sensitive works and also decreases their visibility due to direct glare.⁶ For low-rise buildings, e.g. schools, gymnasiums and commercial and convention centers, the use of skylights diffusing daylight inside the building constitute an efficient solution to reduce electricity consumption, whereby a minimum translucency of 0.90 (haze of 90%) and a minimum visible total light transmittance of 0.50 are recommended.^{7,8} For this purpose translucent structural GFRP components may be a valuable option. In addition to light transmittance requirements, the design of skylights has also to take into account fire resistance requirements. Flame retardant transparent resins, however, exist which provide transmittances higher than the 0.50 minimum value.

multifunctional translucent GFRP structures with minimum light transmittance of 0.83 are also being investigated for the encapsulation of photovoltaic (PV) cells,^{9,10} for solar energy building applications, particularly of low cost amorphous silicon (a-Si) cells because of their higher performance under diffuse light conditions compared to crystalline silicon (c-Si) cells.^{11,12}

Ray-tracing software, based on ray optics (also known as geometrical optics), is used in architectural applications for simulating the realistic illumination of virtual environments.^{13,14} According to this theory, a refractive index, n , defined as the ratio between the velocity of light in the vacuum and in the medium, optically characterizes the medium and the light propagated in it in the form of straight lines (rays). Parts of these rays can be absorbed by the medium, and – according to the laws of reflection and refraction – parts are reflected and transmitted at the boundaries between the different refractive index media. However, the most complete modeling of light (apart from its quantum nature) is provided by electromagnetic optics, which describes the propagation of light in the form of two mutually coupled vector waves: an electric-field wave and a magnetic-field wave.¹⁵ According to this theory, and depending on the polarization and phase of light, the reflectance at interfaces can be quantified and the interference of light waves explained. However, as long as light waves propagate through and around objects whose dimensions are much greater than the wavelength, λ , ray optics theory is sufficiently accurate for describing light scattering.^{15,16} The more this condition is unsatisfied, the more interference phenomena between light waves are relevant and therefore the general theory of electromagnetic optics has to be applied.

The refractive index of a material depends on the wavelength of light. This wavelength dependency – called dispersion – can be described using the Cauchy dispersion formula.¹⁷ The principal dispersion, D , of a material is defined as the difference between refractive indices at the 486- and 656-nm wavelengths.¹⁷ In optical applications, this material is usually glass and its refractive index depends on its oxide chemical composition.^{17,18} Furthermore, the refractive indices of glass can be modified by the manufacturing process (melting and thermal treatments).¹⁷ The refractive index of glass fibers is thus lower than that of bulk glass and further decreases with decreasing fiber diameter due to the faster cooling rate of thinner fibers.¹⁹⁻²¹ E-glass fibers with an oxide chemical composition defined in ASTM D578/D578M-05²² are used as reinforcement of polyester matrices in translucent structural GFRP applications for building construction. The refractive index of bulk E-glass was reported as being 1.56,²³⁻²⁵ whereas that of polyester resins increases during the curing process.²⁶ Kister et al.²⁵ reported a change from 1.53 in the liquid state to 1.56 in the cured solid state.

Translucency models for GFRP as a function of the reinforcement weight and total transmittance are helpful tools for designing load-bearing translucent GFRP facade building components. A theoretical model for the light scattering through unidirectional (UD) fiber-reinforced composites was proposed by Iba and Kagawa²⁷ and Iba et al.²⁸ based on electromagnetic optics. This model is applicable for composites having a larger fiber radius, R_f , than the light wavelength, λ , and where the order of the refractive index mismatch between fibers and resin is $\Delta n \leq 0.001$. Under these conditions, the model disregards the reflection and refraction of light in fiber/resin interfaces, scattering is assumed as being concentrated only in the forward direction (the regular transmittance direction) as an interference phenomenon and therefore translucency cannot be evaluated.

The objectives of this work are the experimental investigation of the diffuse light transmittance and modeling of the translucency of GFRP laminates (not considered in former light scattering studies^{27,28}) as a function of the reinforcement weight and total transmittance. The influence of fiber volume fraction, fiber architecture and resin gel time on translucency were also investigated. Ray-tracing analysis was performed to study the effect of refractive index mismatch, Δn , and air flaws on the wavelength-dependent diffuse transmittance of GFRP laminates.

3.2. Experimental procedure

3.2.1. Overview

Polyester resin and E-glass fibers with similar refractive indices were selected for the fabrication of GFRP laminates. The diffuse light transmittance of these laminates, surrounded by air, was investigated by spectrophotometry using an integrating sphere that collected the diffuse light transmitted after scattering inside the laminates. Spectrophotometric total transmittance and reflectance experiments were also performed on pure polyester specimens in order to investigate the refractive index and absorptance.

3.2.2. Materials

Unidirectional E-glass fabrics from Tissa (Oberkulm, Switzerland) with a reinforcement weight, w , of 410 g/m² were used for the laminate reinforcement. Longitudinal rovings constituted 78% of the reinforcement weight, 17% of the weight corresponding to twisted longitudinal yarns and 5% to transversal yarns. The rovings (reference code ACF407-600) were manufactured by Taiwan Glass Industry Corporation (Taipei, Taiwan). The measured fiber diameter was 12.8±1.3 μm. Roving fibers had a silane sizing on their surface with a weight fraction with respect to the glass fiber of around 0.5%. The yarns (reference code EC9-68-620) were manufactured by AGY (Aiken, United States). The measured fiber diameter was 8.9±0.8 μm. Yarn fibers had a starch sizing on their surface with a weight fraction with respect to the glass fiber of around 1.2%. The refractive index of the E-glass fibers, n_f , ranged between 1.55 and 1.56 according to Dunkers et al.²⁹ and Kinsella et al.³⁰.

Polylyte 420-181 unsaturated polyester resin, manufactured by Reichhold Inc. (Durham, United States), was used. This orthophthalic polyester resin, designed for translucent GFRP components, has a refractive index, n_r , adjusted to match the refractive index of E-glass mats according to the manufacturer's data sheet. Laminates of pure resin (without fibers) are colorless. The resin is pre-accelerated with a cobalt solution and UV-stabilized by a BASF Tinuvin[®] additive, absorbing the UV radiation below 380 nm.¹⁰ The low viscosity (330-360 mPa·s) of the resin makes it suitable for hand lay-up lamination. Butanox M-60 organic peroxide from AkzoNobel (Amsterdam, Netherlands) was the catalyst used to initiate the polymerization reaction.

3.2.3. Specimen fabrication

Unidirectional (UD) and cross-ply (CP) symmetric GFRP laminates with reinforcement weights, w , of between 410 and 3280 g/m² were fabricated by hand lay-up at room temperature (23±2 °C). The catalyst weight was 1% of the resin weight. Gel times (time lapse before significant increase in resin viscosity) were around 15 min. The laminates were cured for 24 h at the same temperature, and then postcured for another 24 h at 60 °C. Another set of UD laminates was fabricated at a lower temperature (18±2 °C) and the catalyst weight was 0.7% of the resin weight, resulting in longer gel times of around 30 min. These laminates were cured for 24 h at the same temperature and then postcured for 48 h at 60 °C. They were manufactured with three different fiber volume fractions: series L with low (0.24±0.03), series M with intermediate (0.34±0.01) and series H with high (0.42±0.01) fiber volume fraction.

Eight UD specimens with different reinforcement weights (from 410 to 3280 g/m²) and four CP symmetric specimens (of 1230 and 1640 g/m²) were cut from the laminates with gel times of around

15 min. Two UD specimens (of 1230 and 1640 g/m²) were cut from laminates with gel times of around 30 min. Specimens were labeled according to their reinforcement weight, fiber architecture and fiber volume fraction, e.g. 1640CP-L designates the specimen reinforced with $w = 1640$ g/m² of E-glass fibers, with cross-ply fiber architecture and low fiber volume fraction. A symbol (*) was added to identify the two specimens with longer gel times. The nominal specimen dimensions were 120x175 mm² for specimens with $w \leq 820$ g/m² and 90x90 mm² for the other specimens. The fiber volume fraction and thickness of all GFRP specimens are given in Table 3.1.

In addition, three square (60x60 mm²) pure resin specimens with thicknesses of 1, 2 and 4 mm were fabricated at 23±2 °C with 1.0% of catalyst, cured for 24 h under the same conditions and postcured for 24 h at 60 °C.

Table 3.1. Fiber volume fraction and thickness of fabricated GFRP specimens.

Series	Property	Unidirectional specimens					Cross-ply specimens	
		410UD	820UD	1230UD	1640UD	3280UD	1230CP	1640CP
L	Volume fraction (-)	0.21	0.23	0.24 0.21*	0.29 0.24*	-	0.22	0.25
	Thickness (mm)	0.8±0.13	1.4±0.09	2.0±0.13 2.4±0.16*	2.2±0.10 2.6±0.10*	-	2.1±0.07	2.6±0.21
M	Volume fraction (-)	-	-	0.33	-	0.34	-	-
	Thickness (mm)	-	-	1.4±0.06	-	3.8±0.09	-	-
H	Volume fraction (-)	-	-	0.41	0.43	-	0.40	0.41
	Thickness (mm)	-	-	1.2±0.07	1.5±0.06	-	1.2±0.03	1.5±0.02

* specimens fabricated with 0.7% of catalyst and cured at 18±2 °C.

3.2.4. Spectrophotometric set-up

The diffuse hemispherical spectral light transmittance of the fourteen GFRP specimens was investigated by spectrophotometry with a 152-mm-diameter integrating sphere. The measurements were performed using a halogen light source (Osram 64642 HLX, 150 W, 24 V, Xenophot[®]), an integrating sphere (LOT RT-060-SF) and a spectrophotometer (Oriel, model 77400, MultiSpec 125[™], type 1/8m) measuring from the 400- to 800-nm wavelengths and connected to a computer equipped with InstaSpec[™] II software for signal analysis. The set-up is schematically shown in Figure 3.1. Optical lenses and a 1-mm diaphragm were used to collimate a beam of light from the source. The beam was reflected in a plane mirror and then passed through a 5-mm-diameter diaphragm. Specimens were located at the entrance port A and crossed by the beam of light at nearly normal incidence (81°). Port B of the sphere remained open in the diffuse transmittance experiments. The light transmitted through the specimen with an angular deviation higher than ±4° was collected inside the sphere (see Figure 3.1), reflected and uniformly scattered by the sphere's white interior barium sulfate coating. The incident light deviating by less than ±4° was directly transmitted out of the sphere through the open port B. Incoming light from point C entered the spectrophotometer where it was split into components of different wavelengths by a diffraction grating. A detector head consisting of photodiode arrays connected to InstaSpec[™] II software allowed the amount of light reaching the detector to be computed. The diffuse transmittance, T_d , of a given specimen was the result of a relative

measurement: first with the specimen located at port A (and port B open) and then without specimen at port A (and port B closed). In addition, total transmittance experiments on the two specimens with longer gel times were performed. In these cases port B remained closed. Four measurements at different locations on each specimen were performed.

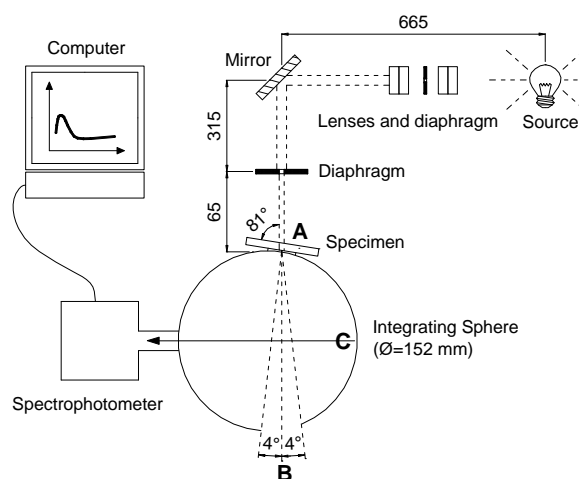


Figure 3.1. Schematic representation of integrating sphere set-up for diffuse transmittance experiments (top view, dimensions in mm).

The total and diffuse transmittance and total reflectance of the three resin specimens (without fibers) were also investigated. For the reflectance experiments specimens were located at port B, with port A open. All measurements were performed at near normal incidence (81°) because, at normal incidence (90°), the reflected beam would escape through the entrance port A. However, based on Fresnel Equations, the difference in reflectance or transmittance at 81° or 90° – for unpolarized light as used in these experiments – is lower than 0.1% and therefore negligible.³¹ One measurement was performed for each resin specimen.

The total light transmittance of the same GFRP specimens with shorter gel times was measured in previous research using the same set-up.¹⁰ In that study, specimens were located at the entrance port A with rovings forming an angle of approximately 45° with the horizontal plane and port B of the sphere was closed. The results of those measurements were reported in the previous study.¹⁰ The influence of the roving orientation at the entrance port of the integrating sphere on the light transmittance measurements was further investigated in specimen 820UD-L. Transmittance measurements were performed with rovings at 0° , 45° and 90° with respect to the horizontal plane; the results are shown in Figure 3.2. Diffuse and total transmittances measured for rovings located at 0° and 45° were almost identical and significantly lower than measurements with rovings at 90° . In the latter case, a ray of light impacting perpendicularly on the fiber is scattered in the plane perpendicular to the fiber and containing the incident ray.^{16,27} Therefore, the main plane of light diffusion for specimen 820UD-L with 90° orientated rovings was a horizontal plane passing through the measuring point C, as shown in Figure 3.3. In this configuration, point C was illuminated by radiation emanating directly from the specimen, i.e. light that had not been uniformly scattered inside the sphere and, therefore spectrophotometer measurements overvalued the

diffuse transmittance. The transmittance overestimation was higher for wavelengths around 430 nm (see Figure 3.2), indicating that light reaching point C contained more violet-blue than other colors. Orienting specimen 820UD-L with rovings at 0° or 45° avoided direct illumination on the target point C. In order to also avoid direct illumination on point C for CP specimens, all the experiments presented in the following were performed with rovings at 45° .

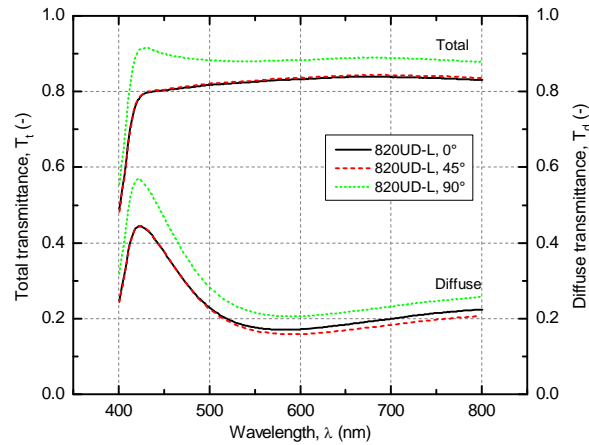


Figure 3.2. Spectral total and diffuse transmittance of specimen 820UD-L with different roving orientations (0° , 45° and 90°) at entrance port A of integrating sphere.

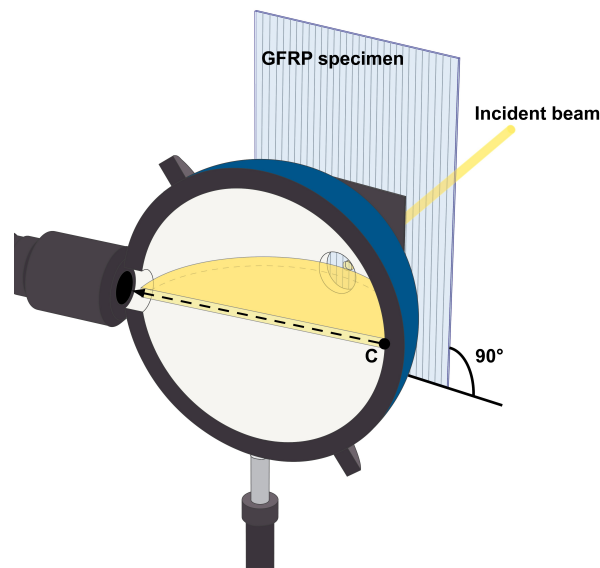


Figure 3.3. Plane of major light diffusion inside integrating sphere for specimen 820UD-L with rovings oriented at 90° with respect to horizontal plane.

3.3. Spectrophotometric results

For specimens with shorter gel times, diffuse light transmittance in the band of 500-800 nm increased when the reinforcement weight was increased (see Figure 3.4). Diffuse transmittances were maximum at approximately 430 nm with violet and blue colored light (430-500 nm) being more diffused than the other colors. However, the wavelength dependency of the diffuse transmittance decreased when the reinforcement weight was increased and the diffuse transmittance of specimen 3280UD-M was almost

constant in the band of 430-800 nm. Therefore the bluish appearance of GFRP specimens illuminated with white light decreased when the reinforcement weight increased, as shown in Figure 3.5, comparing the blue light diffusion of specimens 820UD-L and 1640UD-L.

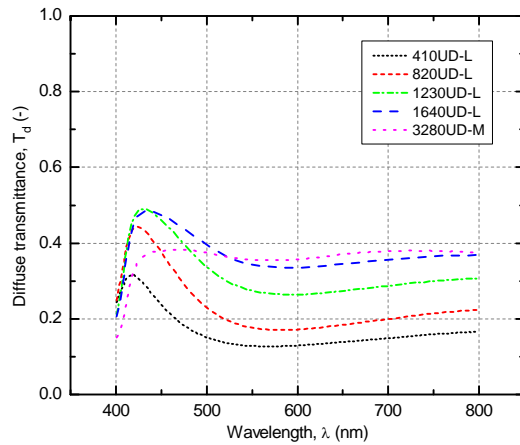


Figure 3.4. Spectral diffuse transmittance of unidirectional specimens at different reinforcement weights.

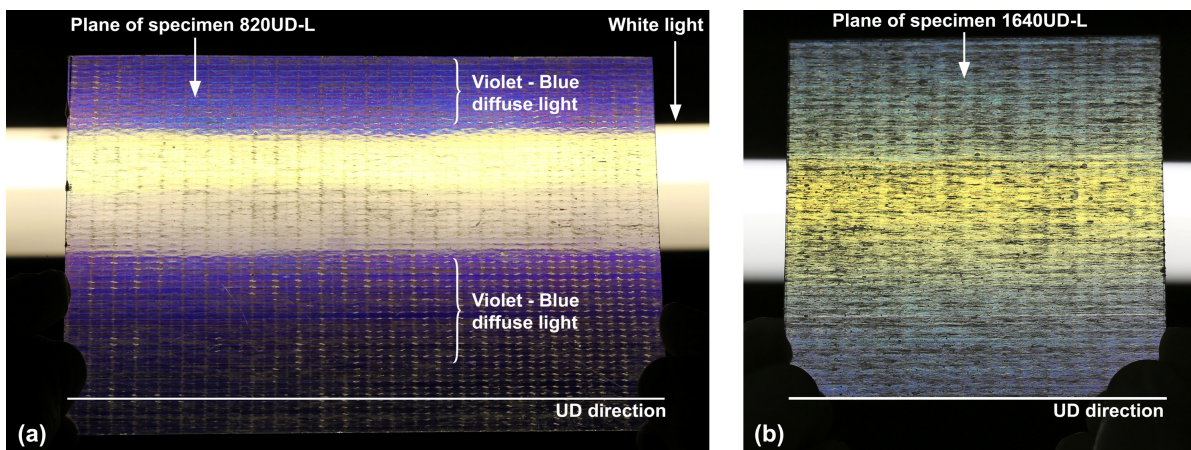


Figure 3.5. Bluish appearance of specimens (a) 820UD-L and (b) 1640UD-L when illuminated with white light.

The effect of the fiber volume fraction on diffuse light transmittance is shown in Figure 3.6. Increasing volume fraction had similar effects to those obtained by increasing reinforcement weight, i.e. diffuse transmittance increased and wavelength dependency decreased. The increase of translucency with the volume fraction was attributed to an increase of air flaws around fibers due to the difficulty in impregnating fibers when less resin was used. The diffuse transmittance of UD and CP specimens is compared in Figure 3.7. The fiber architecture had a small influence on light diffusion at low fiber volume fractions. However, at high volume fractions the diffuse transmittance of CP specimens was higher than that of the corresponding UD specimens in the band 500-800 nm. This effect was attributed to the hand lay-up fabrication process and the more difficult fiber impregnation for CP laminates than for UD laminates, especially at high fiber volume fractions.

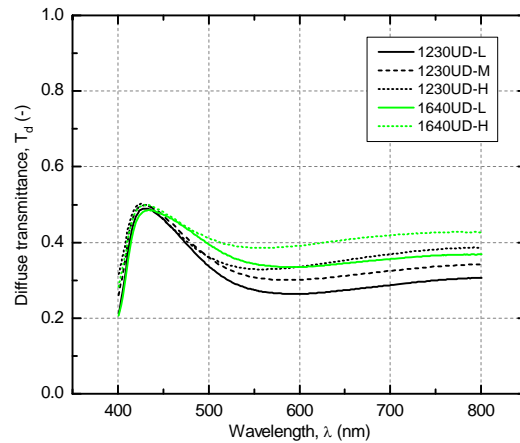


Figure 3.6. Spectral diffuse transmittance of specimens 1230UD and 1640UD at different volume fractions.

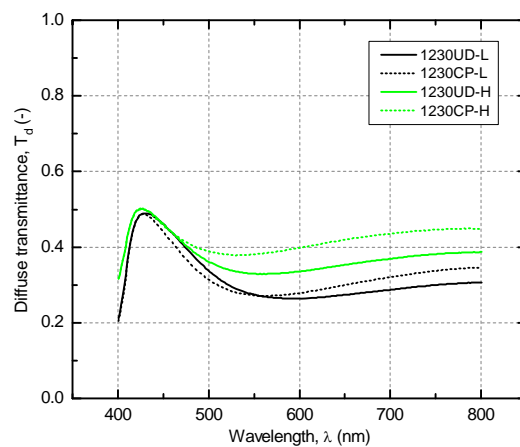


Figure 3.7. Spectral diffuse transmittance of unidirectional and cross-ply specimens ($w = 1230 \text{ g/m}^2$) at different volume fractions.

The total and diffuse transmittance curves of specimens with long and short gel times are compared in Figure 3.8. Longer gel times increased the measured total transmittance by around 0.07 for $w = 1230 \text{ g/m}^2$ and 0.12 for $w = 1640 \text{ g/m}^2$. This increase was attributed to better impregnation of fibers and therefore lower air and void content in the laminates, as can be observed in Figure 3.9. Longer gel times can reduce not only the speed of the curing process but also the heat generation and shrinkage of the resin, thus reducing debonding – and therefore void interfaces – between resin and fibers. Increasing gel times also reduced the diffuse transmittance of GFRP specimens by 0.10 for $w = 1230 \text{ g/m}^2$ and 0.13 for $w = 1640 \text{ g/m}^2$ at 555 nm, which was again attributed to a lower void content. However, increasing gel times increased the slope of the diffuse transmittance curves below the 555-nm wavelength and therefore the bluish appearance of the diffuse transmitted light.

For the diffuse light transmittance results concerning the GFRP laminates, the maximum standard deviations of the four measurements per specimen were in the order of ± 0.02 at 555 nm. Similar standard deviations were observed in the total light transmittance experiments performed on specimens with shorter gel times in the previous research.¹⁰

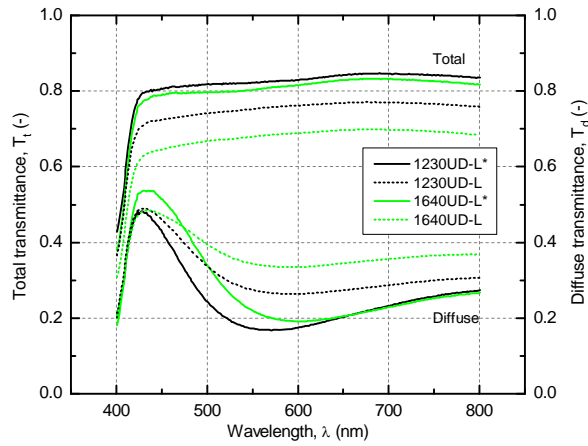


Figure 3.8. Spectral total and diffuse transmittance measured with integrating sphere set-up of unidirectional specimens with 15- and 30- (*) minute gel times.

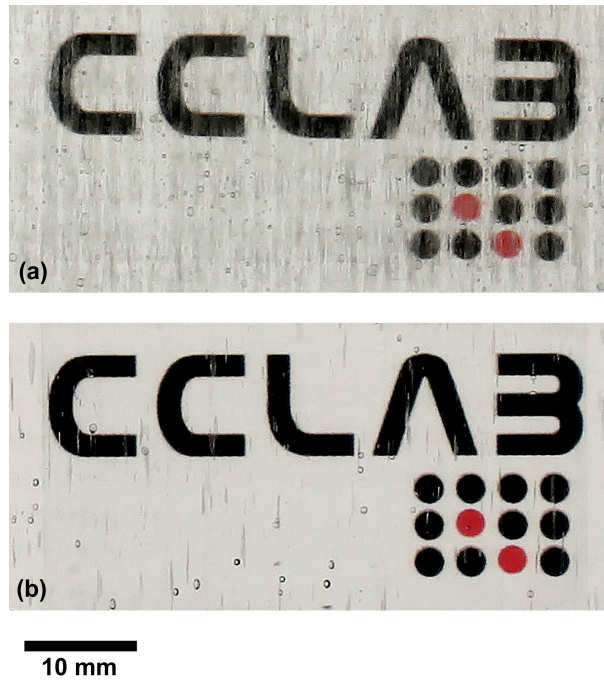


Figure 3.9. Detailed view of specimen (a) 1640 UD-L (15-min gel time) and (b) 1640 UD-L* (30-min gel time) with text behind the specimens.

The total and diffuse light transmittance of resin specimens are shown in Figure 3.10. Total transmittance decreased with the thickness of the specimen, which was caused by a corresponding increase of light absorptance (see Section 3.4). The diffuse transmittance of the three resin specimens was very small: around 0.02 at 555 nm and 0.04 at 430 nm. The total reflectance of the resin specimens is shown in Figure 3.11. Reflectance slightly decreased with the thickness of the specimen, which was also due to the increase of light absorptance (see Section 3.4).

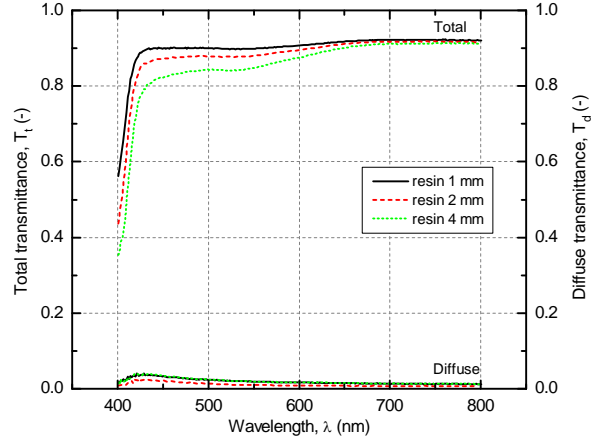


Figure 3.10. Spectral total and diffuse transmittance of three polyester specimens.

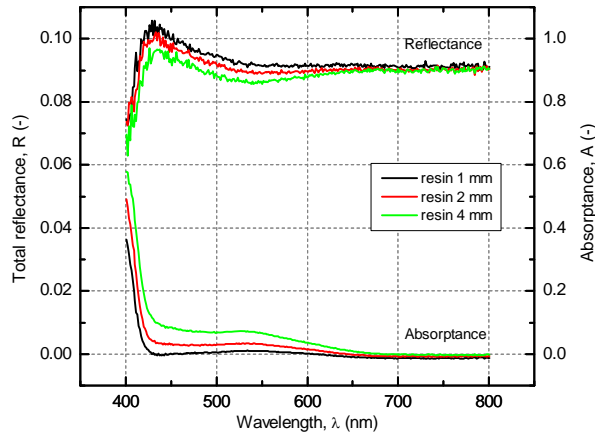


Figure 3.11. Spectral total reflectance and absorbance of three polyester specimens.

3.4. Analysis of spectrophotometric results

3.4.1. Overview

The refractive index mismatch between resin and fibers for wavelengths lower than around 500 nm was considered responsible for the experimentally observed diffusion of violet-blue colors in GFRP laminates. To confirm this hypothesis, refractive indices of resin and fiber were investigated and a ray-tracing analysis was performed on a GFRP laminate.

3.4.2. Characterization of polyester resin refractive index

The refractive index of cured polyester resin, n_r , was obtained from the spectrophotometric total transmittance, T , and total reflectance, R , experimental results, shown in Figures 3.10 and 3.11. Considering the Lambert-Beer law,¹⁷ the thickness, d , of the resin specimen, the attenuation coefficient, α_r , of the bulk resin and the reflectance, r , at one air/resin interface, T and R are given by:

$$T = (1-r)^2 \cdot e^{-\alpha_r \cdot d} \quad (3.1)$$

$$R = r + (1-r)^2 \cdot r \cdot e^{-2\alpha_r \cdot d} \quad (3.2)$$

where multiple reflections inside the resin are disregarded and coefficient α_r takes the absorptance, A , of the resin into account (see Figure 3.11), obtained from $A = 1 - T - R$. Combining equations (3.1) and (3.2), the interface reflectance is given by:

$$r = \frac{R}{1 + T \cdot e^{-\alpha_r \cdot d}} \quad (3.3)$$

From equation (3.1) the interface reflectance can also be expressed as:

$$r = 1 - \sqrt{\frac{T}{e^{-\alpha_r \cdot d}}} \quad (3.4)$$

by operating a variable change given by:

$$Y = \sqrt{e^{-\alpha_r \cdot d}} \quad (3.5)$$

and combining equations (3.3) and (3.4), results in:

$$Y^3 \cdot \sqrt{T} - Y^2 \cdot T + Y \cdot \left(\frac{1-R}{\sqrt{T}} \right) - 1 = 0 \quad (3.6)$$

from which one real root Y – and therefore one α_r according to equation (3.5) – can be obtained for each resin specimen at each wavelength. Interface reflectance, r , is obtained by substituting the obtained α_r into equation (3.3). Taking the absorptance of the resin into account, the relationship between the refractive index of the resin, n_r , and the air/resin interface reflectance, r , is³¹:

$$r = \frac{(n_r - 1)^2 + k_r^2}{(n_r + 1)^2 + k_r^2} \quad (3.7)$$

where k_r is the extinction coefficient of the resin given by³¹:

$$k_r = \frac{\alpha_r \cdot \lambda}{4 \cdot \pi} \quad (3.8)$$

By substituting equation (3.8) into equation (3.7), the refractive index, n_r , for each resin specimen was obtained. The resulting average curves of n_r and α_r of the three resin specimens, as a function of the wavelength, are shown in Figure 3.12.

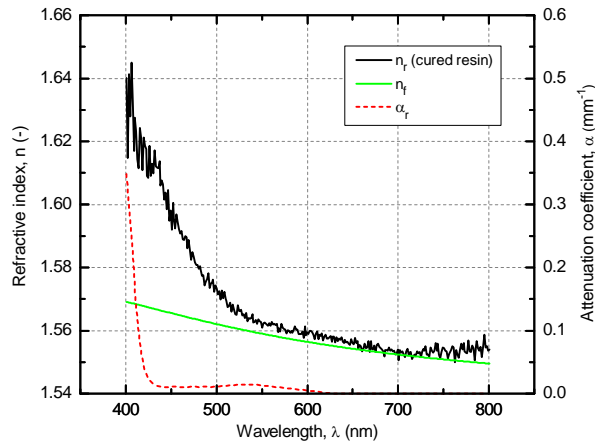


Figure 3.12. Refractive indices of E-glass fiber, n_f , and polyester resin, n_r , and attenuation coefficient, α_r , of polyester resin.

3.4.3. Characterization of E-glass fiber refractive index

The principal dispersion, D , of a glass component is defined as¹⁷:

$$D = n_{486} - n_{656} \quad (3.9)$$

where n_{486} and n_{656} are the refractive indices of glass at the 486-nm and 656-nm wavelengths respectively. The refractive index and principal dispersion are primarily determined by the chemical oxide composition of the glass. For bulk glass these parameters are¹⁷:

$$D = \frac{\sum_{i=1}^m D_i \cdot c_i}{100} \quad (3.10)$$

$$n_{588} = \frac{\sum_{i=1}^m n_{588,i} \cdot c_i}{100} \quad (3.11)$$

where D_i is the principal dispersion of oxide i , c_i is the concentration in mole percentage of oxide i , $n_{588,i}$ is the refractive index of oxide i at 588 nm and n_{588} is the refractive index of the bulk glass at 588 nm. The oxide concentration in mole percentage, c_i , and in weight percentage, w_i , are related by¹⁷:

$$c_i = \frac{100 \cdot w_i}{M_i \cdot \sum_{j=1}^m \frac{w_j}{M_j}} \quad (3.12)$$

where M_i is the molar mass of oxide i calculated from the molar mass of the atoms in the oxide. Average values of w_i for the main oxide components of E-glass were obtained from ASTM D578/D578M-05²² and are summarized in Table 3.2. In addition, the calculated values M_i and c_i , and the values of $n_{588,i}$ and D_i adopted from Bach and Neuroth¹⁷ are also indicated in Table 3.2. Finally, according to equations (3.10) and (3.11), $D = 0.0092$ and $n_{588} = 1.560$ for bulk E-glass.

Table 3.2. Main oxide components of E-glass fibers and their concentration in weight (w_i) according to ASTM D578/D578M-05,²² molar mass (M_i), concentration in mole (c_i) according to equation (3.12), and refractive index at 588 nm ($n_{588,i}$) and principal dispersion (D_i) from Bach and Neuroth¹⁷.

Oxide	SiO ₂	Al ₂ O ₃	B ₂ O ₃	CaO	MgO	Na ₂ O	K ₂ O
w_i (%)	54	14	7	21	2.5	0.75	0.75
M_i (g/mol)	60.1	102.0	69.6	56.1	40.3	62.0	94.2
c_i (%)	56.4	8.6	6.3	23.5	3.9	0.8	0.5
$n_{588,i}$ (-)	1.475	1.520	1.710	1.730	1.610	1.590	1.575
D_i (-)	0.0068	0.0085	0.0090	0.0148	0.0111	0.0142	0.0130

The wavelength-dependent refractive index of roving E-glass fibers, n_f , was modeled with the Cauchy dispersion formula¹⁷:

$$n_f = g + \frac{h}{\lambda^2} + \frac{i}{\lambda^4} \quad (3.13)$$

where λ is the wavelength of light and g , h and i are three parameters of the model which were determined from the n_f values at the 486-, 588- and 656-nm wavelengths as follows. The refractive index of E-glass

fibers at 588 nm was obtained by reducing the calculated value of 1.560 for bulk E-glass by 0.2% as indicated by Bateson²⁰ for a fiber diameter of 12.8 μm , resulting in $n_{f588} = 1.557$. Furthermore, for commercial glass K5 ($D = 0.0088$) and SK5 ($D = 0.0096$) – i.e. glass with dispersions almost identical to E-glass – 70% of the dispersion D is attributed to the range below the 588-nm wavelength and 30% above the 588-nm wavelength.¹⁷ Assuming that the dispersion $D = 0.0092$ of E-glass is distributed in these same proportions below and above 588 nm results in:

$$n_{f486} = n_{f588} + 0.7 \cdot D = 1.563 \quad (3.14)$$

$$n_{f656} = n_{f588} - 0.3 \cdot D = 1.554 \quad (3.15)$$

The refractive index model of E-glass fibers is thus given by:

$$n_f = 1.5389 + \frac{7.4719 \cdot 10^3}{\lambda^2} - \frac{4.2087 \cdot 10^8}{\lambda^4} \quad (3.16)$$

where the wavelength, λ , is in nanometers. The resulting refractive index curve, n_f , is shown in Figure 3.12. The variation of the refractive index of E-glass fibers with the wavelength is small, decreasing from around 1.57 at 400 nm to 1.55 at 800 nm. The refractive index mismatch between fiber and resin was lower than 0.01 in the range from 500 to 800 nm. However the mismatch increased progressively below 500 nm and was around 0.06 at 400 nm.

3.4.4. Ray-tracing simulation of GFRP spectral light transmittance

The spectral total and diffuse light transmittance of laminate 1640UD-L* was investigated by performing ray-tracing Monte Carlo simulations in CFS-PRO software.³² Optical microscopy measurements showed that fibers were distributed in four layers of an approximate thickness of 290 μm , separated by resin layers of the same thickness (see Figure 3.13). The geometry and layer distribution considered in the ray-tracing model are shown in Figure 3.14(a). A laminate width of 150 μm was considered for the analysis. The total reinforcement weight of the laminate was modeled in the form of roving fibers (12.8- μm diameter) distributed inside each fiber layer with 4300 fibers/ mm^2 . The refractive indices obtained above were assigned to resin and fibers. In addition, light absorptance was considered by attributing to the resin the attenuation coefficient, α_r , shown in Figure 3.12. The modeled laminate was considered surrounded by air. A collimated (150- μm wide) beam of light composed of rays from 400 nm to 800 nm was directed at normal incidence onto the laminate. The central part of the incident beam is shown in Figure 3.14(b). Rays that escaped laterally from the laminate during propagation were redirected inside the laminate with the same propagation direction but on the opposite side. For a given wavelength, the ratio between the number of diffused transmitted rays, i.e. rays transmitted with an angular deviation higher than 4°, and the number of incident rays defined the diffuse transmittance of the laminate at the considered wavelength. Similarly, the ratio between the number of transmitted rays and the number of incident rays defined the total transmittance of the laminate.

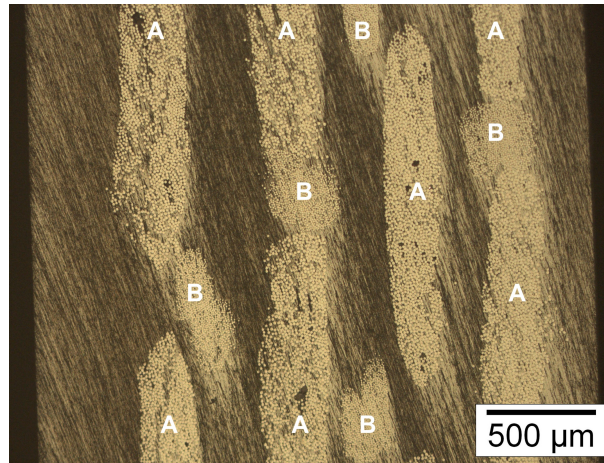


Figure 3.13. Through-thickness optical microscopy image of specimen 1640UD-L* (A: rovings, 12.8 μm diameter, B: yarns, 8.9 μm diameter).

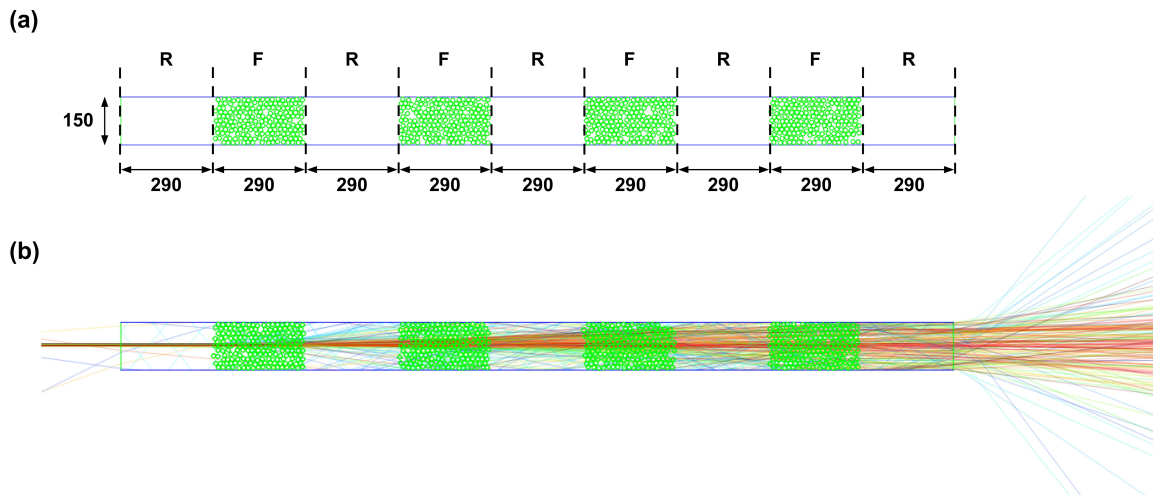


Figure 3.14. Ray-tracing geometrical model (a) of a 2.6-mm-thick GFRP laminate with $w = 1640 \text{ g/m}^2$ (R = resin, F = fiber layer), and (b) partial representation of light rays (units in μm).

A first ray-tracing simulation was performed considering a GFRP laminate without air inclusions. The diffuse and total transmittance results obtained from simulation and experiments on specimen 1640UD-L* are shown in Figures 3.15 and 3.16 respectively. The simulated diffuse transmittance curve followed the same trend as the refractive index mismatch, Δn , between fiber and resin, also shown in Figure 3.15. No light was diffused where no mismatch existed (at around 700 nm), corresponding to the red rays transmitted almost straight ahead in Figure 3.14(b). The light was particularly diffused where the mismatch was highest (below 500 nm), corresponding to the blue rays more laterally deviated in Figure 3.14(b), thus confirming that Δn was responsible for the violet-blue light diffusion of GFRP laminates observed in Figure 3.5. However the plateau of the simulated total transmittance, shown in Figure 3.16, was around 0.90 and therefore approximately 0.10 higher than the measurement. This discrepancy was mostly attributed to the effect of air flaws not considered in the model.

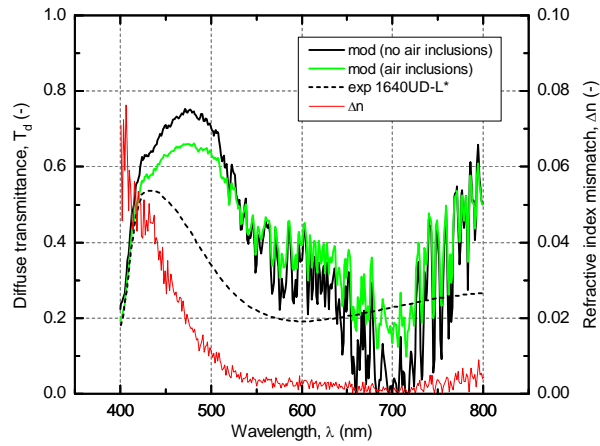


Figure 3.15. Diffuse transmittance simulated by ray-tracing model, experimental results for specimen 1640UD-L* and refractive index mismatch between resin and fibers.

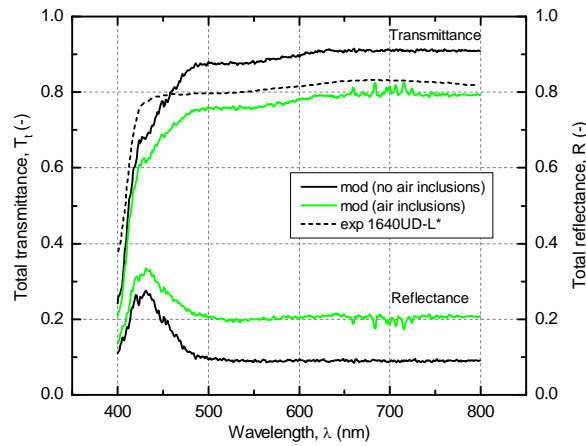


Figure 3.16. Total transmittance and total reflectance simulated by ray-tracing model and total transmittance experimental results for specimen 1640UD-L*.

A second ray-tracing simulation was therefore performed adding circular air pockets of 100-nm thickness – with refractive index $n_{air} = 1$ – around 1% of the fibers. The diffuse and total transmittance results are given in Figures 3.15 and 3.16. Simulated total transmittance was around 0.12 lower than the transmittance of the laminate without air inclusions. This reduction corresponded to an identical increase in the simulated total reflectance as shown in Figure 3.16. Therefore, air flaws reduced transmittance by increasing reflectance. Where an almost perfect matching of refractive indices between resin and fibers existed (between 650 and 725 nm), air inclusions caused a large mismatch and therefore increased the diffused transmittance (see Figure 3.15). However, where a mismatch higher than 0.01 already existed between fiber and resin (below 500 nm), laminates with more total transmittance (without air inclusions) diffused more light than laminates with lower total transmittance (with air inclusions).

The trend of the simulated diffuse transmittance curves agreed with the experimental results but the higher values below 555 nm of the simulated curves indicate that the refractive index mismatch below this wavelength was slightly overestimated. This overestimation also resulted in an increase of reflectance below 480 nm (where $\Delta n = 0.016$ according to Figure 3.15) and therefore in a decrease in total and diffuse transmittance below this wavelength (see Figures 3.15 and 3.16). The high fiber content of structural GFRP laminates – and therefore the high number of interfaces where light is refracted during its

propagation inside the laminate – explains the high sensitivity of light diffusion to small Δn between resin and fibers. In a perfect laminate without air, $\Delta n = 0$ and $T_d = 0$, while $\Delta n = 0.01$ already results in $T_d = 0.70$ (see Figure 3.15). Small oscillations in the refractive index mismatch curve are therefore responsible for the wide scatter observed in the simulated diffuse transmittance curves shown in Figure 3.15.

The only fair agreement between simulation and experimental results can be explained by three factors: 1) Light diffusion is extremely sensitive to very small refractive index mismatches, as discussed above; 2) fibers have a silane or starch coating on their surface, which is not taken into account in the simulations; and 3) interference phenomena (not considered in ray optics) may develop inside the laminate since spacing between fibers can be in the same order of magnitude as the wavelength of light.

3.5. Analytical modeling of GFRP translucency

3.5.1. Model for 555-nm wavelength depending on reinforcement weight

A model characterizing the translucency of GFRP was developed based on experimental results. The translucency of the fourteen specimens in Table 3.1 was investigated at 555 nm corresponding to the wavelength of the maximum spectral sensitivity of the human eye.³³ Table 3.3 summarizes the experimental average results of diffuse transmittance at 555 nm, $T_{d,555 \text{ exp}}$, (see Figures 3.4 and 3.6 to 3.8) and of total transmittance at 555 nm, $T_{t,555 \text{ exp}}$, obtained in this research for specimens with 30-min gel time (see Figure 3.8) and in previous research¹⁰ for specimens with 15-min gel time. In that research an analytical model was developed for the total transmittance prediction at 555 nm of laminates with 15-min gel time, $T_{t,555 \text{ mod}}$, and these predictions are also shown in Table 3.3. The difference between $T_{t,555 \text{ mod}}$ and $T_{t,555 \text{ exp}}$ was designated as $\Delta T_{d,555}$ (see Table 3.3) and attributed to the loss of diffuse light at the entrance port A of the integrating sphere.^{10,34} Experimental values of translucency at the 555-nm wavelength, designated as the diffused fraction, $DF_{555 \text{ exp}}$, are therefore given by:

$$DF_{555 \text{ exp}} = \frac{T_{d,555 \text{ exp}} + \Delta T_{d,555}}{T_{t,555 \text{ exp}} + \Delta T_{d,555}} \quad (3.17)$$

and the results are also given in Table 3.3. The translucency at 555 nm of specimens with similar gel times increased with the reinforcement weight, w , and fiber volume fraction, f . A parameter taking the reinforcement weight, w , and fiber volume fraction, f , into account was defined and was referred to as equivalent reinforcement weight, w_{eq} , of the laminate, in (g/m²), as follows:

$$w_{eq} = w \cdot (0.67 + f) \quad (3.18)$$

with $w_{eq} = w$ for an intermediate volume fraction of $f = 0.33$. The corresponding values of w_{eq} for the resin and GFRP specimens are shown in Table 3.3. In order to model the translucent behavior of GFRP laminates, an asymptotic exponential law is proposed:

$$DF_{555 \text{ mod}} = 1 - e^{-a \cdot w_{eq}} \quad (3.19)$$

where the exponential term represents the transparency of the laminate and parameter a , in (m²/g), indicates the rate at which transparency is lost. Parameter a is given in Table 3.4 for UD and CP laminates

with 15-min gel time and good agreement between exponential models and experimental results is shown in Figure 3.17.

Table 3.3. Diffuse and total transmittance (average) measurements at 555 nm, total transmittance according to model developed by Pascual et al.¹⁰ given in equation (3.22), estimation of entrance loss of integrating sphere, experimental translucency at 555 nm according to equation (3.17) and equivalent reinforcement weight from equation (3.18).

Specimens	$T_{d,555 \text{ exp}}$ (-)	$T_{l,555 \text{ exp}}$ (-)	$T_{l,555 \text{ mod}}$ (-)	$\Delta T_{d,555}$ (-)	$DF_{555 \text{ exp}}$ (-)	w_{eq} (g/m ²)
1-mm resin	0.02	0.90	0.91	0.01	0.03	0
410UD-L	0.13	0.87	0.87	0.00	0.15	361
820UD-L	0.17	0.83	0.82	-0.01	0.20	738
1230UD-L	0.27	0.75	0.78	0.03	0.38	1119
1230UD-M	0.31	0.75	0.78	0.03	0.44	1230
1230UD-H	0.33	0.75	0.78	0.03	0.46	1328
1640UD-L	0.34	0.68	0.75	0.07	0.55	1574
1640UD-H	0.39	0.69	0.75	0.06	0.60	1804
3280UD-M	0.36	0.48	0.61	0.13	0.80	3313
1230CP-L	0.27	0.72	0.76	0.04	0.41	1095
1230CP-H	0.38	0.71	0.76	0.05	0.57	1316
1640CP-L	0.32	0.64	0.72	0.08	0.56	1509
1640CP-H	0.41	0.66	0.72	0.06	0.65	1771
1230UD-L*	0.17	0.82	-	-	0.21	1082
1640UD-L*	0.21	0.80	-	-	0.26	1492

Table 3.4. Parameter a and R-square factor for exponential translucency model.

Specimens	a ($\cdot 10^{-4} \text{ m}^2 \cdot \text{g}^{-1}$)	R^2 (-)
CP (15-min gel time)	5.7	0.98
UD (15-min gel time)	4.6	0.97

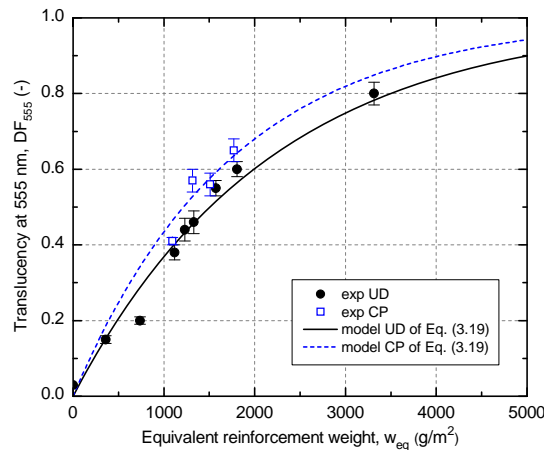


Figure 3.17. Exponential model of translucency at 555 nm as function of equivalent reinforcement weight w_{eq} of UD and CP laminates (for gel time of 15 min).

For $w_{eq} < 2000 \text{ g/m}^2$, the exponential model can be approached by a linear regression model as follows:

$$DF_{555 \text{ mod}} = b \cdot w_{eq} \quad (3.20)$$

where b depends on the fiber architecture and resin gel time (see Table 3.5). The modeling and experimental results are presented in Figure 3.18 where losses of diffuse light at the entrance port A of the

sphere for specimens with longer gel times were disregarded due to their low diffuse transmittance (see Table 3.3). For the same gel time and equivalent reinforcement weight, CP laminates were around 10% more translucent than UD laminates. This increase was attributed to a higher content of voids in the former – particularly at fiber-crossing locations – than in the latter. Increasing the gel times of UD laminates from 15 to 30 min decreased translucency by around 50%. This reduction was attributed to better fiber impregnation and fewer air interfaces around fibers when gel times increased.

Table 3.5. Slope b and R-square factor for linear translucency model, for $w_{eq} < 2000 \text{ g/m}^2$.

Specimens	b ($\cdot 10^{-4} \text{ m}^2 \cdot \text{g}^{-1}$)	R^2 (-)
CP (15-min gel time)	3.8	0.97
UD (15-min gel time)	3.4	0.98
UD (30-min gel time)	1.8	0.96

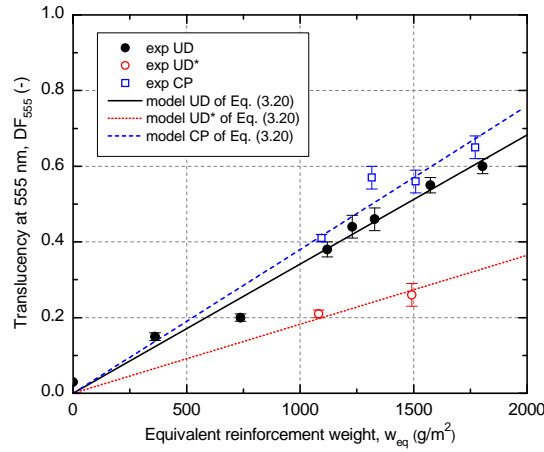


Figure 3.18. Linear model of translucency at 555 nm as function of equivalent reinforcement weight $w_{eq} < 2000 \text{ g/m}^2$ of UD and CP laminates for short and long (*) gel times.

Based on equation (3.19) and for 15-min gel time, the diffuse transmittance of GFRP laminates at 555 nm can be modeled as:

$$T_{d,555 \text{ mod}} = T_{t,555 \text{ mod}} \cdot \left(1 - e^{-a \cdot w_{eq}}\right) \quad (3.21)$$

where a is given in Table 3.4, w_{eq} is obtained according to equation (3.18) and $T_{t,555 \text{ mod}}$ is equal to the total transmittance at 555 nm and is given by¹⁰:

$$T_{t,555 \text{ mod}} = 0.909 \cdot \left(1 - L_{555}(w)\right) \quad (3.22)$$

where L_{555} is the loss of light transmittance inside the laminate at 555 nm and depends on the reinforcement weight, w , and fiber architecture as follows¹⁰:

$$L_{555}(w) = 1 - c^{\frac{w}{410}} \quad (3.23)$$

with $c = 0.952$ for UD laminates and $c = 0.942$ for CP laminates. The diffuse and total transmittance models of equations (3.21) and (3.22) are represented in Figure 3.19 considering $w = w_{eq}$. Diffuse

transmittance increased with reinforcement weight to a maximum of 0.48 at around $w = 2800 \text{ g/m}^2$ for CP laminates and $w = 3400 \text{ g/m}^2$ for UD laminates from which point it decreased asymptotically to the values of total transmittance.

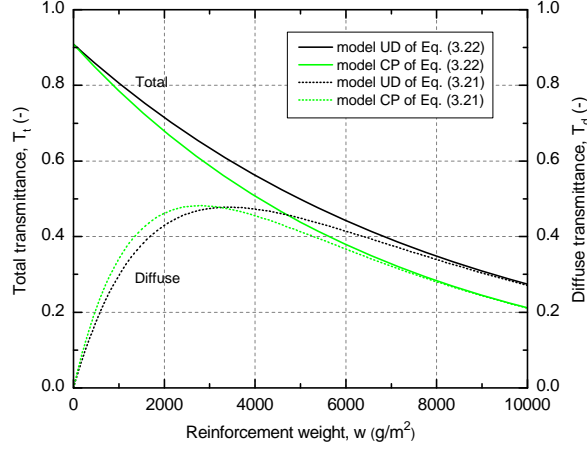


Figure 3.19. Models of total and diffuse transmittance as function of reinforcement weight of UD and CP laminates, considering $w = w_{eq}$.

3.5.2. Model for visible spectrum depending on reinforcement weight

The translucency in the visible spectrum of light – i.e. from 380 to 780 nm – is given by:

$$DF_{vis} = \frac{T_{d,vis}}{T_{t,vis}} \quad (3.24)$$

where $T_{d,vis}$ and $T_{t,vis}$ are the visible diffuse and total transmittances calculated as:

$$T_{vis} = \frac{\int_{380}^{780} V(\lambda) \cdot T(\lambda) \cdot E(\lambda) \cdot d\lambda}{\int_{380}^{780} V(\lambda) \cdot E(\lambda) \cdot d\lambda} \quad (3.25)$$

where $V(\lambda)$ is the spectral luminous efficiency function of the human eye for photopic vision,³³ $E(\lambda)$ is the solar spectral irradiance,³⁵ $T(\lambda)$ is the measured spectral transmittance – total or diffuse – and T_{vis} is the corresponding – total or diffuse – transmittance in the visible range. Visible translucency, DF_{vis} , was calculated from experimental results for specimens 410UD-L and 820UD-L. Translucency at 430 nm (peak region of light diffusion), DF_{430} , and at 555 nm (peak region of eye sensitivity), DF_{555} , was also calculated and compared in Table 3.6. DF_{430} was between 2.2 and 2.4 times higher than DF_{vis} due to the high diffusion of violet-blue colors. However, DF_{555} values were similar to DF_{vis} and therefore a model for the visible translucency of GFRP laminates was deduced as follows:

$$DF_{vis\ mod} \approx DF_{555\ mod} \quad (3.26)$$

Since the visible total transmittance of the GFRP laminates is equal to their transmittance at 555 nm,¹⁰ a model for diffuse visible transmittance can therefore be approximated by:

$$T_{d,vis\ mod} \approx T_{d,555\ mod} \quad (3.27)$$

where $T_{d,555\ mod}$ is given in equation (3.21).

Table 3.6. Translucency at 430 nm, 555 nm and in visible range of specimens 410UD-L and 820UD-L.

Specimens	410UD-L	820UD-L
DF_{430} (-)	0.35	0.55
DF_{555} (-)	0.15	0.20
DF_{vis} (-)	0.16	0.23

3.5.3. Model for 555-nm wavelength depending on total transmittance

The translucency at 555 nm of UD and CP GFRP laminates with 15-min gel time, given by the model of equation (3.19), was plotted in Figure 3.20 versus the total transmittance at 555 nm, predicted by the model of equation (3.22) and assuming $w = w_{eq}$. The overlay of UD and CP models indicated that the relationship between translucency and total transmittance was independent of fiber architecture and good agreement with experimental results was observed.

For $DF_{555} < 0.7$ and 15-min gel time, a linear regression model was fitted as follows:

$$DF_{555\ mod} = \frac{0.91 - T_{t,555\ mod}}{0.31} \quad (3.28)$$

where $T_{t,555\ mod}$ and 0.91 are respectively the total transmittance of the GFRP laminate and the 1-mm-thick resin according to model of equation (3.22) (see Table 3.3). The linear model is shown in Figure 3.20 and agrees well with experimental results.

Experimental results for specimens with 30-min gel time also fitted well with the linear trend, indicating that the relationship between total transmittance and translucency may also be independent of resin gel time. Further investigations are required to confirm this hypothesis however.

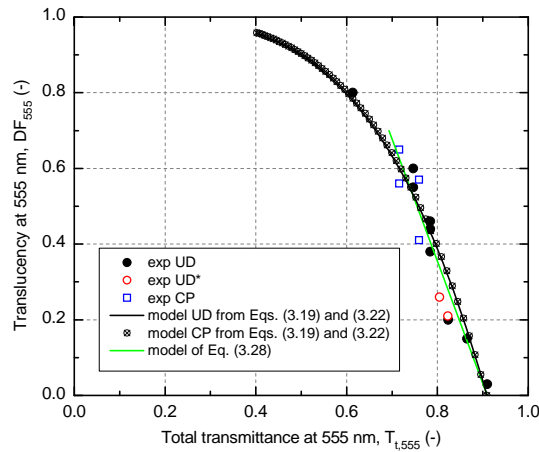


Figure 3.20. Models of translucency as function of total transmittance at 555 nm and experimental results.

3.6. Evaluation of applications

The optical performance of GFRP laminates is evaluated regarding two architectural applications: translucent load-bearing skylights and the encapsulation of PV cells in the translucent GFRP skins of sandwich structures. These two applications require different optical properties that are discussed in the following.

The skylights of toplighted energy-efficient low-rise buildings require total transmittances of at least 0.50 to provide sufficient illumination to the interior building space and minimum translucencies of 0.90 to avoid glare from sunlight. According to the model of equation (3.22), a total transmittance of 0.50 is achieved for GFRP laminates with reinforcement weights up to $w = 4100 \text{ g/m}^2$ in CP laminates and $w = 5000 \text{ g/m}^2$ in UD laminates (see Figure 3.19). For these reinforcement weights – and considering an intermediate volume fraction of 0.33 – the model of equation (3.19) predicts a translucency of 0.90 (see Figure 3.17), thus broadening the application field of GFRP laminates to the design of structural skylights for building construction.

For the encapsulation of PV cells in multifunctional GFRP laminates, the main optical condition for the encapsulant is that it presents a high total light transmittance. In architecturally well-integrated PV modules a 10% loss in efficiency compared to traditional encapsulations is well accepted.³⁶ Therefore, for GFRP encapsulants of PV cells minimum total transmittances of 0.83 are required,¹⁰ corresponding to UD laminates with $w = 800 \text{ g/m}^2$ and CP laminates with $w = 600 \text{ g/m}^2$ according to the model of equation (3.22), shown in Figure 3.19. Based on the non-linear models shown in Figure 3.20, the required total transmittance is satisfied by GFRP laminates with maximum translucencies of around 0.30. Therefore, unlike in skylight applications, GFRP translucency has to be minimized in order to increase the optical performance of PV cell encapsulation.

Optimized GFRP laminates for applications requiring high degrees of transparency and light transmittance, i.e. GFRP encapsulants of PV cells, have to minimize air inclusions in the laminates and refractive index mismatch between fibers and resin. Ray-tracing analysis on an almost perfect UD laminate (without air inclusions) with $\Delta n = 0.0005$ and $w = 1640 \text{ g/m}^2$ results in a transparent laminate with total transmittance of around 0.90 – value obtained from Figures 3.15 and 3.16 at the 700-nm wavelength – that therefore has optical properties comparable to pure glass laminates. However, the superior mechanical properties, light weight and freeform shapes of GFRP compared to glass components can open up new application fields in architectural design.

3.7. Conclusions

The translucency of GFRP laminates for building construction applications was investigated. The following conclusions were drawn:

1. Exponential and linear models were developed for modeling the translucency (haze) of structural GFRP laminates. Air inclusions around fibers and small refractive index mismatches between resin and fibers caused an increase in translucency with an increasing reinforcement weight and fiber volume fraction of the laminates.

2. Air inclusions in the fiber/resin interfaces of GFRP laminates may be reduced by increasing resin gel time. Increasing gel time from 15 to 30 minutes increased total transmittance from 0.75 to around 0.80 for a unidirectional reinforcement weight of 1640 g/m².
3. Ray-tracing analysis was successfully used to model the trend of spectral total and diffuse light transmittance of GFRP laminates. Refractive index mismatches between resin and fiber higher than 0.01 below the 500-nm wavelength caused a bluish appearance of the diffused light.
4. Multifunctional GFRP skylights with minimum total transmittance of 0.50 and translucency of 0.90 (90% haze) could be designed using GFRP cross-ply laminates with a reinforcement weight of $w = 4100 \text{ g/m}^2$.
5. Multifunctional sandwich structures encapsulating PV cells in GFRP skins with total transmittances of 0.83 could be designed using GFRP cross-ply laminates with $w = 600 \text{ g/m}^2$. Higher total transmittance can be obtained by increasing the transparency of the laminate by increasing resin gel time.
6. According to ray-tracing simulation, GFRP laminates with a reinforcement weight up to 1640 g/m², presenting a refractive index mismatch of 0.0005 between resin and fibers and no air inclusions, are transparent and exhibit a total transmittance of around 0.90, which is similar to the properties of pure glass laminates.

3.8. References

1. Jeska S. *Transparent Plastics – Design and Technology*. Basel: Birkhauser, 2008.
2. Keller T, de Castro J and Schollmayer M. Adhesively Bonded and Translucent Glass Fiber Reinforced Polymer Sandwich Girders. *J Compos Constr* 2004; 8(5):461-470.
3. ASTM Standard E284-12, 2012. *Standard Terminology of Appearance*. West Conshohocken, PA: American Society for Testing and Materials, August 2012.
4. Heschong L. Daylighting and Human Performance. *ASHRAE J* 2002; 44(6):65-67.
5. Eckerlin H, Manning M, Atre U, et al. A new daylighting strategy for a middle school in North Carolina. In: *Proceedings of Solar 2007: Sustainable Energy Puts America to Work*, Cleveland, USA, 7-12 July 2007, pp.734-741. Boulder, CO: ASES.
6. Kesner CW. Analysis of the Museum Lighting Environment. *J Interior Des* 1997; 23(2):28-41.
7. Keeler M and Burke B. *Fundamentals of Integrated Design for Sustainable Building*. Hoboken: John Wiley & Sons, 2009.
8. *2012 International Energy Conservation Code*. Washington: International Code Council, 2011.
9. Keller T, Vassilopoulos AP and Manshadi BD. Thermomechanical Behavior of Multifunctional GFRP Sandwich Structures with Encapsulated Photovoltaic Cells. *J Compos Constr* 2010; 14(4):470-478.
10. Pascual C, de Castro J, Schueler A, et al. Total light transmittance of glass fiber-reinforced polymer laminates for multifunctional load-bearing structures. Accepted for publication in *J Compos Mater*, 2013; DOI: 10.1177/0021998313511653.
11. Pagliario M, Palmisano G and Ciriminna R. *Flexible Solar cells*. Weinheim: Wiley-VCH, 2008.
12. Mohring H-D and Stellbogen D. Annual energy harvest of PV systems – Advantages and drawbacks of different PV technologies. In: *Proceedings of the 23rd European Photovoltaic Solar Energy Conference*, Valencia, Spain, 1-5 September 2008, pp.2781-2785. Munich: EU PVSEC.

13. Larson GW and Shakespeare R. *Rendering with Radiance – The Art and Science of Lighting Visualization*. Seattle: Randolph M. Fritz, 2011.
14. Andersen M, Kleindienst S, Yi L, et al. An intuitive daylighting performance analysis and optimization approach. *Build Res Inf* 2008; 36(6):593-607.
15. Saleh BEA and Teich MC. *Fundamentals of photonics*, 2nd ed. Hoboken: John Wiley & Sons, 2007.
16. van de Hulst HC. *Light scattering by small particles*. New York: Dover Publications, 1981.
17. Bach H and Neuroth N (eds). *The Properties of Optical Glass*. Berlin: Springer, 1995.
18. Weber MJ. *Handbook of optical materials*. Boca Raton, FL: CRC Press, 2003.
19. Kang S, Day DE and Stoffer JO. Measurement of the refractive index of glass fibers by the Christiansen-Shelyubskii method. *J Non-Cryst Solids* 1997; 220(2-3):299-308.
20. Bateson S. Critical Study of the Optical and Mechanical Properties of Glass Fibers. *J Appl Phys* 1958; 29(1):13-21.
21. Corpus JM and Gupta PK. Diameter Dependence of the Refractive Index of Melt-Drawn Glass Fibers. *J Am Ceram Soc* 1993; 76(5):1390-1392.
22. ASTM Standard D578/D578M-05, 2011. *Standard Specification for Glass Fiber Strands*. West Conshohocken, PA: American Society for Testing and Materials, September 2011.
23. Wang L, Kister G, Ralph B, et al. Conventional E-glass fibre light guides: self-sensing composite based on sol-gel cladding. *Smart Mater Struct* 2004; 13(1):73-81.
24. Wang L, Pandita S, Machavaram VR, et al. Characterization of the cross-linking process in an E-glass fibre/epoxy composite using evanescent wave spectroscopy. *Compos Sci Technol* 2009; 69(13):2069-2074.
25. Kister G, Wang L, Ralph B, et al. Self-sensing E-glass fibres. *Opt Mater* 2003; 21(4):713-727.
26. Todoroki A, Hana N and Ueda M. Luminance Change Method for Cure Monitoring of GFRP. *Key Eng Mater* 2006; 321-323:1316-1321.
27. Iba H and Kagawa Y. Light transmittance of continuous fibre-reinforced composites: analysis, model experiment and parametric study. *Philos Mag B* 1998; 78(1):37-52.
28. Iba H, Naganuma T, Matsumura K, et al. Fabrication of transparent continuous oxynitride glass fiber-reinforced glass matrix composite. *J Mater Sci* 1999; 34(23):5701-5705.
29. Dunkers JP, Parnas RS, Zimba CG, et al. Optical coherence tomography of glass reinforced polymer composites. *Compos Part A* 1999; 30(2):139-145.
30. Kinsella M, Murray D, Crane D, et al. Mechanical properties of polymeric composites reinforced with high strength glass fibers. In: *Proceedings of the 33rd International SAMPE Technical Conference*, Seattle, USA, 5-8 November 2001, pp.1644-1657. Covina, CA: SAMPE.
31. Hecht E. *Optics*, 4th ed. San Francisco: Addison Wesley, 2002.
32. Kostro A, Geiger M, Jolissaint N, et al. Embedded microstructures for daylighting and seasonal thermal control. In: *Proceedings of SPIE Conference*, San Diego, USA, 12-14 August 2012, volume 8485, article number 84850L. Bellingham: SPIE.
33. CIE 1932. In: *Report of activities and proceedings of the Commission Internationale de l'Eclairage*, Cambridge, United Kingdom, 14-19 September 1931, pp.25-26. Cambridge: Cambridge University Press.
34. Jonsson JC, Rubin M. Light-loss when measuring transmittance of thick scattering samples with an integrating sphere. In: *Proceedings of SPIE Conference*, San Diego, USA, 26-30 August 2007, volume 6670, article number 667007. Bellingham: SPIE.

35. ASTM Standard G173-03, 2008. *Standard Tables for Reference Solar Spectral Irradiances: Direct Normal and Hemispherical on 37° tilted Surface*. West Conshohocken, PA: American Society for Testing and Materials, October 2008.
36. Pélisset S, Joly M, Chapuis V, et al. Efficiency of silicon thin-film photovoltaic modules with a front coloured glass. In: *Proceedings of CISBAT International Conference*, Lausanne, Switzerland, 14-16 September 2011, pp.37-42. Lausanne: LESO-PB.

4 Optomechanical investigation of GFRP laminates

4.1. Introduction

Traditionally glass components have been used in architectural design for creating transparent building envelopes.¹⁻³ However, nowadays polymer materials are considered as an effective alternative for constructing low-cost, lightweight and freeform transparent façades compared to glass solutions.^{4,5} Transparent polymers can be used in optical applications^{6,7} and replace glass components in solar thermal collectors⁸⁻¹⁰ and photovoltaic (PV) cell modules¹¹. However most polymers cannot be used as thin structural load-bearing elements due to their low stiffness and strength.^{12,13}

To resist high stresses, polymeric resins are reinforced with fibers and this combination results in a composite material. Fabrication of transparent composite materials is based on the perfect matching of the refractive indices of a transparent resin and a transparent reinforcement.¹⁴ These composites offer potential for designing lightweight, load-bearing and impact-resistant laminates, e.g. aircraft windshields and windows,¹⁵⁻¹⁷ and encapsulants of PV cells¹⁸. Perfectly transparent laminates do not diffuse light and are therefore characterized by a high regular transmittance, i.e. the amount of light emanating from the laminate in the same direction as the incident light. However, refractive index mismatches, Δn , as small as 0.001 between fiber and resin are already responsible for light scattering inside the composite.¹⁹ The non-straight path propagation of light rays through the thickness of a laminate increases with Δn and produces a loss of transparency: light is laterally diffused and the laminate becomes translucent.²⁰ Translucent components are frequently used in daylit buildings to avoid glare from sunlight. For this purpose structural lightweight dome skylights with a span of up to 5.5 m and 4-mm thickness made of glass fiber-reinforced polymer (GFRP) have been constructed for low-rise buildings.²¹

The diffuse transmittance of the laminate – especially relevant for designing daylit buildings – can be investigated by spectrophotometry using an integrating sphere set-up to collect the non-straight transmitted light rays.²² However for computing precisely the radiation emanating from the laminate in a given direction, and therefore the light transmittance in this direction, goniophotometry is required. Most goniophotometers are based on a scanning process performed by a movable sensor, e.g. silicon photodiode, measuring the radiation emerging from the laminate along all directions in the transmission hemisphere.^{23,24}

E-glass fibers and orthophthalic polyester resins, both transparent and low-cost materials, are used for designing translucent GFRP laminates due to a close matching of their refractive indices at around 1.56.²² However the fabrication of highly transparent laminates also requires good wettability and adhesion between fibers and resin: non-wet fibers and air bubbles act as light-scattering centers, increasing light diffusion in all directions. Based on the electromagnetic theory of light scattering,²⁵ Lin et al.²⁶ concluded

that as little as 2% of non-wet fibers in a unidirectional (UD) composite made of poly(methyl methacrylate) resin and glass fibers – with fiber volume fraction of 0.072 and laminate thickness of 0.5 mm – could reduce the regular transmittance by 0.17, thus increasing the light scattering caused by the composite.

In the last decades the light transmittance of UD laminates and their mechanical properties in the UD direction have been investigated in order to evaluate the performance of these materials for translucent structural components.^{27,28} Iba et al.²⁹ performed an optomechanical study on UD laminates and experimentally showed that increasing reinforcement weight and fiber volume fraction – and therefore elastic modulus and tensile strength – in the UD direction led to a decrease in the regular transmittance of the laminates. However UD laminates have few applications in load-bearing structures due to their low strength and stiffness in the transverse direction to the fibers. Cross-ply (CP) laminates are therefore preferred for structural components, e.g. face sheets of sandwich structures for building and bridge construction^{30,31} and reinforcement of aircraft windshields¹⁵. In recent research, CP laminates with a regular transmittance of 0.84 were fabricated using an epoxy resin matching the refractive index (1.52) of the S-glass fibers reinforcement.³² In another recent investigation, UD and CP transparent laminates with regular transmittances of up to 0.90 were fabricated also using an epoxy resin with the same refractive index (1.52) as the glass reinforcement made of rectangular ribbons.¹⁵ This study showed the directional dependence of tensile strength and E-modulus on the fiber volume fraction of each reinforced direction: 300 MPa (strength) and 19 GPa (E-modulus) were obtained in symmetric balanced CP laminates with a ribbon volume fraction of 0.19 in each direction, however the mechanical properties increased up to 770 MPa (strength) and 40.5 GPa (E-modulus) in the reinforced direction of UD laminates with a 0.60 ribbon volume fraction. The modeling of the tensile strength and E-modulus of GFRP laminates based on optical measurements has however remained unexplored in existing optomechanical studies due to the complexity of determining the fiber architecture from optical measurements. However goniophotometry can be a valuable non-destructive testing (NDT) method for the rapid evaluation of the fiber architecture of translucent GFRP laminates. Existing NDT methods such as optical coherence tomography are limited regarding the analysis of highly transparent laminates and other techniques such as micro-computed tomography require unwieldy equipment for the in-situ evaluation of structures.³³⁻³⁵

The objective of this work was to develop an optically-based model of the directional fiber volume fraction, and therefore tensile strength and E-modulus, of GFRP laminates based on the total and diffuse transmittance and directional light scattering of the composite. Model predictions were validated by tensile experiments performed on GFRP laminates. Optimum GFRP laminates in terms of optical and mechanical performances for translucent skylights of daylit buildings and encapsulation of PV cells were determined.

4.2. Theoretical background of light scattering in GFRP laminates

4.2.1. Directional scattering by UD aligned fibers

The scattering of light corresponds to the energy emanating from a beam of light caused by particles, e.g. glass fibers embedded in a resin laminate. Light rays propagating in a plane P and incident on the surface of a cylindrical fiber perpendicular to that plane are scattered in the same plane P .^{19,25,36} However in fiber

systems, e.g. UD composite laminates, misaligned fibers not perpendicular to that plane and the presence of twisted fibers contribute to out-of-plane scattering.³⁶

4.2.2. Single and multiple light scattering

Single scattering occurs when all particles in a given medium are exposed to the same radiation, i.e. the light of the original beam. The radiation scattered by a group of particles is thus simply proportional to the number of particles in the group. However if radiation is significantly scattered, reflected or absorbed through the thickness of the medium this simple proportionality no longer exists and multiple scattering effects dominate.

Based on the work of Lin et al.²⁶ the regular transmittance, T_r , of a fiber-reinforced laminate can be approximated by an exponential law, such as:

$$T_r = (1 - R) \cdot e^{-\tau} \quad (4.1)$$

where R is the reflectance of the pure resin laminate (without fibers) and τ is the optical depth of the fiber-reinforced laminate. A non-scattering medium, e.g. GFRP laminate with perfect impregnation and matching of refractive indices between fibers and a transparent resin, has $\tau = 0$. Single scattering prevails for $\tau < 0.1$;²⁵ however, experimental studies have shown that a transition to multiple scattering occurs for values of τ close to unity^{37,38} and $\tau = 1$ is considered as an approximate upper limit for observing single light scattering effects³⁹.

4.3. Experimental procedure

4.3.1. Materials

Unidirectional (UD) E-glass fabrics from Tissa (Oberkulm, Switzerland) with a reinforcement weight, w , of 410 g/m² were used as reinforcement of the GFRP laminates. Longitudinal rovings constituted 78% of the reinforcement weight, 17% of the weight corresponded to twisted longitudinal yarns and 5% to transversal yarns. The rovings (reference code ACF407-600) were manufactured by Taiwan Glass Industry Corporation (Taipei, Taiwan). The measured fiber diameter was 12.8±1.3 μm. The roving fibers had a silane sizing on their surface with a weight fraction with respect to the glass fiber of around 0.5%. Yarns (reference code EC9-68-620) were manufactured by AGY (Aiken, United States). The measured fiber diameter was 8.9±0.8 μm. Yarn fibers had a starch sizing on their surface with a weight fraction with respect to the glass fiber of around 1.2%. The refractive index of fibers, n_f , ranged from 1.56 at 500 nm to 1.55 at 800 nm.²²

Polylite 420-181 unsaturated polyester resin, manufactured by Reichhold Inc. (Durham, United States), was selected. The refractive index of this orthophthalic polyester resin, n_r , was investigated in previous research²² and varied between 1.57 and 1.55 in the 500-nm to 800-nm wavelength range and therefore closely matched that of the E-glass fibers. The resin was pre-accelerated with a cobalt solution and UV-stabilized by a BASF Tinuvin® additive absorbing the UV radiation below 380 nm.¹⁸ The resin also had low viscosity (330-360 mPa·s) making it suitable for hand lay-up lamination. Butanox M-60 organic peroxide from AkzoNobel (Amsterdam, Netherlands) was the catalyst used to initiate the polymerization reaction.

4.3.2. Specimen fabrication

Unidirectional (UD) and cross-ply (CP) [0/90/0] (unbalanced) and [0/90/90/0] (balanced) GFRP laminates with reinforcement weights, w , of between 410 and 1640 g/m² (from one to four layers of E-glass fabrics) were fabricated by hand lay-up at room temperature (23±2 °C). The weight of the catalyst was 1% of the resin weight and gel times, before a significant increase of resin viscosity, were around 15 min. These laminates were cured for 24 h at room temperature, and then postcured for 24 h at 60 °C. Another set of two UD laminates with reinforcement weights, w , of 1230 and 1640 g/m² was fabricated at a lower temperature (18±2 °C) using 0.7% of catalyst resulting in longer gel times of around 30 min. These laminates were also cured for 24 h at room temperature and then postcured for 48 h at 60 °C. The laminates were manufactured with two different fiber volume fractions, f : series L with low (0.24±0.03) and series H with high (0.42±0.01) fiber volume fractions. Laminates were labeled according to their total reinforcement weight, fiber architecture and fiber volume fraction, e.g. 410UD-L refers to the laminate reinforced with $w = 410$ g/m² of E-glass fibers, with unidirectional fiber architecture and low fiber volume fraction. A symbol (*) was added to identify laminates with longer gel times.

The directional reinforcement weight fraction of each laminate was defined as:

$$f_{w,i} = \frac{w_i}{w} \quad (4.2)$$

where w_i is the directional reinforcement weight ($i = 0$ or 90) and w is the total reinforcement weight. The results for UD and CP laminates are shown in Table 4.1. For each laminate a reinforcement weight ratio, R_w , characterizing the distribution of the reinforcement weight in the laminate, is given by:

$$R_w = \frac{w_0}{w_{90}} \quad (4.3)$$

The results for R_w are also reported in Table 4.1 where values $R_w \gg 1$ indicate an unbalanced distribution of the reinforcement weight in the laminate.

Two goniophotometric specimens of dimensions 75x25 mm² were cut from each GFRP laminate fabricated with 15-min gel time: one specimen had the 25-mm side oriented along the 0°-direction of the laminate and the other had the 25-mm side oriented along the 90°-direction of the laminate (see Figure 4.1(a)). Specimens were labeled with the laminate code followed by the directional orientation of the 25-mm side designated the examined direction, e.g. 1230CP-L-0 refers to a specimen cut from laminate 1230CP-L and having the 25-mm side in the 0°-direction (see Figure 4.1(a)). The fiber volume fraction and thickness of UD and CP specimens for goniophotometric experiments are reported in Tables 4.2 and 4.3.

From each GFRP laminate with 15-min gel time tensile specimens were cut in the two orthogonal reinforced directions according to the dimensional specifications of ASTM D3039/D3039M-08⁴⁰. For UD specimens loaded in the 0°-direction and for all CP specimens nominal dimensions were 250x25 mm² and for UD specimens loaded in the 90°-direction nominal dimensions were 175x25 mm². Specimens were labeled with the laminate code followed by the loading direction, e.g. 1230CP-L-0 refers to a specimen cut from laminate 1230CP-L and loaded in the 0°-direction. Three specimens were cut and examined for each label code. The average values of fiber volume fraction and thickness of UD and CP tensile specimens are given in Tables 4.2 and 4.3. Aluminum tabs were glued to the gripping areas at both sides of the specimen to avoid crushing of the specimen by the jaw faces of the machine.

In addition one specimen was cut from each laminate (15- and 30-min gel times) to investigate total and diffuse transmittance by spectrophotometry. The results of these investigations were reported in previous studies.^{18,22}

Table 4.1. Total and directional reinforcement weights, directional reinforcement weight fractions and ratio of reinforcement weight of unidirectional (UD) and cross-ply (CP) laminates.

Fiber architecture	UD				CP (unbal.)	CP (bal.)
w (g/m ²)	410	820	1230	1640	1230	1640
w_0 (g/m ²)	389.5	779	1168.5	1558	799.5	820
w_{90} (g/m ²)	20.5	41	61.5	82	430.5	820
$f_{w,0}$ (-)	0.95	0.95	0.95	0.95	0.65	0.5
$f_{w,90}$ (-)	0.05	0.05	0.05	0.05	0.35	0.5
R_w (-)	19	19	19	19	1.9	1

Table 4.2. Fiber volume fraction and thickness of unidirectional (UD) GFRP specimens for goniophotometric, tensile and spectrophotometric experiments.

Series	UD specimens	Goniophotometric exp.		Tensile exp.		Spectrophotometric exp.	
		Vol. fraction (-)	Thickness (mm)	Vol. fraction (-)	Thickness (mm)	Vol. fraction (-)	Thickness (mm)
L	410UD-L-0	0.20	0.8±0.06	0.17±0.01	0.9±0.03	0.21	0.8±0.13
	410UD-L-90	0.15	1.0±0.04	0.19±0.02	0.9±0.06		
	820UD-L-0	0.23	1.4±0.06	0.23±0.01	1.4±0.10	0.23	1.4±0.09
	820UD-L-90	0.23	1.4±0.11	0.26±0.01	1.2±0.05		
	1230UD-L-0	0.25	1.9±0.06	0.25±0.01	1.9±0.06	0.24	2.0±0.13
	1230UD-L-90	0.26	1.8±0.07	0.24±0.01	2.0±0.05		
	1640UD-L-0	0.29	2.2±0.07	0.26±0.01	2.5±0.07	0.29	2.2±0.10
	1640UD-L-90	0.29	2.2±0.04	0.25±0.01	2.6±0.10		
	1230UD-L*	-	-	-	-	0.21	2.4±0.16
	1640UD-L*	-	-	-	-	0.24	2.6±0.10
H	1230UD-H-0	0.43	1.1±0.06	0.41±0.02	1.2±0.03	0.41	1.2±0.07
	1230UD-H-90	0.42	1.1±0.04	0.41±0.00	1.2±0.02		
	1640UD-H-0	0.44	1.5±0.06	0.42±0.01	1.5±0.03	0.43	1.5±0.06
	1640UD-H-90	0.44	1.5±0.01	0.43±0.01	1.5±0.02		

Table 4.3. Fiber volume fraction and thickness of cross-ply (CP) GFRP specimens for goniophotometric, tensile and spectrophotometric experiments.

Series	CP specimens	Goniophotometric exp.		Tensile exp.		Spectrophotometric exp.	
		Vol. fraction (-)	Thickness (mm)	Vol. fraction (-)	Thickness (mm)	Vol. fraction (-)	Thickness (mm)
L	1230CP-L-0	0.29	1.7±0.03	0.22±0.00	2.1±0.05	0.22	2.1±0.07
	1230CP-L-90	0.27	1.8±0.03	0.22±0.01	2.2±0.06		
	1640CP-L-0	0.23	2.8±0.05	0.26±0.00	2.5±0.04	0.25	2.6±0.21
	1640CP-L-90	0.24	2.7±0.08	0.25±0.01	2.5±0.09		
H	1230CP-H-0	0.40	1.2±0.01	0.42±0.01	1.2±0.02	0.40	1.2±0.03
	1230CP-H-90	0.41	1.2±0.03	0.42±0.01	1.2±0.01		
	1640CP-H-0	0.41	1.6±0.05	0.43±0.01	1.5±0.01	0.41	1.5±0.02
	1640CP-H-90	0.40	1.6±0.06	0.41±0.01	1.6±0.02		

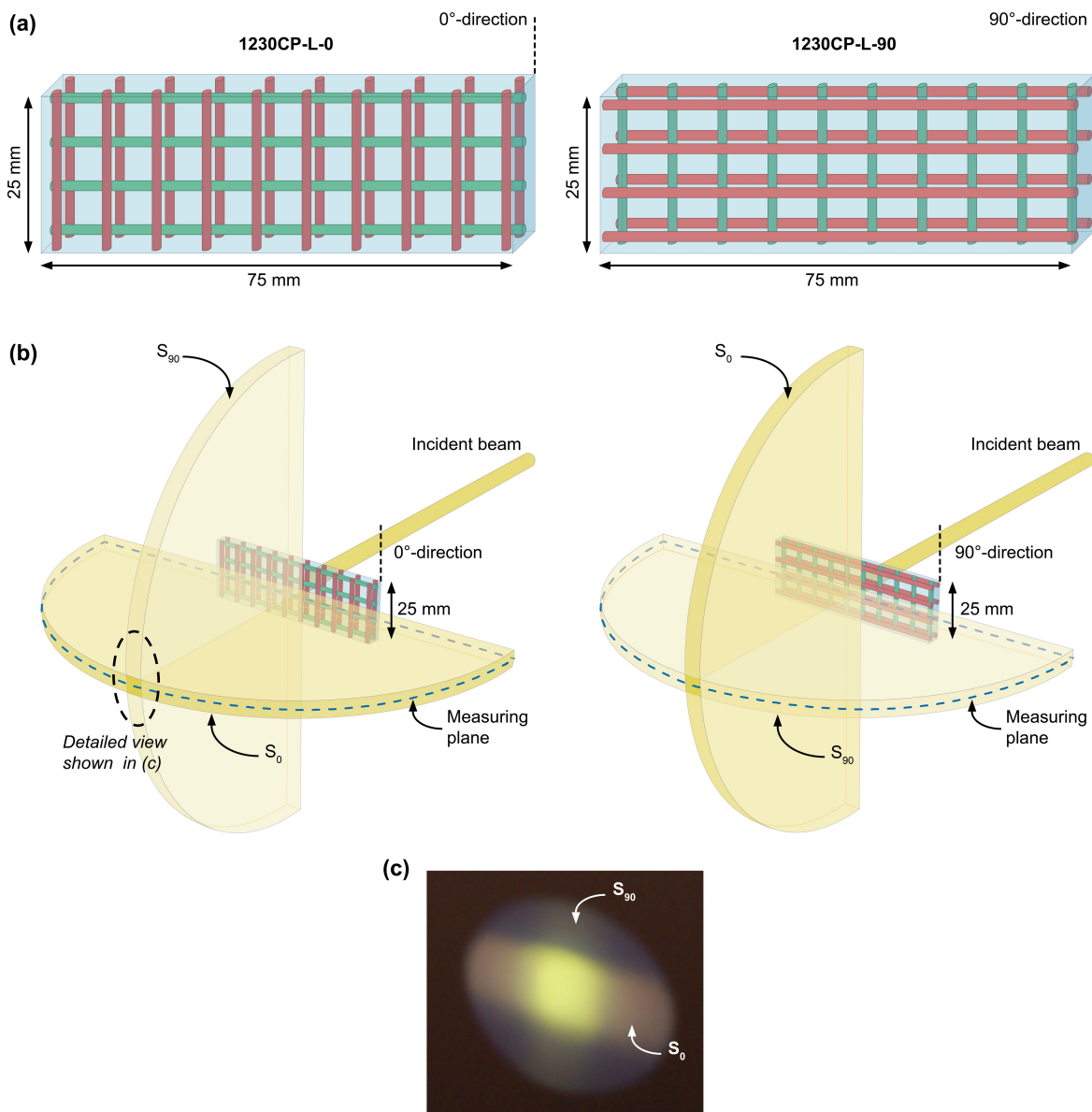


Figure 4.1. Goniophotometric specimens indicating (a) orientation of 0°- and 90°-directions, (b) major planes of light diffusion when illuminated by a concentrated beam and (c) detailed view of light scattering around the forward direction (laminare 1230CP-L).

4.3.3. Goniophotometric experiments

A goniophotometer – developed for studying the angle-dependent transmittance of complex fenestration systems⁴¹ – was used to characterize the light diffusion of UD and CP GFRP laminates. The set-up is shown in Figure 4.2. Light was emitted from a halogen light source (Osram 64642 HLX, 150 W, 24 V, Xenophot®) and passed through a set of optical lenses and diaphragms collimating a 7-mm diameter beam. The light of the beam was modulated to high frequency with a chopper wheel and then impacted at normal incidence on the GFRP specimen located on a frame support with the 25-mm side of the specimen in the vertical position. The light transmitted and diffused in the horizontal plane by the specimen was measured by an optical system rotating (in the horizontal plane) around the specimen. The transmittance angle, θ , was defined as the angle sustained by the axis of the incident beam and the axis of the rotating

optical system and varied from -90° to 90° . The measuring optical system was composed of a lens, a 1-mm diaphragm and a silicon photodiode (Silonex, model SLSD-71N3) sensitive to wavelengths in the 400- to 1100-nm band. The current generated by the photodiode was amplified and converted to a voltage. A digital lock-in amplifier was then used to measure only the voltage generated by the modulated light and not due to the surrounding noise (light of the room).⁴¹ The lock-in amplifier was integrated into software also controlling the motor for rotating the optical system around the specimen.

A first reference measurement without specimen was performed and the maximum voltage recorded. For all goniophotometric measurements a normalized voltage, U_{norm} , was defined as the voltage measured at angle θ divided by the maximum voltage recorded from the reference measurement. The scattering diagrams below show the normalized voltage, U_{norm} , as function of the transmittance angle, θ . The reference measurement (without specimen) resulted in $U_{norm} = 0$ for $|\theta| > 1^\circ$ (see Figure 4.3). Therefore, for experiments performed on GFRP specimens, normalized voltages detected at $|\theta| > 1^\circ$ were assumed to indicate light scattered by the specimen.

Three measurements were performed on each GFRP specimen at different locations around the central area. In the following the scattering diagrams of the average values are presented.

4.3.4. Tensile experiments

An Instron 8800 servohydraulic machine of 100-kN capacity was used for performing the tensile experiments on all CP specimens and on UD specimens with $w \geq 1230 \text{ g/m}^2$ loaded in the 0° -direction. An MTS servohydraulic machine of 25-kN capacity was used for performing the tensile experiments on the remaining specimens. Experiments were performed under displacement control at a rate of 1 mm/min for CP specimens and for UD specimens loaded in the 0° -direction. A rate of 0.5 mm/min was used for experiments on UD specimens loaded in the 90° -direction. All experiments were performed up to failure (final drop in the resisted load) in laboratory conditions at $23 \pm 5^\circ \text{C}$ and $50 \pm 10\% \text{RH}$.

Two specimens of each label code were equipped with a linear HBM strain gage (1-LY11-6/120) of 6-mm grid length in the central zone of the specimens (see Figure 4.4).

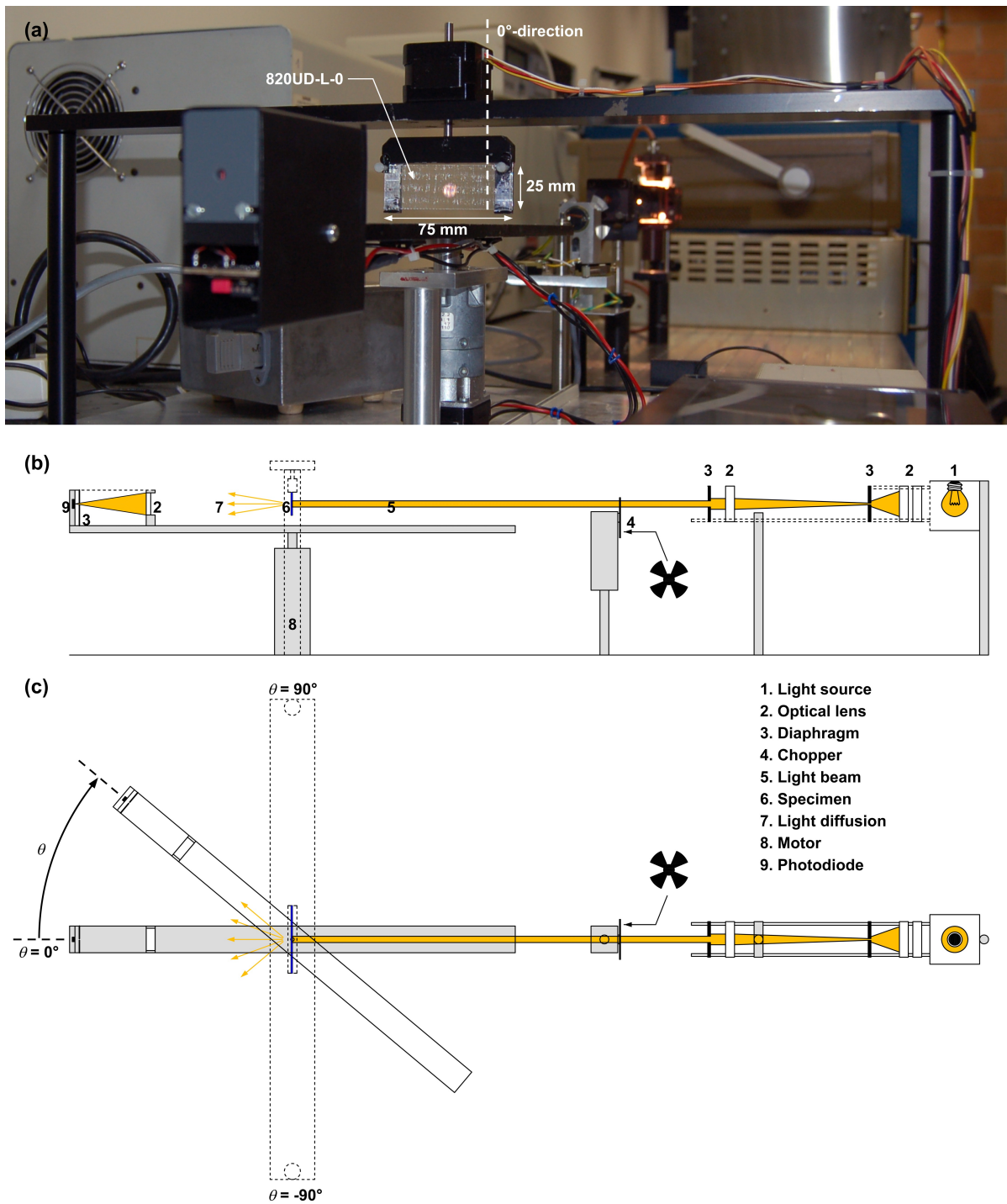


Figure 4.2. Goniophotometric set-up (a) view of sensor and specimen, (b) lateral view and (c) top view.

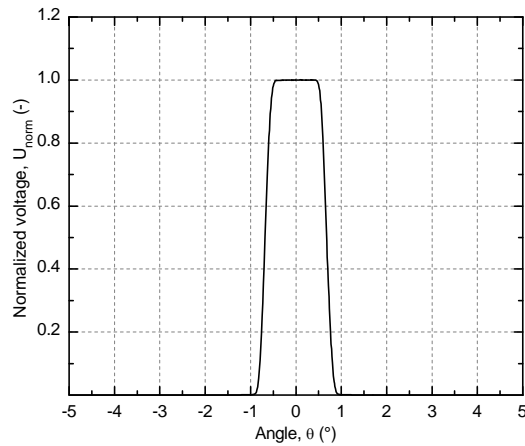


Figure 4.3. Scattering diagram of reference measurement (without specimen).

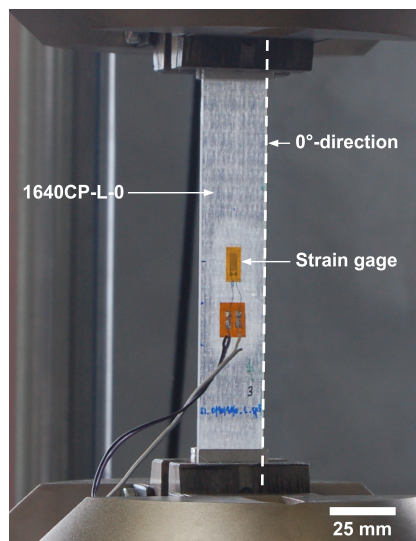


Figure 4.4. Tensile experiment on GFRP specimen with strain gage located in center.

4.4. Experimental results

4.4.1. Goniophotometric results

0°-direction. The scattering diagrams of UD-L specimens examined in the 0°-direction with reinforcement weights from $w = 410 \text{ g/m}^2$ to $w = 1640 \text{ g/m}^2$ are presented in logarithmic scale in Figure 4.5. The diagrams were almost symmetric with respect to $\theta = 0^\circ$ where they reached a maximum value representing the regular transmittance, T_r , of the specimen. The normalized voltage, U_{norm} , decreased when $|\theta|$ increased and for $|\theta| > 20^\circ$ normalized voltages were already lower than around 0.001. However, for $|\theta| > 20^\circ$ normalized voltages increased with the reinforcement weight, demonstrating that fibers were responsible for the lateral diffusion of light.

For $w \leq 820 \text{ g/m}^2$ and $|\theta| < 20^\circ$ the scattering diagrams of specimens UD-L-0 are shown in Figure 4.6. Regular transmittance (at $\theta = 0^\circ$) decreased with the reinforcement weight by 33% from 0.54 at $w = 410 \text{ g/m}^2$ to 0.36 at $w = 820 \text{ g/m}^2$. However light scattering for $|\theta| > 1^\circ$ increased with the

reinforcement weight, indicating that part of the light emanating from the original beam was deviated into the plane perpendicular to the 0°-direction of the specimen, thus reducing the regular transmittance.

For $w \geq 1230 \text{ g/m}^2$ and $|\theta| < 20^\circ$ the influence of fiber volume fraction on the scattering diagrams is shown in Figure 4.7 for UD specimens. Increasing the fiber volume fraction from around 0.27 (L) to 0.43 (H) had little influence on the scattering diagrams for $|\theta| > 1^\circ$, however it reduced the regular transmittance by 50% for $w = 1230 \text{ g/m}^2$ and by 40% for $w = 1640 \text{ g/m}^2$. Since total light transmittance is independent of fiber volume fraction and only decreases with reinforcement weight,¹⁸ the reduction of regular transmittance was attributed to the increase of light scattering out of the measuring plane due to two effects: 1) the increase of flaws with fiber volume fraction due to hand lay-up lamination, 2) the increase of misaligned fibers and twisted yarns with increased reinforcement weight.

90°-direction. The amount of light scattered by specimen 410UD-L-90 in the measuring plane was significantly lower than for specimen 410UD-L-0 (see Figures 4.5 and 4.6). This behavior was attributed to the low amount of fibers oriented in the 90°-direction compared to the 0°-direction. The small difference in regular transmittance (0.03) between both specimens was attributed to the high sensitivity of regular transmittance to very small differences in fiber impregnation and flaw content. The angular range of the peak was localized between $[-1^\circ; 1^\circ]$ and normalized voltages were close to zero outside this range. This result was observed in all UD specimens examined in the 90°-direction.

Ratio of scattered radiation in orthogonal planes. The scattered radiation of GFRP specimens in the plane orthogonal to i -direction ($i = 0^\circ$ or 90°), S_i (see Figure 4.1(b)) is calculated as:

$$S_i = \int_{-90}^{-1} U_{norm\ i} \cdot d\theta + \int_1^{90} U_{norm\ i} \cdot d\theta \quad (4.4)$$

where the angular range $[-1^\circ; 1^\circ]$ associated to the regular transmittance is excluded in the integration. Increasing the amount of fibers in i -direction increases the scattered radiation S_i as shown in Figure 4.1(c) by the brighter intensity in the S_0 than in the S_{90} plane for specimen 1230CP-L-0. The ratio of scattered radiation in planes orthogonal to the 0- and 90°-directions is defined as:

$$R_{scat} = \frac{S_0}{S_{90}} \quad (4.5)$$

and the average results of the three measurements per specimen are shown, together with R_w , in Table 4.4 and Figure 4.8 for different fiber architectures, reinforcement weights and volume fraction series.

The theoretical result $R_{scat} = R_w$, i.e. proportionality between scattered radiation and fiber content, was expected to be reached for single light scattering conditions ($\tau < 1$). For laminates with $w \leq 820 \text{ g/m}^2$ R_{scat} and R_w closely matched (see Table 4.4 and Figure 4.8) and based on equation (4.1) their optical depth can be calculated as:

$$\tau = -\ln\left(\frac{T_r}{1-R}\right) \quad (4.6)$$

where $R = 0.09$ for a pure resin laminate,¹⁸ $T_r = 0.55$ for laminate 410UD-L and $T_r = 0.36$ for laminate 820UD-L (see Figure 4.6). Optical depths resulted in $\tau = 0.50$ (410UD-L) and $\tau = 0.93$ (820UD-L), both lower than 1 and therefore explaining the single scattering observation $R_{scat} \approx R_w$. The imperfect overlapping of scattering diagrams for balanced laminate 1640CP-L in the 0°- and 90°-directions (see

Figure 4.9) was attributed to relevant multiple scattering effects inside the specimens due to an optical depth $\tau = 2.71$ and therefore higher than 1.

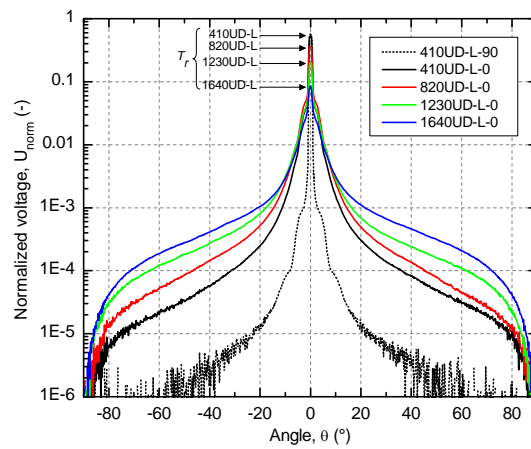


Figure 4.5. Scattering diagrams of UD-L specimens with $410 \leq w \leq 1640 \text{ g/m}^2$ in 0° -direction and UD-L specimen with $w = 410 \text{ g/m}^2$ in 90° -direction (representation in logarithmic scale).

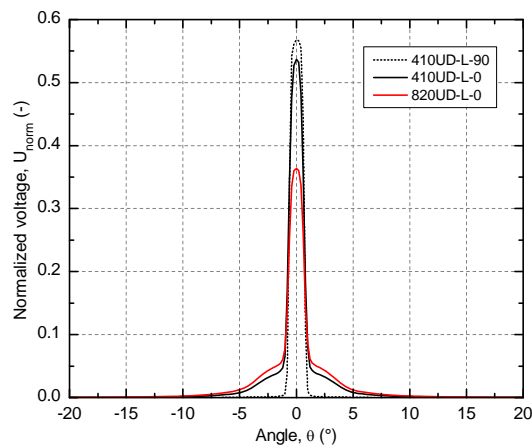


Figure 4.6. Scattering diagrams of specimens 410UD-L in 0° - and 90° -directions and specimen 820UD-L in 0° -direction.

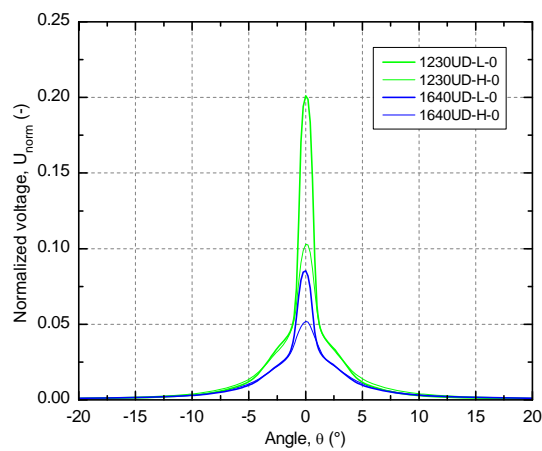


Figure 4.7. Scattering diagrams of UD specimens in 0° -direction at different fiber volume fractions.

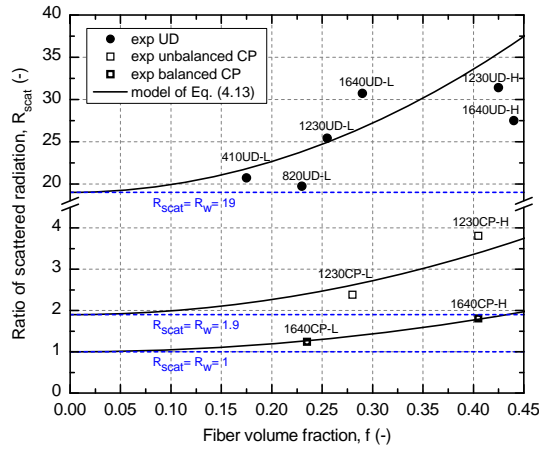


Figure 4.8. Experimental results of scattered radiation ratio, R_{scat} , as function of average fiber volume fraction of goniphotometric specimens and model predictions according to equation (4.13).

Table 4.4. Ratio of reinforcement weights (R_w), ratio of ultimate loads (R_F) and ratio of scattered radiation (R_{scat}) for unidirectional (UD) and cross-ply (CP) laminates.

Fiber architecture		UD				CP (unbal.)	CP (bal.)
w (g/m ²)		410 ^a	820 ^a	1230	1640	1230	1640
R_w (-)	Series L and H	19	19	19	19	1.9	1
R_{scat} (-)	Series L	20.7	19.7	25.4	30.7	2.38	1.24
	Series H	-	-	31.4	27.5	3.81	1.81
R_F (-)	Series L	16.2	17.5	18.0	17.1	2.0	1.0
	Series H	-	-	18.6	17.5	1.7	1.0

^a Laminates with optical depth $\tau < 1$

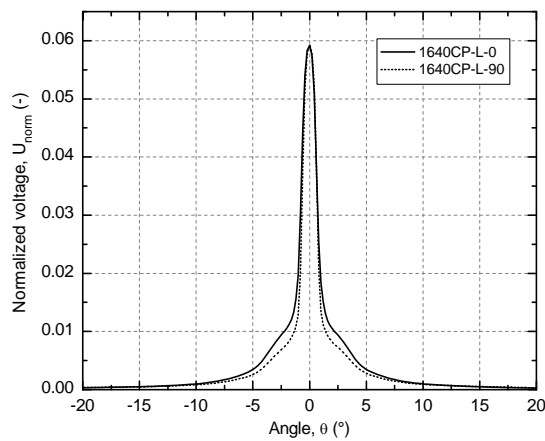


Figure 4.9. Scattering diagrams of specimens 1640CP-L in 0°- and 90°-directions.

4.4.2. Tensile results

0°-direction. The average experimental ultimate loads of UD specimens loaded in the 0°-direction, $F_{u,0 exp}$, at different reinforcement weights and volume fractions are given in Table 4.5. Independently of fiber volume fraction, ultimate loads increased proportionally with the directional reinforcement weight from 6.8 kN at $w_0 = 389.5$ g/m² to around 28 kN at $w_0 = 1558$ g/m², indicating that in the 0°-direction the fiber content determined the ultimate load of GFRP specimens. The load-strain curves of representative UD specimens loaded in the 0°-direction with different reinforcement weights and fiber volume fractions are

given in Figure 4.10. For the same reinforcement weight, the slightly steeper slope of series L than series H curves indicated a higher stiffness due to the higher resin content. The ultimate strains of GFRP specimens ranged between 1.8% and 2.4%.

The average experimental ultimate loads of CP specimens loaded in the 0°-direction, $F_{u,0\text{ exp}}$, are also reported in Table 4.5. The directional reinforcement weights for these specimens were very similar, $w_0 = 799.5\text{ g/m}^2$ and $w_0 = 820\text{ g/m}^2$, resulting in almost identical ultimate loads around 14 kN. The load-strain curves of representative 1640CP-L-0 and 1640CP-H-0 specimens are shown in Figure 4.11 and ultimate loads were observed to be independent of fiber volume fraction. The ultimate strains ranged between 2.0% and 2.5% and were therefore similar to those of UD specimens in the 0°-direction.

Table 4.5. Experimental ultimate loads of unidirectional (UD) and cross-ply (CP) tensile specimens.

w_i (g/m ²)	i -direction	Reinforcement configuration	$F_{u,i\text{ exp}}$ (kN)	
			Series L	Series H
20.5	90°	410UD	0.42±0.01	-
41	90°	820UD	0.77±0.03	-
61.5	90°	1230UD	1.19±0.03	1.14±0.07
82	90°	1640UD	1.65±0.02	1.58±0.06
389.5	0°	410UD	6.80±0.27	-
430.5	90°	1230CP	7.10±0.27	7.90±0.12
779	0°	820UD	13.50±0.46	-
799.5	0°	1230CP	14.00±0.41	13.80±0.26
820	0°	1640CP	14.60±0.69	14.20±0.67
820	90°	1640CP	14.80±0.21	14.60±1.00
1168.5	0°	1230UD	21.40±0.59	21.20±0.83
1558	0°	1640UD	28.20±1.18	27.70±0.98

shaded background indicates specimens loaded in 90°-direction.

90°-direction. The average experimental ultimate loads of UD specimens loaded in the 90°-direction, $F_{u,90\text{ exp}}$, at different reinforcement weights and volume fractions are given in Table 4.5. Ultimate loads increased proportionally with the directional reinforcement weight from 0.42 kN at $w_{90} = 20.5\text{ g/m}^2$ to around 1.6 kN at $w_{90} = 82\text{ g/m}^2$, indicating that in the 90°-direction fiber content was also the major parameter determining the ultimate load of specimens. The load-strain curves of representative UD specimens loaded in the 90°-direction are given in Figure 4.12 and showed the independence of ultimate loads on fiber volume fraction. For series L few transversal cracks were observed at strains around 0.3% and led to the immediate failure of the specimen. For series H transversal cracks appeared from strains of around 0.3% up to 1.0% – resulting in a loss of stiffness and therefore significant non-linearity of load-strain curves – and failure was reached at ultimate strains of around 2.0%. Crack formation significantly reduced the transparency of series H compared to series L as shown in Figure 4.13 for specimens with $w = 1640\text{ g/m}^2$ that initially had the same total light transmittance.

The average experimental ultimate loads of CP specimens loaded in the 90°-direction, $F_{u,90\text{ exp}}$, are also summarized in Table 4.5. As described above, ultimate loads increased proportionally with the directional reinforcement weight from around 7.5 kN at $w_{90} = 430.5\text{ g/m}^2$ to around 14.7 kN at $w_{90} = 820\text{ g/m}^2$. The load-strain curves of representative 1640CP-L-90 and 1640CP-H-90 specimens are shown in Figure 4.11; ultimate strains ranged between 2.0% and 2.4%.

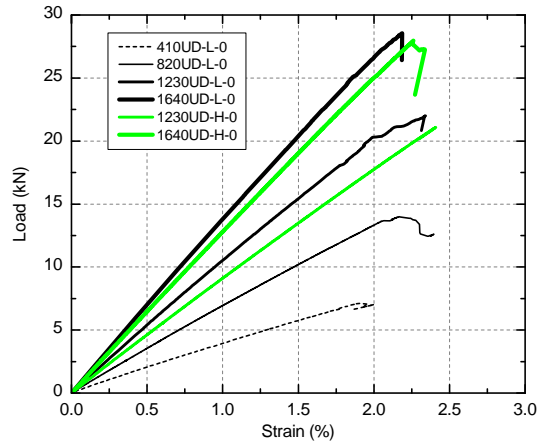


Figure 4.10. Load-strain curves for UD-L and UD-H specimens loaded in 0°-direction.

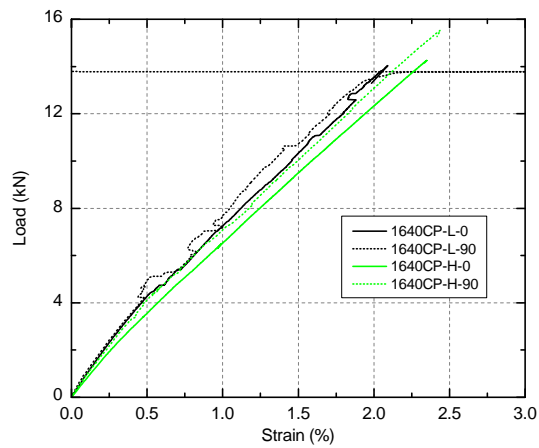


Figure 4.11. Load-strain curves of 1640CP-L and 1640CP-H specimens loaded in 0°- and 90°-directions.

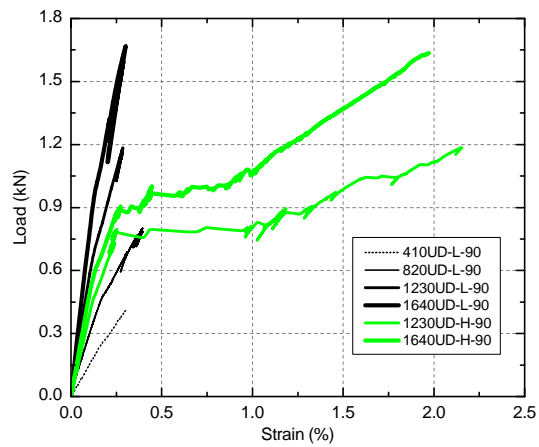


Figure 4.12. Load-strain curves of UD-L and UD-H specimens loaded in 90°-direction.

Ratio of ultimate loads in 0°- and 90°-directions. The ratio of ultimate loads in the two orthogonal reinforced directions, R_F , was defined for each laminate as:

$$R_F = \frac{F_{u,0 \text{ exp}}}{F_{u,90 \text{ exp}}} \quad (4.7)$$

The results of R_F for each laminate are presented in Table 4.4 and approximately matched reinforcement weight ratios due to the proportionality between ultimate loads and reinforcement weight described above.

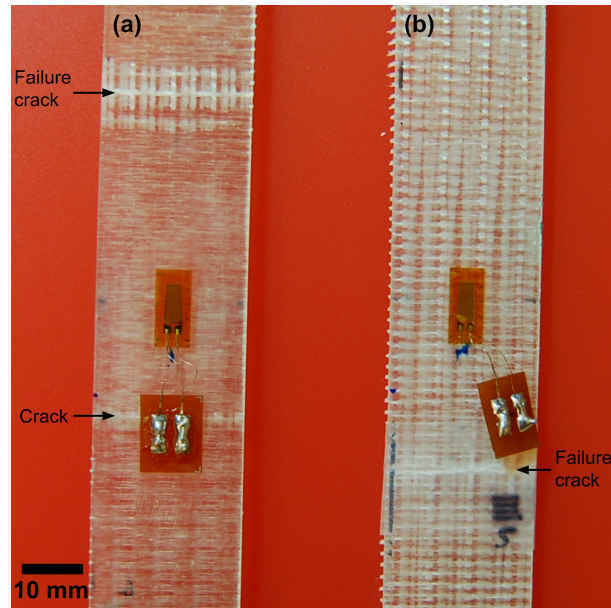


Figure 4.13. Failure modes of specimen (a) 1640UD-L exhibiting more transparency than specimen (b) 1640UD-H.

4.5. Analytical modeling of tensile properties of GFRP laminates

4.5.1. Overview

The fiber volume fraction of GFRP laminates was modeled based on the spectrophotometric results of total light transmittance, $T_{t,555}$, and translucency, DF_{555} , at 555-nm wavelength obtained in previous works^{18,22} and reported in Table 4.6. Directional reinforcement weight fractions were modeled based on goniophotometric experimental results. Finally the directional fiber volume fractions were modeled and results were validated by GFRP strength and E-modulus obtained from tensile experiments.

Table 4.6. Total transmittance and translucency at 555 nm, fiber volume fraction modeled by equation (4.12) and reinforcement weight fractions modeled by equation (4.16) of UD and CP laminates.

Fiber architecture	UD								CP (unbal.)		CP (bal.)	
	410	820	1230	1230	1640	1640	1230	1640	1230	H	L	H
Series	L	L	L	H	L	H	L*	L*	L	H	L	H
$T_{t,555}$ (-)	0.87	0.82	0.78	0.78	0.75	0.75	0.82	0.80	0.76	0.76	0.72	0.72
DF_{555} (-)	0.15	0.2	0.38	0.46	0.55	0.60	0.21	0.26	0.41	0.57	0.56	0.65
f_{mod} (-)	0.27	-	0.14	0.37	0.41	0.57	0.13	0.16	0.08	0.53	0.23	0.48
$f_{w,0 mod}$ (-)	0.94	0.95	0.96	0.95	0.94	0.92	-	-	0.70	0.62	0.50	0.46
$f_{w,90 mod}$ (-)	0.06	0.95	0.04	0.05	0.06	0.08	-	-	0.30	0.38	0.50	0.54

4.5.2. Optically-based model of fiber volume fraction

The translucency of a laminate at 555-nm wavelength, i.e. wavelength of maximum sensitivity of human eye, designated $DF_{555 mod}$, is derived from previous research²² as follows:

$$DF_{555\ mod} = 1 - e^{-a \cdot w_{eq}} \quad (4.8)$$

where a indicates the rate at which transparency is lost (for values fitted to experimental results, see Table 4.7) and w_{eq} is the equivalent reinforcement weight of the laminate defined as²²:

$$w_{eq} = w \cdot (0.67 + f) \quad (4.9)$$

with $w_{eq} = w$ for an intermediate volume fraction of $f = 0.33$ and the predictions of equation (4.8) are shown in Figure 4.14.

In addition, the reinforcement weight, w , of laminates and their total transmittance at 555-nm wavelength are related as follows¹⁸:

$$T_{t,555} = T_{t\ resin,555} \cdot c^{\frac{w}{410}} \quad (4.10)$$

where $T_{t\ resin,555} = 0.909$ is the total transmittance of a 1-mm-thick resin specimen at 555 nm and c was obtained from 410UD-L and 1640CP-L measurements (see previous work¹⁸) and 1640UD-L* ($T_{t,555} = 0.805$), see Table 4.7. Based on equation (4.10) the reinforcement weight results in:

$$w = \ln \left(\frac{T_{t,555}}{T_{t\ resin,555}} \right) \cdot \frac{410}{\ln c} \quad (4.11)$$

and combining equations (4.8) to (4.11), the fiber volume fraction of laminates can be estimated as:

$$f_{mod} = \frac{-\ln(1 - DF_{555})}{a} \cdot \frac{\ln c}{\ln \left(\frac{T_{t,555}}{T_{t\ resin,555}} \right)} \cdot \frac{1}{410} - 0.67 \quad (4.12)$$

The results for all GFRP laminates are presented in Table 4.6. The average volume fraction of series L (0.24 ± 0.03) and H (0.42 ± 0.01) agreed well with predicted values (0.20 ± 0.11 and 0.49 ± 0.09 respectively). Laminate 820UD-L was disregarded in this analysis since a slower polymerization rate of the resin was observed in this laminate – around 3 hours, i.e. double that for the other laminates – resulting in better fiber impregnation and a significant mismatch with the translucency predictions of equation (4.8) (see Figure 4.14).

Table 4.7. Parameters of translucency and total transmittance models according to equations (4.8) and (4.10).

Laminates	a (10^{-4} m ² /g)	c (-)
UD (15-min gel time)	4.6	0.952
CP (15-min gel time)	5.7	0.942
UD (30-min gel time)	2.1	0.970
CP (30-min gel time)	2.6*	0.960*

* Values obtained assuming same UD/CP ratio as with 15-min gel time.

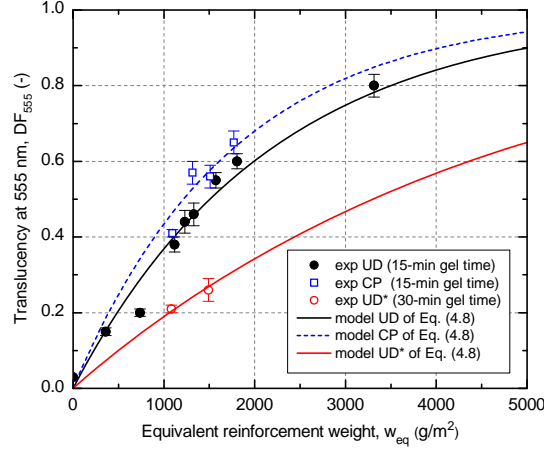


Figure 4.14. Experimental results of translucency at 555 nm as function of equivalent reinforcement weight and modeling predictions according to equation (4.8).

4.5.3. Optically-based model of directional fiber volume fraction

The experimental results shown in Figure 4.7 demonstrate that the regular transmittance decreases with increasing fiber volume fraction. Therefore, the optical depth according to equation (4.6) and the multiple scattering increase with increasing fiber volume fraction, which can be taken into account in the scattered radiation as follows:

$$R_{scat} = R_w \cdot (1+q) \quad (4.13)$$

where the coefficient q increases with the fiber volume fraction according to the experimental results:

$$q = 4.8 \cdot f^2 \quad (4.14)$$

A good agreement between equation (4.13) and the experimental results was obtained, see Figure 4.8.

Dividing the numerator and denominator of equation (4.2) by $w-w_i$, results in:

$$f_{w,i} = \frac{x}{R_w + 1} \quad (4.15)$$

where $x = R_w$ for $i = 0^\circ$ and $x = 1$ for $i = 90^\circ$. From equations (4.13) and (4.15), the directional reinforcement weight fraction is obtained as:

$$f_{w,i mod} = \frac{z}{R_{scat} + (1+q)} \quad (4.16)$$

where $z = R_{scat}$ for $i = 0^\circ$, $z = 1+q$ for $i = 90^\circ$ and coefficient q is calculated integrating equation (4.12) into equation (4.14). The optically-based predictions of equation (4.16) are presented in Table 4.6. The directional reinforcement weights in the 0° -direction of UD laminates (see Table 4.1) and predicted values differed by a maximum of only 3%. For the unbalanced CP laminates this difference was 14% and for CP balanced 8%, demonstrating the good accuracy of goniophotometry for predicting the reinforcement weight fractions, and therefore the fiber architecture, of UD and CP GFRP laminates.

The directional fiber volume fraction in i -direction, f_i , is calculated by multiplying the fiber volume fraction by the directional reinforcement weight and can therefore be estimated by multiplying equations (4.12) and (4.16):

$$f_{i\,mod} = \left(\frac{-\ln(1-DF_{555})}{a} \cdot \frac{\ln c}{\ln\left(\frac{T_{t,555}}{T_{t\,resin,555}}\right)} \cdot \frac{1}{410} - 0.67 \right) \cdot \frac{z}{R_{scat} + (1+q)} \quad (4.17)$$

The comparison of the average directional fiber volume fractions of the goniophotometric and spectrophotometric specimens with the predictions of equation (4.17) is shown in Figure 4.15. Linear regression ($R^2 = 0.83$) resulted in an average overestimation of directional fiber volume fractions of 8%. For other fabrication processes coefficients a , c and q have to be calibrated.

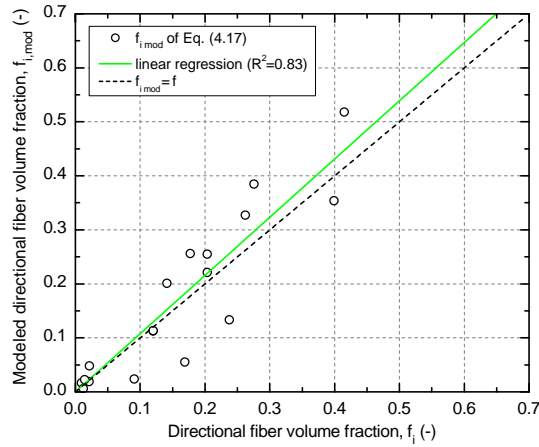


Figure 4.15. Directional fiber volume fraction, $f_{i\,mod}$, from equation (4.17) compared to average directional volume fraction, f_i , from gonio- and spectrophotometric results (dotted line indicates a model that would exhibit perfect accuracy).

4.5.4. Strength and E-modulus models of translucent GFRP laminates

Disregarding the stress contribution of the resin at the ultimate state, the tensile strength in i -direction of GFRP laminates is obtained as follows:

$$\sigma_{u,i\,mod} = \sigma_f \cdot f_i \quad (4.18)$$

where σ_f represents the strength of the E-glass fibers. Linear regression of strengths obtained from tensile experiments resulted in $\sigma_f = 1779$ MPa and $R^2 = 0.99$ (see Figure 4.16) – closely matching the tensile strength of 1750 MPa for E-glass fibers in GFRP laminates.¹² Integrating equation (4.17) in equation (4.18) defines an optomechanical model of the directional strength of GFRP laminates. Linear regression of the results ($R^2 = 0.83$) – from spectrophotometric and goniophotometric experiments – also gave an overestimation of 8% with respect to the predictions of equation (4.18) (see Figure 4.16).

The E-modulus of UD laminates in the fiber direction can be estimated using the rule of mixtures (ROM) given by:

$$E_i = E_r + (E_f - E_r) \cdot f_i \quad (4.19)$$

where E_r is the E-modulus of the resin, E_f is the E-modulus of the fibers and f_i is the fiber volume fraction of the laminate in the reinforced i -direction. The predictions of equation (4.19) together with the E-

modulus of the examined GFRP specimens – calculated according to ASTM D3039/D3039M-08⁴⁰ – are shown in Figure 4.17, assuming $E_r = 3.4$ GPa for orthophthalic polyester resin and $E_f = 72$ GPa for E-glass fibers.¹² For UD-H-0 specimens ($f_i = f_0 = 0.37$ to 0.41) the ROM was particularly accurate, indicating little influence of transversal fibers on the E-modulus in the 0° -direction. For CP specimens ($f_i = f_0 = 0.13$ to 0.27 and $f_i = f_0 = 0.08$ to 0.21) higher experimental results than those predicted by equation (4.11) were attributed to the contribution of transversal rovings, which increased the specimen stiffness. Finally, for UD specimens examined in the 90° -direction ($f_{90} = 0.01$ to 0.02) the ROM is not applicable and a better approximation of the E-modulus was obtained by applying the Halpin-Tsai model.¹² According to this model and considering $f_{90} = 0$, the transverse E-modulus is obtained as:

$$E_{90} = E_r \cdot \left(\frac{1 + \zeta \cdot \mu \cdot f_0}{1 - \mu \cdot f_0} \right) \quad (4.20)$$

where $\zeta = 2$ for circular fibers and μ is given by¹²:

$$\mu = \frac{E_f / E_r - 1}{E_f / E_r + \zeta} \quad (4.21)$$

resulting in $\mu = 0.87$ and $E_{90} = 7.5$ GPa for an intermediate fiber volume fraction $f_0 = 0.33$. Considering equation (4.19) as being accurate for high directional fiber volume fractions, and $f_i = f_0 = 0.45$, results in $E_0 = 34.3$ GPa. With both sets of results, $E_{90} = 7.5$ GPa at $f_{90} = 0$ and $E_0 = 34.3$ GPa at $f_0 = 0.45$, the E-modulus in i -direction of GFRP laminates is :

$$E_{i\text{mod}} = 7.5 + 58.9 \cdot f_i \quad (4.22)$$

and good agreement with experimental results ($R^2 = 0.96$) is shown in Figure 4.17. Integrating equation (4.17) into equation (4.22) allows the establishment of an optomechanical model of the directional E-modulus. Linear regression of the results ($R^2 = 0.83$) – from spectrophotometric and goniophotometric experiments – closely matched the predictions of equation (4.22) and overestimations of maximum 7% were observed (see Figure 4.17).

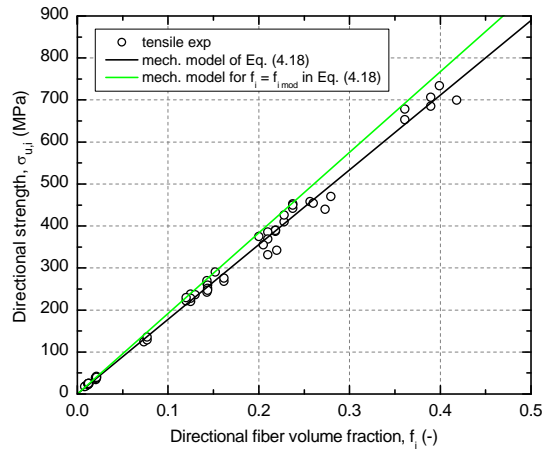


Figure 4.16. Directional strength as function of directional fiber volume fraction, mechanical model predictions according to equation (4.18) and model resulting when considering $f_i = f_{i\text{mod}}$.

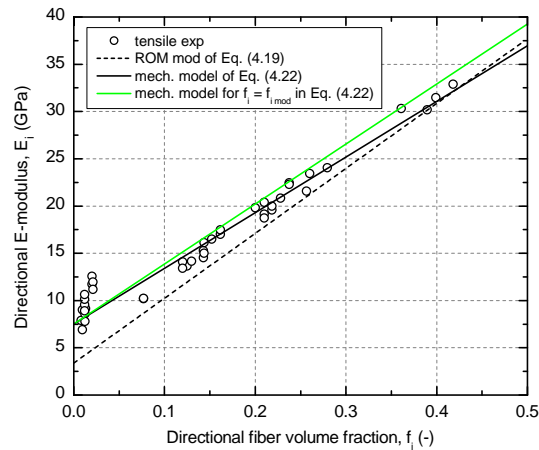


Figure 4.17. Directional E-modulus as function of directional fiber volume fraction, model predictions according to the ROM, predictions of mechanical model from equation (4.22) and model resulting when considering $f_i = f_{i,mod}$.

4.6. Evaluation of applications

To apply the obtained results, a case study is performed using the GFRP/polyurethane sandwich roof of the Novartis Campus Main Gate Building, see Figure 4.18(a) and (b).⁴³ An analysis is made as to what extent the GFRP face sheets of this sandwich structure fulfill the requirements 1) for daylighting and 2) PV cell integration – i.e. whether skylights and PV cells could have been integrated into this specific sandwich structure (maintaining the fiber architecture optimized for the structural function). In the former case, a minimum translucency of 0.90 and a minimum visible total light transmittance of 0.50 are recommended while in the latter case the minimum light transmittance of the top encapsulant should not fall below 0.83.^{18,44} The fiber architecture of the hand-laminated 6-mm-thick face sheets and the examined integration of skylights and PV cells are shown in Figure 4.18(c) and (d) respectively.

The foam core of the sandwich structure is reinforced by an orthogonal grid of GFRP webs, spaced at a distance of 925 mm, see Figure 4.18(c). Skylights could thus be integrated into individual cells of this grid by merging top and bottom face sheets, as shown in Figure 4.18(d). The resulting 12-mm-thick face sheet has $w = 8680 \text{ g/m}^2$ and $f = 0.28$. Assuming a 30-min gel time (a - and c -values from Table 4.7) in equations (4.8) and (4.10) leads to $DF_{555} = 0.88$ and $T_{t,555} = 0.38$. The recommended values (0.9 and 0.5) are thus almost achieved. For recommended values, equation (4.12) results in $f = 0.81$, which is too high for any manufacturing process however. An optimized solution with $DF_{555} = 0.85$ and $T_{t,555} = 0.45$ could be achieved for $f = 0.36$. A reinforcement weight of $w = 7062 \text{ g/m}^2$ would result from equation (4.11) and could in practice be obtained by merging the top skin with the 920g-CP/800g-UD(0°)/800g-UD(90°)/225g-mat layers from the bottom skin.

Concerning the potential encapsulation of PV cells into the top face sheet, integrating the cell below the first mat- and UD-layer results in $T_{t,555} = 0.84$ according to equation (4.10), which slightly exceeds the required minimum value of 0.83.

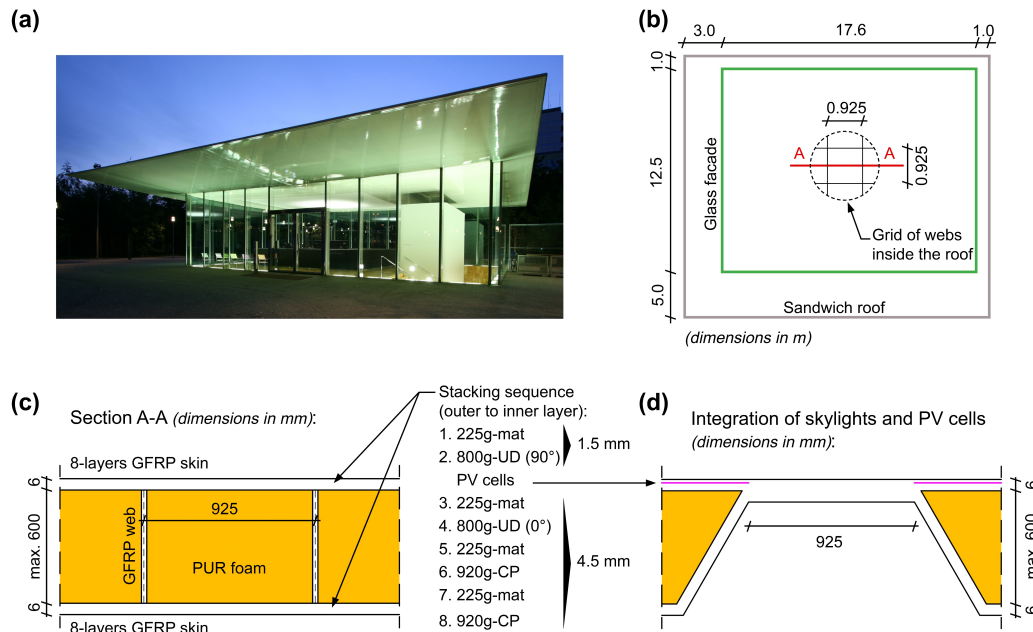


Figure 4.18. (a) Novartis Campus Main Gate Building, Basel, (b) roof top view, (c) roof cross section and (d) concept for integrating PV cells and skylights.

4.7. Conclusions

An optically based model of the directional fiber volume fraction, and therefore tensile strength and E-modulus, of GFRP laminates was developed. The following conclusions were drawn:

1. Goniophotometry proved to be an effective method for evaluating the GFRP fiber architecture of UD and CP laminates. The directional reinforcement weight fractions of UD and CP laminates were predicted with average maximum errors of 8%. Experimental results indicated that goniophotometry could be especially effective for predicting the fiber architecture of highly transparent laminates (regular transmittance $T_r \geq 0.36$) which exhibit optical depths of lower than one.
2. An optomechanical model to estimate the directional fiber volume fractions of GFRP laminates, and therefore directional strength and E-modulus, based on spectrophotometric and goniophotometric experiments has been developed. The average predictions overestimated by maximum 8% the directional fiber volume fraction, strength and E-modulus of hand lay-up GFRP laminates.
3. A case study using an existing GFRP-sandwich roof demonstrated that structurally optimized GFRP face sheets could meet the requirements for skylights. Furthermore, PV cells can be integrated below the structural fiber layers of such laminates as long as the fiber weight of the top layer does not exceed approximately 1000 g/m^2 .

4.8. References

1. Wurm J. *Glass structures*. Basel: Birkhäuser, 2007.
2. Nijssse R. *Glass in structures*. Basel: Birkhäuser, 2003.
3. Schittich C, Staib G, Balkow D, et al. *Glass Construction Manual*. Basel: Birkhäuser, 1999.

4. Engelsmann S, Spalding V and Peters S. *Plastics in Architecture and Construction*. Basel: Birkhäuser, 2010
5. Kaltenbach F (ed). *Translucent Materials*. Basel: Birkhäuser; 2004.
6. Kasarova S, Sultanova N, Ivanov C, et al. Analysis of the dispersion of optical plastic materials. *Opt Mater* 2007; 29:1481-1490 .
7. Sultanova N, Kasarova S and Nikolov I. Dispersion Properties of Optical Polymers. In: *Proceedings of the International School and Conference on Photonics, PHOTONICA09*, Belgrade, Serbia, 24-28 August 2009, pp.585-587. Warsaw: Institute of Physics.
8. Blaga, A. Use of plastics in solar energy applications. *Sol Energy* 1978; 21(4):331-378.
9. Meir M, Mathisen Ø, Olivares A, et al. Façade integration of polymeric solar collectors. *Official Journal of the Lithuanian Applied Sciences Academy* 2005; 2:132-141.
10. Köhl M, Meir MG, Papillon P, et al. (eds). *Polymeric Materials for Solar Thermal Applications*. Weinheim: Wiley-VCH, 2012.
11. Pagliario M, Palmisano G and Ciriminna R. *Flexible solar Cells*. Weinheim: Wiley-VCH, 2008.
12. Barbero E. *Introduction to composite materials design*, 2nd ed. Boca Raton, FL: CRC Press, 2011.
13. van Krevelen DW. *Properties of polymers*. Amsterdam: Elsevier, 1997.
14. Sato H, Iba H, Naganuma T, et al. Effects of the difference between the refractive indices of constituent materials on the light transmittance of glass-particle-dispersed epoxy-matrix optical composites. *Philos Mag B* 2002; 82(13):1369-1386.
15. Velez M, Braisted WR, Frank GJ, et al. Impact strength of optically transparent glass ribbon composites. *J Compos Mater* 2012; 46(14):1677-1695.
16. Velez M, Schuman TP and Day DE. Optical properties of optically transparent glass-ribbon composites. Accepted for publication in *J Compos Mater* 2013; DOI: 10.1177/0021998313513204.
17. Chandrashekhara K, Schuman T and Sundararaman S. Manufacturing and performance evaluation of glass-ribbon reinforced transparent composites. In: *Proceedings of 52nd International SAMPE Symposium – Material and Process Innovations: Changing our World*, Long Beach, USA, 18-22 May 2008, volume 52. Covina, CA: SAMPE.
18. Pascual C, de Castro J, Schueler A, et al. Total light transmittance of glass fiber-reinforced polymer laminates for multifunctional load-bearing structures. Accepted for publication in *J Compos Mater* 2013; DOI: 10.1177/0021998313511653.
19. Iba H and Kagawa Y. Light transmittance of continuous fibre-reinforced composites: analysis, model experiment and parametric study. *Philos Mag B* 1998; 78(1):37-52.
20. Matsumura K and Kagawa Y. Evaluation in "transparency" of glass particle-dispersed optical composites by pico-second order pulse profile. *J Mat Sci Lett* 2001; 20(23):2101-2104.
21. Chilton J. *Heinz Isler – The Engineer's Contribution to Contemporary Architecture*. London: Thomas Telford, 2000.
22. Pascual C, de Castro J, Kostro A, et al. Diffuse light transmittance of glass fiber-reinforced polymer laminates for multifunctional load-bearing structures. Accepted for publication in *J Compos Mater* 2013; DOI: 10.1177/0021998313511655.
23. Andersen M. *Innovative Bidirectional Video-Goniophotometer for Advanced Fenestration Systems*. PhD thesis, Ecole Polytechnique Fédérale de Lausanne, Switzerland, 2004.

24. Mohanty L, Yang X and Wittkopf SK. Optical scatter measurement and analysis of innovative daylight scattering materials. *Sol Energy* 2012; 86(1):505-519.
25. van de Hulst HC. *Light scattering by small particles*. New York: Dover Publications, 1981.
26. Lin H, Day DE, Weaver KD, et al. Temperature and wavelength dependent transmission of optically transparent glass fiber poly(methyl methacrylate) composites. *J Mater Sci* 1994; 29(19):5193-5198.
27. Olson JR, Day DE and Stoffer JO. Fabrication and Mechanical Properties of an Optically Transparent Glass Fiber/Polymer Matrix Composite. *J Compos Mater* 1992; 26(8):1181-1192.
28. Lin H. *Optical and mechanical properties of optically transparent PMMA composites at elevated temperatures*. PhD thesis, Missouri-Rolla University, USA, 1991.
29. Iba H, Chang T and Kagawa Y. Optically transparent continuous glass fibre-reinforced epoxy matrix composite: fabrication, optical and mechanical properties. *Compos Sci Technol* 2002; 62(15):2043-2052.
30. Keller T, Haas C and Vallée T. Structural concept, design, and experimental verification of a glass fiber-reinforced polymer sandwich roof structure. *J Compos Constr* 2008; 12(4):454-468.
31. Keller T, Rothe J, de Castro J, et al. GFRP-balsa sandwich bridge deck – concept, design and experimental validation. *J Compos Constr* 2014; 18(2): article number 04013043.
32. Krug DJ, Asuncion MZ, Popova V, et al. Transparent fiber glass reinforced composites. *Compos Sci Technol* 2013; 77:95-100.
33. Schell JSU, Renggli M, van Lenthe GH, et al. Micro-computed tomography determination of glass fibre reinforced polymer meso-structure. *Compos Sci Technol* 2006; 66(13):2016-2022.
34. Wiesauer K, Pircher M, Götzinger E, et al. Investigation of glass-fibre reinforced polymers by polarisation-sensitive, ultra-high resolution optical coherence tomography: Internal structure, defects and stress. *Compos Sci Technol* 2007; 67(15-16):3051-3058.
35. Stifter D, Wiesauer K, Wurm M, et al. Investigation of polymer and polymer/fibre composite materials with optical coherence tomography. *Meas Sci Technol* 2008; 19(7) article number 074011.
36. Bickel WS, Gilliar W and Bell B. Light scattering from fibers: a closer look with a new twist. *Appl Optics* 1980; 19(21):3671-3675.
37. Woodward DH. Multiple Light Scattering by Spherical Dielectric Particles. *J Opt Soc Am* 1964; 54(11):1325-1331.
38. Smart C, Jacobsen R, Kerker M, et al. Experimental Study of Multiple Light Scattering. *J Opt Soc Am* 1965; 55(8):947-955.
39. Quirantes A, Francisco A and Quirantes-Ros J. Multiple Light Scattering by Spherical Particle Systems and Its Dependence on Concentration: A T-Matrix Study. *J Colloid Interf Science* 2001; 240(1):78-82.
40. ASTM Standard D3039/D3039M-08. *Standard Test Method for Tensile Properties of Polymer Matrix Composite Materials*. West Conshohocken, PA: American Society for Testing and Materials, October 2008.
41. Kostro A, Geiger M, Jolissaint N, et al. Embedded microstructures for daylighting and seasonal thermal control. In: *Proceedings of SPIE Conference*, San Diego, USA, 12-14 August 2012, volume 8485, article number 84850L. Bellingham: SPIE.
42. Keller T, Vassilopoulos AP and Manshadi BD. Thermomechanical behavior of multifunctional GFRP sandwich structures with encapsulated photovoltaic cells. *J Compos Constr* 2010; 14(4):470-478.
43. Keller T, Haas C and Vallée T. Structural concept, design, and experimental verification of a glass fiber-reinforced polymer sandwich roof structure. *J Compos Constr* 2008; 12(4):454-468.

44. Keeler M and Burke B. *Fundamentals of Integrated Design for Sustainable Building*. Hoboken: John Wiley & Sons, 2009.

5 Integration of dye solar cells in GFRP laminates

5.1. Introduction

The integration of solar cells in building construction is of increasing interest at a time of rising finite fossil fuel costs and environmental concerns about climate change and the greenhouse effect.¹ The benefits of building integrated solar cells are multiple: power is generated near to where it is consumed – thus reducing transportation losses – no pollutants are emitted and energy efficiency on the part of building users is encouraged.²

Solar cells convert sunlight to electric power by the photovoltaic (PV) effect.³ Since the 1950s different types of opaque solar cells have been introduced onto the market, mostly based on silicon technology, but also on other semiconductors such as cadmium telluride and copper indium gallium selenide, with energy conversion efficiencies of around 10 to 20%.⁴ Solar cells absorb sunlight, transform a small part of it into electricity and the remaining part into heat which raises the cell temperature to around 45-50 °C in normal operation conditions – and reduces cell efficiency at rates of between 0.45% °C⁻¹ (for crystalline silicon) and 0.25% °C⁻¹ (for other semiconductors).^{5,6} Building envelopes constructed with laminated glass – two glass panes glued together by a thin adhesive – are architecturally attractive solutions for encapsulating solar cells in the adhesive interlayer.^{2,4} Modifying the spacing between encapsulated opaque cells allows the filtering of sunlight inside the building, thus providing daylight and sun-shading. However glass encapsulation presents disadvantages: sunlight projects cell shadows onto living and working spaces and may create visual discomfort and overhead glazing incorporates risks associated with the brittleness and generally low structural capacity of glass.

Since the early 1990s, research on dye solar cells (DSC) has offered the possibility of designing transparent colored cells.⁷ Nowadays, the first commercial products exhibit efficiencies of around 2 to 4%, although values higher than 8% have been obtained at the research level.⁸ Unlike traditional (silicon) cells, DSCs have a stable efficiency of up to around 60 °C and excellent performance in diffuse light conditions.^{9,10} In addition DSCs can capture light from both sides of the cell due to their transparency and can also be used for indoor applications.^{11,12} Conversion of sunlight into electricity is performed by an electrochemical reaction between a dye (ruthenium light absorbers) and an ionic electrolyte (iodide/triiodide redox couple) confined between two glass substrates coated with an electrically conductive fluorine doped tin oxide (FTO) layer (see Figure 5.1(a)).⁸ The kinetics of the reaction and efficiency of the cell are enhanced by a platinum catalyst and the mesoporous structure of the titanium dioxide (TiO₂) semiconductor deposited over the FTO layers. The edges of the cell are sealed with a polymer gasket to prevent electrolyte leakage. Generally DSCs are commercialized in the form of modules, i.e. group of cells fabricated together between two electrically conductive glass substrates (see Figure 5.1(b)).¹³ Building-

integrated DSC modules are embedded in a thin soft silicone interlayer between two laminated glasses, forming a DSC panel used as colored and transparent PV facade component. However such panels are structurally inefficient and heavy (around 50 kg/m^2) thus limiting their easy integration in building construction.

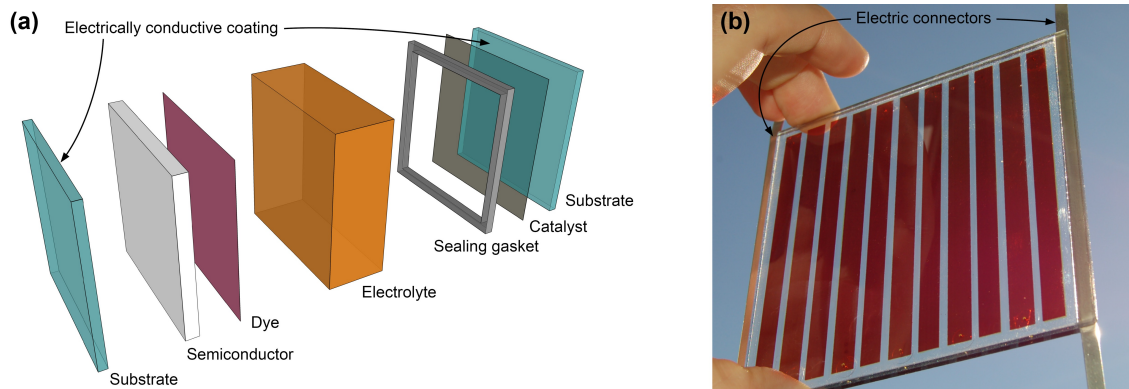


Figure 5.1. (a) Exploded view of dye solar cell and (b) module formed by eleven cells between two electrically conductive glass substrates.

The weight of DSC panels could be reduced and impact resistance increased by encapsulating DSC modules in lightweight translucent glass fiber-reinforced polymer (GFRP) laminates. This composite material, made of polyester resin and E-glass fibers, has already been explored as structural support and translucent encapsulant of flexible opaque PV cells.¹⁴⁻¹⁶ The encapsulation of DSC glass modules in a translucent GFRP building envelope would allow the integration of structural, energy production and daylighting functions in a single component and would furthermore contribute to increasing the acoustic insulation properties of the GFRP facade.¹⁷ However polyesters adhere poorly to glass and silane components at the glass/polyester interface are required to improve adhesion.^{18,19}

Transparent polymeric cell substrates are a potential alternative to glass if the temperature for sintering the TiO_2 is reduced from $450 \text{ }^\circ\text{C}$ to $150 \text{ }^\circ\text{C}$ – which however reduces cell efficiency by half – and if solid electrolytes (still under investigation) are used.^{8,20} Cells fabricated on acrylic polymeric substrates such as poly(methyl methacrylate) (PMMA) would exhibit some advantages compared to glass: PMMA is two times lighter than glass and can be doped with fluorescent components, increasing the efficiency of PV cells.²¹ It can be reinforced with PMMA fibers, increasing the strength, ductility and fracture toughness of the brittle polymer.^{22,23} In addition acrylic components exhibit good adhesion to polyester resins and can also be used for bonding GFRP to glass substrates.¹⁷

The temperature of DSC panels is daily subjected to high variations: $50 \text{ }^\circ\text{C}$ is expected under normal solar radiation (800 W/m^2) – around $60 \text{ }^\circ\text{C}$ for full sunlight (1000 W/m^2) – and depending on the altitude and latitude night-time temperatures of below $0 \text{ }^\circ\text{C}$ can be reached– around $-20 \text{ }^\circ\text{C}$ for cold winter nights. This temperature variation produces thermal stresses in the panel that can lead to cracking and mechanical failure of the different components. Investigation of the thermal behavior of the panel, and particularly the maximum thermal stresses in DSC modules, is of prime importance for validating an encapsulation design.

The objectives of this research are to investigate the feasibility of manufacturing solar panels with DSC modules encapsulated in GFRP laminates, to study their electrical efficiency and to evaluate the

performance of the encapsulation under thermal loads. Different fiber architectures of GFRP encapsulants, substrate materials for DSCs and interlayers between substrates and encapsulant are investigated. Two electrically functional panels with DSC glass modules and two electrically non-functional panels with glass and PMMA dummy modules were fabricated. The electrical efficiency of the panels exposed to simulated solar radiation was experimentally investigated and analytically modeled as a function of the reinforcement weight of the upper encapsulant. The performance of the encapsulant under thermal loads was evaluated, subjecting the panels to cycles of +60/-20 °C. Delaminations and cracks were investigated by numerical finite element analyses. Conceptual designs for load-bearing composite components integrating DSC modules are proposed.

5.2. Experimental procedure

5.2.1. Overview

First, DSC and dummy modules were fabricated. Then, two functional and two non-functional panels were fabricated respectively by encapsulating the DSC and dummy modules in GFRP. The functional panels were exposed to simulated solar radiation and all the panels to thermal cycles of +60 °C/-20 °C. An additional fabrication of GFRP laminates was performed to investigate the light transmittance of the GFRP encapsulant as a function of the reinforcement weight by spectrophotometry.

5.2.2. Materials

The materials selected for the fabrication of the GFRP encapsulants (fibers and resin), the DSC and dummy modules (substrate materials and sealants) and interlayers between modules and encapsulant are presented in the following.

Biaxial woven E-glass fabric (twill weave) manufactured by P-D Interglas Technologies (Erbach, Germany) and distributed by Swiss-Composite (reference n° 190.1458) with reinforcement weight, w , of 390 g/m² (50% in each direction) was selected as structural reinforcement for the panels. The lubricants on the fiber surface – required to prevent the abrasion and fracture of fibers during weaving but counteracting adhesion with the resin – were removed after fabric weaving and replaced by a proprietary finish coupling agent to optimize the bonding between resin and fibers. The mechanical properties (E -modulus, E , shear modulus, G , and Poisson ratio, ν) and thermal expansion coefficient, α , of the E-glass fibers are given in Table 5.1.²⁴

Uniconform 1A continuous filament mat manufactured by Owens Corning (Toledo, United States) and made of E-CR glass fibers (Advantex™) with $w = 600$ g/m² was used as non-structural reinforcement. The fibers had a proprietary surface treatment optimized for the fabrication of highly transparent laminates. The mechanical properties and thermal expansion coefficient of the E-CR glass fibers are also reported in Table 5.1.²⁵

The resin selected for fabricating the GFRP encapsulants was a transparent UV-stabilized orthophthalic polyester manufactured by CCP Composites (Courbevoie, France) and distributed by Swiss-Composite (reference n° 140.1812). The resin had a volumetric shrinkage of 6.5% – therefore a directional shrinkage of one third of that value (2.2%) –,²⁴ a heat distortion temperature of 72 °C and a tensile strength of 60 MPa according to the manufacturer data sheet. Two peroxide catalysts were selected from

Swiss-Composite: M20 (reference n° 145.1304) manufactured by Pergan (Bocholt, Germany) – giving gel times of around 15 min – and Cenox 51 (reference n° 119.1000) manufactured by Promox (Leggiuno, Italy) – giving gel times of around 180 min. The catalyst Cenox 51 was used for the panels fabricated by infusion and M20 was used for the hand lay-up fabrication. The mechanical properties and thermal expansion coefficient of the resin are also shown in Table 5.1.²⁴

Soda-lime silica annealed glass (2.2-mm thickness) manufactured by Pilkington (St Helens, United Kingdom) was selected for the glass substrates of six DSC and three dummy modules. Extruded Visacryl PMMA sheets (2-mm thickness) were chosen for the fabrication of the polymeric substrates of another three dummy modules.

The sealant used for the glass substrates was a 25- μm -thick gasket made of Surlyn 1702 (DuPont) while the sealant used for the PMMA substrates was a 120- μm -thick layer of UV-curing acrylic resin ThreeBond (TB) 3035B.

Three interlayer materials between the glass substrates and the GFRP encapsulant were investigated: orthophthalic polyester resin (indicated above), silicone gel and 3M silane primer.

Table 5.1. Mechanical properties, thermal expansion coefficient and density considered for glass fibers and polyester resin used in this research.

Property	E (GPa)	G (GPa)	ν (-)	α ($\cdot 10^{-6} \text{ } ^\circ\text{C}^{-1}$)	ρ (g/cm^3)
E-glass (fabric)	72.0	29.5	0.22	5.4	2.55
E-CR glass (mat)	80.0	32.8	0.22	5.8	2.62
Polyester resin	3.4	1.2	0.38	60	1.20

5.2.3. Fabrication

Modules. Six DSC glass modules, three glass dummy modules and three PMMA dummy modules were fabricated in collaboration with Solaronix SA (Aubonne, Switzerland).¹³

The fabrication procedure of a DSC glass module is shown in Figure 5.2(a) to (d) and explained in the following. Titanium dioxide (TiO_2) bands were printed over the FTO coatings of two glass substrates ($100 \times 100 \times 2.2 \text{ m}^3$). The substrates were then immersed in a ruthenium dye solution (Ruthenizer 535-bisTBA) and dye particles fixed to the TiO_2 bands. A Surlyn sealant grid was placed around the TiO_2 and dye bands of one substrate (see Figure 5.2(a)). The other substrate was then placed over this grid (see Figure 5.2(b)) and the whole was pressed for 2 min at $130 \text{ } ^\circ\text{C}$ to melt the Surlyn and gluing substrates together. Finally the electrolyte was introduced through eleven holes (one per cell) existing in one of the substrates (see Figure 5.2(c)). Holes were then sealed with Surlyn and covered with 7-mm-diameter glass disks of 100- μm thickness (see Figure 5.2(d)).

The three glass dummy modules were fabricated without TiO_2 , dye and electrolyte components. Each module was composed of two glass substrates with a Surlyn sealant grid between them – the whole was pressed for 2 min at $130 \text{ } ^\circ\text{C}$ to glue the substrates together.

The three PMMA dummy modules – each composed of two PMMA substrates ($100 \times 100 \times 2 \text{ mm}^3$) – were fabricated as shown in Figure 5.2(e) to (h). First, substrates were cut from a PMMA extruded sheet using a laser cutting machine. Then the substrates were placed below a screen printer and the sealant TB 3035B was poured on top of the screen and spread with a rubber spatula (see Figure 5.2(e)). The sealant filtered through the screen and deposited an approximately 60- μm -thick layer on the top surface of

the PMMA substrate (see Figure 5.2(f)). The process was repeated for all the substrates. Each module was composed of two PMMA substrates with the sealant layers of TB 3035B between them – the whole was pressed for 2 min at 105 °C and then exposed to UV radiation to polymerize the sealant that glued the substrates together (see Figures 5.2(g) and (h)).

Substrates of DSC and dummy modules were glued with a lateral shift of around 4 mm. This shift allowed the contact between the electric connectors and the electrically conductive coatings of the DSC modules (see Figure 5.3(a)). A reference group (Ref) of three DSC glass modules connected in parallel was fabricated to characterize its electrical properties before encapsulation (see Figure 5.3(b)). This group of modules was later encapsulated in the solar panel with the DSC modules embedded in silicone.

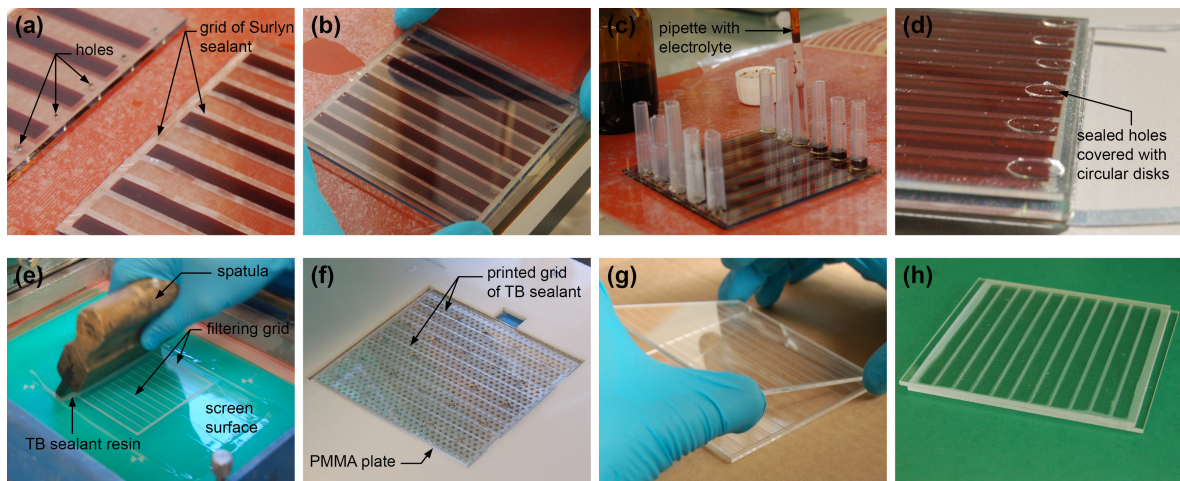


Figure 5.2. Fabrication of (a-d) functional DSC module on glass substrates and (e-h) dummy module with PMMA substrates.

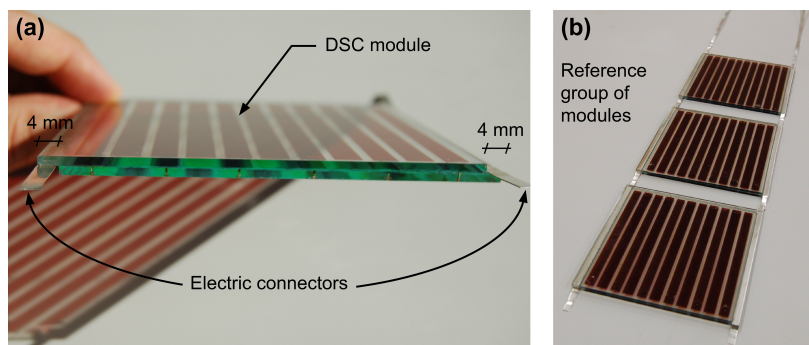


Figure 5.3. (a) Module showing 4-mm lateral shift of glass substrates and (b) reference group of three DSC modules connected in parallel.

Panels. Four GFRP panels were fabricated at a room temperature of 20 ± 2 °C. The in-plane geometry of the panels is defined in Figure 5.4(a) and Table 5.2 and the through-thickness components – inner and outer GFRP encapsulants, module substrates, sealant and material at interfaces between modules and GFRP – are indicated in Figure 5.4(b) to (d) and detailed in Table 5.3. Hand lamination and the infusion were explored as fabrication processes – in the first case fabrics were cut by hand and in the latter case by computerized numerical control machine. The GFRP panels were labeled according to the material of the module substrate and the material at the module-GFRP interface, e.g. the glass-silicone panel had DSC modules fabricated with glass substrates and connected to the GFRP encapsulant by a silicone layer.

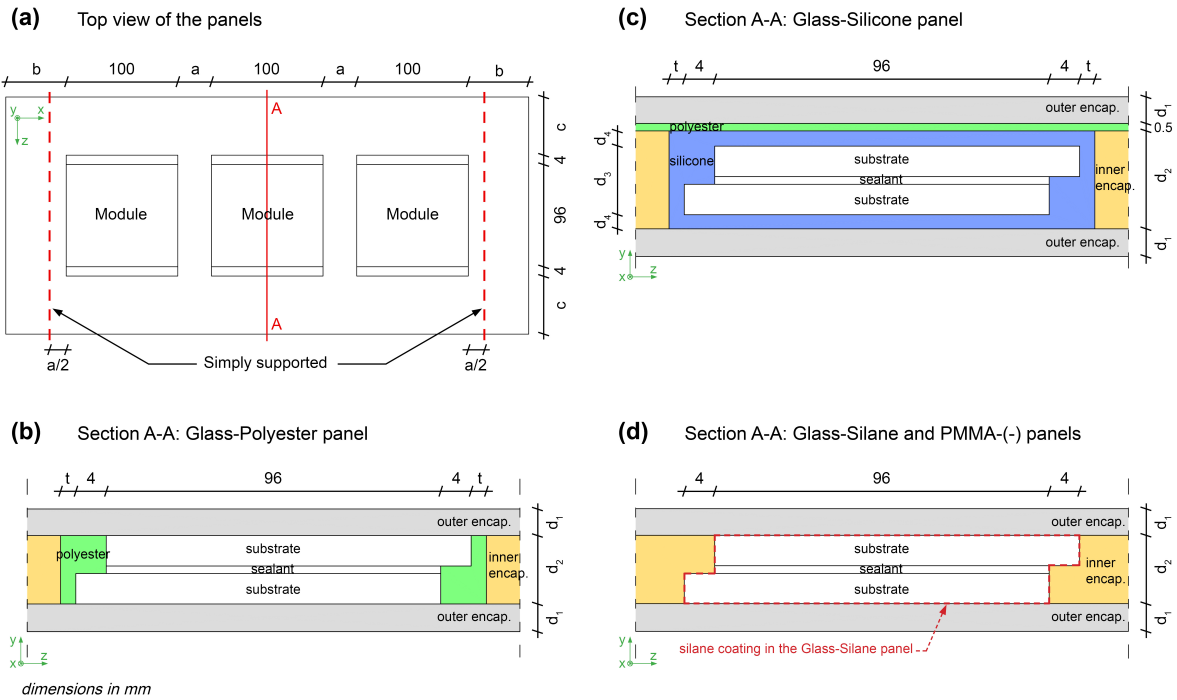


Figure 5.4. Geometry and components of solar panels (not to scale).

Table 5.2. In-plane dimensions a , b and c (see Figure 5.4(a)) and total thickness d of fabricated panels.

Panel code	a (mm)	b (mm)	c (mm)	d (mm)
Glass-Polyester	25	55	53	14
Glass-Silicone	22	103	65	15
Glass-Silane	22	103	73	10
PMMA-(-)	22	28	23	11

A glass-polyester panel ($460 \times 210 \times 14 \text{ mm}^3$) with three glass dummy modules was fabricated by hand lay-up (see Figure 5.4(b)). The lower outer encapsulant was laminated and cured for two days at room temperature. Resin was then poured on this laminate, the modules were placed on the wet resin, and the fabrics of the inner encapsulant were laminated (see Figure 5.5(a)). An approximately 2-mm lateral gap filled with pure polyester resin existed between the edges of the modules and the surrounding fabrics of the inner encapsulant. The plate was cured for two days at room temperature and then the upper outer encapsulant was laminated over the modules. Due to the hand lay-up process, some air bubbles cumulated around the edges and corners of the modules. The panel was cured for one day at room temperature and was then postcured for one day at 60°C .

The three following panels were fabricated by infusion and had the entire inner encapsulant – as well as layers of the outer encapsulant in contact with the inner encapsulant side – reinforced with mat to allow the flow of resin and impregnation of outer fabrics (see Table 5.3).

An electrically functional glass-silane panel ($550 \times 250 \times 10 \text{ mm}^3$) with three DSC glass modules was fabricated by an infusion process. Modules were first cleaned with isopropyl alcohol and then wiped with a tissue moistened in silane primer. Five minutes later, modules were brushed with polyester resin and left to cure for one day at room temperature. The modules were laterally surrounded by the mat layers of the inner encapsulant and covered top and bottom by mat and fabric layers of outer encapsulants. The whole

stack was infused as shown in Figure 5.5(b). The panel was cured for two days inside the vacuum bag at room temperature, then eight hours outside the vacuum bag at 40 °C.

A PMMA(-) panel (400x150x11 mm³) with three PMMA dummy modules was also fabricated by an infusion process and cured for two days inside the vacuum bag at room temperature, then four hours at 40 °C inside the bag and finally four hours at 40 °C out of the bag. A small crack was observed in the edge of one substrate after fabrication – probably caused by an existing microcrack produced during the laser cutting or handling of the substrate that propagated during the infusion process.

An electrically functional glass-silicone panel (550x234x15 mm³) was fabricated by sandwiching three DSC glass modules between two GFRP plates produced by an infusion process – one plate constituted the upper outer encapsulant and the other the remaining inner and lower outer encapsulants (see Figure 5.6(a)). The latter plate contained a PVC mold reproducing the shape of the modules. Three days after infusion, the mold was removed and the modules were inserted in the empty space and embedded in silicone gel and left to cure for one day at room temperature (see Figure 5.6(b) to (d)). The two plates were then bonded together with polyester resin (catalyzed with M20) (see Figure 5.6(e)). The panel was cured for one day under weight (see Figure 5.6(f)) at room temperature and then eight hours at 40 °C. The panel side corresponding to the upper outer encapsulant exhibited a milky cloudiness over the DSC modules indicating that a reaction had occurred between the silicone and the liquid polyester resin.

Table 5.3. Fabrication process, fiber volume fraction and through-thickness components of the four fabricated solar panels.

Panel code		Glass-Polyester	Glass-Silicone	Glass-Silane	PMMA(-)
Fabrication process		Hand lay-up	Infusion	Infusion	Infusion
Fiber volume fraction, $f(-)$		0.35	0.32	0.33	0.34
1. Outer GFRP encapsulant *	w (g/m ²)	3900W	1200m+1560W	600m+1560W	1200m+1560W
	d_1 (mm)	4.3	1.5 + 2.0	0.8 + 2.0	1.5 + 2.0
2. Inner GFRP encapsulant	w (g/m ²)	4680W	6600m	4200m	4200m
	d_2 (mm)	4.4	7.4	4.4	4.1
3. Module	Substrate	2.2-mm Glass	2.2-mm Glass	2.2-mm Glass	2.0-mm PMMA
	Sealant	25- μ m Surlyn	25- μ m Surlyn	25- μ m Surlyn	120- μ m TB
	d_3 (mm)	4.4	4.4	4.4	4.1
4. Interface module/GFRP	Type	Polyester	Silicone	Silane	-
	d_4 (mm)	-	1.5	-	-
	t (mm)	2.0	1.5	-	-

* m and W are used to designate mat- and woven fabric-reinforced layers respectively.

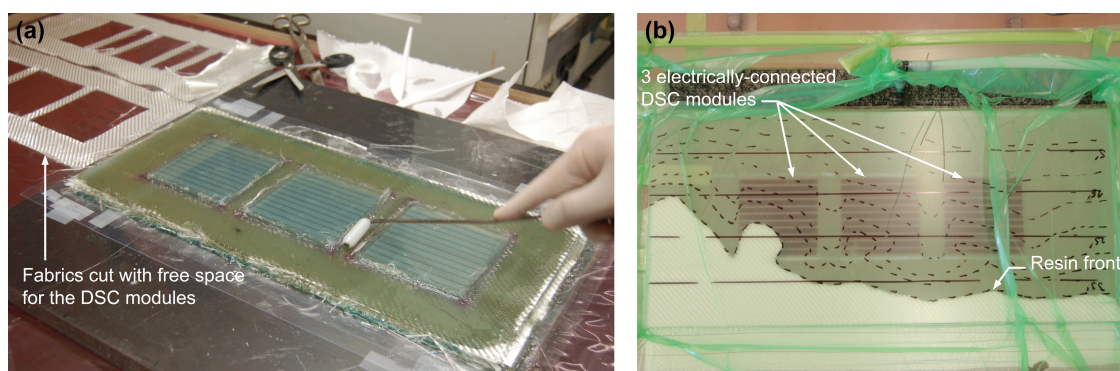


Figure 5.5. Fabrication of (a) Glass-Polyester panel by hand lamination and (b) Glass-Silane panel by infusion.

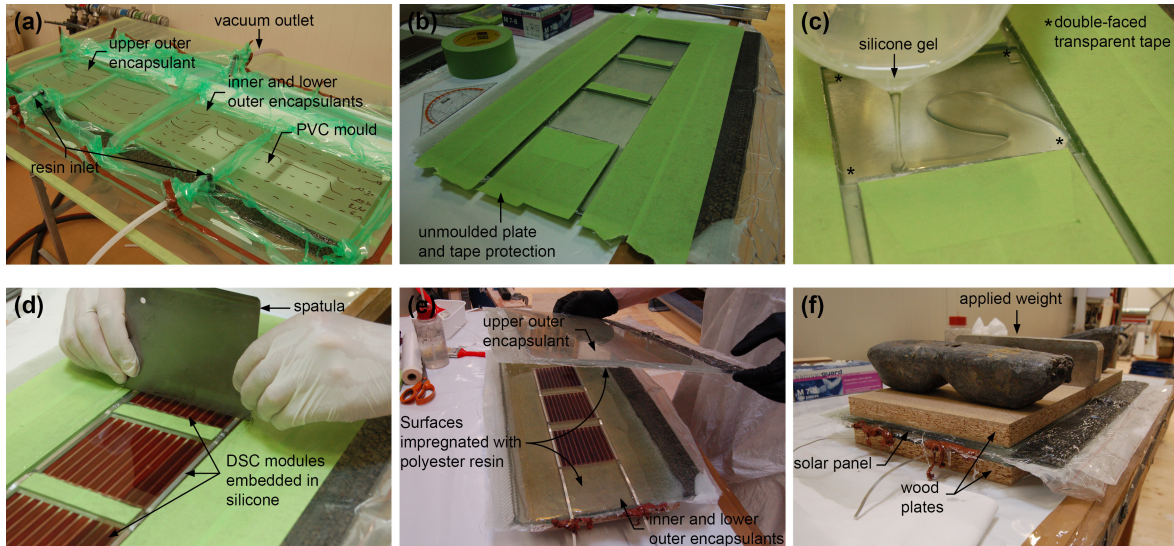


Figure 5.6. Fabrication of Glass-Silicone panel.

Laminates. Four GFRP laminates with reinforcement weights, w , of from 390 to 3120 g/m² (from one to eight woven layers of E-glass fabrics) were fabricated by hand lay-up in order to investigate the influence of w on the light transmittance of the outer GFRP encapsulants – this influence was assumed identical both for fabric and mat reinforcement. The laminates were cured at room temperature (20±2 °C) for one month – before experiments were performed – and one specimen with dimensions 90x90 mm² was cut from each laminate (see Figure 5.7). Specimens were labeled according to their reinforcement weight and fiber architecture, e.g. 390W indicates a specimen reinforced with one woven (W) fabric. Taking into account the E-glass fiber density, ρ_f (see Table 5.1) and the thickness, d , of the specimen (see Table 5.4), the fiber volume fraction was calculated as:

$$f = \frac{w}{\rho_f \cdot d} \tag{5.1}$$

and the results are shown in Table 5.4. A PMMA specimen with dimensions 100x100x2 mm³ (see Figure 5.7) was also cut from an extruded sheet to investigate its light transmittance and compare it with that of the GFRP specimens.

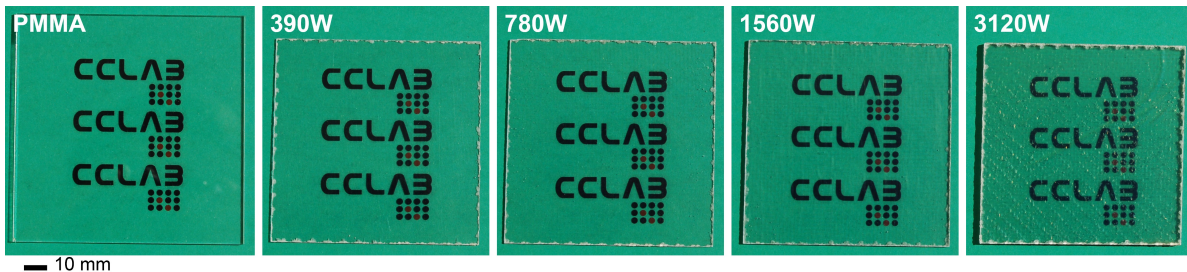


Figure 5.7. PMMA and GFRP specimens for optical experiments with text behind the specimens.

Table 5.4. Thickness, fiber volume fraction and total transmittance at 535-nm wavelength of the four GFRP specimens.

Specimen	d (mm)	f (-)	$T_{t,535 \text{ exp}}$ (-)	$T_{t,535 \text{ mod}}$ (-)
390W	0.5	0.31	0.89	0.89
780W	0.9	0.34	0.86	0.87
1560W	1.7	0.36	0.84	0.83
3120W	3.0	0.41	0.79	0.75

5.2.4. Experiments

Electrical experiments on panels. The electrically functional glass-silane and glass-silicone panels and the reference group of three DSC modules were subjected to a simulated solar irradiance, S , of 1000 W/m^2 (see Figure 5.8). The I - V curves of the panels, i.e. combinations of current I and voltage V generated from sunlight, and P - V curves, i.e. combinations of power P and voltage V , were determined. For the glass-silicone panel, the lower outer encapsulant side was exposed to the solar irradiance, i.e. the side without the milky cloudiness.

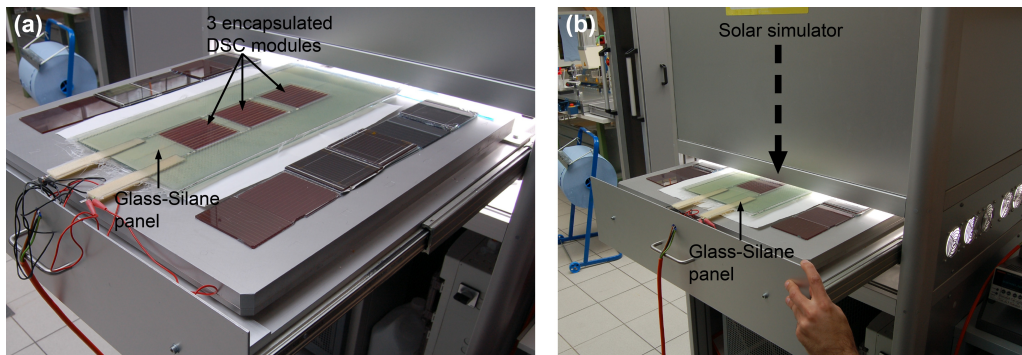


Figure 5.8. Glass-Silane panel (a) out of solar simulator and (b) being introduced into solar simulator.

Optical experiments on GFRP specimens and PMMA substrate. The total and diffuse light transmittance of the four hand-laminated GFRP specimens ($90 \times 90 \text{ mm}^2$) and a 2-mm-thick PMMA substrate ($100 \times 100 \text{ mm}^2$) were investigated from a 400- to 800-nm wavelength by spectrophotometry using an integrating sphere set-up shown in Figure 5.9(a) and described in detail in previous research.^{16,26} Specimens were located at the entrance port A and crossed by a beam of light at near normal incidence. The light transmitted by the specimen was collected inside the sphere, reflected and uniformly scattered by the sphere's white interior (barium sulfate) coating while port B remained close (total transmittance measurement). Only the diffuse light transmitted by the specimen was collected inside the sphere when port B was open (diffuse transmittance measurement, see Figure 5.9(b)). Incoming light from point C (located in the inner surface of the sphere) entered the spectrophotometer where it was split into radiation of different wavelengths that was computed by a detector head composed of photodiode arrays.

Thermal experiments on panels. A 3101 RUMED incubator was used for performing thermal cycles of $+60/-20 \text{ }^\circ\text{C}$ on the fabricated panels. The duration of each cycle was six hours, the extreme temperatures were sustained during 90 minutes and the temperature ramps were fixed at a rate of $0.9 \text{ }^\circ\text{C}/\text{min}$ (see Figure 5.10(a)). Panels were simply supported as indicated in Figure 5.4(a) and shown in Figure 5.10(b) and were subjected to thermal cycles until 1) 50 cycles (300 hours) were reached, or 2) relevant damage on the panels, e.g. delaminations or cracks, was observed.

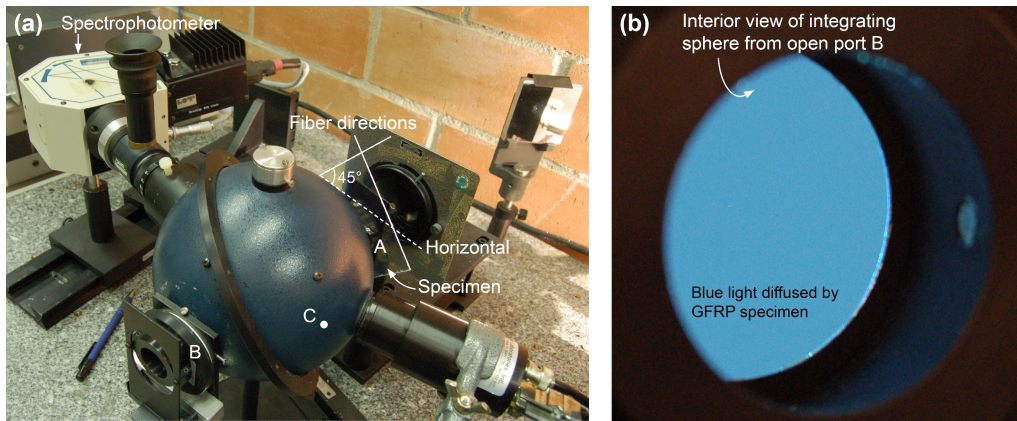


Figure 5.9. Integrating sphere (a) set-up with port B closed for total transmittance experiment and (b) detailed view through open port B (diffuse transmittance experiment).

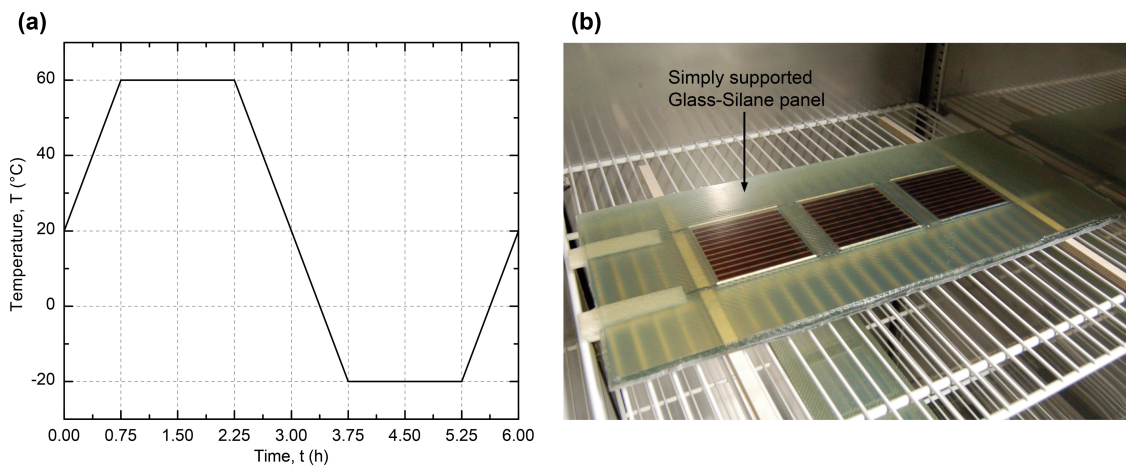


Figure 5.10. (a) Six-hour thermal cycle with extreme temperatures at 60 °C and -20 °C and (b) Glass-Silane panel subjected to thermal cycles in RUMED incubator.

5.3. Experimental results

5.3.1. Electrical results for panels

The I - V curves characterizing the electrical performance of the two functional panels and the reference group of DSC modules are shown in Figure 5.11. The generated electric power, P , of the panels – calculated as the product of I and V values – is also represented as function of the voltage in Figure 5.11. The efficiency, η , of the solar panels is given (in percentage) by:

$$\eta = \frac{P_{max}}{S \cdot A_{cells}} \cdot 100 \tag{5.2}$$

where P_{max} is the maximum generated power, S is the solar irradiance (1000 W/m^2) and A_{cells} is the total area of cells (195.3 cm^2) in the panel. The resulting efficiencies (before the thermal experiments) are shown in Table 5.5. The loss of efficiency, L_η , with respect to the reference group of DSC modules was calculated according to:

$$L_{\eta} = \left(1 - \frac{\eta}{\eta_{Ref}} \right) \cdot 100 \quad (5.3)$$

and the results are reported in Table 5.5. The slightly higher loss of efficiency of the glass-silicone panel ($L_{\eta} = 17\%$) compared to that of the glass-silane panel ($L_{\eta} = 13\%$) was attributed to the additional mat layer in the outer encapsulant of the former panel – thus reducing the light transmittance.

The short circuit currents, I_{sc} – corresponding to the generated current for a zero voltage between the two electric connectors of a solar panel – are also reported in Table 5.5. The loss of short circuit current, L_I , with respect to the reference group of DSC modules was calculated as:

$$L_I = \left(1 - \frac{I_{sc}}{I_{sc,Ref}} \right) \cdot 100 \quad (5.4)$$

and the results are also given in Table 5.5 showing a close match between L_{η} and L_I .

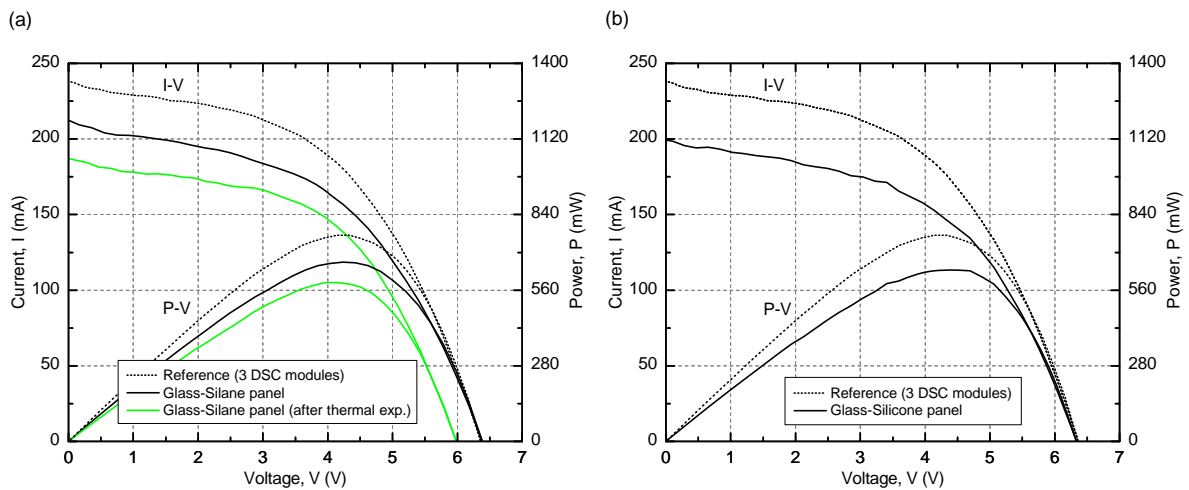


Figure 5.11. I-V and P-V curves of reference group of three modules together with those of (a) Glass-Silane panel and (b) Glass-Silicone panel.

Table 5.5. Electrical properties of electrically functional solar panels and reference group of three DSC modules.

Electrical device	Glass-Silicone panel	Glass-Silane panel	Reference (3 modules)
η (%)	3.25	3.40	3.91
η_{mod} (%) (Eq. 5.9)	3.28	3.40	-
I_{sc} (mA)	199	212	239
L_{η} (%) (Eq. 5.3)	17	13	-
L_I (%) (Eq. 5.4)	17	11	-

5.3.2. Optical results for GFRP specimens and PMMA substrate

The light transmittance results through the GFRP laminates and the PMMA substrate are shown in Figure 5.12. The total light transmittance of the GFRP specimens decreased when the reinforcement weight increased and varied approximately between 0.6 and 0.9 in the 400-800-nm range. However diffuse transmittance increased with the reinforcement weight, and moreover exhibited considerable sensitivity to the light wavelength: light was particularly diffused at short wavelengths – maximum diffusion occurred

for wavelengths below 500 nm – resulting in the bluish appearance of the sphere’s interior walls (see Figure 5.9(b)). This wavelength dependency was modeled in previous research and was due to a refractive index mismatch between fiber and resin at short wavelengths.²⁶

The total light transmittance of PMMA was almost constant at around 0.93 in the range 400-800 nm – closely matching the transmittance of pure glass (0.92).²⁷ The PMMA substrate exhibited a transparent behavior since no light was diffused.

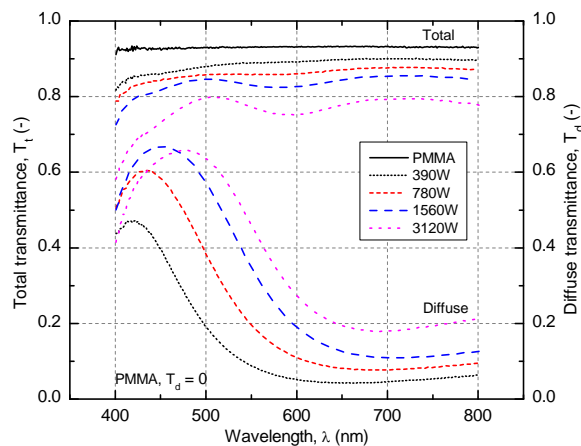


Figure 5.12. Spectral total and diffuse transmittance of GFRP and PMMA specimens.

5.3.3. Thermal cycle results for panels

The number of thermal cycles performed on each panel and the observed delaminations and cracks are indicated in Table 5.6 and described in the following.

The glass-polyester panel was subjected to one thermal cycle. After the first three hours (warm conditions) no delaminations and no cracks were observed. However during the next three hours (cold conditions), around 50% of the modules’ surface delaminated – at the glass/GFRP interface – and the pure polyester bands around the modules cracked (see Figure 5.13).

The glass-silane panel did not present any delamination after exposure to the first three hours of warm conditions. Around 2% of the modules’ surface delaminated during the next three hours of cold conditions. After the following four thermal cycles, delaminations had progressed up to around 14% of the modules’ surface and some yellow electrolyte was observed in a delaminated area – it seemed to have escaped through a poorly sealed hole in a DSC module (see Figure 5.14). The loss of electrolyte and the delaminations were considered responsible for the reduction of the panel’s electrical performance after the thermal experiments (see Figure 5.11(a)).

The PMMA(-) panel shown in Figure 5.15(a) was subjected to 50 thermal cycles and no cracks or delaminations developed in the panel during the experiments (see Figure 5.15(b) and (c)).

The glass-silicone panel was exposed to one thermal cycle. The panel resisted the warm conditions without cracking and delaminating. After exposure to the cold conditions, the lower encapsulant side of the panel looked intact: no cracks and no delaminations were observed (see Figure 5.16(a)). Inspection of the panel from the upper encapsulant-side revealed that the pure polyester layer – bonding the upper outer encapsulant plate and the inner and lower outer encapsulants plate – was completely cracked (see Figure 5.16(b)), although no delaminations were observed.

Table 5.6. Number of thermal cycles performed on fabricated panels, delaminated surfaces and crack locations.

Panel Code	N° of cycles	Delaminated surface	Crack location
Glass-Polyester	1	50% of module surface	Polyester bonding interlayer
Glass-Silicone	1	none	Polyester adhesive layer
Glass-Silane	5	14% of module surface	none
PMMA-(-)	50	none	none

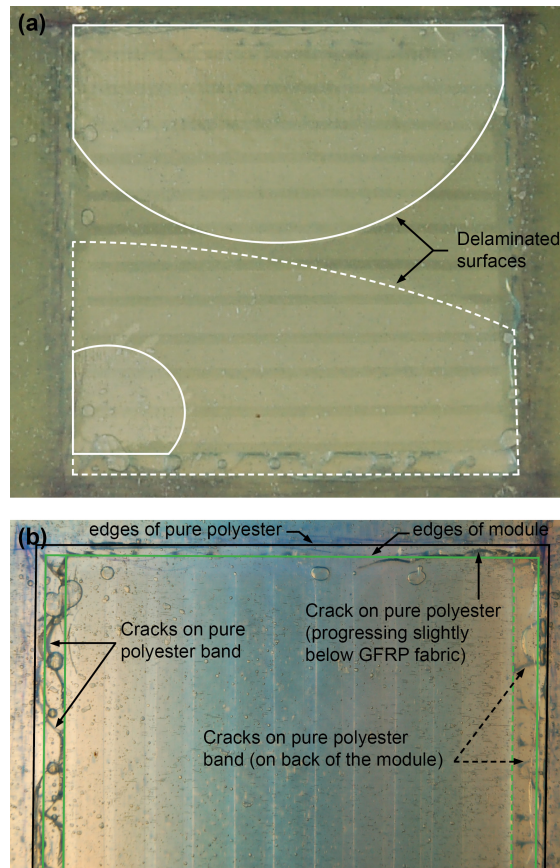


Figure 5.13. Glass-Polyester panel exhibiting after one thermal cycle (a) large delaminated surfaces and (b) large amount of cracks in pure polyester bands around modules (dotted lines indicate cracks and delaminations on rear side of module).

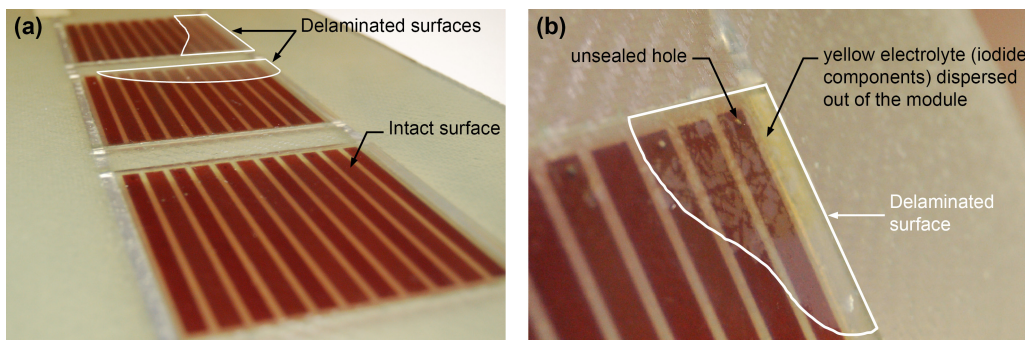


Figure 5.14. Glass-Silane panel exhibiting no cracks after five thermal cycles and (a) few delaminations and (b) loss of electrolyte in delaminated surface (photographs correspond to opposite sides of panel).

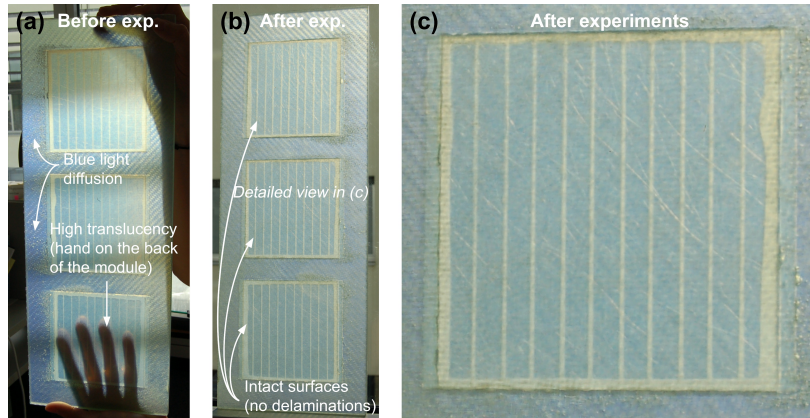


Figure 5.15. PMMA(-) panel exhibiting (a) high transluency and blue light diffusion and (b-c) no delaminations on module surface after 50 thermal cycles (photographs taken under different conditions of illumination).

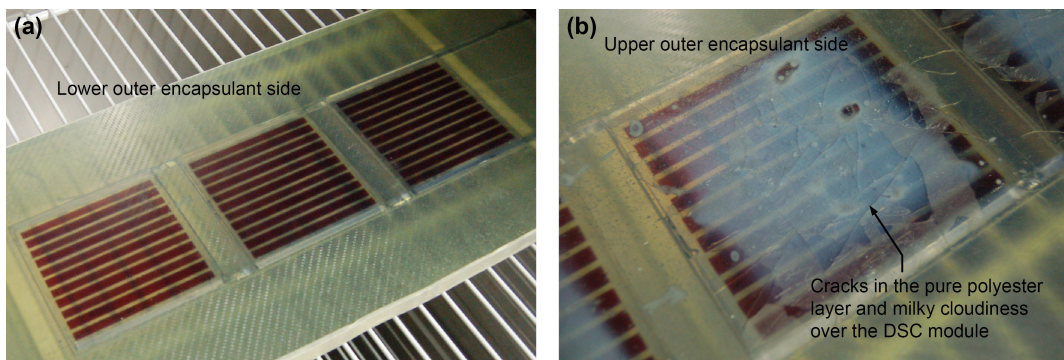


Figure 5.16. Glass-Silicone exhibiting after one thermal cycle (a) no cracks and no delaminations (lower outer encapsulant side), and (b) cracks in adhesive polyester layer and milky cloudiness over DSC modules (upper outer encapsulant side).

5.4. Modeling

5.4.1. Overview

First, an analytical model of the GFRP light transmittance was developed from the experimental results for laminates. Then, based on this model, an analytical model of the solar panel's electrical efficiency was established and validated. Finally, numerical simulations of the thermal experiments were performed in order to investigate the thermal stresses responsible for the observed cracks and delaminations.

5.4.2. Analytical modeling of total light transmittance

Based on the results of previous research,¹⁶ the total light transmittance of GFRP laminates (surrounded by air) at 535 nm (wavelength of maximum light absorptance of dye sensitizer Ruthenizer 535-bisTBA) can be modeled as:

$$T_{t,535 \text{ mod}} = (1-r)^2 \cdot c^{\frac{w}{390}} \quad (5.5)$$

where $r = 0.046$ is the reflectance at the air/resin interface for a UV-stabilized orthophthalic polyester (half of the resin's total reflectance at 535 nm),²⁶ and c is calibrated from the experimental total transmittance

($T_{t,535 \text{ exp}} = 0.888$) of one-layer-reinforced laminate (390W) and results in $c = 0.976$. The values predicted by equation (5.5) were in good agreement with experimental results (see Table 5.4). However the slightly higher experimental values than predictions at 535 nm for 1560W and 3120W were attributed to the high amount of light scattered below 550 nm by the specimens. Point C of the integrated sphere (see Figure 5.9(a)) could therefore be partly illuminated by radiation emanating directly from the specimens, i.e. light that had not been uniformly scattered inside the sphere, thus overvaluing the spectrophotometric measurements. This was experimentally confirmed by the increase of the total transmittance for 1560W and 3120W at wavelengths where the diffuse transmittance also increased, i.e. below 550 nm (see Figure 5.12).

5.4.3. Analytical modeling of solar panel efficiency

From the experimental results shown in Table 5.5, the relationship between the efficiencies and short circuit currents of solar panels can be approximated by:

$$\frac{\eta}{\eta_{Ref}} = \frac{I_{sc}}{I_{sc, Ref}} \quad (5.6)$$

Furthermore short circuit currents are directly proportional to the irradiance reaching the solar cells and therefore to the total light transmittance of the upper encapsulant layers of the cells, T_{encap} .¹⁶ Thus panel efficiency can be modeled as:

$$\eta_{mod} = \eta_{Ref} \cdot \frac{T_{encap}}{T_{encap, Ref}} \quad (5.7)$$

where $T_{encap, Ref} = 0.96$ corresponds to the transmittance of annealed glass – considering one air/glass interface and disregarding reflections in the glass/cell interface.²⁷ For the solar panels the transmittance of the upper GFRP encapsulant layers is given by:

$$T_{encap} = (1-r) \cdot c^{\frac{w}{390}} \quad (5.8)$$

where exponent 2 in the reflectance term of equation (5.5) has been replaced by unity, i.e. only the reflections at the air/GFRP interface are considered and other reflections are disregarded due to the similar refractive indices of GFRP (1.56), silicone (1.40) and glass (1.52).²⁶⁻²⁸ In fact, reflectance at an interface between materials with refractive indices of 1.40 and 1.56 results in only 0.003 according to Fresnel equations.²⁹ For the glass-silicone panel, equation (5.8) resulted in $T_{encap} = 0.80$ ($w = 2760 \text{ g/m}^2$) and for the glass-silane panel in $T_{encap} = 0.83$ ($w = 2160 \text{ g/m}^2$). The integration of equation (5.8) into equation (5.7) gives the following model of solar panel efficiency:

$$\eta_{mod} = 3.89 \cdot 0.976^{\frac{w}{390}} \quad (5.9)$$

where $r = 0.046$, $c = 0.976$, $\eta_{Ref} = 3.91$ and $T_{encap, Ref} = 0.96$ have been considered. The predicted values for η_{mod} for the glass-silicone (3.28%) and glass-silane (3.40%) panels are reported in Table 5.5 and closely match experimental results.

5.4.4. Numerical modeling of thermal experiments

Material properties. Substrates, sealants and module/GFRP interlayers were considered as isotropic linear elastic materials. The GFRP inner and outer encapsulants were modeled as linear elastic orthotropic materials and in the following their mechanical and thermal properties are defined in the coordinate system shown in Figure 5.4.

The properties of fabric- and mat-reinforced layers were estimated for $f = 0.34$ corresponding to the average fiber volume fraction of the four fabricated panels – calculated according to equation (5.1). The E-modulus and shear modulus are calculated in the following based on the Halpin-Tsai and rule of mixture models – empirical reduction factors (between 3% and 7%) were however disregarded in this analysis.^{24,30}

For in-plane x - and z -directions (see Figure 5.4), the E-modulus of fabric-reinforced layers was calculated as follows:

$$E_x = E_z = \frac{1}{2} \cdot \left(E_r + (E_f - E_r) \cdot f + E_{90} \right) \quad (5.10)$$

where E_f and E_r are the E-modulus of the fibers and polyester resin respectively (see Table 5.1), and E_{90} represents the E-modulus of a unidirectional (UD) layer in the 90°- direction and is given by:

$$E_{90} = E_r \cdot \frac{1 + \zeta \cdot \mu \cdot f}{1 - \mu \cdot f} \quad (5.11)$$

where $\zeta = 2$ for circular fibers and μ is given by:

$$\mu = \frac{E_f / E_r - 1}{E_f / E_r + \zeta} \quad (5.12)$$

Finally an E-modulus of 17.2 GPa resulted in x - and z -directions. In the through-thickness y -direction the E-modulus was considered equal to E_{90} (7.7 GPa).

The in-plane E-modulus of mat-reinforced layers was approximated according to³¹:

$$E_x = E_z = \frac{3}{8} \cdot E_0 + \frac{5}{8} \cdot E_{90} \quad (5.13)$$

where E_0 and E_{90} are the E-moduli in the 0°- and 90°-direction of a UD laminate with the same fiber volume fraction as the mat-reinforced layer. Equation (5.13) resulted in 15.8 GPa – where E_0 was approximated by the rule of mixtures. In the through-thickness y -direction the E-modulus was assumed as being the same as that for fabric-reinforced layers.

The Poisson ratios of fabric- and mat-reinforced layers were estimated based on database values.^{24,30} The shear modulus of the fabric-reinforced layers was calculated using a model analog to equations (5.11) and (5.12) replacing E_r and E_f by the shear moduli of the resin and fiber respectively and adopting $\zeta = 1$.³⁰ The in-plane (xz) shear modulus resulted in 2.4 GPa. Considering planes (xy) and (yz) as UD-reinforced with $f = 0.17$ (half of the total fiber volume fraction), and applying the same model, a shear modulus of 1.7 GPa was estimated. For mat-reinforced layers the in-plane shear modulus was calculated as:

$$G_{xz} = \frac{E}{2 \cdot (1 + \nu_{xz})} \quad (5.14)$$

resulting in 5.9 GPa. For (xy) and (yz) planes the shear modulus was considered as being the same as that for fabric-reinforced layers.

For mat-reinforced layers the coefficient of thermal expansion in x - and z -directions was calculated by the following model²⁴:

$$\alpha_x = \alpha_z = \frac{\alpha_0 + \alpha_{90}}{2} + \frac{\alpha_0 - \alpha_{90}}{2} \cdot \frac{E_0 - E_{90}}{E_0 + (1 + 2 \cdot \nu_{0-90}) \cdot E_{90}} \quad (5.15)$$

where α_0 , α_{90} , E_0 , E_{90} and ν_{0-90} correspond to the coefficients of thermal expansion, E-moduli and Poisson ratio of a UD laminate with $f=0.34$, i.e. the fiber volume fraction of the mat-reinforced layers. The values of E_0 and E_{90} were calculated as already discussed above, $\nu_{0-90} = 0.30$ was assumed and coefficients of thermal expansion were given by²⁴:

$$\alpha_0 = \frac{\alpha_f \cdot f \cdot E_f + \alpha_r \cdot (1-f) \cdot E_r}{E_0} \quad (5.16)$$

and

$$\alpha_{90} = \alpha_f \cdot \sqrt{f} + (1 - \sqrt{f}) \cdot \left(1 + f \cdot \nu_r \cdot \frac{E_f}{E_0} \right) \cdot \alpha_r \quad (5.17)$$

where α_f and α_r are the thermal expansion coefficients of fiber and resin respectively and ν_r is the Poisson ratio of the resin. The in-plane thermal expansion of fabric-reinforced layers was also estimated with equation (5.15) and predictions matched the recommended values for biaxial woven-reinforced layers given in CUR96.³⁰ The thermal expansion in the through-thickness y -direction of fabric- and mat-reinforced layers was assumed as being α_{90} . Finally, the E-modulus, shear modulus, Poisson ratio and coefficients of thermal expansion of fabric- and mat-reinforced layers are reported in Table 5.7.

Table 5.7. Material properties of substrates, sealants and unreinforced encapsulants (all isotropic) and reinforced encapsulants (orthotropic) considered for numerical simulations.

Application Material	Substrate of modules		Sealant		Unreinf. encapsulant		Reinf. encapsulant *	
	Glass	PMMA	Surlyn	TB	Silicone	Polyester	Fabric	Mat
$E_x = E_z$ E_y (GPa)	72.0	3.0	$2.2 \cdot 10^{-1}$	$4.6 \cdot 10^{-2}$	$5 \cdot 10^{-6}$	3.4	17.2	15.8
G_{xz} $G_{xy} = G_y$ (GPa)	30.0	1.1	$7.7 \cdot 10^{-2}$	$1.6 \cdot 10^{-2}$	$1.7 \cdot 10^{-6}$	1.2	2.4	5.9
ν_{xz} $\nu_{xy} = \nu_{yz}$ (-)	0.23	0.38	0.40	0.40	0.49	0.38	0.20	0.33
$\alpha_x = \alpha_z$ α_y ($10^{-6} \text{ } ^\circ\text{C}^{-1}$)	8.3	78	150	200	300	60	16.9	16.5
							36.9	37.2

* Properties are given in the coordinate system shown in Figure 5.4.

The properties of glass and PMMA substrates were obtained from manufacturer information and material databases.³²⁻³⁴ The properties of the sealant Surlyn 1702 were obtained as follows: the E-modulus from manufacturer information,³⁵ the Poisson ratio from Huber and Hinkley³⁶ and the coefficient of thermal expansion from a material database.³⁷ For the sealant TB 3035B the E-modulus was estimated using the linear model given by Qi et al.³⁸ – depending exclusively on the durometer hardness (reported as D48 in manufacturer datasheet). The coefficient of thermal expansion was selected as indicated by

Rhodes³⁹ for UV curing acrylic adhesives and the Poisson ratio was assumed as being 0.40. The properties of silicone gel used as module/GFRP interlayer were taken from the datasheet of a similar product and a Poisson ratio of 0.49 was considered.^{28,40} For the pure polyester resin interlayers, properties corresponded to values already indicated in Table 5.1. The properties of all materials are reported in Table 5.7.

Geometry of the models. Three-dimensional finite element models of the thermal experiments were established using Ansys v15 APDL software. Half-panels were modeled considering boundary conditions for symmetry in section A-A (see Figure 5.4). The estimated thicknesses of the different components are summarized in Table 5.3 and the corresponding fiber volume fraction of the outer and inner encapsulants – calculated according to equation (5.1) – was 0.34.

A mapped orthogonal mesh was defined. For x - and z -directions a 1-mm mesh size was selected. The through-thickness y -direction was meshed as follows: 1) one element (SOLSH190) between the substrates, 2) eight elements (SOLID45) in each substrate and 3) twelve elements (SOLID45) in each outer encapsulant – with four additional elements in the pure polyester of the glass-silicone panel. Aspect ratio (length-to-height ratio), AR , resulted in $AR = 40$ for SOLSH190 elements – larger therefore than the maximum recommended value of 20 for solid elements. A sensitivity analysis performed for $10 \leq AR \leq 40$ showed no influence of this parameter on the numerical results and therefore $AR = 40$ was selected to reduce the computational time of the models – similar sensitivity analysis results were obtained by Shi and Zhang.⁴¹

Numerical results of simulated thermal experiments. Linear elastic simulations were performed introducing a thermal load $\Delta T = -40$ °C in all the nodes of the modeled panels – this value being the difference between the temperatures at which cracks and delaminations were observed (-20°C) and at which panels were fabricated (20 °C). A perfect bonding between all materials was assumed.

The observed delaminations were investigated by analyzing the shear stresses developing on the top and bottom module surfaces. Stresses τ_{xy} and τ_{yz} appeared along edges located in the z - and x -direction respectively and were similar along all the edges of the modules. The larger delaminations observed in the glass-polyester panel compared to those observed in the glass-silane panel were attributed to the combination of two effects: 1) the higher shear stresses in the former (12 MPa on edges and 28 MPa on corners) compared to those in the latter (4 to 10 MPa, see Figure 5.17(a) and (b)), and 2) the silane treatment in the latter panel improving the adhesion between GFRP and glass. In the PMMA(-) panel the absence of delaminations was also explained by two effects: 1) the absence of shear stress concentration on the module corners and the low shear stresses (4 MPa) along module edges (see Figure 5.17(c) and (d)) and 2) the good adhesion between polyesters and acrylic components.¹⁷ Finally, in the glass-silicone panel no thermal stresses developed in the glass modules due to the very low E-modulus of the silicone gel (0.005 MPa), allowing the module to contract freely.

The cracks observed in the unreinforced polyester volumes of the glass-polyester and glass-silicone panels were attributed to the effect of tensile stresses developing due to: 1) the resin volumetric shrinkage constrained by the stiffer GFRP encapsulant and glass modules, producing microcracks in the resin,²⁴ and 2) the resin thermal deformations, i.e. the tendency of resin to reduce its volume when it cools, also constrained by the GFRP encapsulant and the glass modules due to their lower coefficients of thermal expansion. The former effect could lead to tensile stresses of $\sigma = 3400 \cdot 0.022 = 75$ MPa – higher than the resin strength of 60 MPa – if the entire directional shrinkage (2.2%) was considered as a tensile strain on the fully cured resin ($E_r = 3400$ MPa). Since the resin was not fully cured nor the shrinkage fully

constrained, lower stresses and only microcrack formation were expected.²⁴ According to the numerical simulations, the latter effect (thermal deformations) led to first principal stresses, σ_1 , of around 10 MPa (tensile) in both panels (see Figure 5.18) – with stress concentrations of up to 25 MPa in the glass-polyester panel – which could result in the development of microcracks and the observed crack formation.

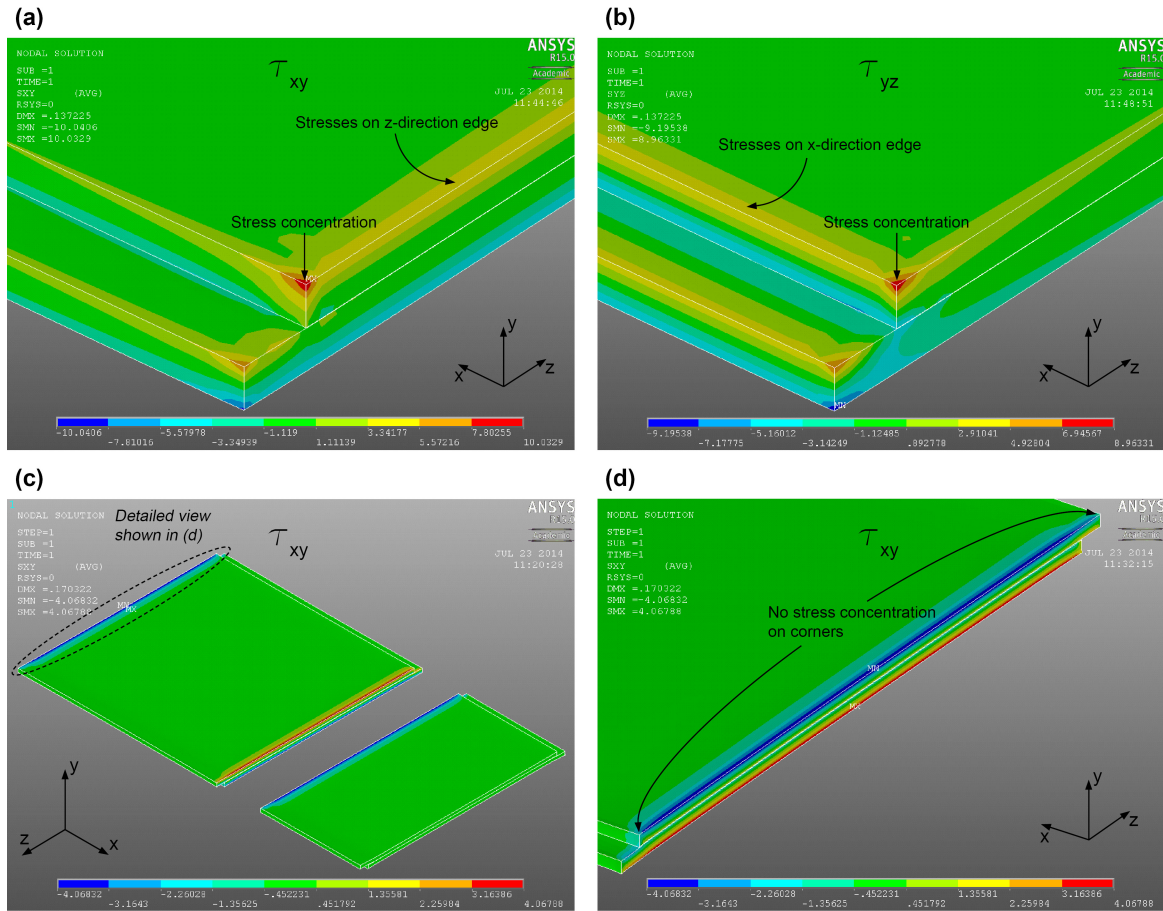


Figure 5.17. Shear stresses (a-b) τ_{xy} and τ_{yz} on modules of Glass-Silane panel and (c-d) τ_{xy} on modules of PMMA(-) panel from numerical simulation at $\Delta T = -40^\circ\text{C}$.

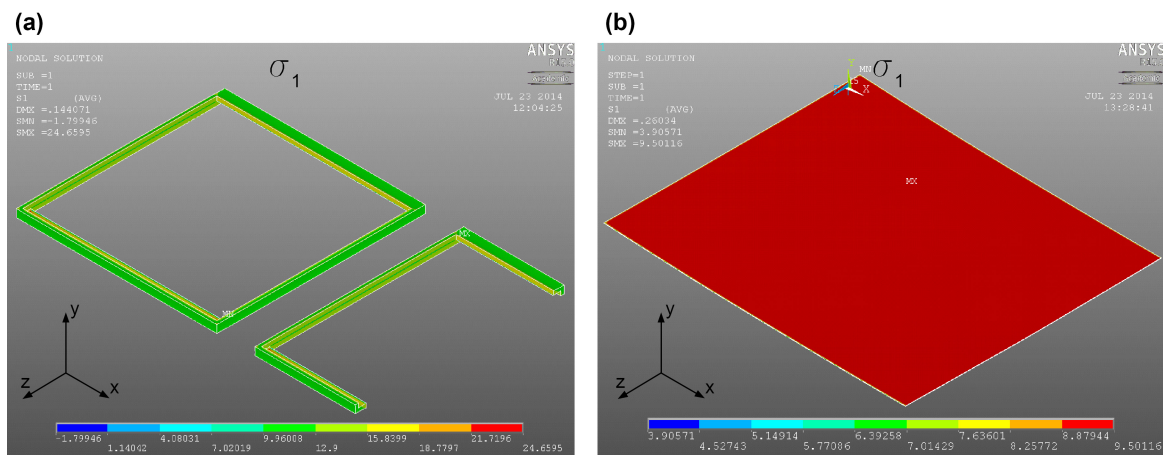


Figure 5.18. First principal stress σ_1 (tensile) for unreinforced volumes of polyester resin in (a) Glass-Polyester panel and (b) Glass-Silicone panel from numerical simulation at $\Delta T = -40^\circ\text{C}$.

As the developed models are linear elastic, reversing the thermal load to $\Delta T = 40\text{ }^{\circ}\text{C}$ also reversed the sign of the obtained stresses. The absence of delaminations during warm conditions could be explained by the softening of the resin at higher temperatures reducing the shear stresses. The absence of cracks in the unreinforced polyester resin was related to the compressive stresses developing for a positive ΔT – the expansion of the resin was constrained by the GFRP and glass – closing the existing microcracks.

5.5. Discussion

The Archinsolar project showed that a 10% loss in efficiency is well accepted for architecturally well-integrated solar panels.^{42,43} Solar panels with GFRP outer encapsulants optimized in terms of mechanical and optical performances could be designed with $w = 1600\text{ g/m}^2$, i.e. reinforcement weight for a loss of electrical efficiency of $L_{\eta} = 10\%$ – obtained by integrating equation (5.9) into equation (5.3). In practice, the outer encapsulant could be obtained by laminating three P-D Interglass woven layers (390 g/m^2 per layer) with one Owens Corning mat layer (Uniconform of 450 g/m^2 per layer) and represents a significant improvement with respect to $w = 1000\text{ g/m}^2$ presented in previous research⁴⁴. The better results obtained here are attributed to the improved wettability of the fabrics used in this research – in the former study lubricants, applied on fibers together with starch and silane sizings, were not removed after fabric weaving, which reduced the wettability and finally the light transmittance of the laminate.

The panel with dummy PMMA modules encapsulated in GFRP exhibited excellent behavior under cyclic thermal loads. Therefore scientific and technological progress regarding DSCs with polymeric substrates would offer potential for encapsulating DSC modules in lightweight and load-bearing GFRP laminates. To guarantee electrical efficiency, an outer encapsulant with a woven reinforcement weight of $w = 1600\text{ g/m}^2$ could be adopted – corresponding to a thickness of $d = 2.0\text{ mm}$ and a fiber volume fraction of $f = 0.31$ based on equation (5.1). A cross-sectional conceptual design of a composite component integrating solar energy production together with architectural (daylighting) and load-bearing functions – based on the sandwich composite action between lightweight balsa webs and translucent GFRP skins – is presented in Figure 5.19(a) and (b) where the space between webs could be filled with translucent aerogel for thermal insulation.

The integration of DSC glass modules in a GFRP encapsulant requires a low E-modulus interface material between the glass substrates and the GFRP encapsulant to release the thermal stresses and avoid cracks and delaminations. The silicone gel used in this research did not show good compatibility with the polyester resin, however soft transparent acrylic adhesives – as used by Tomasi et al.¹⁷ for bonding glass panes to translucent GFRP plates in structural facade components – could constitute a valuable alternative. The potential integration of DSC glass modules in the external skin of the sandwich structure described above is shown in Figure 5.19(c). In this case, the GFRP laminate of the skin gives structural support to the DSC modules – similarly to the plate shown in Figure 5.6(b) – and a transparent PMMA plate constitutes the upper encapsulant, increasing the electrical efficiency, UV-protection and long-term environmental stability of the solar panel.⁴⁵ In the proposed design, the DSC modules are embedded in a soft transparent acrylic adhesive, also bonding the GFRP skin to the PMMA plate.

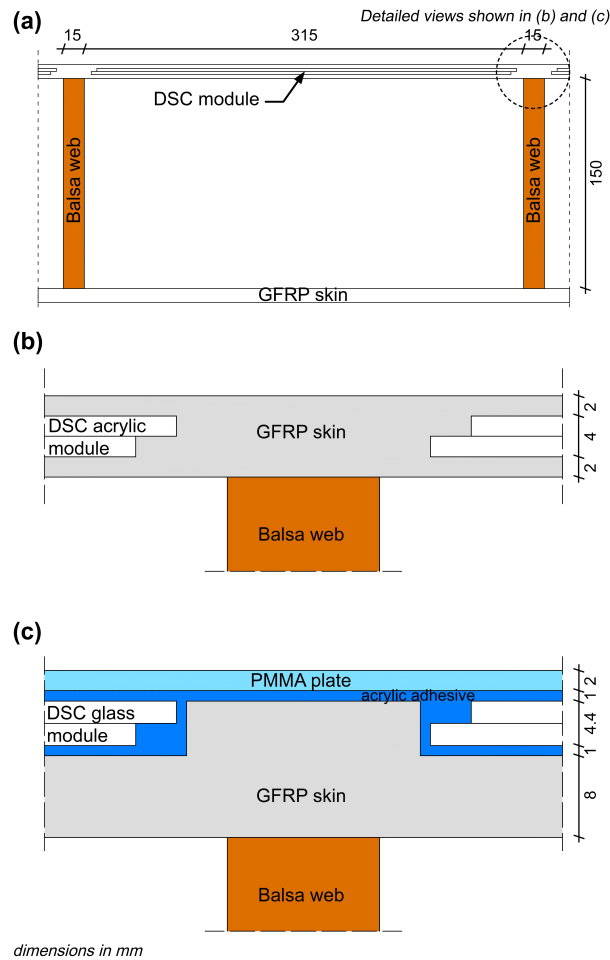


Figure 5.19. (a) Conceptual through-thickness design of translucent sandwich structure integrating solar energy production and detailed views of external skin with (b) DSC acrylic (PMMA) modules and (c) DSC glass modules.

5.6. Conclusions

The integration of DSC modules in GFRP laminates has been investigated and the following conclusions were drawn:

1. The feasibility of fabricating by infusion translucent solar panels encapsulating DSC modules in GFRP laminates has been demonstrated. Solar panels with electrical efficiencies of 3.25% and 3.40% have been successfully fabricated.
2. An analytical model of solar panel electrical efficiency as a function of the reinforcement weight of the upper GFRP encapsulant has been established and validated. To calibrate the model the total light transmittance of a one-layer GFRP laminate has to be measured.
3. The optimized GFRP upper encapsulants of DSC modules exhibit a 2-mm thickness with reinforcement weight of 1600 g/m² and reduce the electrical efficiency of the non-encapsulated DSC modules by 10%.
4. A panel with dummy modules on acrylic (PMMA) substrates directly encapsulated in GFRP exhibited no cracks and no delaminations after exposure to 50 thermal cycles (300 hours) of +60/-20 °C. Unlike for the glass modules, the numerical model indicates that no shear stress concentration occurs on the corners of the acrylic modules.

5. The soft interlayers between the GFRP encapsulant and the DSC glass modules release the thermal stresses on the modules. Transparent acrylic adhesives exhibiting good adherence with glass and GFRP may constitute a valuable option as interlayer material.

5.7. References

1. Jelle BP, Breivik C and Rokenes HD. Building integrated photovoltaic products: A state-of-the-art review and future research opportunities. *Sol Energ Mat Sol C* 2012; 100:69-96.
2. Roberts S, Guariento N. *Building integrated photovoltaics / a handbook*. Basel: Birkhäuser, 2009.
3. Hersch P, Zweibel K. *Basic Photovoltaic Principles and Methods*. Washington DC: US Government Printing Office; 1982.
4. Weller B, Hemmerle C, Jakubetz S, et al. *Photovoltaics – Technology Architecture Installation*. Basel: Birkhäuser, 2010.
5. Raga SR, Fabregat-Santiago F. Temperature effects in dye-sensitized solar cells. *Physl Chem Chem Phys* 2013; 15(7):2328-2336.
6. Davis MW, Fanney AH and Dougherty BP. Prediction of Building Integrated Photovoltaic Cell Temperatures. *J Sol Energ-T Asme* 2001; 123(3):200-210.
7. O'Reagan B and Grätzel M. A low-cost, high efficiency solar cell based on dye-sensitized colloidal TiO₂ films. *Nature* 1991; 353(6346):737-740.
8. Bai Y, Cao Y, Zhang J, et al. High-performance dye-sensitized solar cells based on solvent-free electrolytes produced from eutectic melts. *Nature Mat* 2008; 7(8):626-630.
9. Yum JH, Humphry-Baker R, Zakeeruddin SM et al. Effect of heat and light on the performance of dye-sensitized solar cells based on organic sensitizers and nanostructured TiO₂. *Nano Today* 2010; 5(2):91-98.
10. Hinsch A, Kroon JM, Kern R, et al. Long-term Stability of Dye-Sensitized Solar Cells. *Prog Photovoltaics* 2001; 9(6):425-438.
11. Grätzel M. Photoelectrochemical cells. *Nature* 2001; 414(6861):338-344.
12. Grätzel M. Photovoltaic and photoelectrochemical conversion of solar energy. *Philos T Roy Soc A* 2007; 365(1853):993-1005.
13. Solaronix company. Product information at: <http://www.solaronix.com/> (accessed 27 April 2014).
14. Velut P, Tween R, Teuscher R, et al. Conformal thin film silicon photovoltaic modules. Accepted for publication in *Int J Sustain Energ* 2013; DOI: 10.1080/14786451.2013.766611.
15. Keller T, Vassilopoulos AP and Manshadi BD. Thermomechanical behavior of multifunctional GFRP sandwich structures with encapsulated photovoltaic cells. *J Compos Constr* 2010; 14(4):470-478.
16. Pascual C, de Castro J, Schueler A, et al. Total light transmittance of glass fiber-reinforced polymer laminates for multifunctional load-bearing structures. Accepted for publication in *J Compos Mater* 2013; DOI: 10.1177/0021998313511653.
17. Tomasi A, Mocibob D, van de Linde B, et al. TEC facade – Glass as functional façade element. In: *Proceedings of COST Action TU0905 Mid-Term Conference on Structural Glass*, Porec, Croatia, 18-19 April 2013, pp.349-357. London: Taylor & Francis Group.

18. Bashore FJ and Price AW. *Evaluation of silane treated glass beads in polyester pavement marking paint*. Report for the U.S. Department of transportation. Report n° R-1269, February 1986. Michigan: Department of transportation.
19. Park SJ and Jin JS. Effect of Silane Coupling Agent on Interphase and Performance of Glass Fibers/Unsaturated Polyester Composites. *J Colloid Interf Sci* 2001; 242(1):174-179.
20. Sommeling PM, Späth M, van Roosmalen JAM, et al. *Dye-sensitized nanocrystalline TiO₂ solar cells on flexible substrates*. Report, Energy Research Center of the Netherlands, NL, 1998.
21. Fathi M, Aissat A and Ayad M. Design of building integrated photovoltaic (BIPV) and integration of photons converters. In: *Proceedings of Clean Energy Solutions for Sustainable Environment*, Beirut, Lebanon, 16-18 February 2012, pp.377-383. Amsterdam: Elsevier.
22. Gilbert JL, Ney DS and Lautenschlager EP. Self-reinforced composite poly(methyl methacrylate): static and fatigue properties. *Biomaterials* 1995; 16(14):1043-1055.
23. Buckley CA, Lautenschlager EP and Gilbert, JL. Deformation Processing of PMMA into High-Strength Fibers. *J Appl Polym Sci* 1992; 44(8):1321-1330.
24. Barbero E. *Introduction to composite materials design*, 2nd ed. Boca Raton, FL: CRC Press, 2011.
25. Kinsella M, Murray D, Crane D, et al. Mechanical properties of polymeric composites reinforced with high strength glass fibers. In: *Proceedings of the 33rd international SAMPE technical conference*, Seattle, USA, 5-8 November 2001, pp.1644-1657. Covina, CA: SAMPE.
26. Pascual C, de Castro J, Schueler A, et al. Diffuse light transmittance of glass fiber-reinforced polymer laminates for multifunctional load-bearing structures. Accepted for publication in *J Compos Mater* 2013; DOI: 10.1177/0021998313511655.
27. Haldimann M, Luible A and Overend M. *Structural Use of Glass*. Zurich: IABSE; 2008.
28. Swiss-Composite company. Product information at:
<http://www.swiss-composite.ch/pdf/t--Silgel-612.pdf> (accessed 30 May 2014).
29. Hecht E. *Optics*, 4th ed. San Francisco: Addison-Wesley, 2002.
30. CUR96. *Recommendation 96: Fibre-Reinforced Polymers in Civil Load-Bearing Structures*. Gouda: CUR commission, 2003.
31. Gay D, Hoa SV and Tsai SW. *Composite materials: design and applications*. Boca Raton, FL: CRC Press, 2003.
32. Pilkington company. Product information at:
<http://www.pilkington.com/resources/ats129propertiesofglass20130114.pdf> (accessed 21 May 2014).
33. GCIP company. Product information at:
<http://www.gcip.co.uk/pdf/perspexdata.pdf> (accessed 21 May 2014).
34. Material database at:
<http://www.goodfellow.com/E/Polymethylmethacrylate.html> (accessed 21 May 2014).
35. DuPont company. Product information at http://www.dupont.com/content/dam/assets/products-and-services/packaging-materials-solutions/assets/Typical_Properties_of_Surlyn.pdf (accessed 21 May 2014).
36. Huber A and Hinkley J. *Impression Testing of Self-Healing Polymers*. Report for the NASA. Report n° TM-2005-213532, March 2005. Springfield: National Technical Information Service.
37. Wolfram Alpha. Search for "thermal expansion DuPont Surlyn" at:
<http://www.wolframalpha.com/>

38. Qi HJ, Joyce K and Boyce MC. Durometer hardness and the stress-strain behavior of elastomeric materials. *Rubber Chem Technol* 2003; 76(2):419-435.
39. Rhodes K. Adhesives Deliver Low Shrink, Low Stress Bonds and Fast UV Cure. In: *Proceedings of SPIE Conference*, San José, USA, 20-21 January 2001, vol.4253, pp.92-107. Bellingham: SPIE.
40. Rion J. *Ultra-light photovoltaic composite sandwich structures*. PhD thesis, Ecole Polytechnique Fédérale de Lausanne, Switzerland, 2008.
41. Shi G and Zhang H. Modeling of adhesive layers of laminated plates in delamination simulation. In: *CD-Rom Proceedings of 17th International Conference on Composite Materials, Edinburgh, UK, 27-31 July 2009*, paper F9:1.
42. Péliisset S, Joly M, Chapuis V, et al. Efficiency of silicon thin-film photovoltaic modules with a front coloured glass. In: *Proceedings of CISBAT international conference*, Lausanne, Switzerland, 14-16 September 2011, pp.37-42. Lausanne: LESO-PB.
43. Roecker C, Munari-Probst MC, Edelman M, et al. *Architectural integration: Survey for PV collectors*. Report, Ecole Polytechnique Fédérale de Lausanne, Switzerland, 2010.
44. Pascual C, de Castro J, Schueler A, et al. Optomechanical investigation of glass fiber-reinforced polymer laminates for multifunctional load-bearing structures. Submitted to *J Compos Mater* in June 2014.
45. Köhl M, Meir MG, Papillon P, et al. (eds). *Polymeric Materials for Solar Thermal Applications*. Weinheim: Wiley-VCH, 2012.

6 Conclusions and future work

6.1. Conclusions

The main conclusions of this thesis related to the integration of daylighting and solar energy production functions in translucent GFRP laminates composed of polyester resin and E-glass fibers are presented below. These conclusions are categorized into four groups: 1) scientific conclusions, 2) applications for building construction, 3) materials and fabrication methods and 4) measurements of light transmittance.

6.1.1. Scientific conclusions

The total light transmittance of GFRP laminates decreases with the reinforcement weight – independently of fiber volume fraction – due to the increase of refraction and reflection of light rays with the amount of fibers in the laminate. The ray-tracing simulations performed showed that flaws, e.g. voids or air pockets around fibers, are the major causes of refraction and reflection of light rays – fiber/resin interfaces only produce little refraction due to the close matching of the refractive indices of fibers and resin at values of around 1.56. These simulations indicated that GFRP laminates with no flaws and approximate reinforcement weights of $w = 1600 \text{ g/m}^2$ exhibit light transmittances of around 0.90 (similar to glass) if refractive index mismatches between fiber and resin are no greater than 0.01. Transmittances of between 0.80 and 0.83 were measured in fabricated GFRP laminates with $w = 1640 \text{ g/m}^2$ and $w = 1560 \text{ g/m}^2$ and were therefore close to the value predicted by the simulations (0.90).

The ray-tracing simulations proved that refractive index mismatches of higher than 0.01 between fibers and resin below the 500-nm wavelength were responsible for the blue light diffusion in the laminates and predictions were in agreement with spectrophotometric measurements of diffuse transmittance. These measurements indicated that the translucency of GFRP laminates increases with the reinforcement weight and fiber volume fraction and decreases with resin gel times. In addition, the experimental investigation of light diffusion demonstrated that the total light transmittance increases with the transparency of the laminates.

Goniophotometric experiments demonstrated that the directional light scattering of GFRP laminates is determined by their fiber architecture: the major planes of light diffusion are perpendicular to the reinforced directions of the laminates. Measuring the scattered radiation in these planes allowed the prediction of the directional reinforcement weight fractions of unidirectional and cross-ply laminates with average maximum errors of only 8%. Experimental results indicated that goniophotometry could be especially accurate for predicting the fiber architecture of highly transparent laminates with optical depths of lower than one.

6.1.2. Applications for building construction

The light transmittances predicted by the developed analytical model – based on spectrophotometric experimental results – have demonstrated that load-bearing GFRP skylights with reinforcement weights of up to around $w = 7000 \text{ g/m}^2$ exhibited total light transmittance of 0.5 and translucency of 0.9, i.e. the minimum values recommended for daylit buildings. In addition, the established model of solar panel efficiency – validated by electrical measurements on panels exposed to simulated solar radiation – predicted that cells encapsulated underneath a significant reinforcement weight of $w = 1600 \text{ g/m}^2$ would exhibit a loss of efficiency of only 10% compared to cells encapsulated in traditional glass materials.

A case study using an existing GFRP/polyurethane sandwich roof (Novartis Campus Main Gate Building) proved that the fiber architecture of structurally optimized GFRP face sheets could meet the requirements for daylighting and solar cell integration, thus demonstrating the basic feasibility of designing multifunctional components integrating structural, architectural (daylighting) and solar energy production functions in single sandwich components. Moreover new design concepts for translucent sandwich structures have been proposed in this research based on the composite action between lightweight balsa webs and translucent GFRP skins – where translucent aerogel could fill the space between webs to integrate the thermal insulation function. The solar cells could be placed in the neutral axis of the skin (exposed to sunlight) to minimize the stresses due to bending loads. Considering the upper and lower encapsulants of the cell as having $w = 1600 \text{ g/m}^2$, the skin would exhibit a significant GFRP thickness of 4 mm (for a fiber volume fraction of around 0.30).

Two types of solar cells have been investigated for encapsulation in lightweight GFRP laminates: opaque thin-film amorphous-silicon (a-Si) cells deposited on a polyethylene flexible polymer substrate and transparent colored dye solar cells (DSCs) fabricated between two rigid and waterproof glass substrates. The flexible a-Si cells present the advantage of allowing the integration of solar energy into the single curvature GFRP envelopes of buildings. However these cells are very fragile and required careful manipulation during the hand lay-up encapsulation process (even small wrinkles can damage the cells). Transparent and colored DSC modules on glass substrates are more robust and easier to manipulate. The feasibility of encapsulating DSC modules in translucent GFRP laminates has been demonstrated using an infusion manufacturing process – thus allowing the integration of solar energy and architectural functions (daylighting and colored lighting effects) into structural GFRP envelopes. In addition the glass substrates represent effective protective water barriers for the cells and GFRP envelopes with encapsulated DSC modules could therefore constitute a valuable source of energy in hot and humid climates.

6.1.3. Materials and fabrication methods

Two types of fabrics – with different treatments on the fiber surfaces – were investigated and resulted in GFRP laminates with significantly different light transmittance. Non-desized fibers (after fabric weaving) exhibited lubricants on their surface and long resin gel times were required to improve the fiber impregnation and therefore the light transmittance of the laminate. On the other hand, desized fibers coated with a finish coupling agent (after fabric weaving) had no lubricants on their surface, were easily impregnated at short gel times and resulted in more transparent GFRP laminates and are therefore recommended for the encapsulation of solar cells.

Two fabrication methods of GFRP laminates have been explored in this study: hand lamination and the infusion process. No difference in the optical properties of the laminates produced by both methods has been observed. However the infusion process was required for encapsulating DSC modules in GFRP laminates – in order to minimize the voids and air bubbles in the solar panels – and mat layers were incorporated in the fiber architecture to allow the flow of resin. For this purpose, continuous filament mats with no binder agent applied on the filaments were successfully used – mat-reinforced layers exhibited similar light transmittance to that of fabric-reinforced layers (with the finishing treatment) – and are therefore recommended for the fabrication of solar panels.

Laminates produced by both methods, i.e. hand lamination and the infusion process, exhibited average fiber volume fractions of around 0.33. This value is therefore recommended for the preliminary design of highly transparent GFRP structures.

The optical models developed in this research have to be calibrated for each combination of materials (resin and fibers) and fabrication process. To calibrate the model of total light transmittance, a reflectance experiment on a pure resin specimen and a total transmittance experiment on a one-layer reinforced specimen are required. For the translucency model, the proposed exponential law has to be calibrated based on a series of total and diffuse transmittance experiments performed on GFRP specimens with different reinforcement weights. Finally, the directional fiber volume fraction model can be calibrated from a series of goniophotometric experiments performed on cross-ply balanced GFRP specimens with different fiber volume fractions.

6.1.4. Measurements of light transmittance

Two sources of inaccuracy were identified during this research in the spectrophotometric measurements of total light transmittance performed on GFRP laminates using a small integrating sphere: 1) light diffused by the laminates was partly lost at the entrance port of the sphere and therefore was not completely collected inside the sphere (underestimating the light transmittance of the laminates), and 2) part of the light transmitted by the laminates was illuminating the measuring sensor before being uniformly scattered inside the sphere (overvaluing the light transmittance of the laminates). The total light transmittance of GFRP laminates was more accurately measured based on the short circuit currents generated by solar cells placed below the investigated laminates. Proportionality between the total light transmittance of the GFRP laminate and the short circuit current (and also electrical efficiency) of the solar cell was demonstrated. However the wavelength dependency of the light transmittance cannot be investigated with this technique. For this purpose, large-diameter integrating spheres (with large-diameter entrance port) coupled to a spectrophotometer may constitute a valuable option.

6.2. Original contributions

The original contributions of the present research to the project topic are listed in the following:

1. Analytical models for predicting the wavelength-dependent total light transmittance and the translucency of GFRP laminates have been established and validated.

2. The light diffusion through GFRP laminates has been investigated by ray-tracing simulations and the trend of the spectral total and diffuse light transmittance of GFRP laminates has been successfully modeled.
3. Goniophotometry has been demonstrated to be an effective method for evaluating the fiber architecture of unidirectional and cross-ply GFRP laminates.
4. An optically-based model of the directional fiber volume fraction (and therefore directional strength and E-modulus) of GFRP laminates has been developed based on the total and diffuse transmittance and directional light scattering of the composite.

6.3. Recommendations for future work

In spite of the promising optical results obtained in this research for load-bearing GFRP laminates, more investigations are required for developing multifunctional components integrating structural, architectural and energy production functions for building construction. Proposed topics for further research are given in the following:

1. The transparency and total light transmittance of GFRP encapsulants for solar cells could still be improved. For this purpose, cylindrical glass fibers could be replaced by glass ribbon reinforcement (with rectangular cross section) that reduces the diffusion of light and may therefore increase the electrical efficiency of solar panels.
2. The long-term stability of GFRP encapsulants exposed to UV radiation, humidity and thermal cycles requires thorough investigation to determine to what extent the structural integrity and operational reliability of the encapsulation can be maintained. The orthophthalic polyester resins used in this research could be replaced by more efficient weather-resistant transparent epoxies. Gel coats made of UV-stabilized isophthalic polyester could also be investigated to increase the long-term stability of GFRP laminates.
3. Investigation of interlayer materials between the solar cells, e.g. dye solar cells on glass substrates, and the GFRP encapsulant is required to avoid delaminations at the GFRP/substrate interface. For this purpose, transparent acrylic adhesives with a low E-modulus could constitute a valuable option.
4. The technical and economic feasibility of designing translucent sandwich components integrating load-bearing and energy supply functions via encapsulated dye solar cells for daylight buildings has to be further proved. The heat transfer through the sandwich and the maximum temperature reached in the GFRP encapsulant – that could lead to the degradation of the composite – have to be studied.
5. Scientific and technological progress concerning dye solar cell modules with polymeric substrates (instead of glass), e.g. acrylic substrates, is required to further reduce the self-weight of the solar panels, to allow good adherence between the substrate and GFRP encapsulant (without interlayer materials) and reduce stress concentrations at the GFRP/substrate interface.

A Laminates and PV modules

A.1. Introduction

The combinations of fibers and resin suitable for the fabrication of translucent GFRP laminates are indicated in Table A.1 and correspond to materials investigated by authors indexed in the references of this thesis. The refractive indices of these materials are also reported in Table A.1.

Table A.1. *Materials used for fabrication of translucent GFRP laminates from literature review.*¹⁻³

Type of resin	Type of reinforcement	Refractive index
Epoxy	S-glass fibers	1.52
Epoxy	Soda-lime silicate glass ribbons	1.52
Polyester	E-glass fibers	1.56

Among the types of fibers indicated in Table A.1, E-glass fibers constitute a compromise solution combining high mechanical and chemical resistance properties and low production costs. Therefore these types of fibers are commonly used in GFRP applications for building construction and were also selected for this research project.

In a preliminary study, three GFRP laminates reinforced with E-glass fabrics manufactured by Tissa (Oberkulm, Switzerland) were fabricated by hand lay-up using the three transparent resins indicated in Table A.2.

Table A.2. *Resins used in preliminary study for fabrication of E-glass reinforced laminates.*

Resin	Type of resin	Viscosity (mPas)
Biothan 1750	Bioresin	2000
Epoxy L	Epoxy	500
Polylite 420-181	Polyester	340

The resin Biothan 1750 could not be easily spread due to its high viscosity (see Table A.2) and the fabricated laminate exhibited poor fiber impregnation and high opacity. The reinforcement was easily impregnated using the Epoxy L resin, however the fabricated laminate did not exhibit a high transparency which was attributed to a significant refractive index mismatch between the fibers and the resin. Finally, the laminate fabricated with the Polylite 420-181 resin exhibited both good fiber impregnation and high transparency and this resin was therefore selected for fabrication of the GFRP laminates in this research.

The pure resin specimens, GFRP specimens and photovoltaic (PV) modules with amorphous silicon (a-Si) cells encapsulated in GFRP laminates fabricated for this research are presented below. The

fabrication of these specimens and modules was performed using PolyLite 420-181 unsaturated polyester resin from Reichhold Inc. (Durham, United States) and unidirectional E-glass fabrics manufactured by Tissa (Oberkulm, Switzerland). The hand lay-up fabrication processes of a GFRP laminate and of an a-Si PV module are also reported in this appendix.

GFRP laminates (from which GFRP specimens were cut) were manufactured with three different fiber volume fractions: series L with low (0.24 ± 0.03), series M with intermediate (0.32 ± 0.02) and series H with high (0.42 ± 0.01) fiber volume fractions. Laminates were fabricated with unidirectional (UD) and cross-ply (CP) fiber architectures and reinforcement weights of from 410 to 3280 g/m² (from one to eight layers of E-glass fabrics). Specimens and laminates were labeled according to their reinforcement weight, fiber architecture and fiber volume fractions, e.g. 1640CP-L refers to the specimen reinforced with 1640 g/m² of glass reinforcement, CP fiber architecture and low fiber volume fraction. Laminates were fabricated with a gel time of around 15 min. Only two laminates were fabricated with gel times of around 30 min and these are identified with a symbol (*) in their labeling.

The PV modules (fabricated with gel times of around 15 min) were labeled according to the reinforcement weight and fiber architecture of the upper encapsulant of the solar cells.

A.2. Spectrophotometric resin specimens

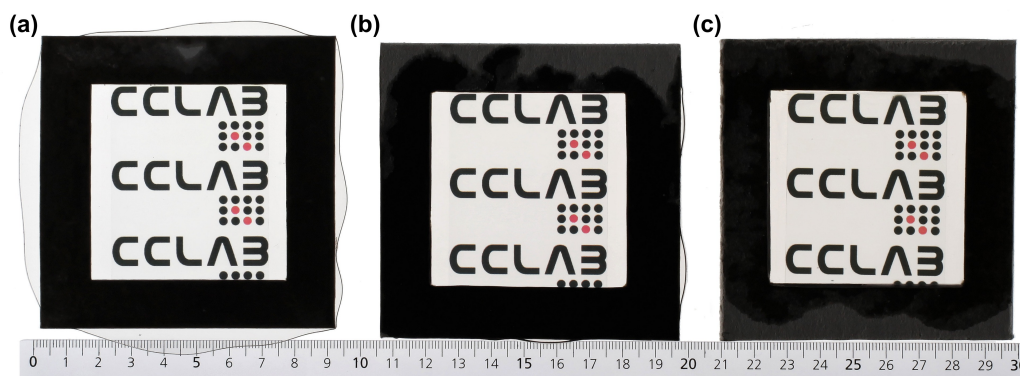


Figure A.1. Spectrophotometric resin specimens of (a) 1-mm, (b) 2-mm and (c) 4-mm thickness.

A.3. Tensile and spectrophotometric GFRP specimens

A.3.1. Series L

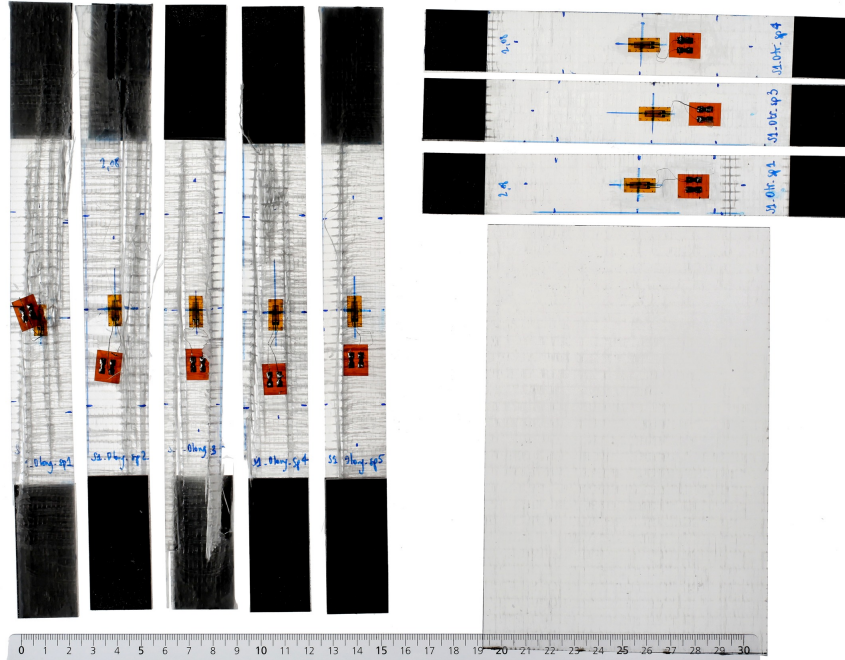


Figure A.2. Tensile (after experiment) and spectrophotometric specimens 410UD-L.

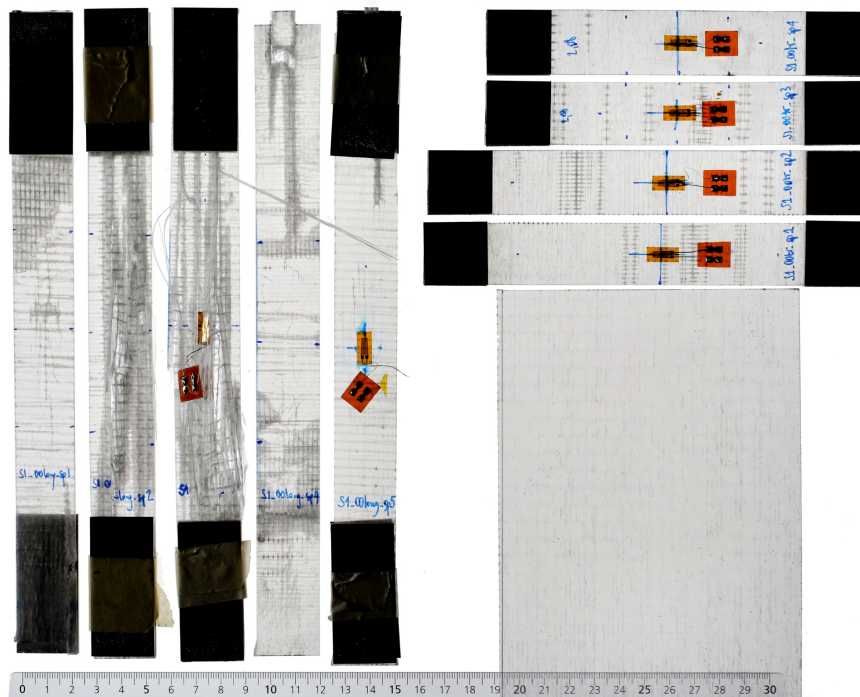


Figure A.3. Tensile (after experiment) and spectrophotometric specimens 820UD-L.

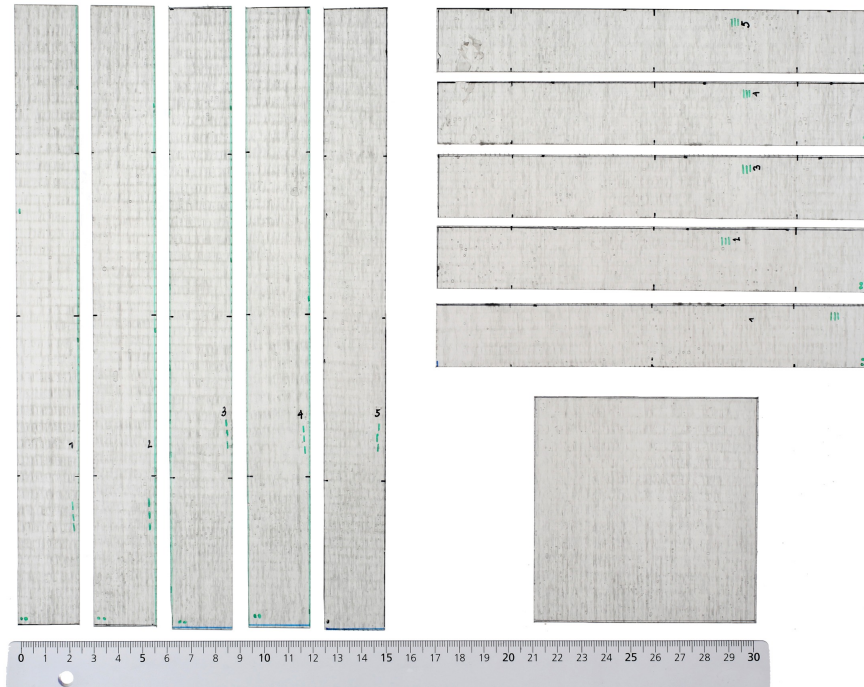


Figure A.4. Tensile and spectrophotometric specimens 1230UD-L.

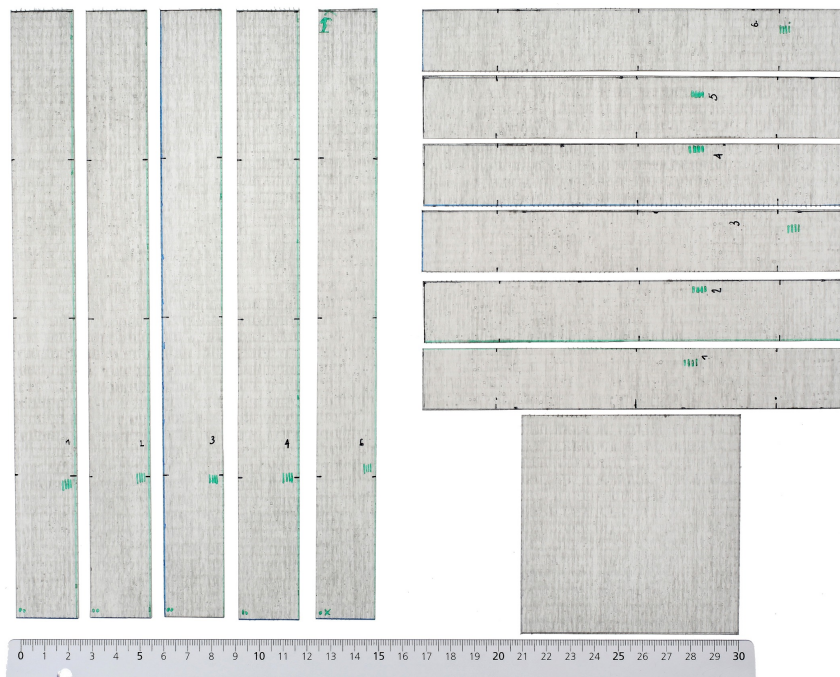


Figure A.5. Tensile and spectrophotometric specimens 1640UD-L.

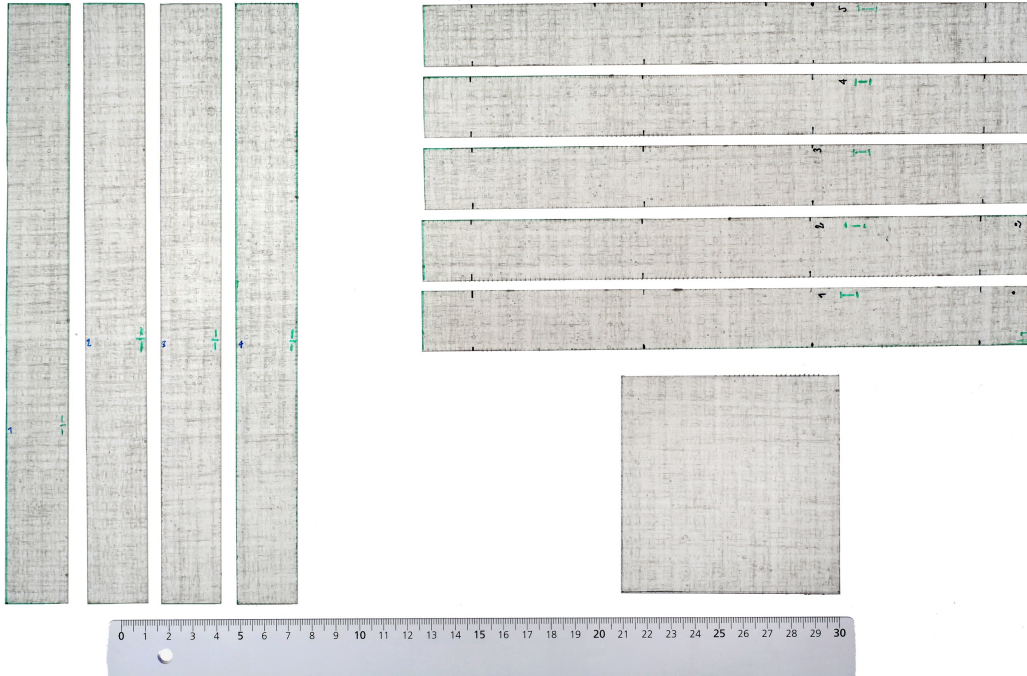


Figure A.6. Tensile and spectrophotometric specimens 1230CP-L.

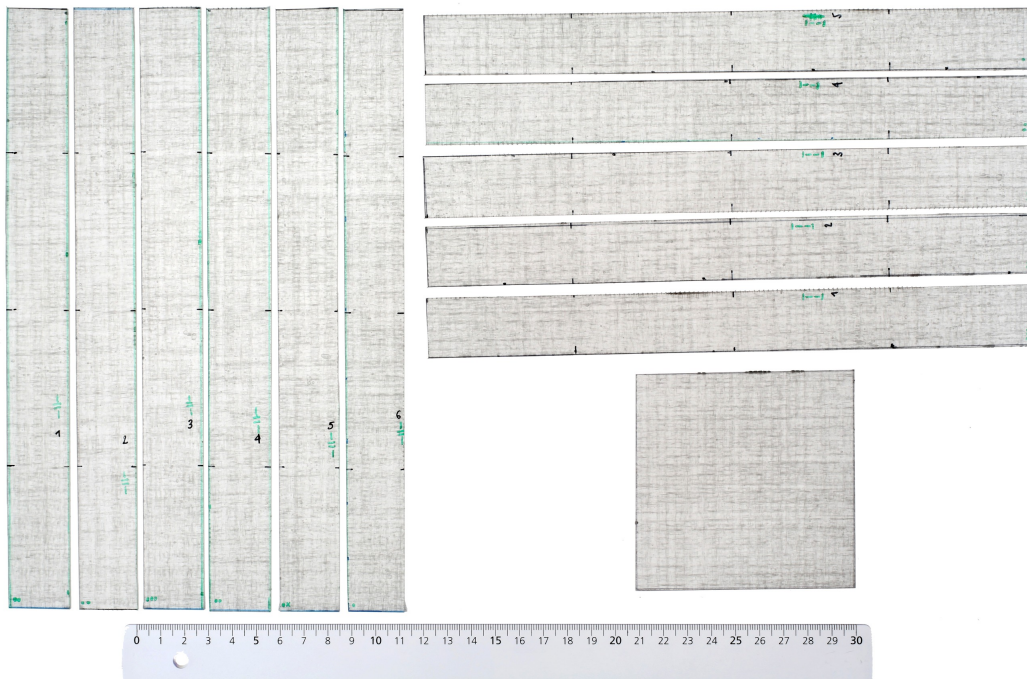


Figure A.7. Tensile and spectrophotometric specimens 1640CP-L.

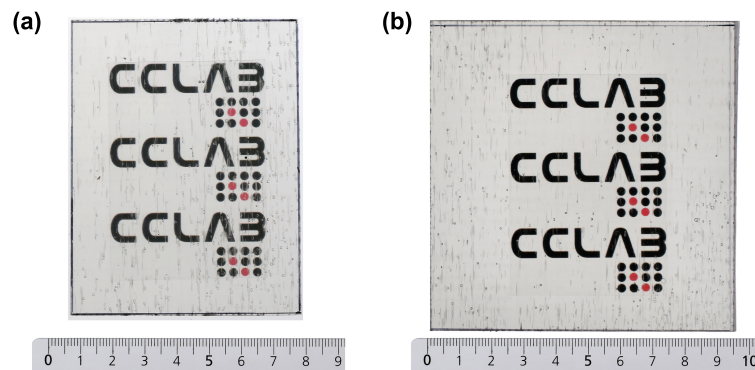


Figure A.8. Spectrophotometric specimens (a) 1230UD-L and (b) 1640UD-L* with 30-min gel time (photographs taken under different conditions of illumination).*

A.3.2. Series M

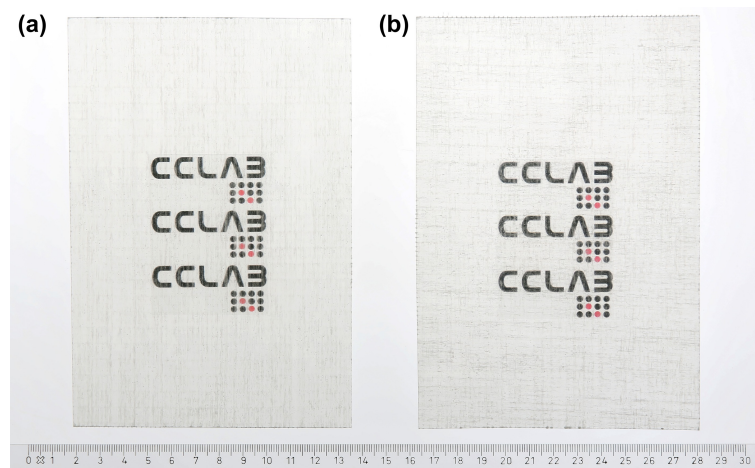


Figure A.9. Spectrophotometric specimens (a) 820UD-M and (b) 820CP-M (fabrication assisted by vacuum bag).

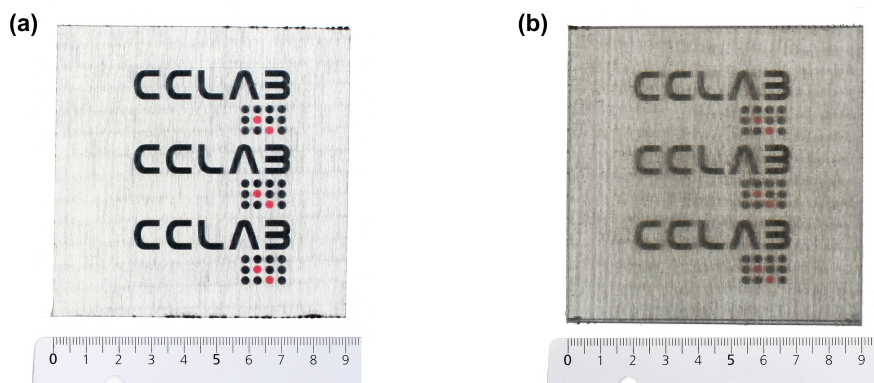


Figure A.10. Spectrophotometric specimens (a) 1230UD-M and (b) 3280UD-M (photographs taken under different conditions of illumination).

A.3.3. Series H

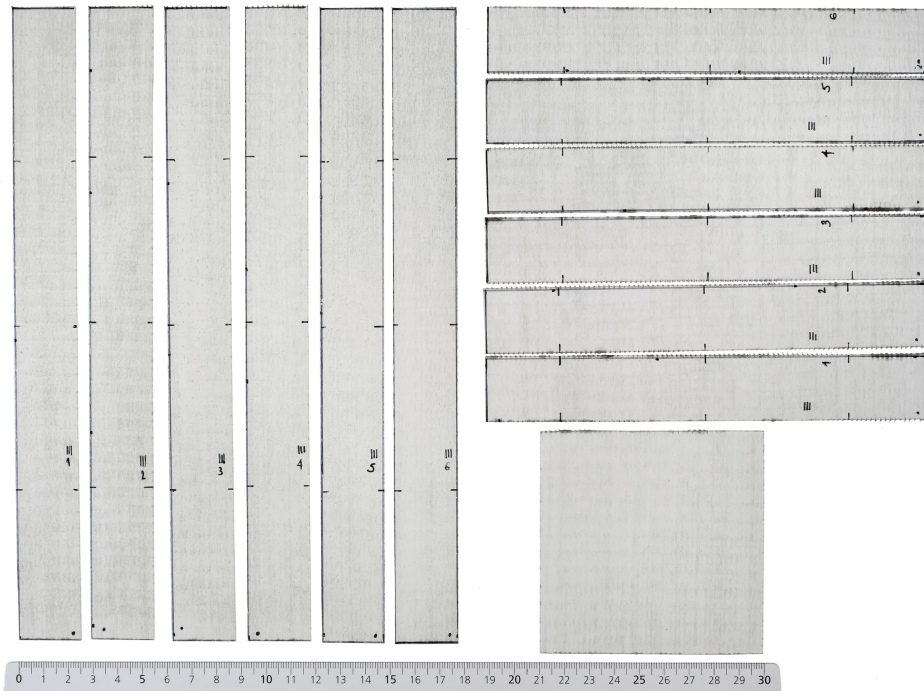


Figure A.11. Tensile and spectrophotometric specimens 1230UD-H.

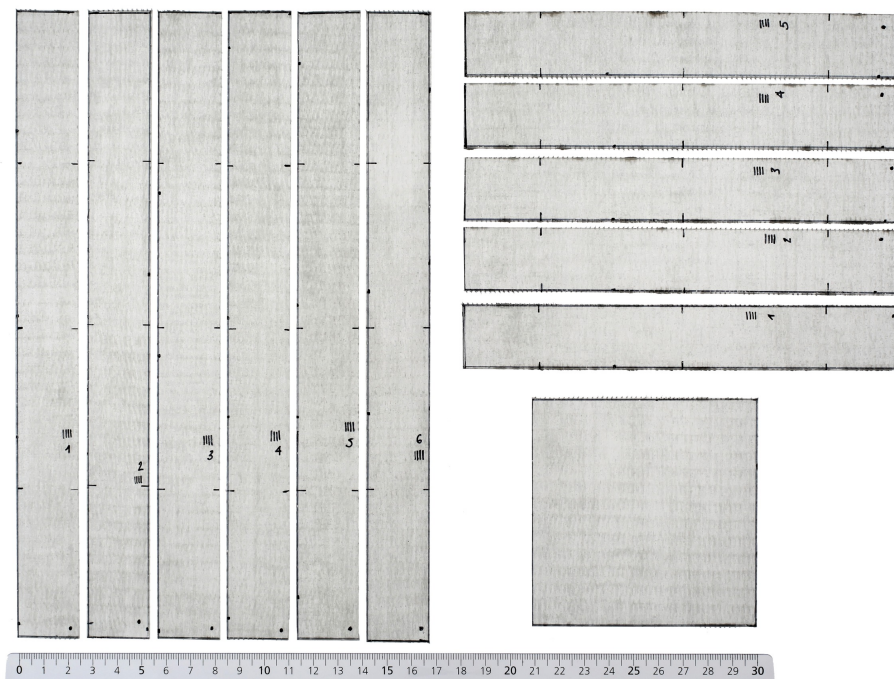


Figure A.12. Tensile and spectrophotometric specimens 1640UD-H.

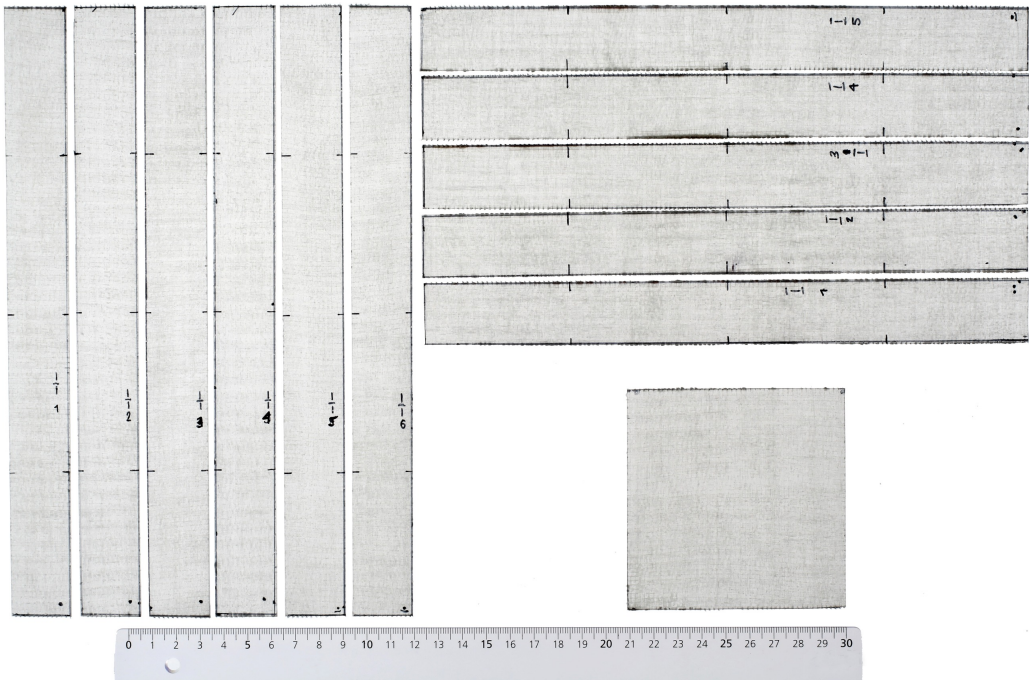


Figure A.13. Tensile and spectrophotometric specimens 1230CP-H.

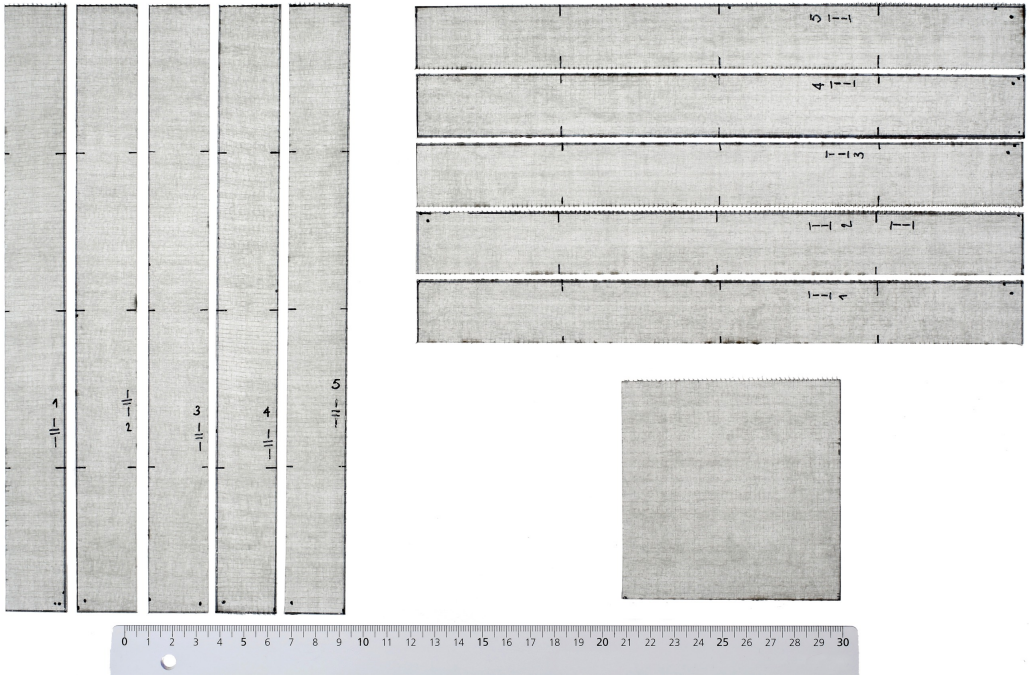


Figure A.14. Tensile and spectrophotometric specimens 1640CP-H.

A.4. Goniophotometric GFRP specimens

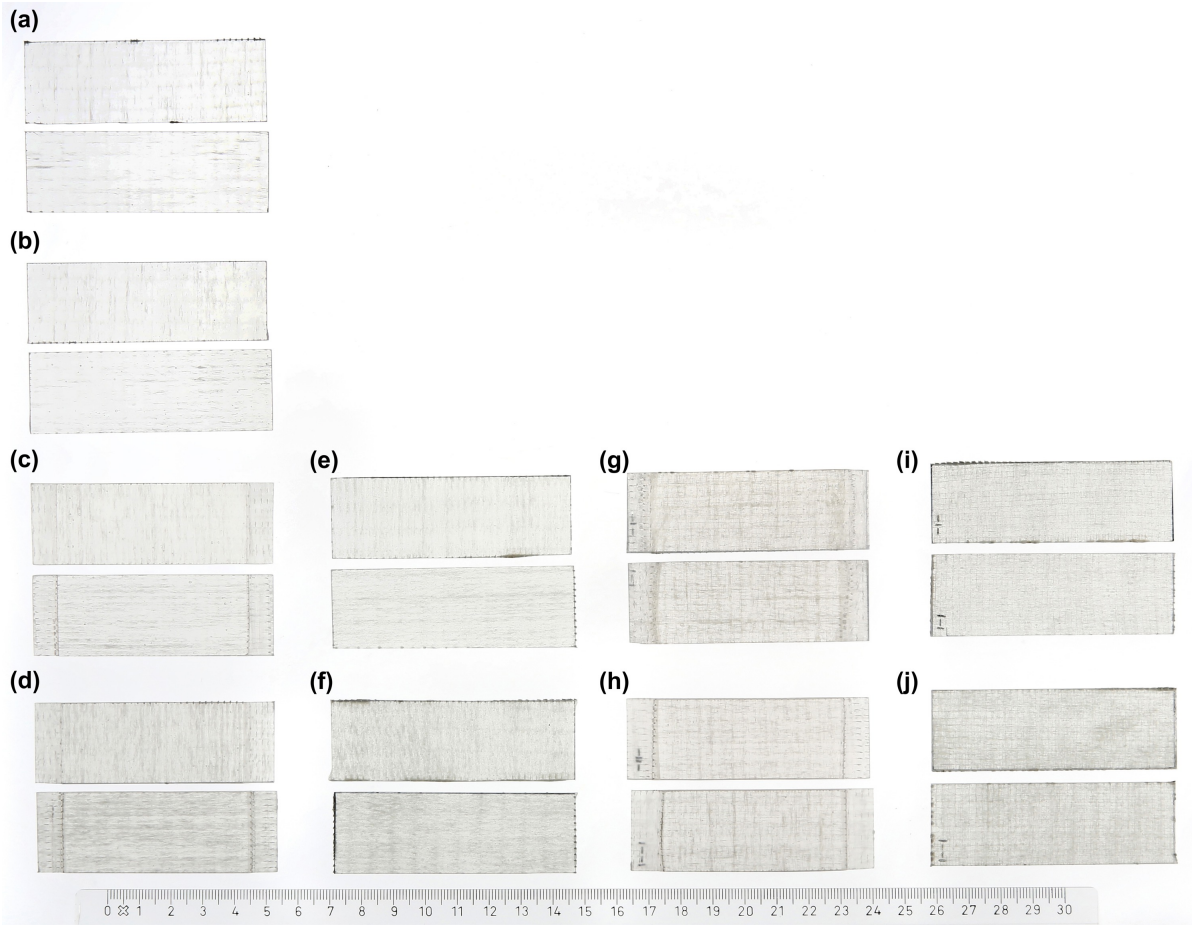


Figure A.15. Goniophotometric specimens from laminates (a) 410UD-L, (b) 820UD-L, (c) 1230UD-L, (d) 1640UD-L, (e) 1230UD-H, (f) 1640UD-H, (g) 1230CP-L, (h) 1640CP-L, (i) 1230CP-H, (j) 1640CP-H.

A.5. a-Si PV modules

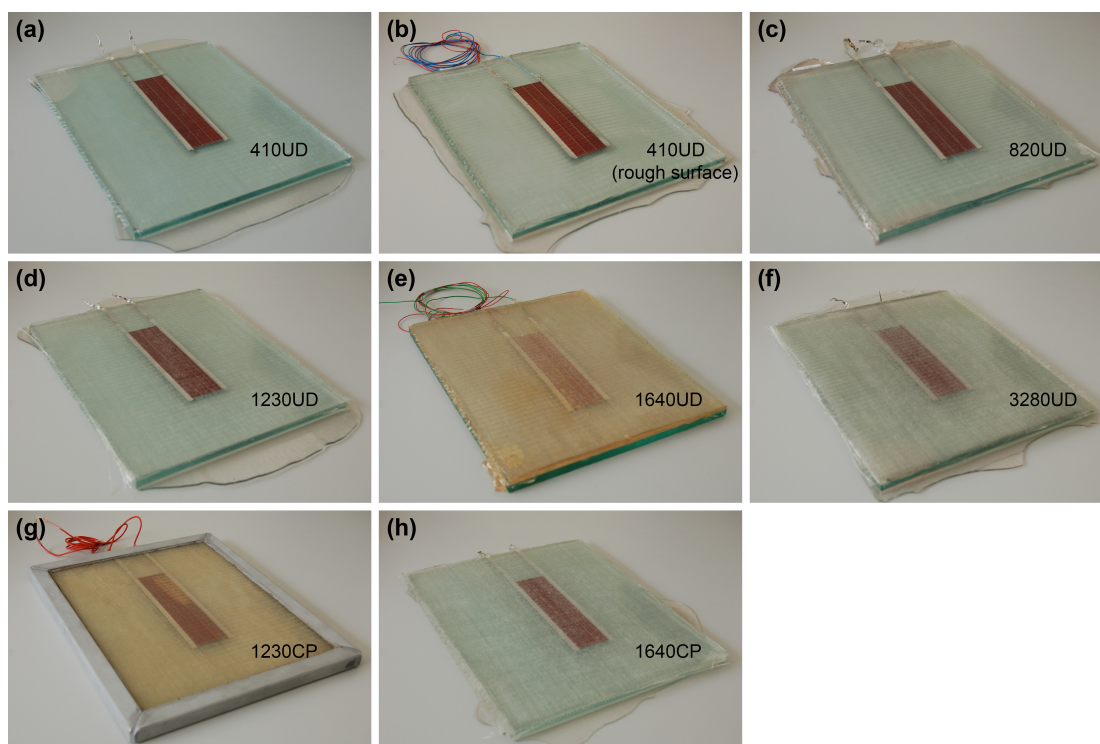


Figure A.16. Fabricated a-Si PV modules with indication of upper encapsulants (photographs (e) and (g) were taken after damp heat experiments).

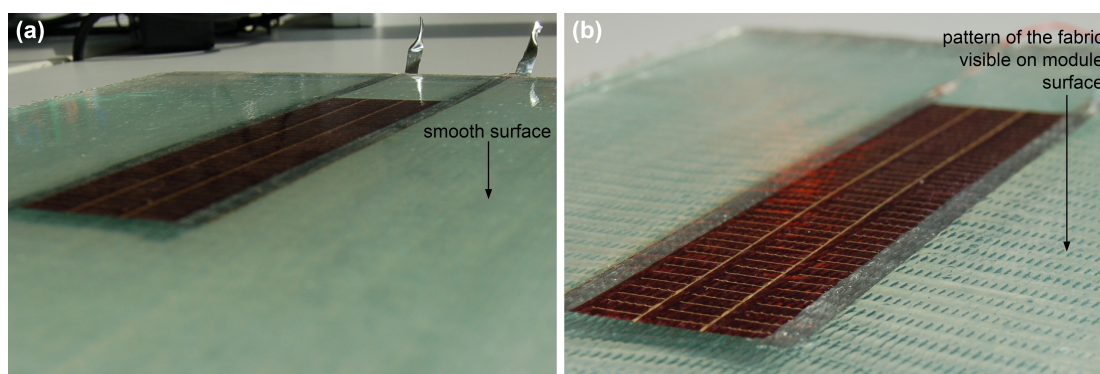


Figure A.17. Detailed views of modules with 410UD upper encapsulants exhibiting (a) smooth surface and (b) rough surface.

Eight PV modules with GFRP encapsulants were fabricated (see Figure A.16) and details of modules with 410UD (rough surface), 1640UD and 1230CP encapsulants are presented in the following:

1. The electrical results for the module with the 410UD rough upper encapsulant (see Figures A.16(b) and A.17(b)) are not included in Chapter 2, however they are presented in Appendix D.
2. The PV modules with the 1640UD and 1230CP upper encapsulants (see Figure A.16(e) and (g)) were subjected to damp heat experiments (temperature of 85 °C and humidity of 85%) during five and 14 days respectively.⁴ The latter module was sealed on the edges and the top surface was also protected with a transparent 100- μm -thickness fluoropolymer film. Both modules exhibited significant yellowing after the experiments (see Figure A.16(e) and (g)).

A.6. Hand lay-up fabrication

A.6.1. GFRP laminate fabrication

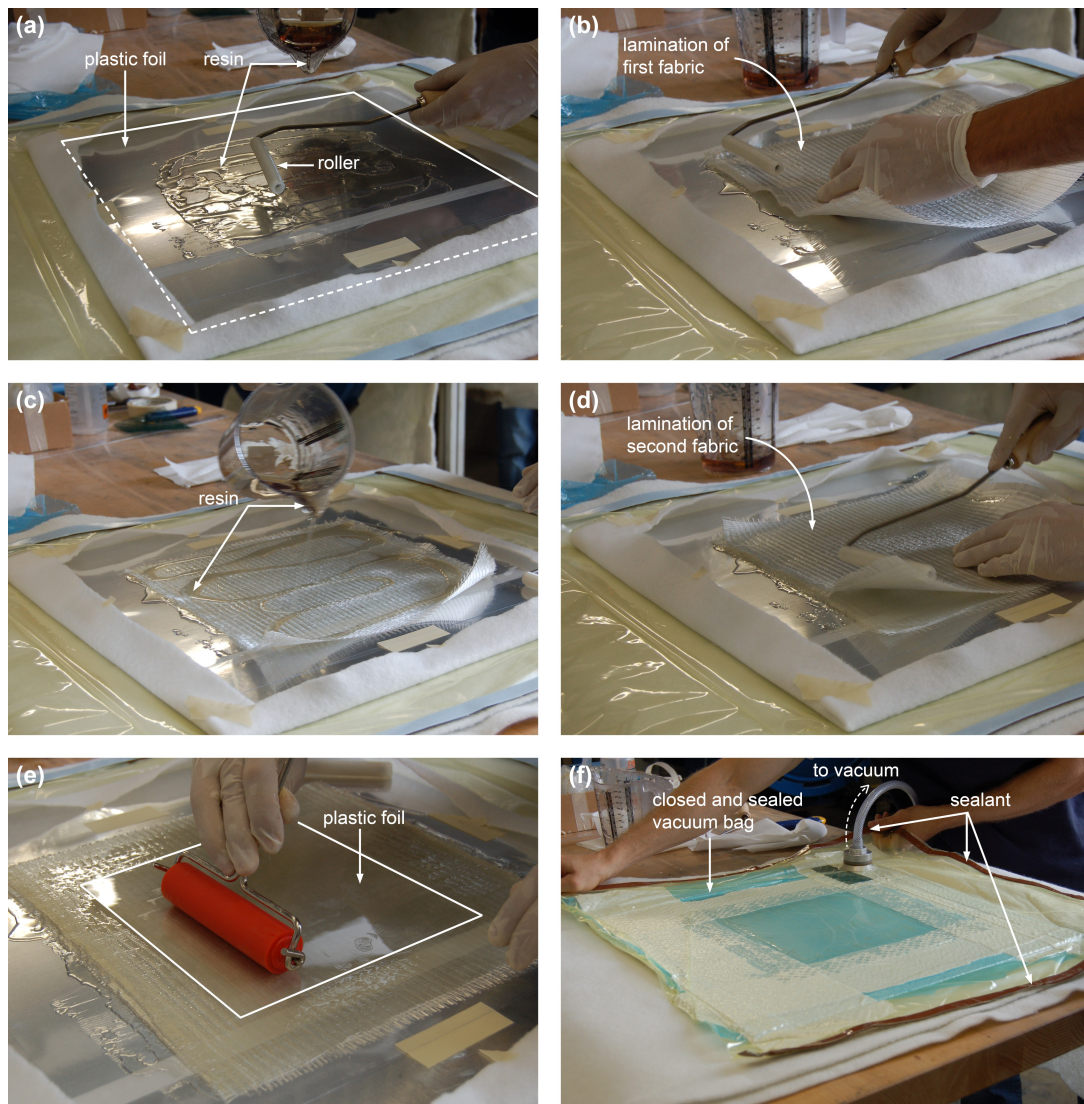


Figure A.18. Hand lay-up fabrication of two-layer GFRP laminate assisted by a vacuum bag.

Fabrication details are listed below:

1. The plastic foils shown in Figure A.18(a) and (e) were removed after curing of the laminates (smooth surfaces were obtained on the GFRP laminates after removing these foils).
2. The plastic foil shown in Figure A.18(e) had a smaller area than the laminate to allow air suction. However for non-vacuum-assisted fabrications plastic foils had larger areas than the laminates.
3. Non-vacuum-assisted fabrications were performed similarly to the process shown in Figure A.18(a) to (e). Only the fabrication of the series M laminates with $w = 820 \text{ g/m}^2$ was assisted by a vacuum bag (see Figure A.18(f)).

A.6.2. a-Si PV module fabrication

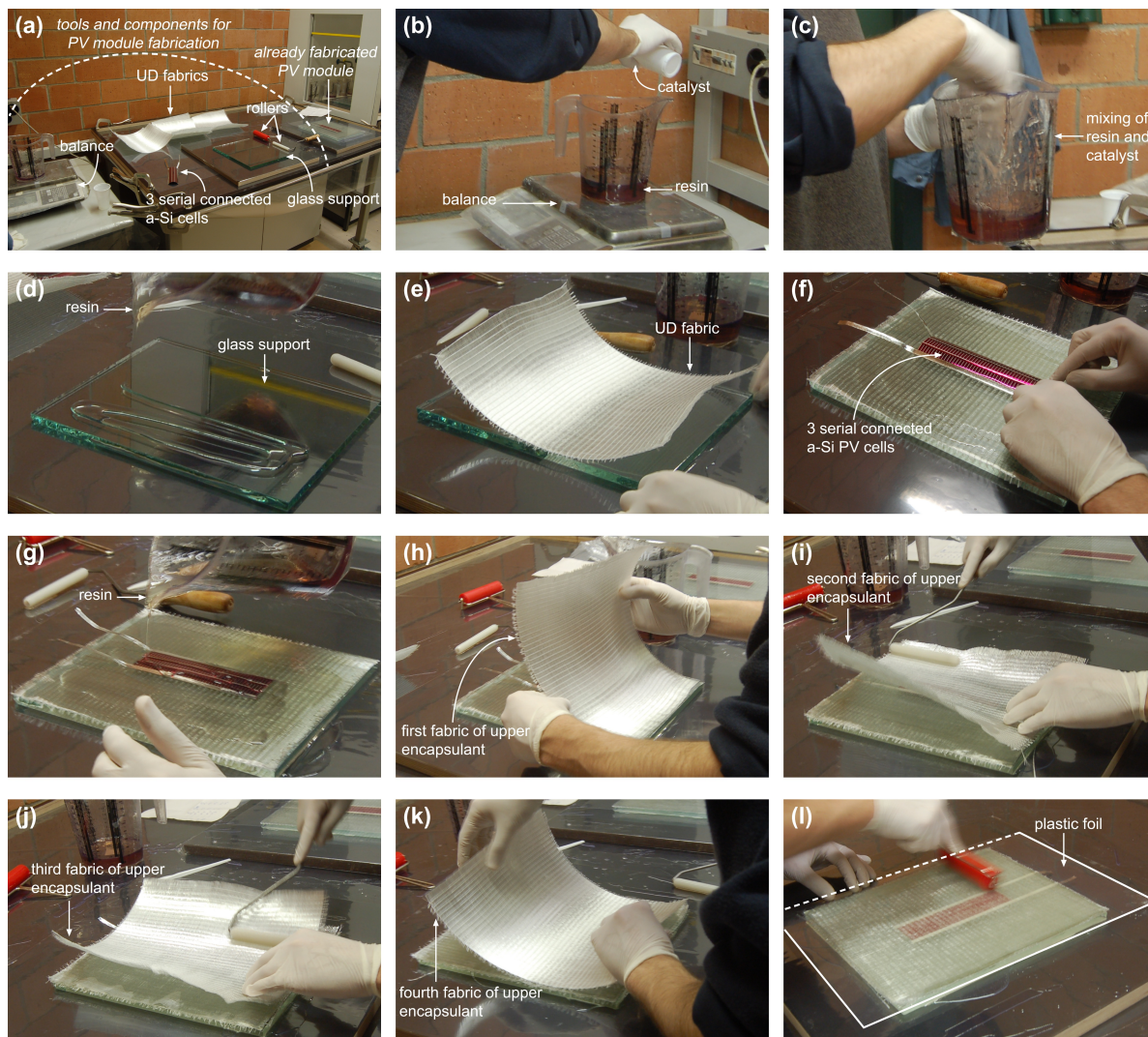


Figure A.19. Hand lay-up fabrication of PV module with three serial connected a-Si cells encapsulated below four layers of GFRP.

Fabrication details are listed below:

1. The plastic foils on top of the modules (see Figure A.19(l)) were removed after curing of the GFRP encapsulants. The smooth top surfaces of the PV modules were obtained after removing these foils.
2. One PV module with $w = 410 \text{ g/m}^2$ in the upper encapsulant was fabricated without using this top plastic foil and therefore exhibited a rough top surface (see Figure A.17(b)).

A.7. References

1. Krug DJ, Asuncion MZ, Popova V, et al. Transparent fiber glass reinforced composites. *Compos Sci Technol* 2013; 77:95-100.
2. Velez M, Braisted WR, Frank GJ, et al. Impact strength of optically transparent glass ribbon composites. *J Compos Mater* 2012; 46(14):1677-1695.

3. Keller T, Vassilopoulos AP and Manshadi BD. Thermomechanical behavior of multifunctional GFRP sandwich structures with encapsulated photovoltaic cells. *J Compos Constr* 2010; 14(4):470-478.
4. CEI Standard 61646. *Thin-film terrestrial photovoltaic (PV) modules – Design qualification and type approval*. Geneva, Switzerland: International Electrotechnical Commission, 2008.

B Optical microscopy

B.1. Introduction

Through-thickness optical microscopy images of specimen 1640UD-L* – with reinforcement weight of 1640 g/m² (four layers of fabrics), UD fiber architecture, low (L) fiber volume fraction and 30 min gel time – are presented below. The objectives of this research were 1) to determine the diameters of the fibers in the longitudinal rovings and yarns and in the transversal yarns of the unidirectional fabric manufactured by Tissa (Oberkulm, Switzerland) shown in Figure B.1 and 2) to determine the spacing between the four fiber layers in order to define the geometry of the ray-tracing model presented in Chapter 3.

The measurements were performed using an OLYMPUSBX60 optical microscope connected to a computer equipped with analySIS docu software for capturing the images and measuring the fiber diameters. Measurements were performed at the Interdisciplinary Centre for Electron Microscopy of the École Polytechnique Fédérale de Lausanne.

B.2. UD fabric from Tissa

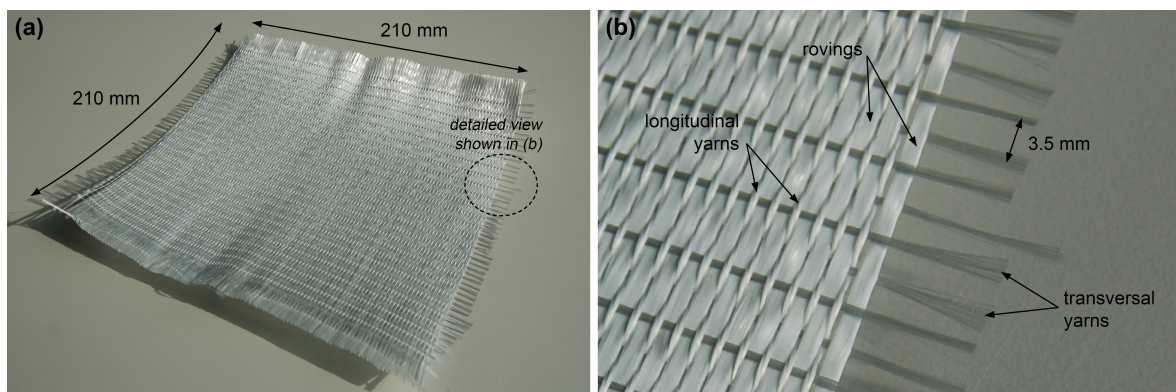


Figure B.1. (a) General view of 210x210-mm² sample of UD fabric from Tissa with a weight of 410 g/m² and (b) detailed view of rovings, longitudinal yarns and transversal yarns.

B.3. Optical microscopy images

B.3.1. Set-up

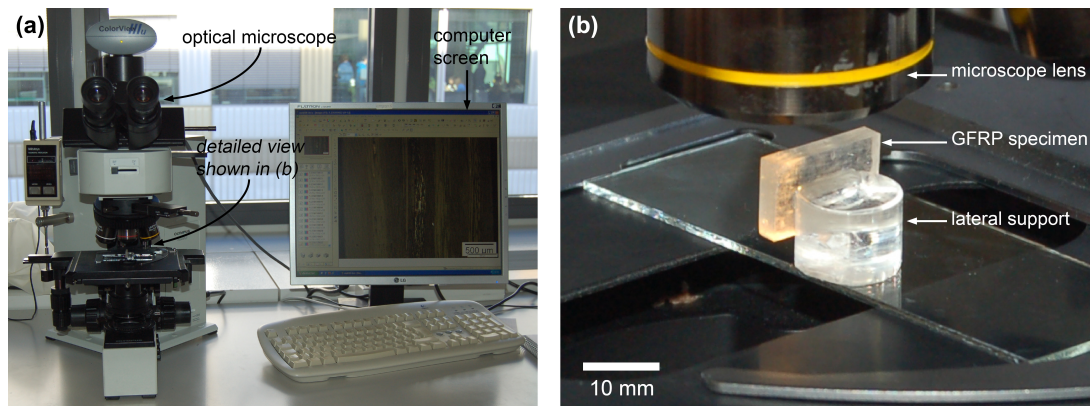


Figure B.2. Optical microscopy set-up: (a) microscope connected to computer screen and (b) detailed view of GFRP specimen (1640UD-L*).

B.3.2. Through-thickness images

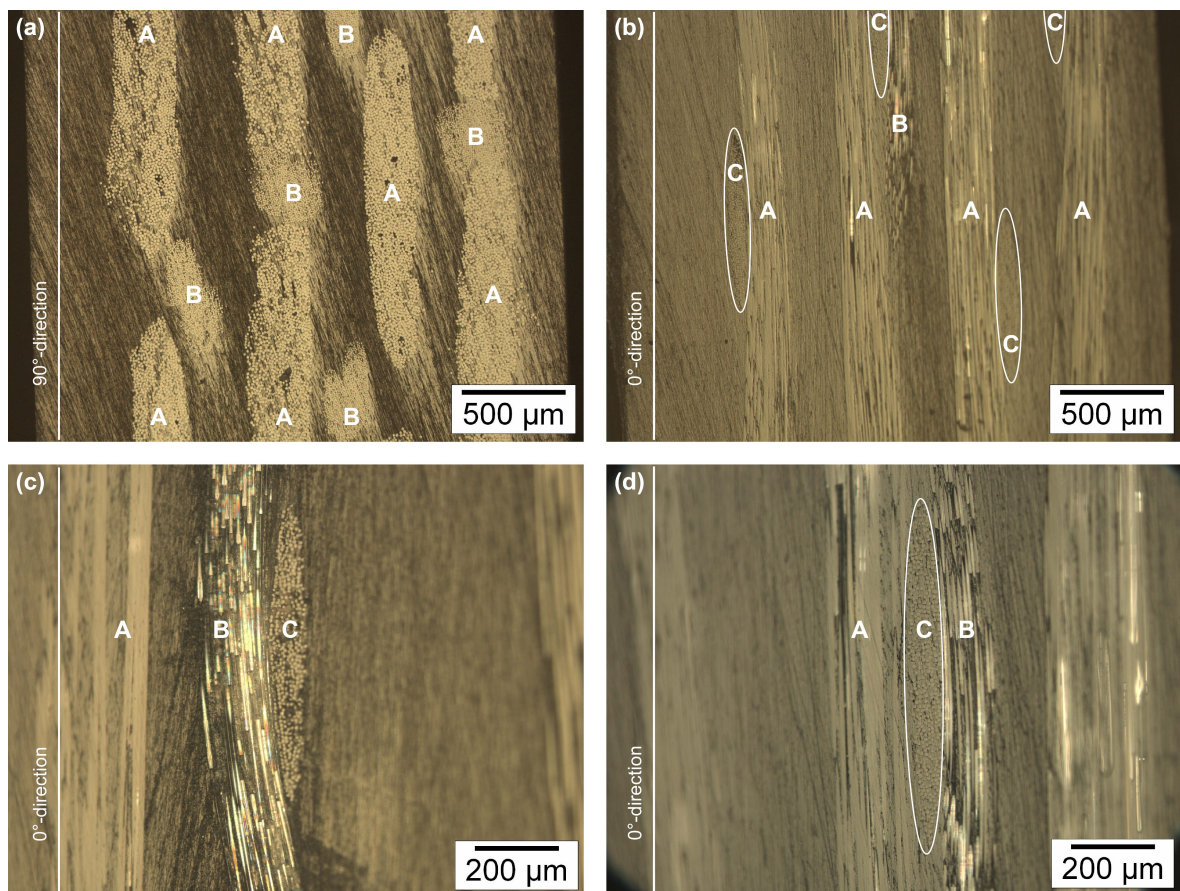


Figure B.3. Through-thickness optical microscopy images of specimen 1640UD-L*: (a) rovings (A) and longitudinal yarns (B) in 0°-direction and (b-d) images of transversal yarns (C) in 90°-direction.

B.3.3. Measurements of fiber diameter

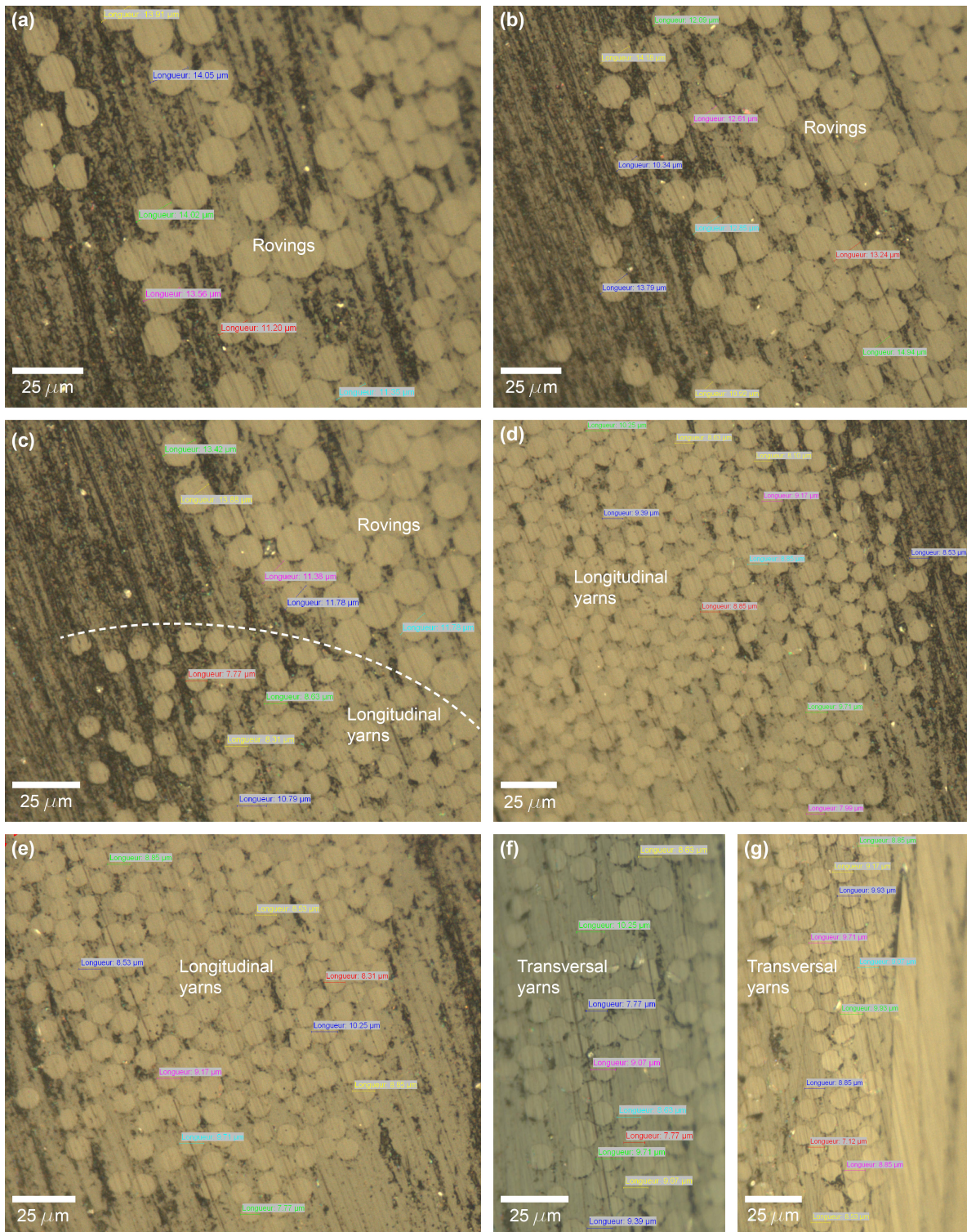


Figure B.4. Measurement of fiber diameters in (a-c) rovings, (c-d) longitudinal yarns and (f-g) transversal yarns.

Resulting diameters from the measurements were $12.8 \pm 1.3 \mu\text{m}$ for the roving fibers and $8.9 \pm 0.8 \mu\text{m}$ for the longitudinal and transversal yarn fibers (manufacturers indicated average diameters of 12 and 9 μm respectively).

C Spectrophotometric results

C.1. Introduction

The spectrophotometric measurements of total and diffuse light transmittance (of GFRP and pure resin specimens) and total reflectance (of pure resin specimens) performed with the integrating sphere set-up (described in Chapters 2 and 3) in the 400- to 800-nm wavelength range are presented below. The measurements of regular light transmittance (of pure resin specimens) performed with a Perkin Elmer Lambda 2 spectrophotometer (see Figure C.1) in the range 190-1100 nm are also reported in this appendix. The objective of the regular transmittance measurements was to verify that the resin specimens were opaque to the UV radiation, i.e. radiation below 380-nm wavelength.

The results presented below correspond to the spectrophotometric specimens shown in Figures A.1 to A.14 and fabricated with PolyLite 420-181 unsaturated polyester resin from Reichhold Inc. (Durham, United States) and unidirectional E-glass fabrics manufactured by Tissa (Oberkulm, Switzerland). Four light transmittance measurements were performed on each GFRP specimen (in well impregnated areas) and one measurement was performed on each pure resin specimen.

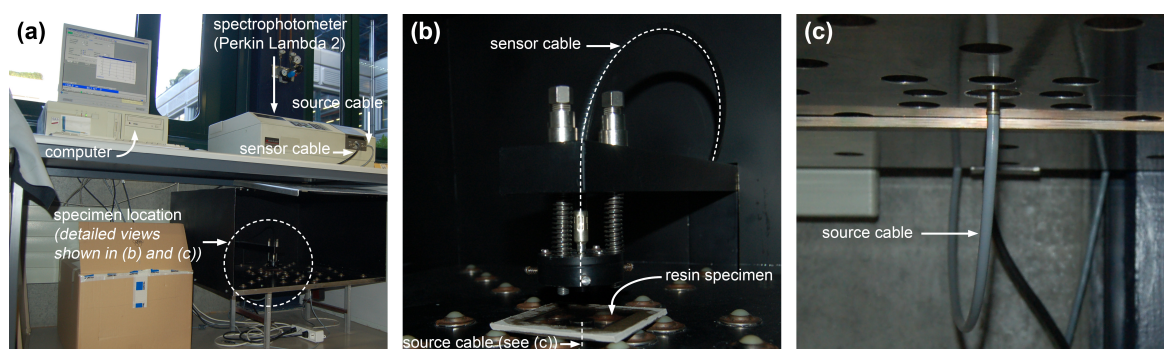


Figure C.1. (a) Set-up for measuring regular transmittance of pure resin specimens and detailed views of (b) specimen location and (c) source cable below specimen.

C.2. Spectrophotometric results

C.2.1. Measurements performed with the integrating sphere set-up

C.2.1.1. Series L

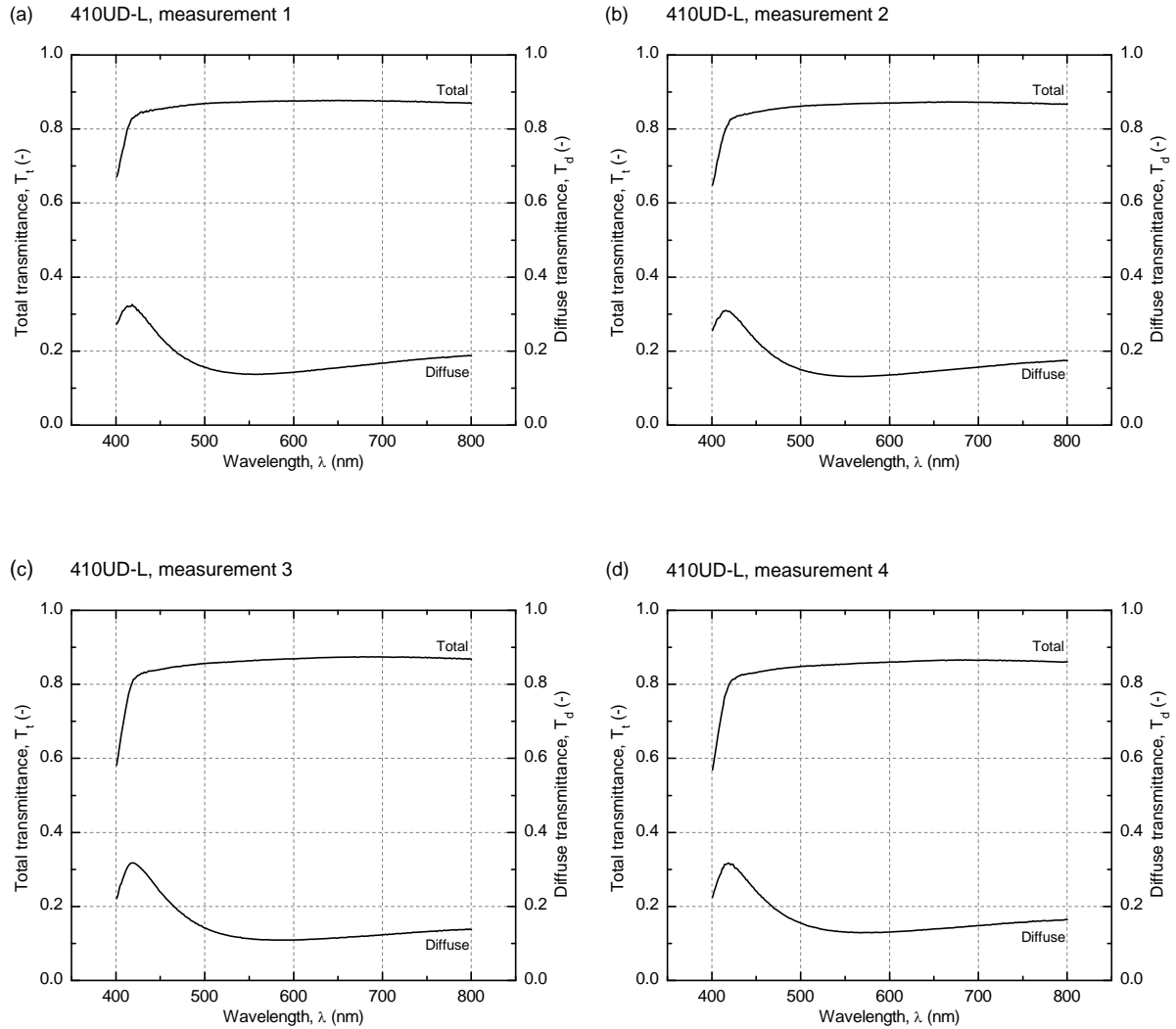


Figure C.2. Total and diffuse transmittance of GFRP specimen 410UD-L.

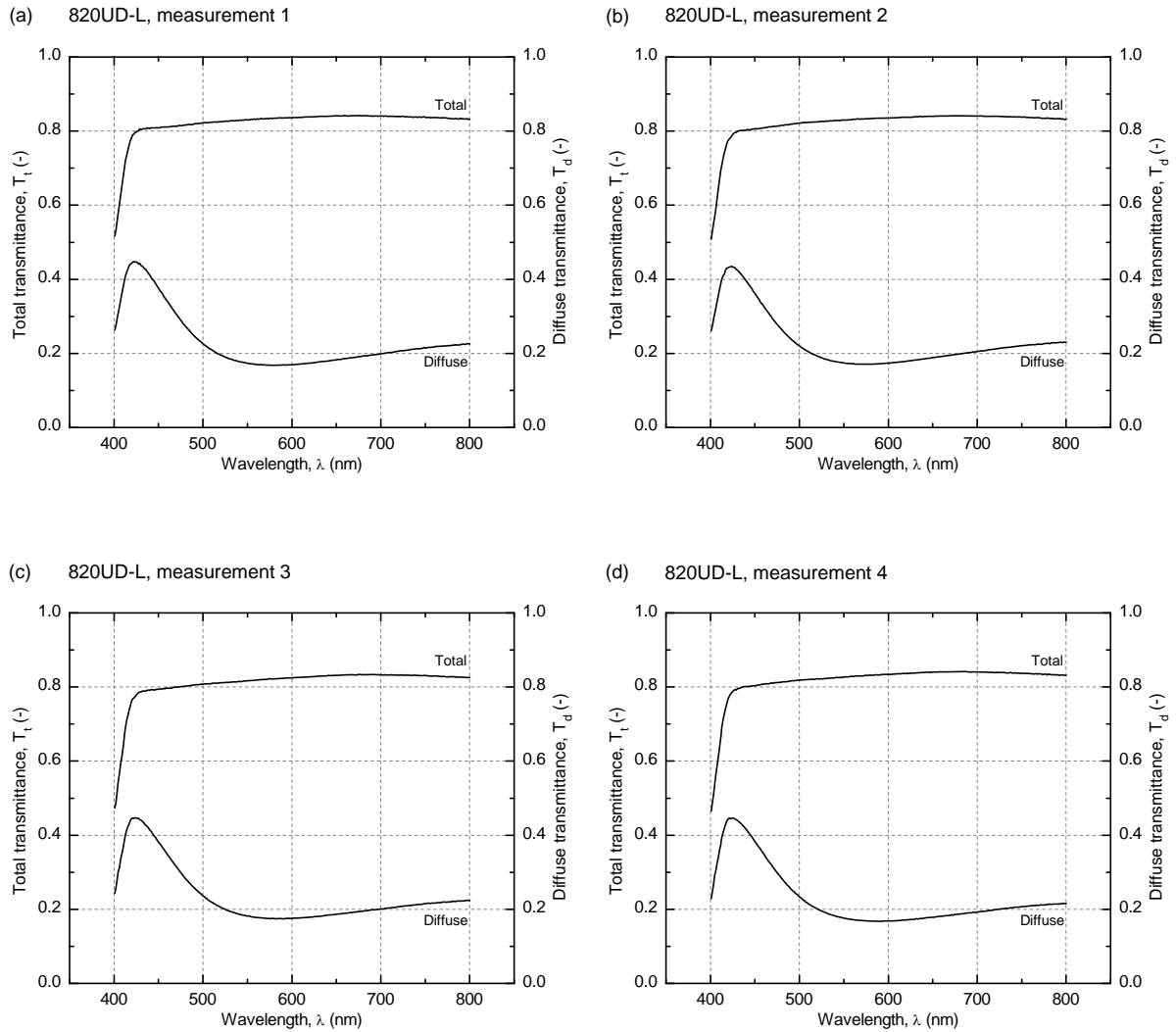
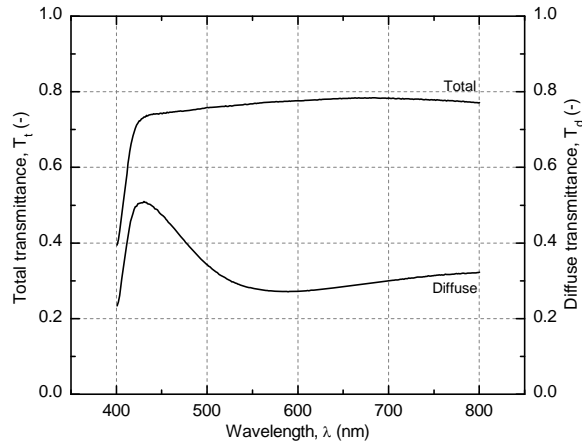
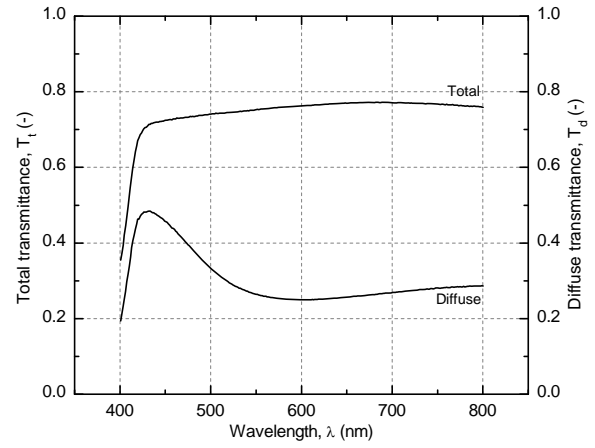


Figure C.3. Total and diffuse transmittance of GFRP specimen 820UD-L.

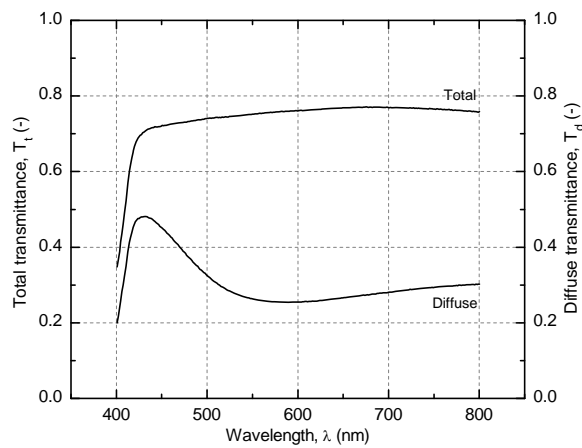
(a) 1230UD-L, measurement 1



(b) 1230UD-L, measurement 2



(c) 1230UD-L, measurement 3



(d) 1230UD-L, measurement 4

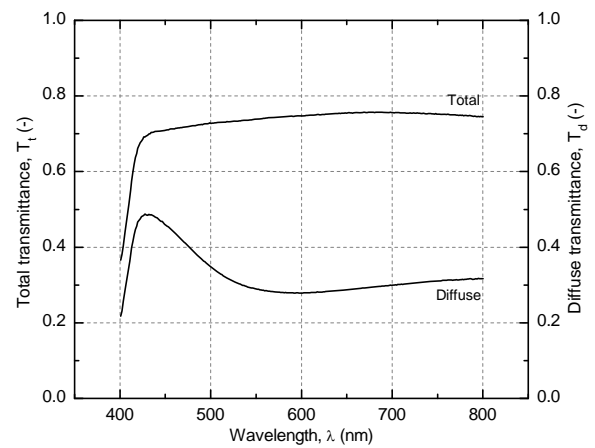


Figure C.4. Total and diffuse transmittance of GFRP specimen 1230UD-L.

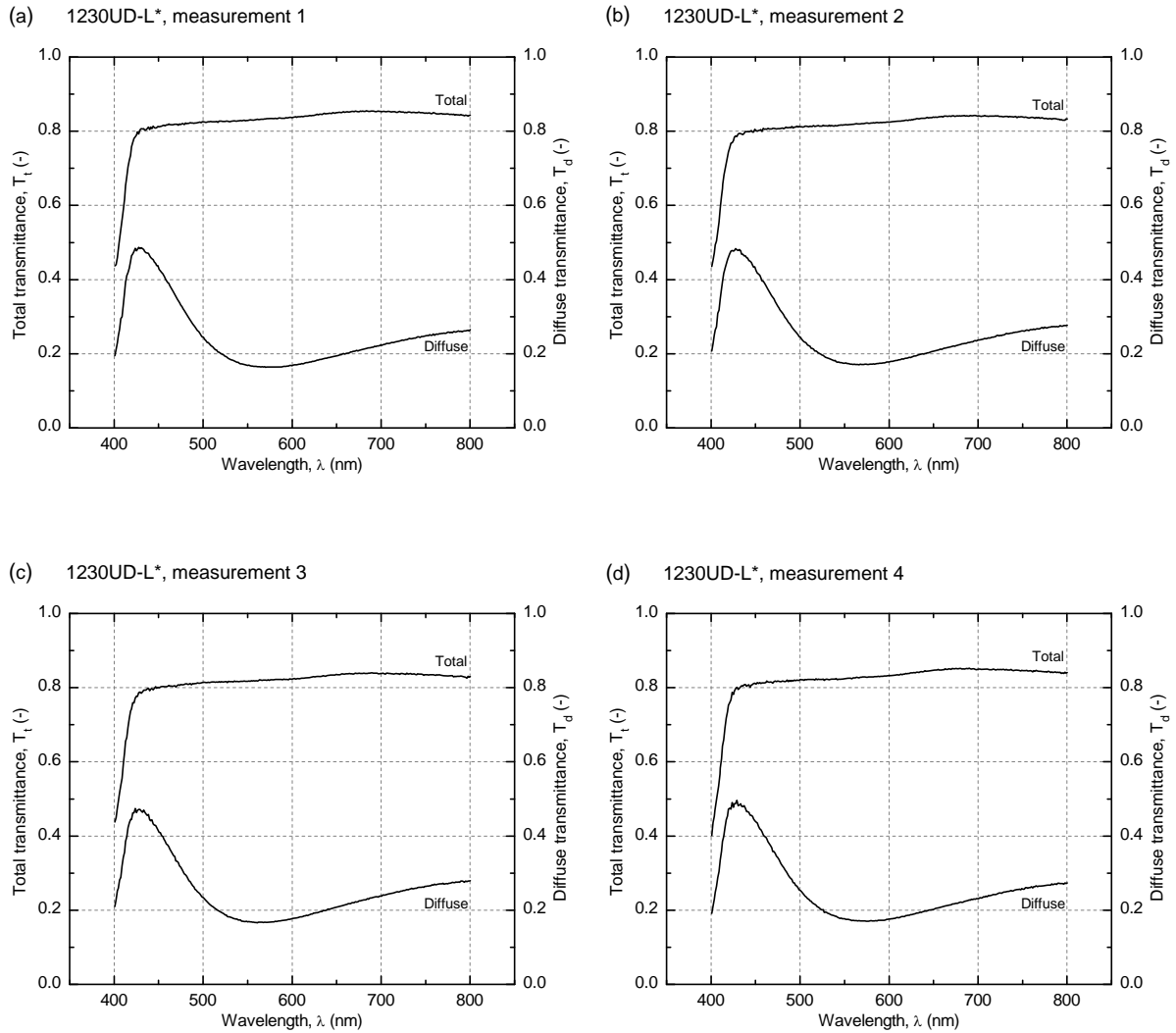
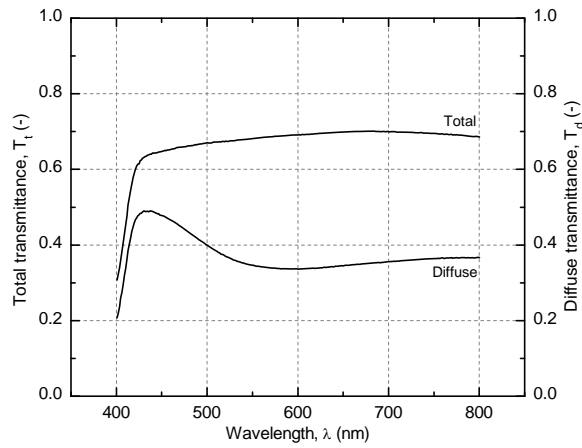
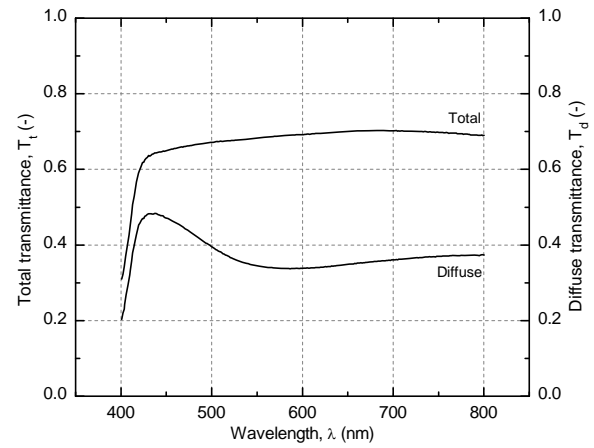


Figure C.5. Total and diffuse transmittance of GFRP specimen 1230UD-L*.

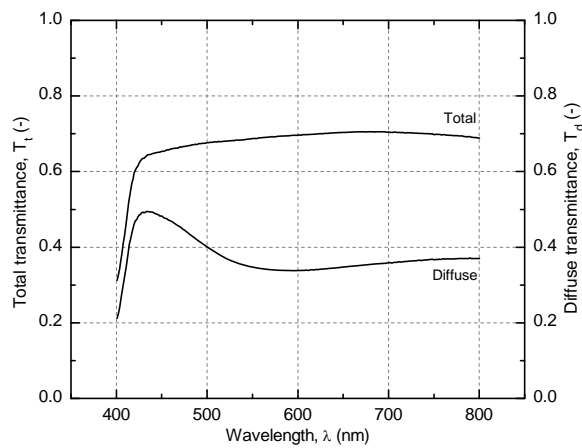
(a) 1640UD-L, measurement 1



(b) 1640UD-L, measurement 2



(c) 1640UD-L, measurement 3



(d) 1640UD-L, measurement 4

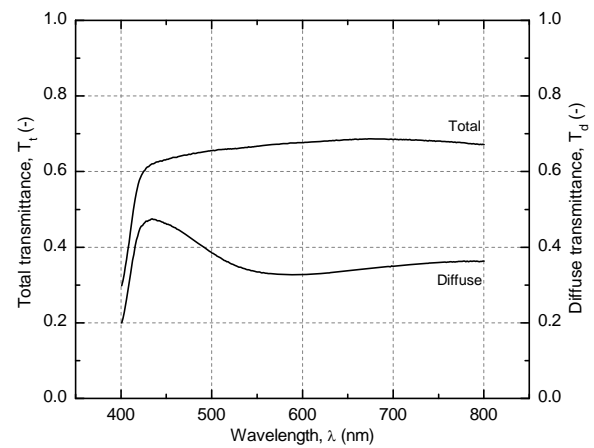
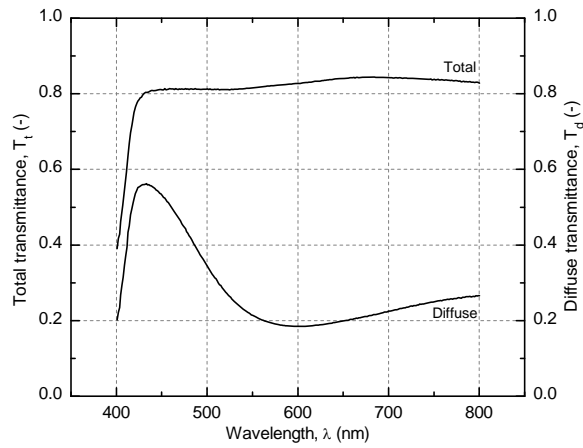
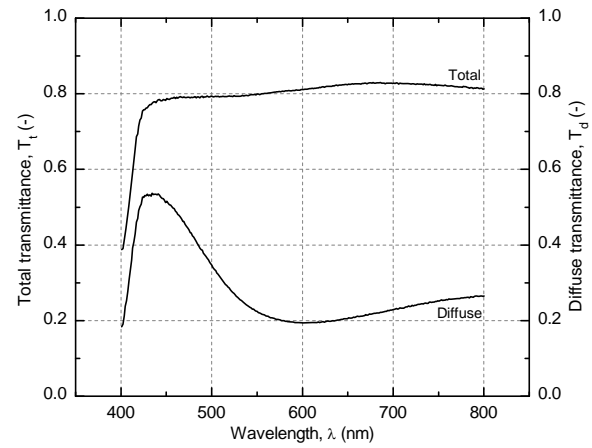


Figure C.6. Total and diffuse transmittance of GFRP specimen 1640UD-L.

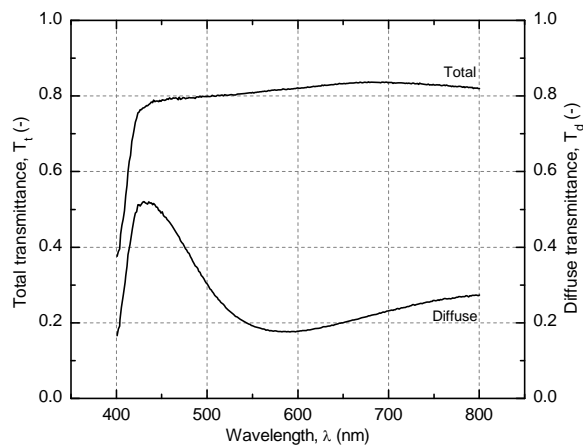
(a) 1640UD-L*, measurement 1



(b) 1640UD-L*, measurement 2



(c) 1640UD-L*, measurement 3



(d) 1640UD-L*, measurement 4

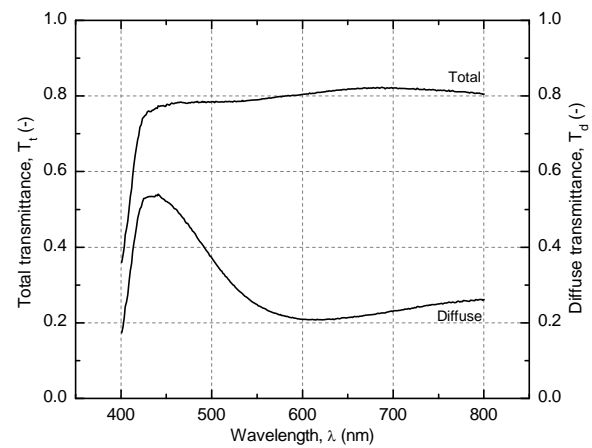
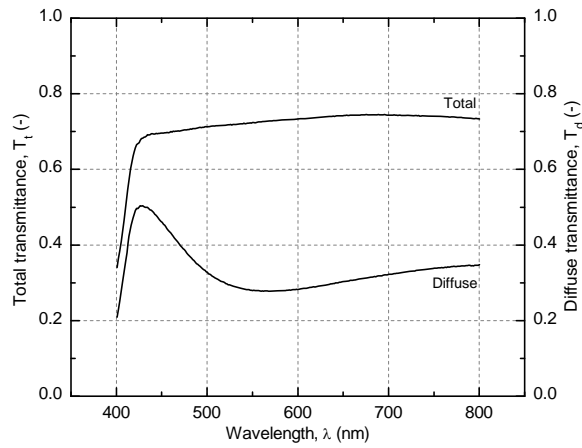
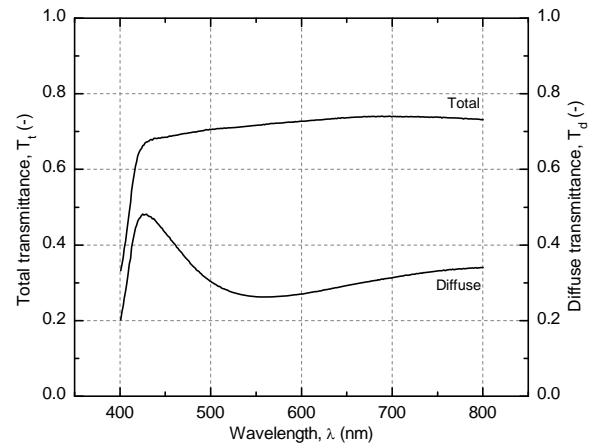


Figure C.7. Total and diffuse transmittance of GFRP specimen 1640UD-L*.

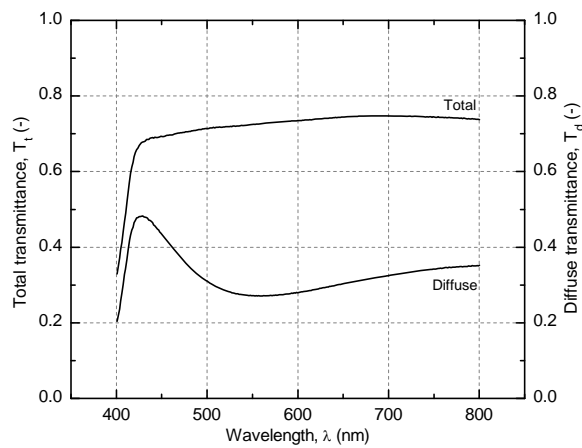
(a) 1230CP-L, measurement 1



(b) 1230CP-L, measurement 2



(c) 1230CP-L, measurement 3



(d) 1230CP-L, measurement 4

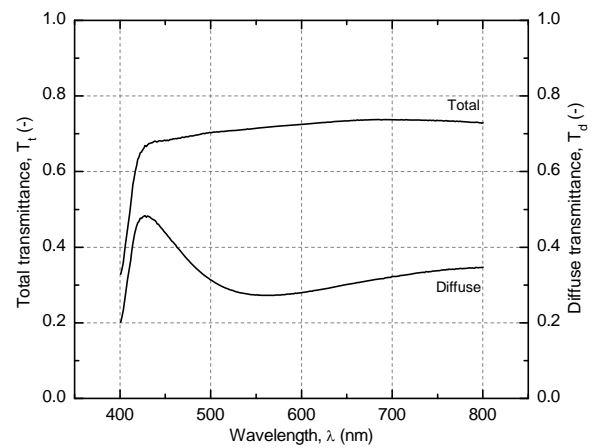
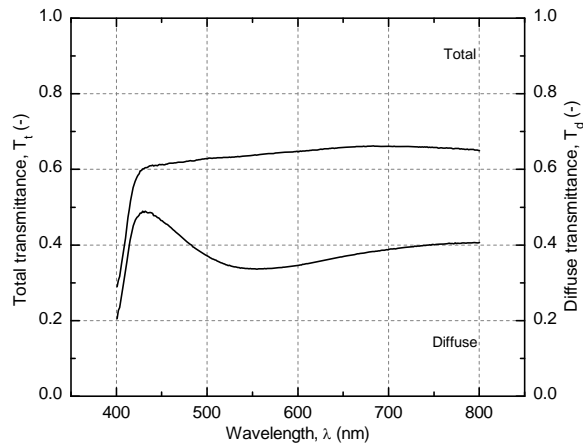
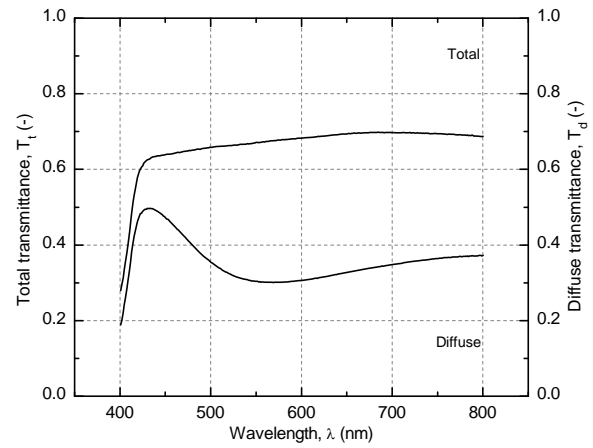


Figure C.8. Total and diffuse transmittance of GFRP specimen 1230CP-L.

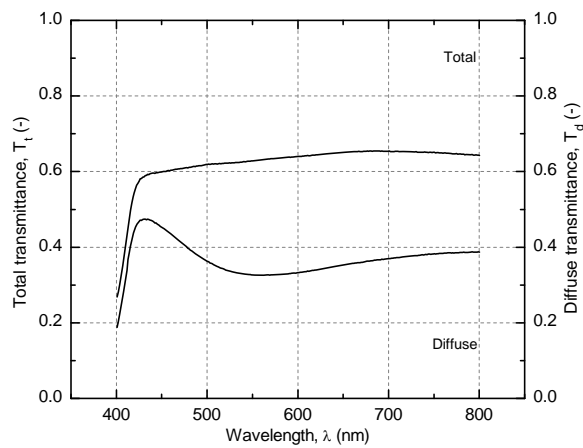
(a) 1640CP-L, measurement 1



(b) 1640CP-L, measurement 2



(c) 1640CP-L, measurement 3



(d) 1640CP-L, measurement 4

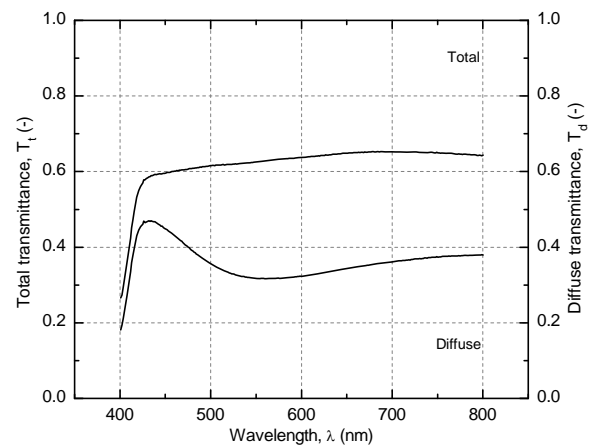
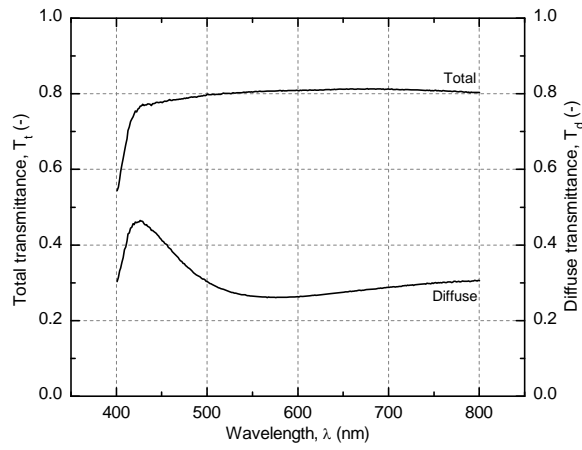


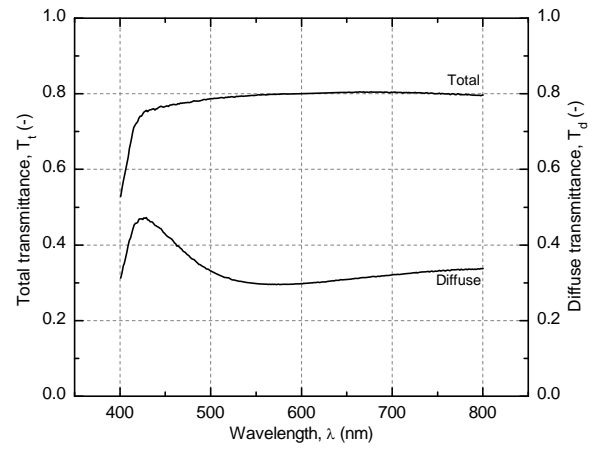
Figure C.9. Total and diffuse transmittance of GFRP specimen 1640CP-L.

C.2.1.2. Series M

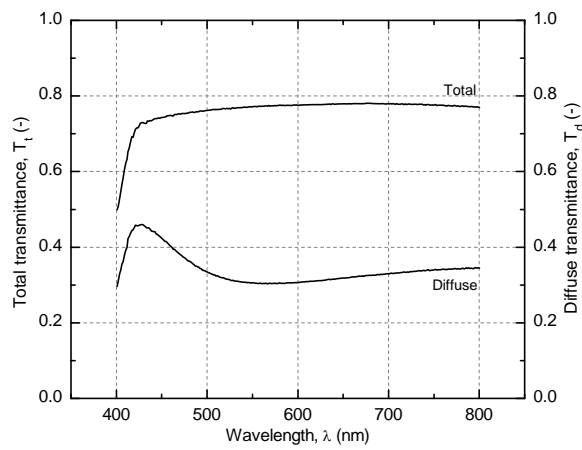
(a) 820UD-M, measurement 1



(b) 820UD-M, measurement 2



(c) 820UD-M, measurement 3



(d) 820UD-M, measurement 4

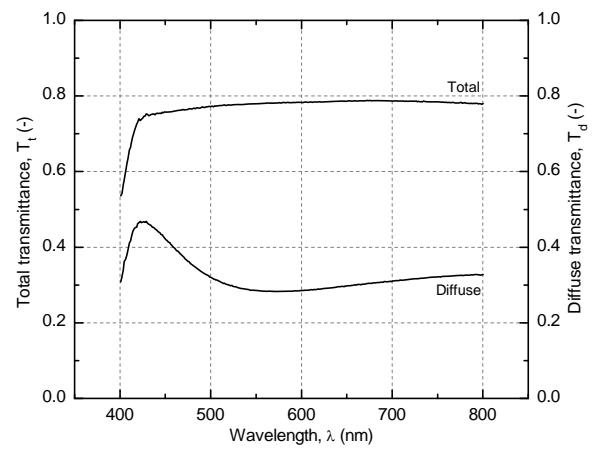
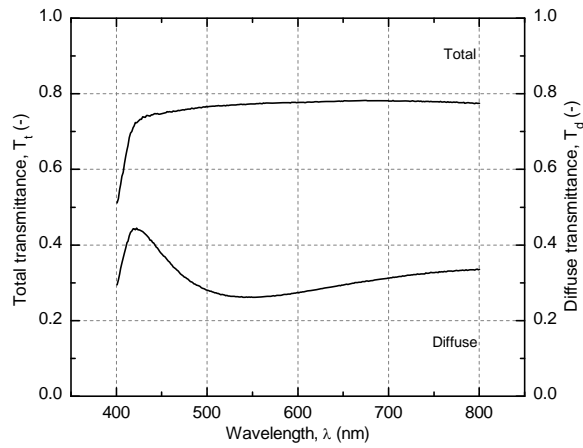
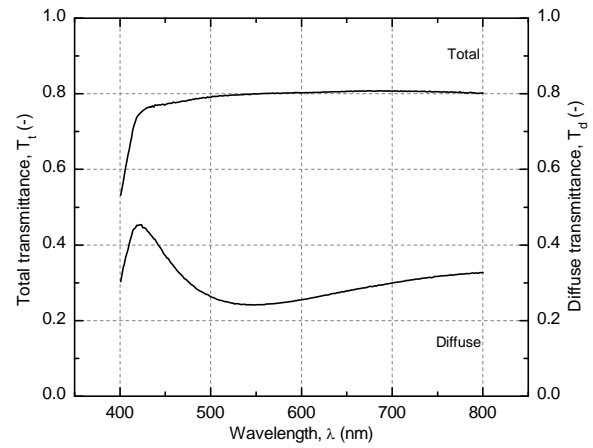


Figure C.10. Total and diffuse transmittance of GFRP specimen 820UD-M (vacuum fabrication).

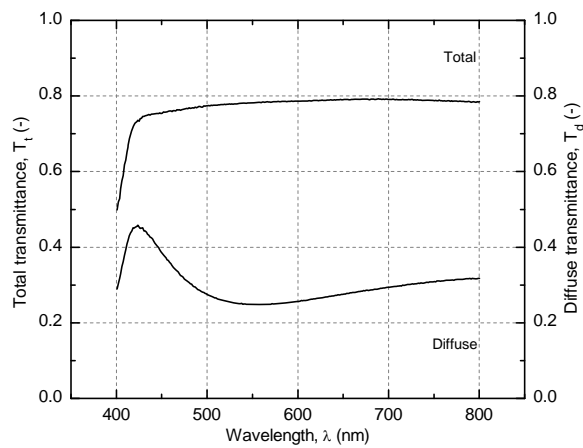
(a) 820CP-M, measurement 1



(b) 820CP-M, measurement 2



(c) 820CP-M, measurement 3



(d) 820CP-M, measurement 4

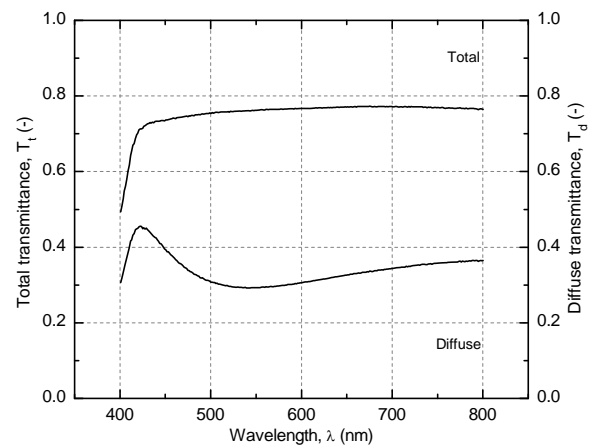
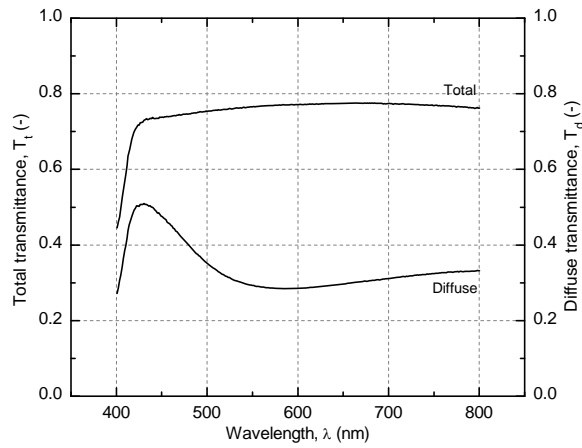
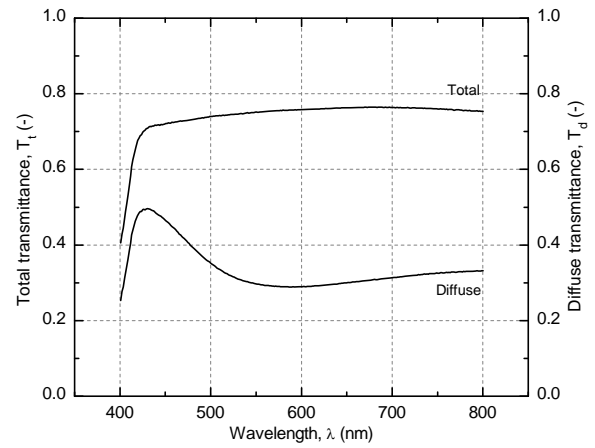


Figure C.11. Total and diffuse transmittance of GFRP specimen 820CP-M (vacuum fabrication).

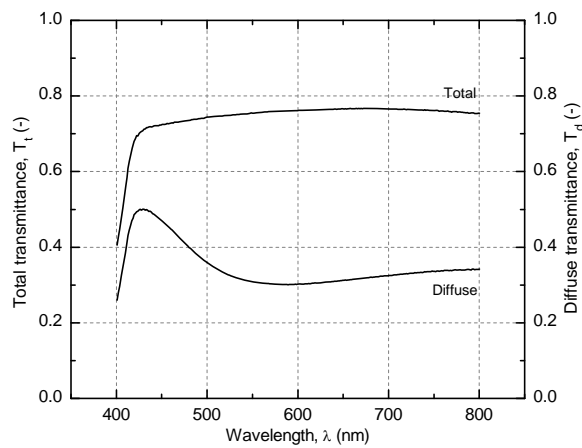
(a) 1230UD-M, measurement 1



(b) 1230UD-M, measurement 2



(c) 1230UD-M, measurement 3



(d) 1230UD-M, measurement 4

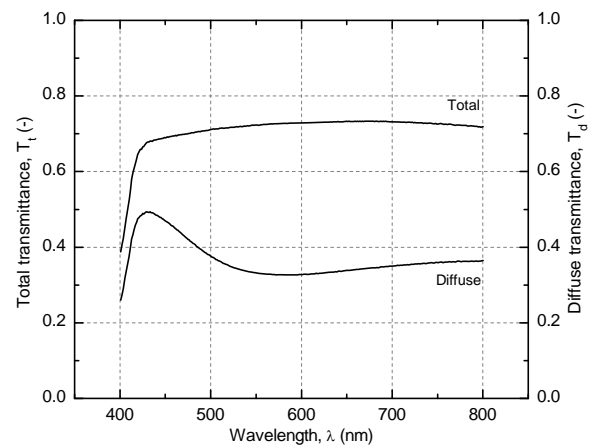
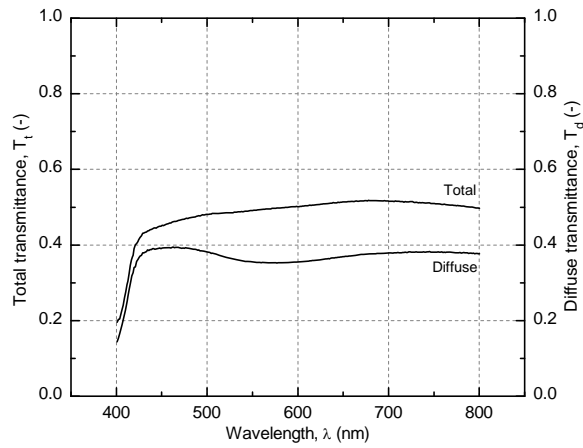
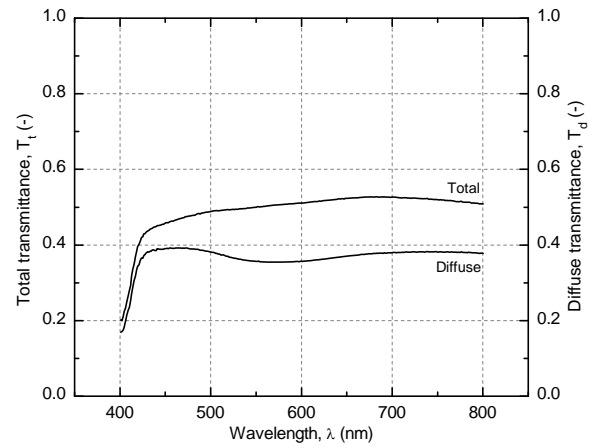


Figure C.12. Total and diffuse transmittance of GFRP specimen 1230UD-M.

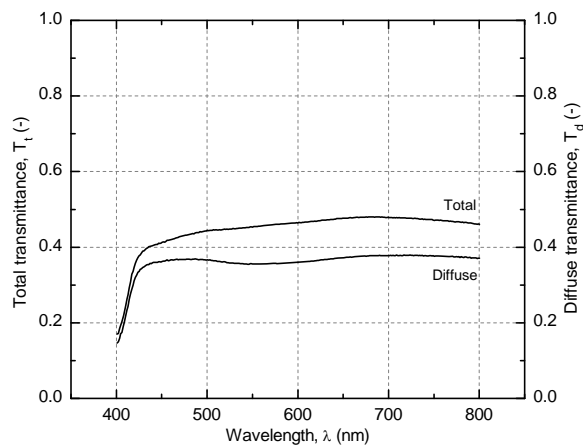
(a) 3280UD-M, measurement 1



(b) 3280UD-M, measurement 2



(c) 3280UD-M, measurement 3



(d) 3280UD-M, measurement 4

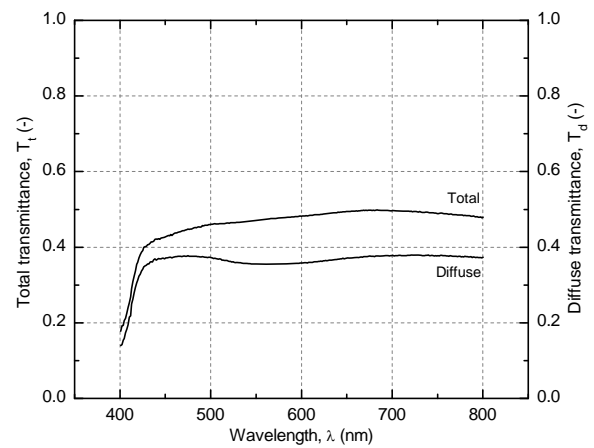
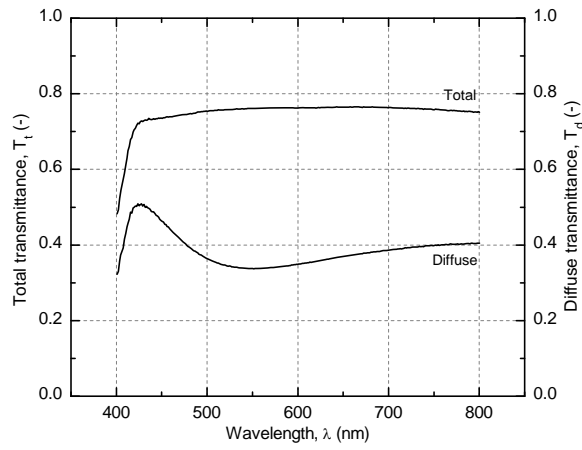


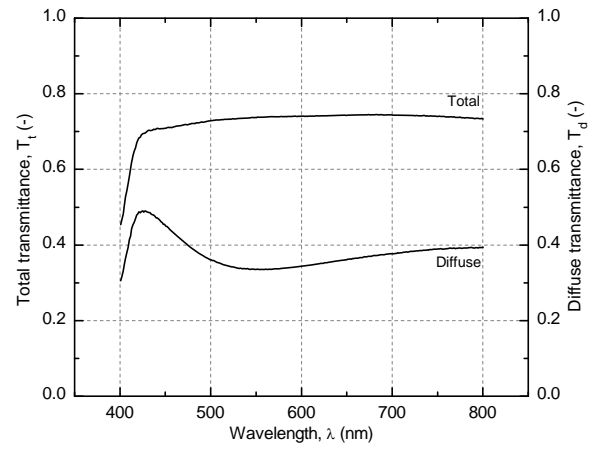
Figure C.13. Total and diffuse transmittance of GFRP specimen 3280UD-M.

C.2.1.3. Series H

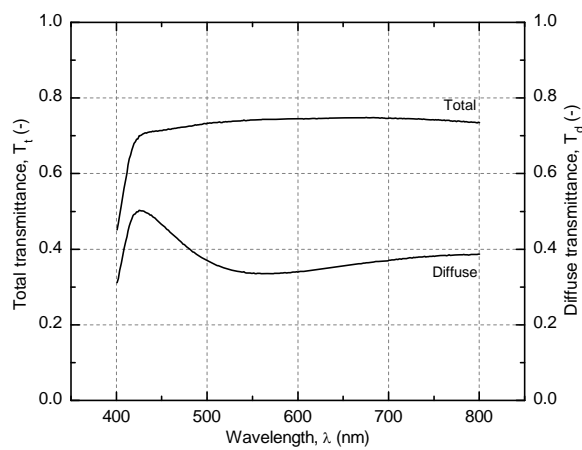
(a) 1230UD-H, measurement 1



(b) 1230UD-H, measurement 2



(c) 1230UD-H, measurement 3



(d) 1230UD-H, measurement 4

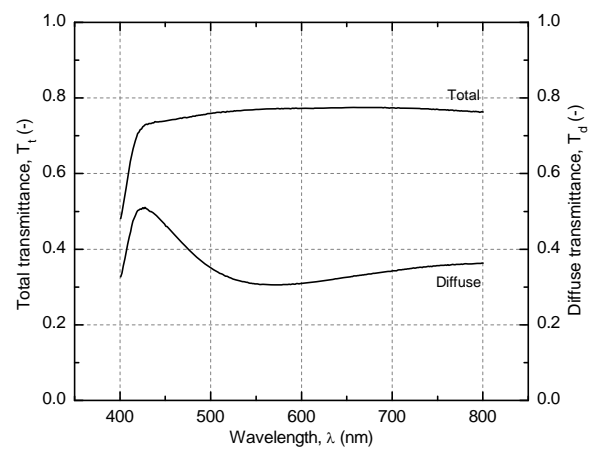
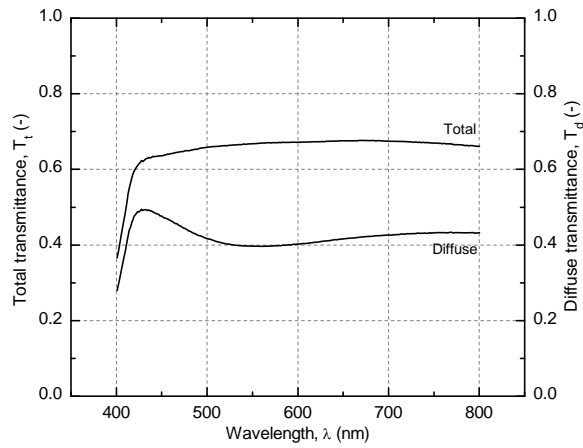
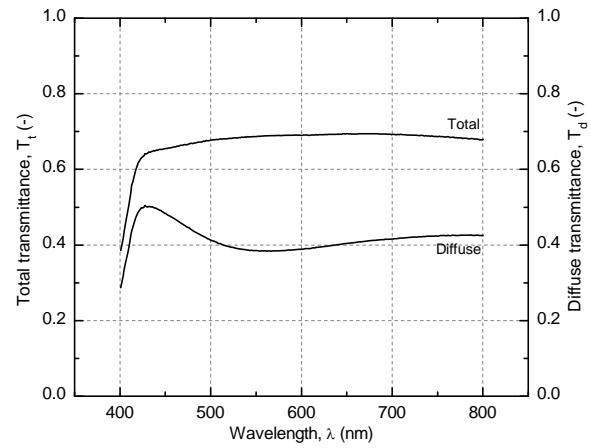


Figure C.14. Total and diffuse transmittance of GFRP specimen 1230UD-H.

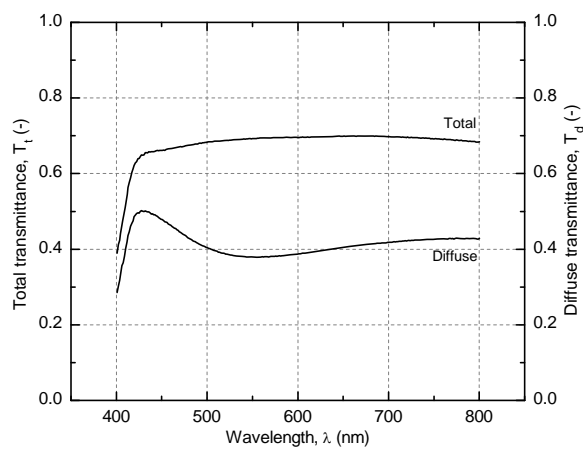
(a) 1640UD-H, measurement 1



(b) 1640UD-H, measurement 2



(c) 1640UD-H, measurement 3



(d) 1640UD-H, measurement 4

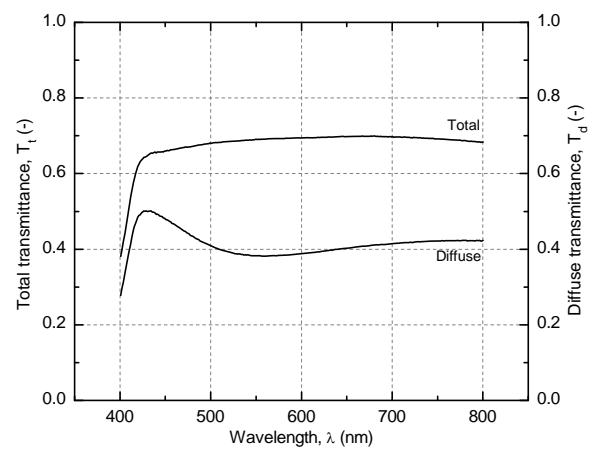
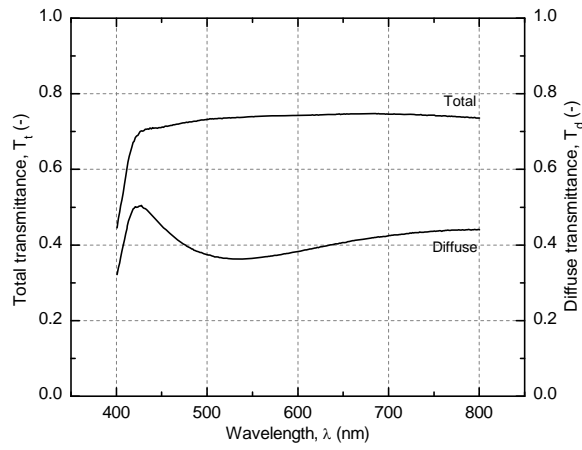
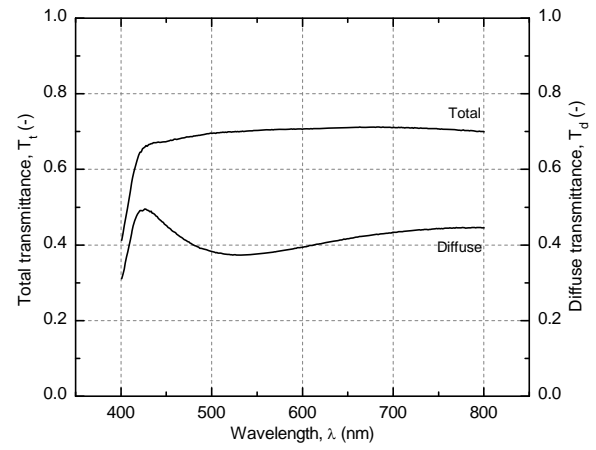


Figure C.15. Total and diffuse transmittance of GFRP specimen 1640UD-H.

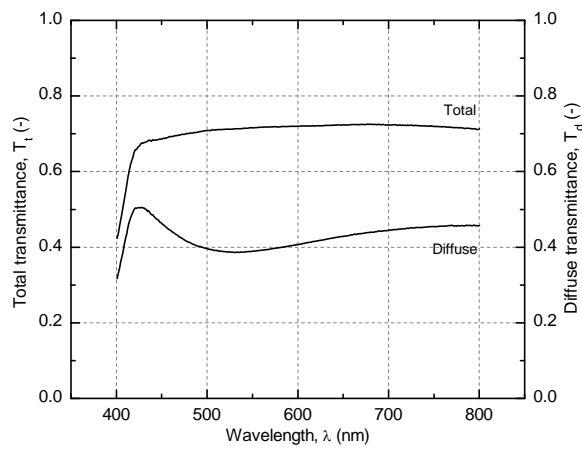
(a) 1230CP-H, measurement 1



(b) 1230CP-H, measurement 2



(c) 1230CP-H, measurement 3



(d) 1230CP-H, measurement 4

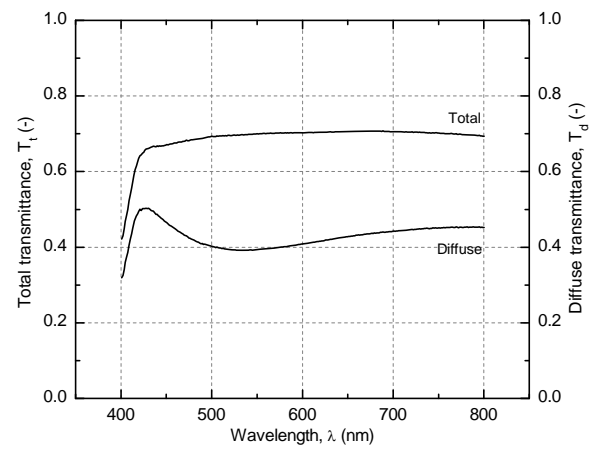
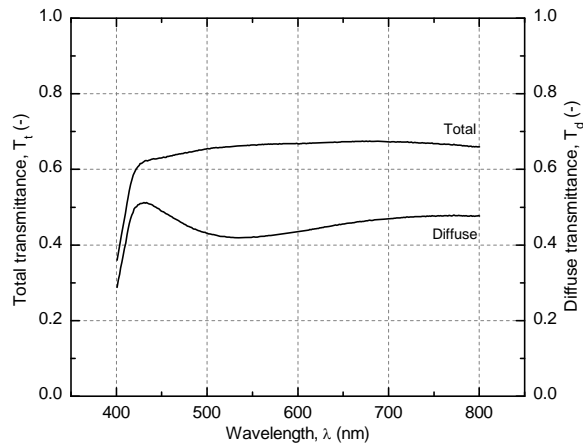
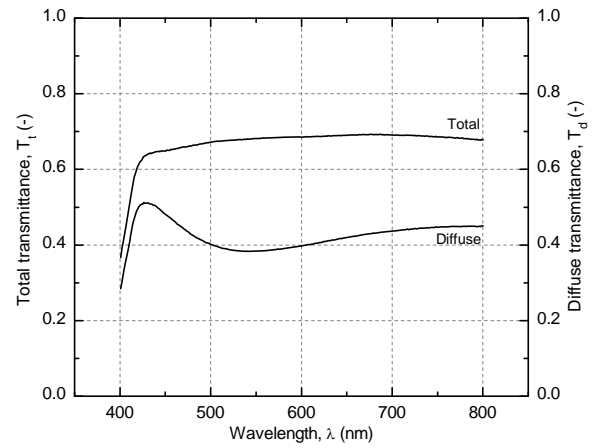


Figure C.16. Total and diffuse transmittance of GFRP specimen 1230CP-H.

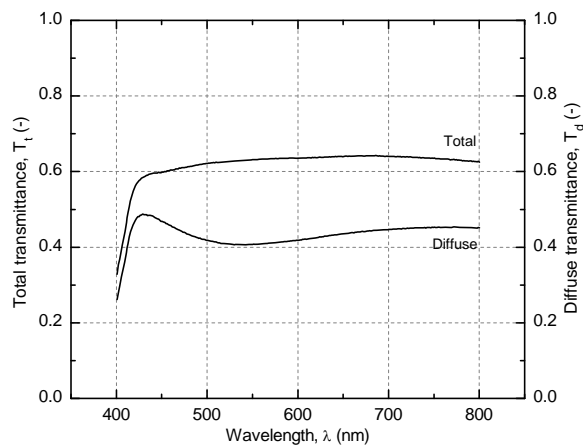
(a) 1640CP-H, measurement 1



(b) 1640CP-H, measurement 2



(c) 1640CP-H, measurement 3



(d) 1640CP-H, measurement 4

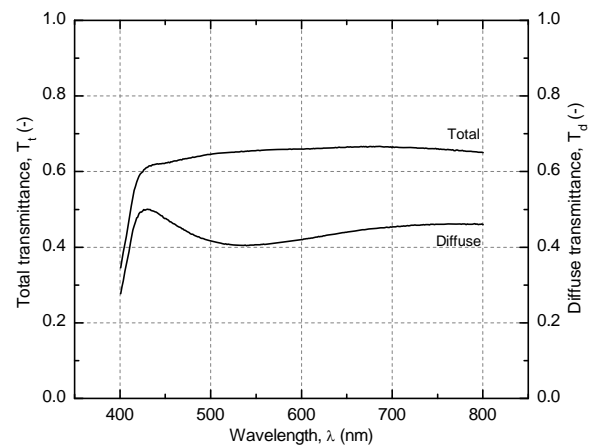


Figure C.17. Total and diffuse transmittance of GFRP specimen 1640CP-H.

C.2.1.4. Pure resin

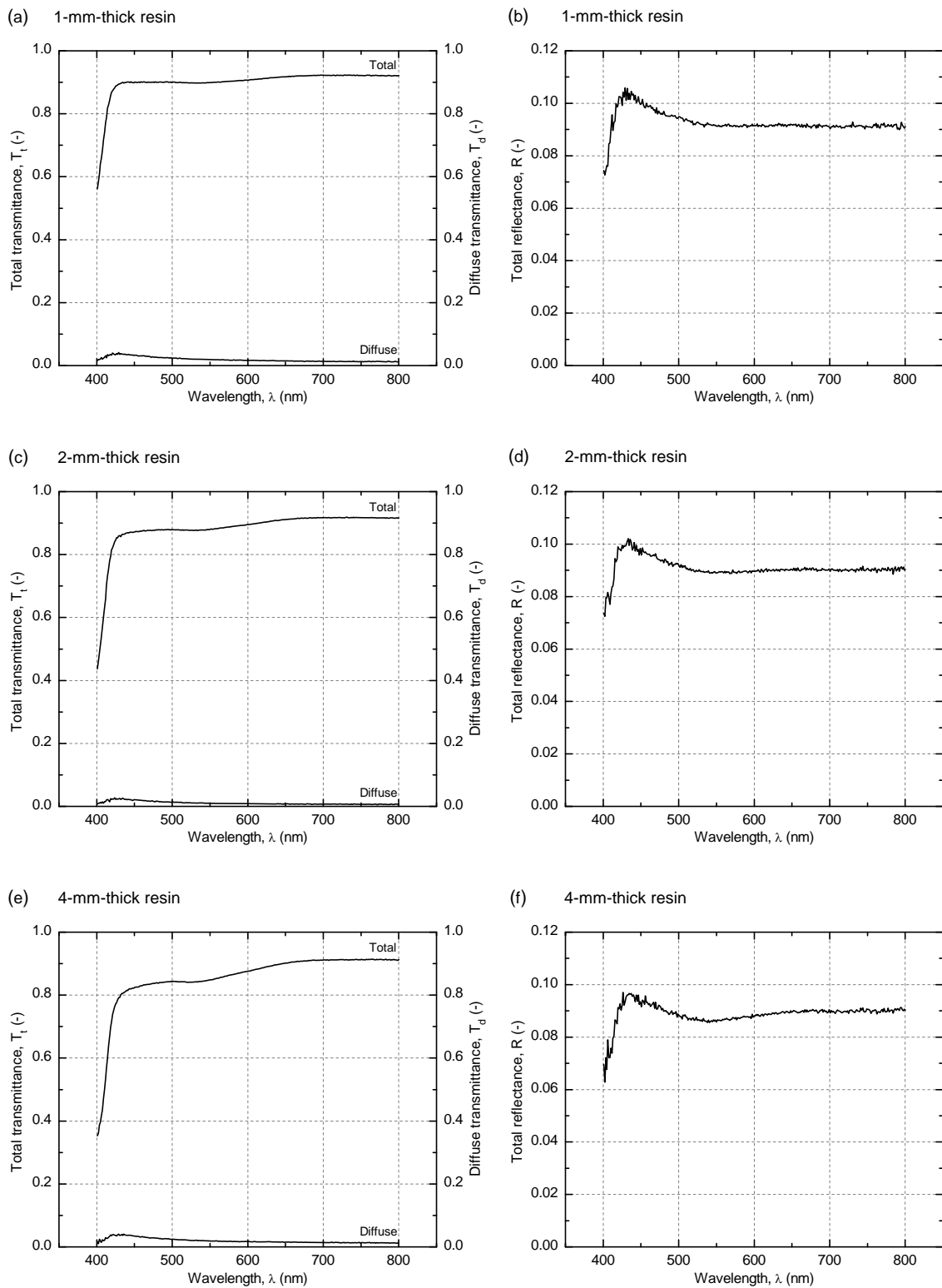
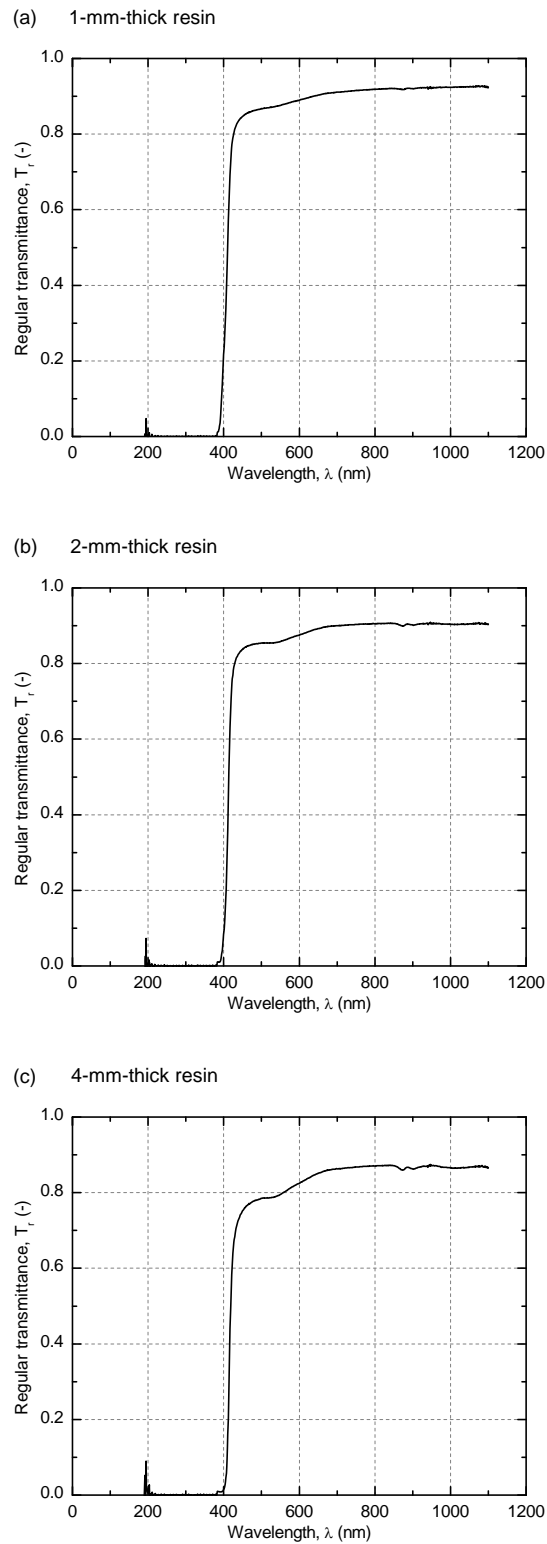


Figure C.18. Total and diffuse transmittance and total reflectance of pure resin specimens.

C.2.2. Measurements performed with the Perkin Elmer Lambda 2 spectrophotometer**Figure C.19.** Regular transmittance of pure resin specimens.

The results of the light transmittance measurements performed on the resin specimens indicated that:

1. The resin was UV-stabilized, i.e. the resin was opaque to the radiation below 380 nm (see Figure C.19).
2. The regular transmittance measurements were slightly lower than the total transmittance measurements, which was attributed to two effects: 1) the low light diffusion of the pure resin and 2) an imperfect orthogonality between the specimen plane and the aligned source and sensor cables shown in Figure C.1(b) – which could refract part of the incident light out of the sensor.

D Solar radiation results

D.1. Introduction

The PV modules with three serial connected a-Si PV cells encapsulated in GFRP – with reinforcement weight, w , of the upper encapsulant ranging from 410 to 3280 g/m², (see Figure A.16) – and the reference non-encapsulated PV module were subjected to a solar flash of 1000 W/m² in Flexcell's solar simulator (see Figure D.1). The I - V curves, i.e. combinations of current I and voltage V generated from sunlight, were measured and are reported in Figure D.2.

For all the reinforcement weights, the upper GFRP encapsulant of the modules had a smooth top surface resulting from the plastic foil used in the fabrication process and removed after curing as explained in Appendix A. However a PV module with $w = 410$ g/m² in the upper encapsulant was fabricated with a rough top surface (no plastic foil was used in the fabrication process) and the corresponding I - V curve is presented in Figure D.2(b).

The PV module with $w = 1640$ g/m² and unidirectional (UD) fiber architecture in the upper encapsulant was exposed to a damp heat experiment (temperature of 85 °C and humidity of 85%) during five days.¹ The I - V curves measured before and after this experiment are shown in Figure D.2(e). The PV module with $w = 1230$ g/m² and cross-ply (CP) fiber architecture in the upper encapsulant did not generate any current after fabrication and it was concluded that the cells were damaged during the encapsulation process. This module was also exposed to a damp heat experiment (for 14 days) after sealing the edges and protecting the top surface with a transparent 100- μ m-thickness fluoropolymer film. Both modules exhibited significant yellowing after these experiments (see Figure A.16(e) and (g)).

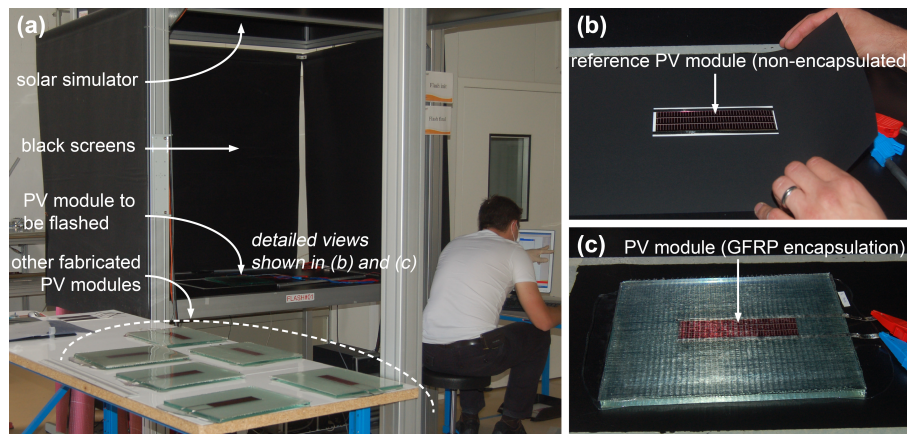


Figure D.1. (a) Solar simulator set-up and detailed views of (b) reference non-encapsulated PV module and (c) PV module with solar cells encapsulated in GFRP.

D.2. Solar radiation results

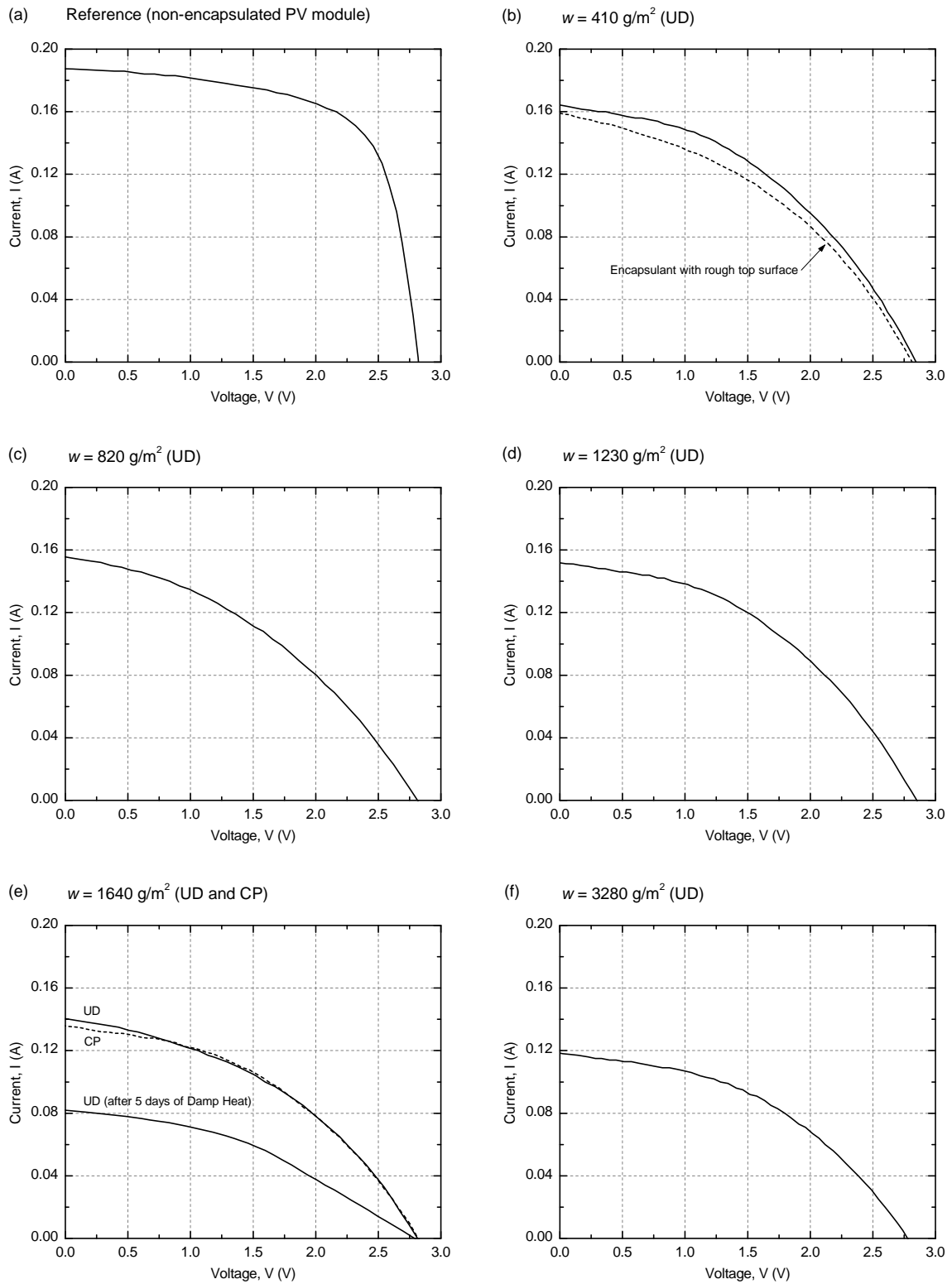


Figure D.2. I-V curves of (a) reference PV module and (b-f) PV modules with reinforcement weights in the upper encapsulant ranging from 410 g/m^2 to 3280 g/m^2 .

The measured I - V curves are analyzed in the following:

1. The steeper slope for $I = 0$ and the flatter slope for $V = 0$ of the reference I - V curve compared to the corresponding slopes of the encapsulated cells indicate that the series and shunt resistances associated with the cells could have been slightly damaged during the hand lay-up encapsulation. However short circuit currents are not affected by the shunt resistance and are only reduced by significantly damaged series resistance.² For the optical analyses of this research the effect of the series resistance on the short circuit currents was disregarded.
2. The short circuit current of the PV module with $w = 1640 \text{ g/m}^2$ (UD) in the upper encapsulant was initially 140 mA and decreased to 82 mA after five days of damp heat experiment which represents a reduction of around 40% (also in terms of electrical power generation) and was attributed to the significant yellowing – and therefore reduction of light transmittance – of the GFRP encapsulant (see Figure A.16(e)). However, the output power must not decrease by more than 5% after 1000 h (42 days) of damp heat experiment according to the requirements of the CEI Standard 61646.¹ More research is therefore required to investigate the long-term stability of transparent resins subjected to high temperatures (85 °C) and humidity (85%).
3. The short circuit currents of the PV modules with $w = 410 \text{ g/m}^2$ in the GFRP upper encapsulant were 159 mA (for rough upper surface) and 164 mA (for smooth upper surface). The total light transmittance of the GFRP encapsulant with rough surface was therefore 3% lower than that of the encapsulant with a smooth surface, which was attributed to a higher amount of reflections on the surface of the former.

D.3. References

1. CEI Standard 61646. *Thin-film terrestrial photovoltaic (PV) modules – Design qualification and type approval*. Geneva, Switzerland: International Electrotechnical Commission, 2008.
2. Wenham SR, Green MA, Watt ME et al. *Applied photovoltaics*, 2nd ed. London: Earthscan, 2008.

E Immersion liquids and refractive indices

E.1. Introduction

To experimentally confirm the refractive index of the E-glass fibers (1.56), roving fibers from the Tissa fabric were immersed in beakers containing different transparent liquids with well-known refractive indices and were lightened with white and monochromatic 555-nm-wavelength light. The objective was to investigate whether the fibers visually disappeared or not when immersed in a liquid with the same refractive index as the fibers.

Fibers were immersed in water and three immersion liquids, IL, from Cargille Laboratories Inc. (New Jersey, United States). The white light illumination of the fibers was performed under the normal lighting conditions of the workroom and the set-up shown in Figure E.1 was developed for illuminating the fibers with monochromatic light in darkroom conditions. The refractive indices at 555-nm wavelength, n_{555} , of the different liquids at 25 °C – temperature at which experiments were performed (see Figure E.2) – are given in Table E.1.

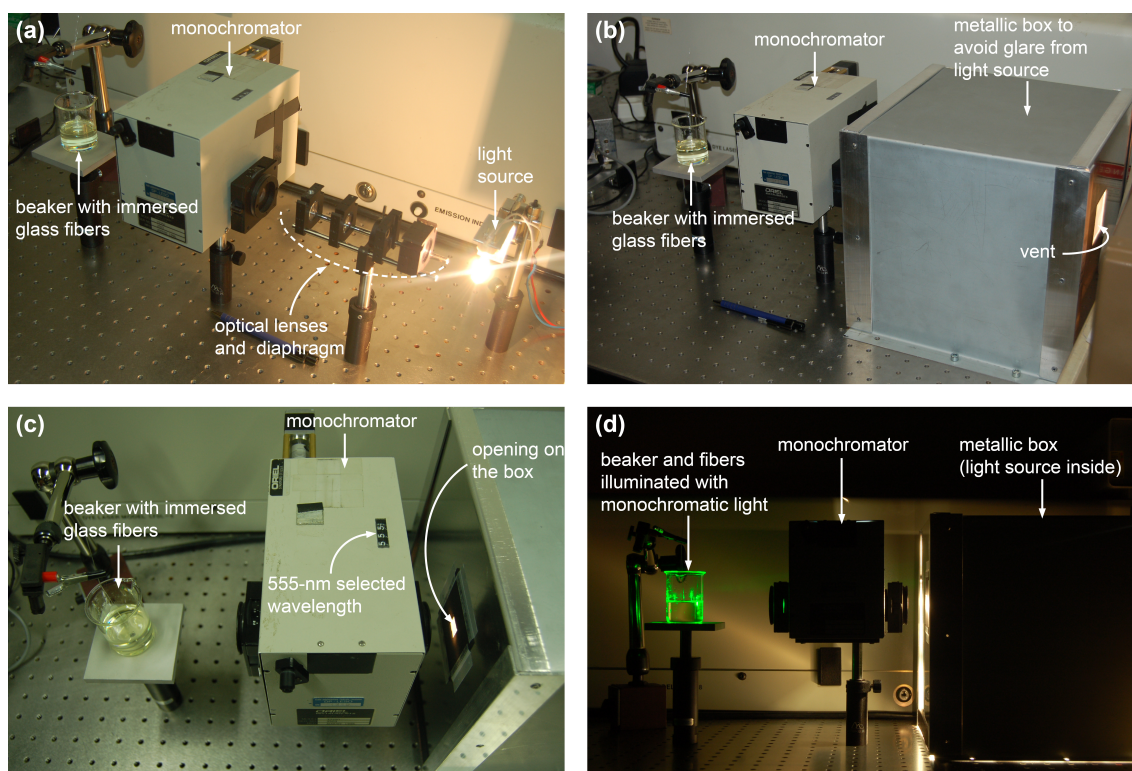
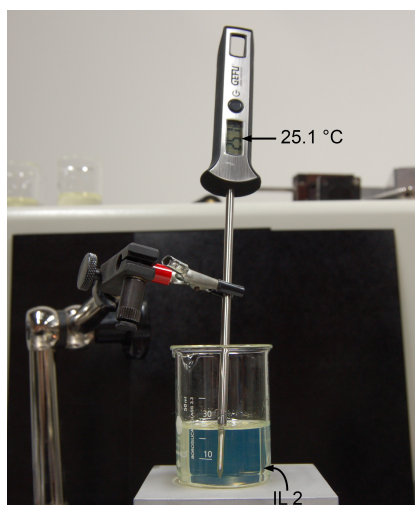


Figure E.1. Set-up for illuminating fibers with monochromatic (555-nm-wavelength) light.

Table E.1. Refractive indices at 555 nm and 25 °C of water and three immersion liquids from Cargille Laboratories Inc.

Liquid	water	IL 1	IL 2	IL 3
n_{555} (-)	1.33	1.50	1.56	1.60

**Figure E.2.** Measurement of temperature in immersion liquid IL 2.

E.2. Immersion liquid images

Detailed views of the glass fibers immersed in water and the three different immersion liquids are given in Figure E.3. In the case of white light illumination (lighting conditions of the workroom) fibers were clearly visible when immersed in the liquid with $n_{555} = 1.33$, almost invisible when immersed in liquids with $n_{555} = 1.50$ and $n_{555} = 1.56$, and slightly visible when immersed in liquid with $n_{555} = 1.60$ (see Figure E.3) indicating that the refractive index of fibers was in the range of 1.33 to 1.60.

In the case of monochromatic illumination at 555-nm wavelength fibers became more visible than for white light illumination. The concentrated beam of light emanating from the monochromator and incident on the beaker seemed to increase the sensitivity of the photo camera (and also of the human eye) to distinguish the fibers from the surrounding liquid. However some regions of the fibers were invisible when immersed in the liquid IL 2 (see Figure E.3(f)) indicating that their refractive index was close to $n_{555} = 1.56$. The fact that fibers could visually appear and disappear was attributed to the effect of the silane sizing on the fiber surfaces – silane components have refractive indices of between 1.39 and 1.50.¹ Reflections could therefore increase where more sizing was concentrated.

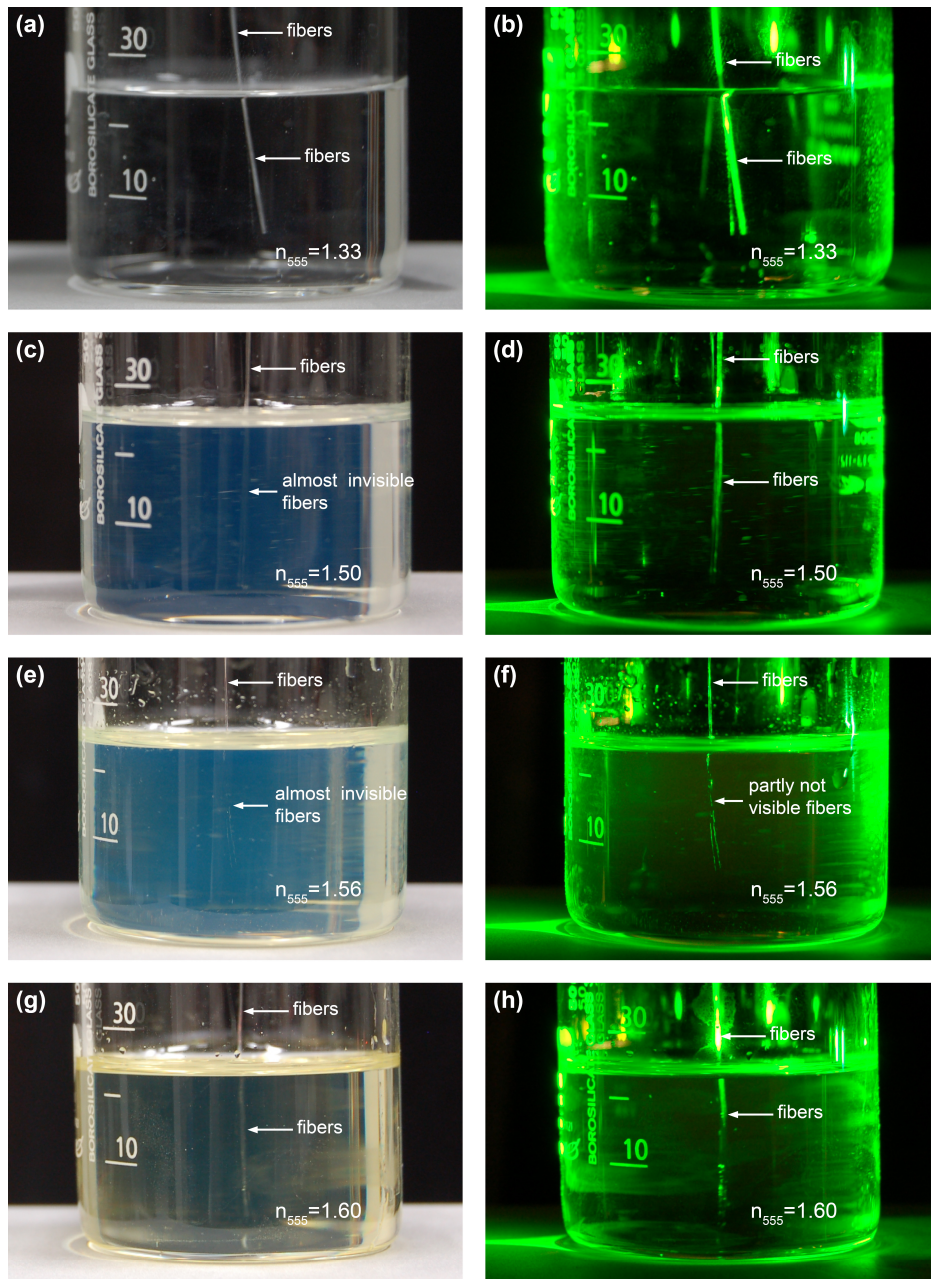


Figure E.3. Detailed views of fibers immersed in (a-b) water, (c-d) IL 1, (e-f) IL 2 and (g-h) IL 3 (left column corresponds to white light illumination and right column to 555-nm light illumination).

E.3. References

1. Shin-Etsu company. Product information at:

http://www.silicone.jp/e/catalog/pdf/SilaneCouplingAgents_e.pdf (accessed 30 July 2014).

F Goniophotometric results

F.1. Introduction

The goniophotometric measurements performed in this research are presented below and the set-up is described in Chapter 4. In order to validate the use of the normalized voltages for quantifying the light diffusion, the linearity between the voltage generated by the photodiode and the radiation reaching the photodiode had to be checked. For this purpose, the radiation of the source of light was varied – and measured with a radiometer – and the voltages generated by the photodiode were recorded. The linearity between both parameters was verified for the wide range of radiation reaching the photodiode in the goniophotometric experiments.

The goniophotometric specimens are shown in Figure A.15 and were fabricated with PolyLite 420-181 unsaturated polyester resin from Reichhold Inc. (Durham, United States) and unidirectional E-glass fabrics manufactured by Tissa (Oberkulm, Switzerland) (see Figure A.15).

The major planes of light diffusion of GFRP laminates illuminated by a concentrated beam are orthogonal to the reinforced directions as explained in Chapter 4. This effect is shown for the spectrophotometric specimens 820UD-L and 1640CP-L in Figure F.1. The objective of the goniophotometric experiments was to measure the radiation scattered by GFRP specimens into planes orthogonal to the reinforced directions in order to relate the directionality of the light diffusion to the fiber architecture of the specimens.

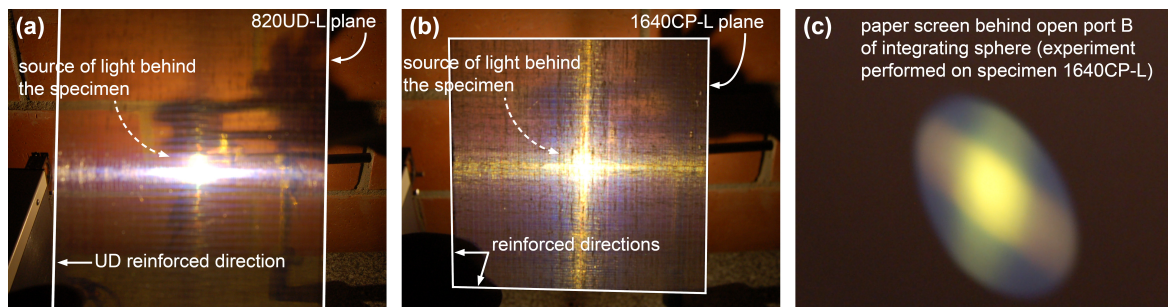
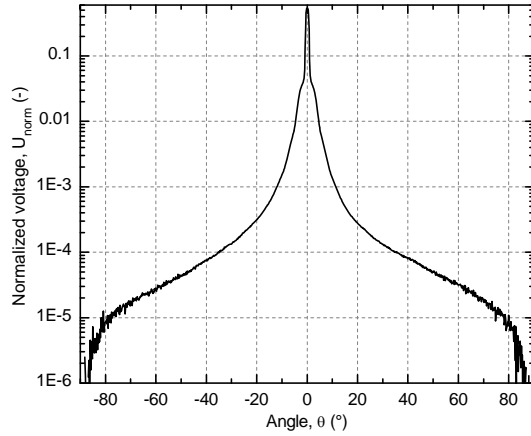


Figure F.1. Light diffused (a) horizontally by spectrophotometric specimen 820UD-L and (b-c) in two orthogonal planes by spectrophotometric specimen 1640CP-L.

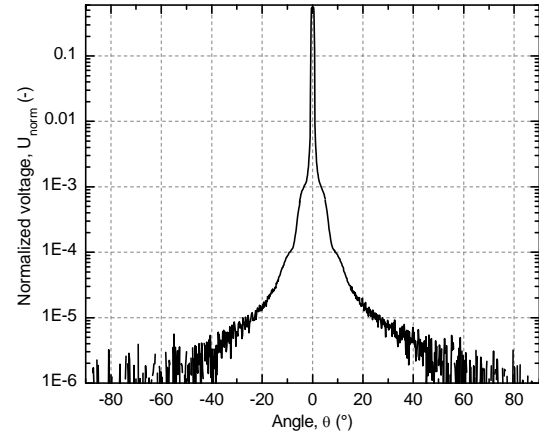
F.2. Goniophotometric results

F.2.1. Series L

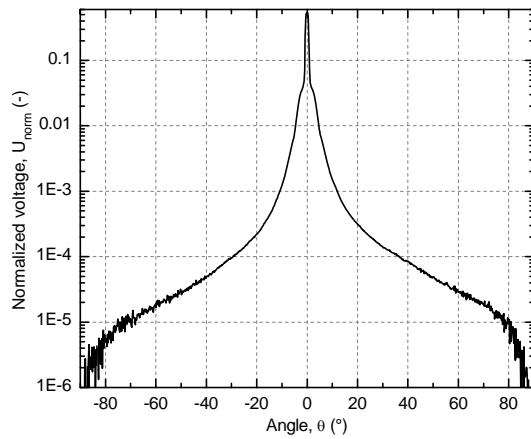
(a) 410UD-L-0, measurement 1



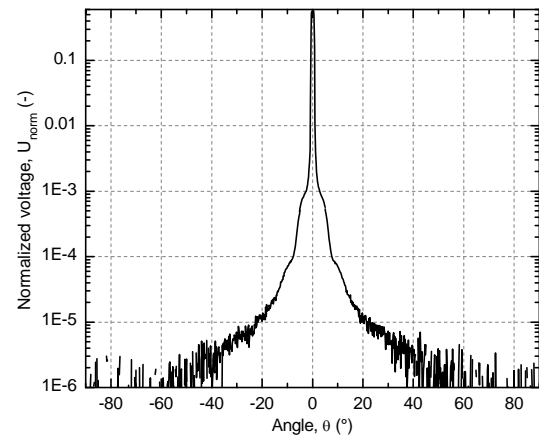
(d) 410UD-L-90, measurement 1



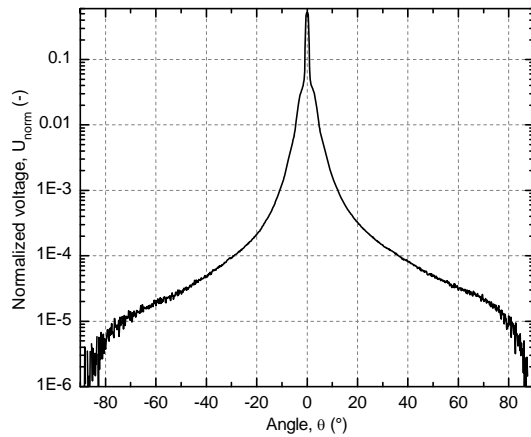
(b) 410UD-L-0, measurement 2



(e) 410UD-L-90, measurement 2



(c) 410UD-L-0, measurement 3



(f) 410UD-L-90, measurement 3

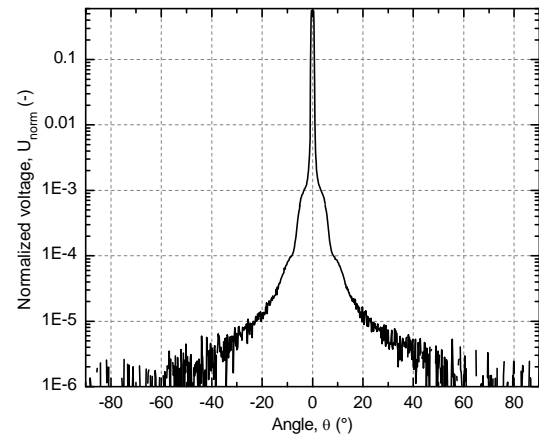
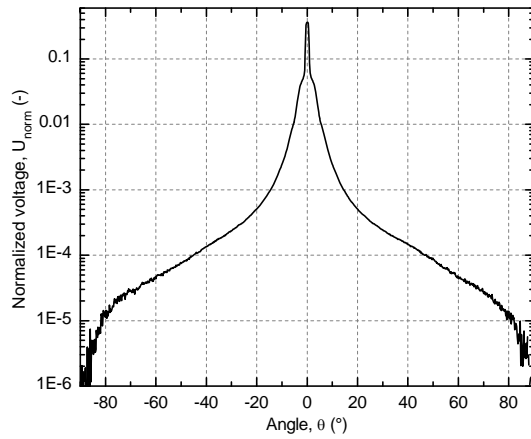
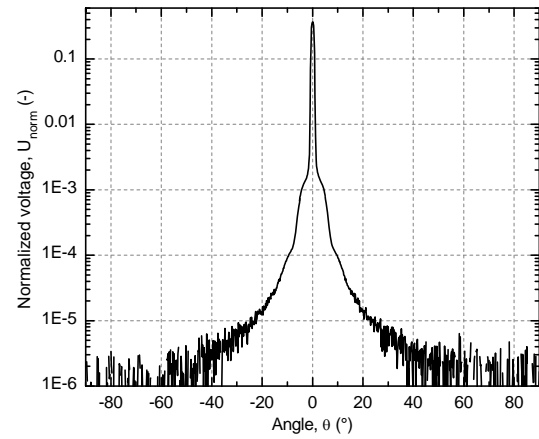


Figure F.2. Scattering diagrams of specimens 410UD-L in (a-c) 0°-direction and (d-f) 90°-direction.

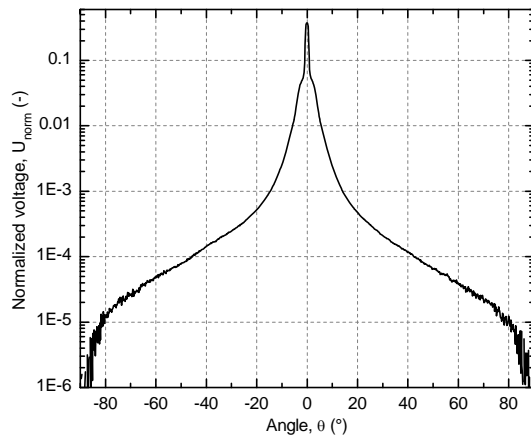
(a) 820UD-L-0, measurement 1



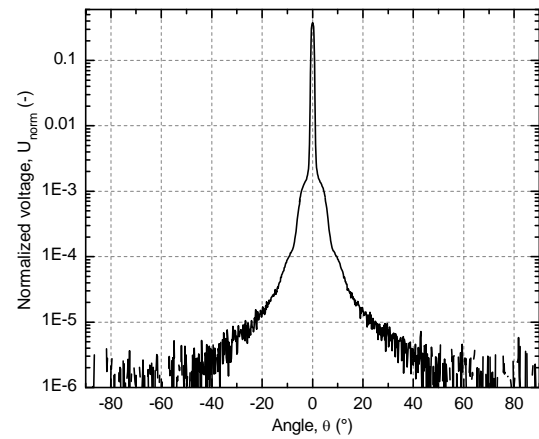
(d) 820UD-L-90, measurement 1



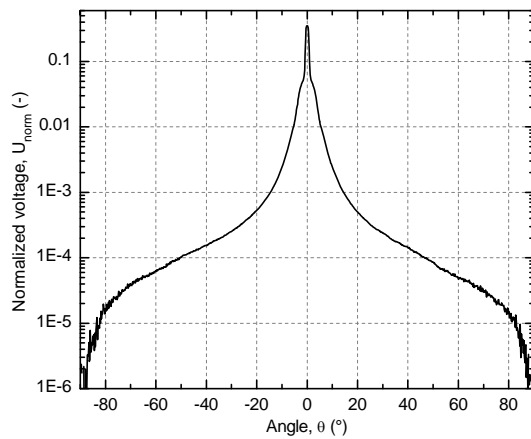
(b) 820UD-L-0, measurement 2



(e) 820UD-L-90, measurement 2



(c) 820UD-L-0, measurement 3



(f) 820UD-L-90, measurement 3

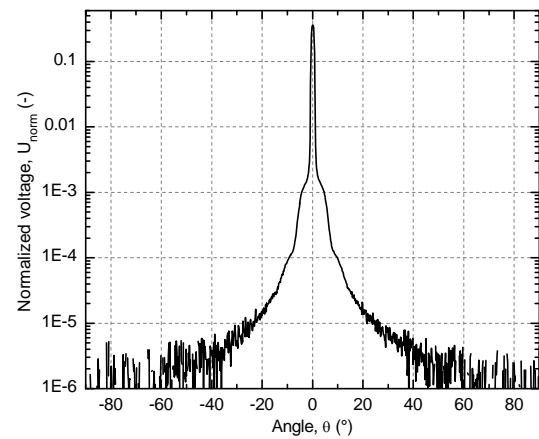
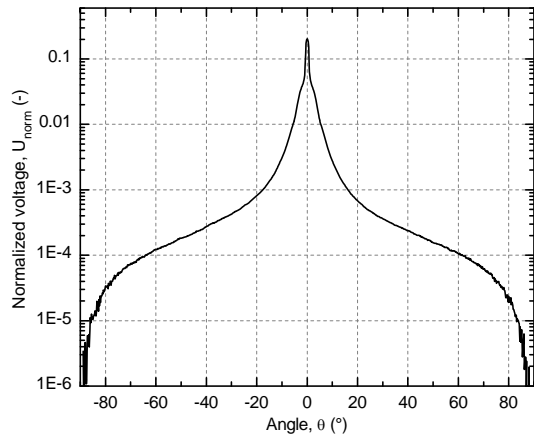
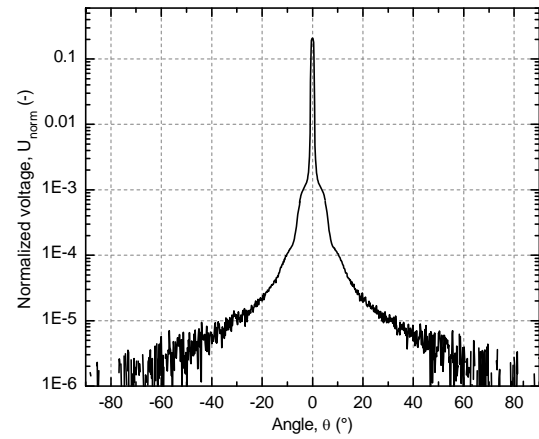


Figure F.3. Scattering diagrams of specimens 820UD-L in (a-c) 0°-direction and (d-f) 90°-direction.

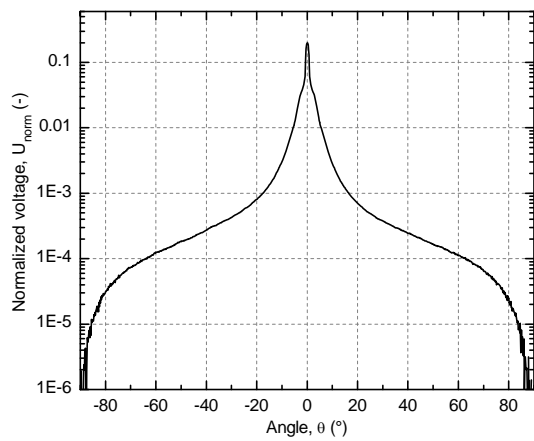
(a) 1230UD-L-0, measurement 1



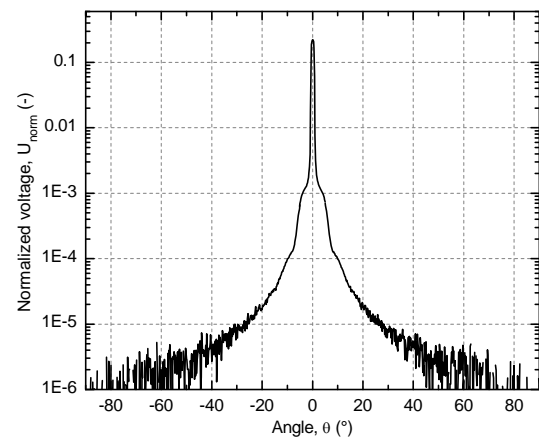
(d) 1230UD-L-90, measurement 1



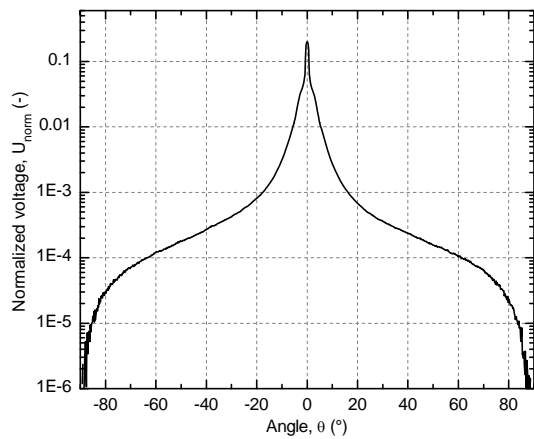
(b) 1230UD-L-0, measurement 2



(e) 1230UD-L-90, measurement 2



(c) 1230UD-L-0, measurement 3



(f) 1230UD-L-90, measurement 3

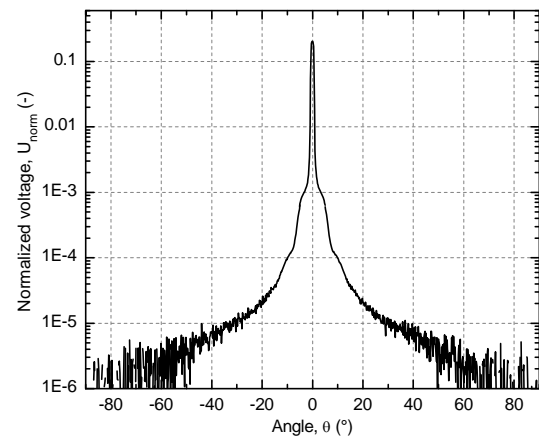
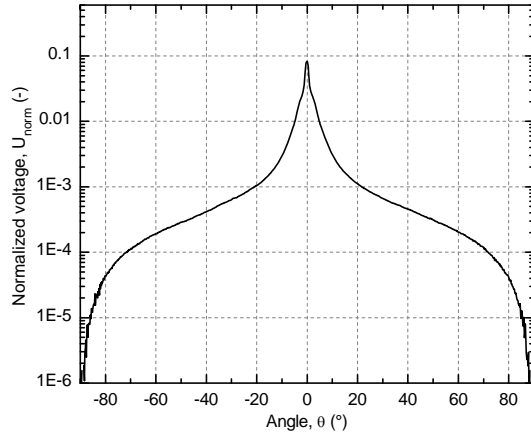
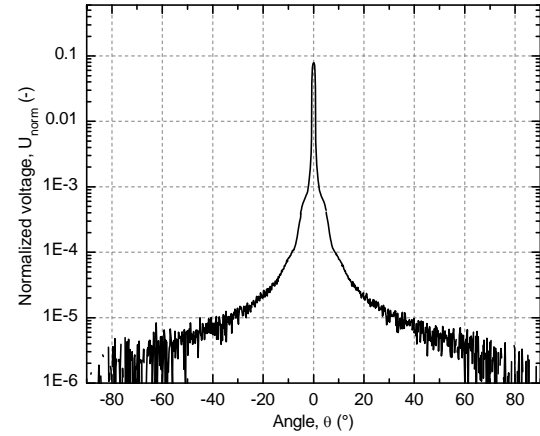


Figure F.4. Scattering diagrams of specimens 1230UD-L in (a-c) 0°-direction and (d-f) 90°-direction.

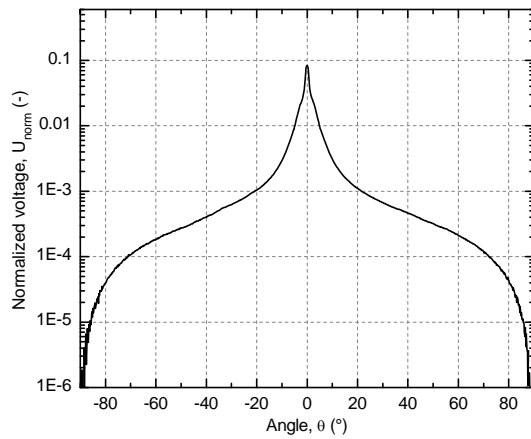
(a) 1640UD-L-0, measurement 1



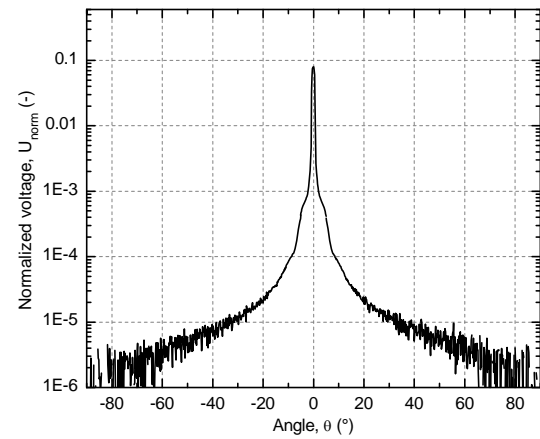
(d) 1640UD-L-90, measurement 1



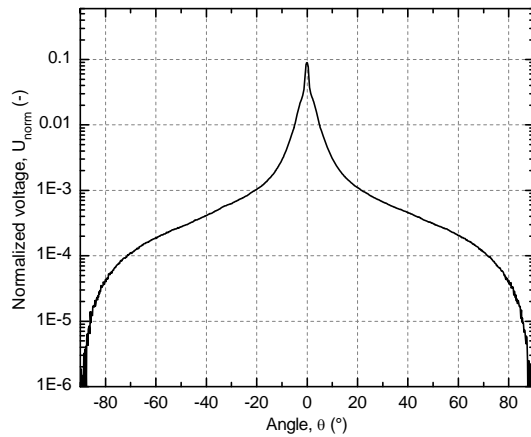
(b) 1640UD-L-0, measurement 2



(e) 1640UD-L-90, measurement 2



(c) 1640UD-L-0, measurement 3



(f) 1640UD-L-90, measurement 3

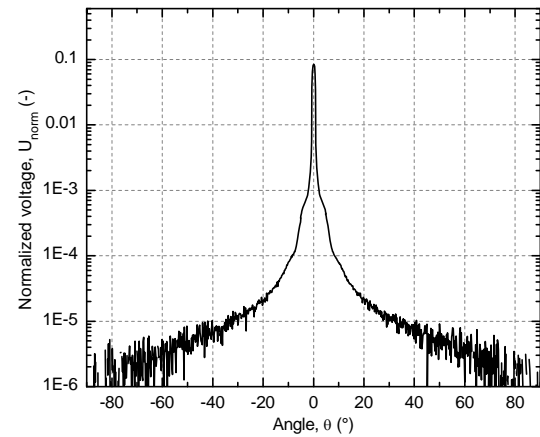
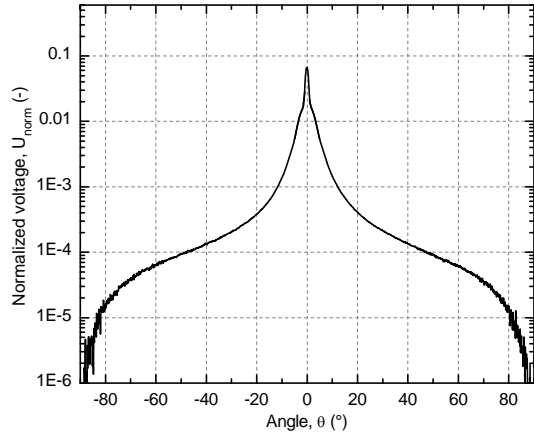
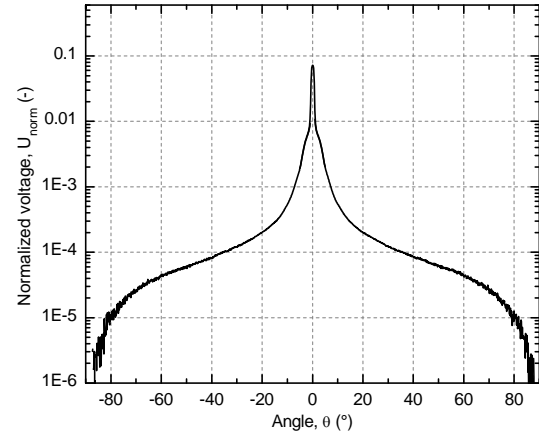


Figure F.5. Scattering diagrams of specimens 1640UD-L in (a-c) 0°-direction and (d-f) 90°-direction.

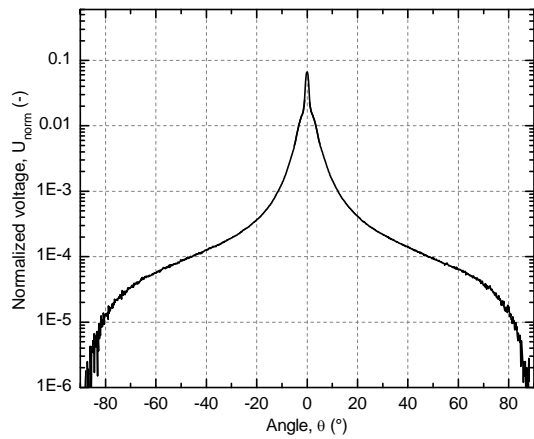
(a) 1230CP-L-0, measurement 1



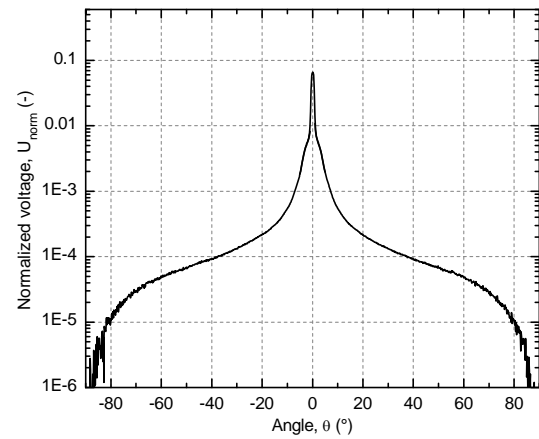
(d) 1230CP-L-90, measurement 1



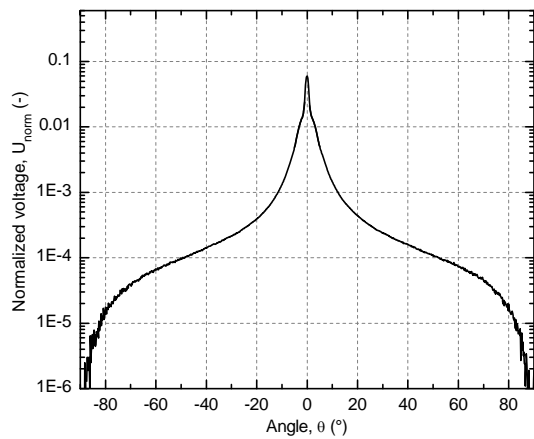
(b) 1230CP-L-0, measurement 2



(e) 1230CP-L-90, measurement 2



(c) 1230CP-L-0, measurement 3



(f) 1230CP-L-90, measurement 3

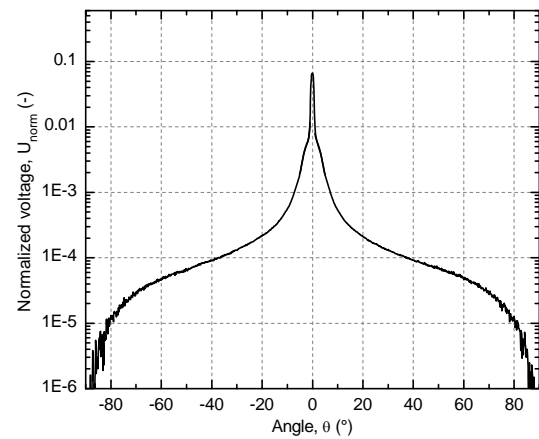
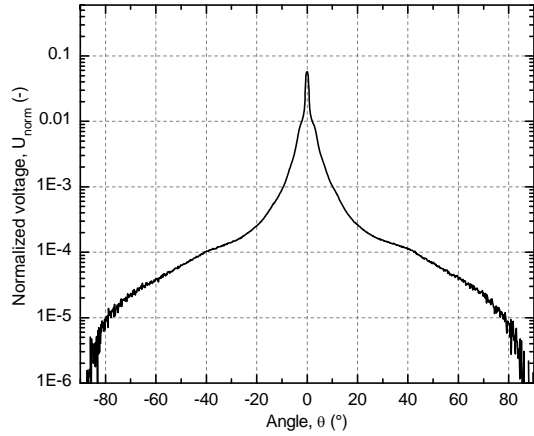
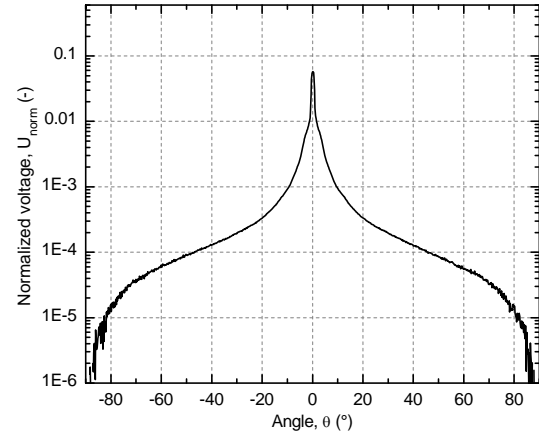


Figure F.6. Scattering diagrams of specimens 1230CP-L in (a-c) 0°-direction and (d-f) 90°-direction.

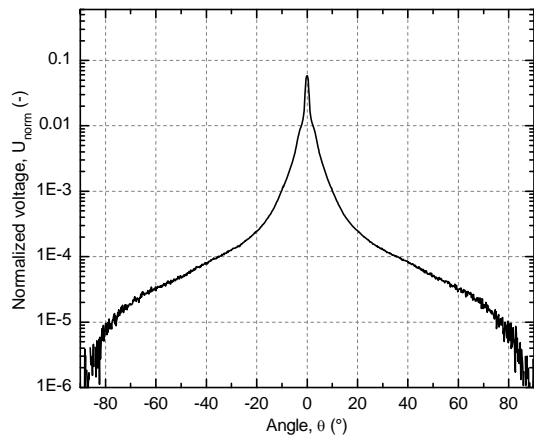
(a) 1640CP-L-0, measurement 1



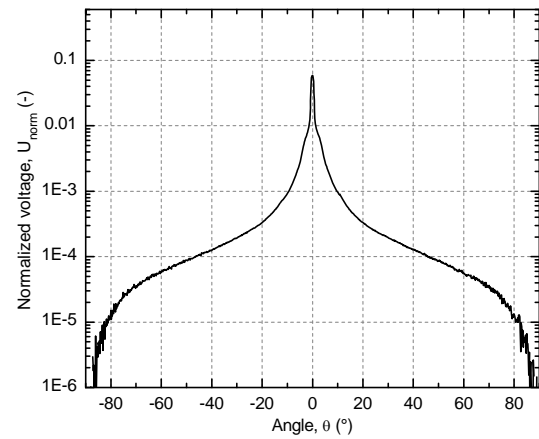
(d) 1640CP-L-90, measurement 1



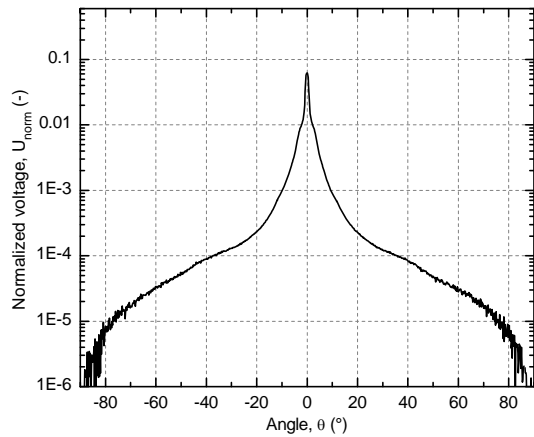
(b) 1640CP-L-0, measurement 2



(e) 1640CP-L-90, measurement 2



(c) 1640CP-L-0, measurement 3



(f) 1640CP-L-90, measurement 3

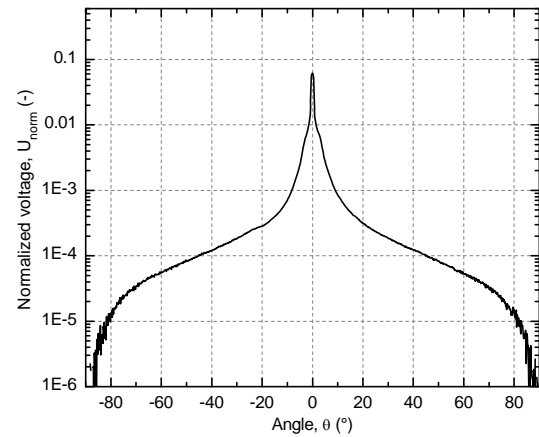
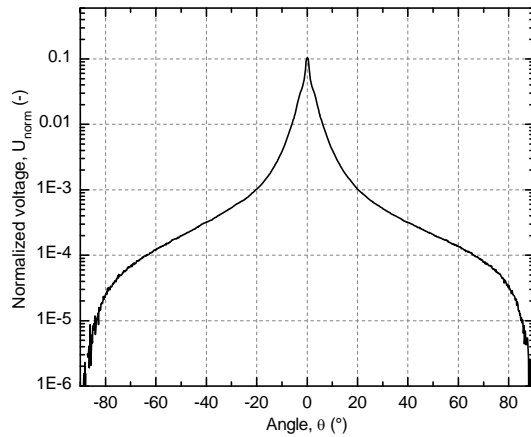


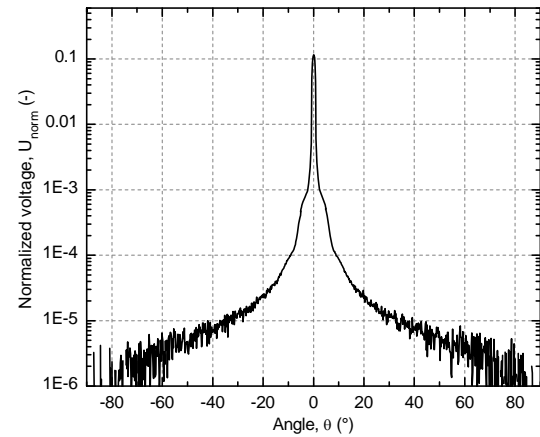
Figure F.7. Scattering diagrams of specimens 1640CP-L in (a-c) 0°-direction and (d-f) 90°-direction.

F.2.2. Series H

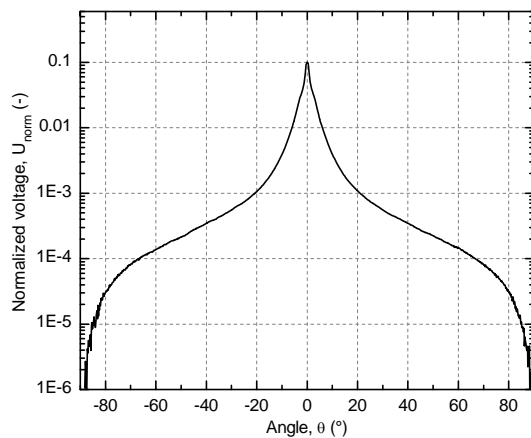
(a) 1230UD-H-0, measurement 1



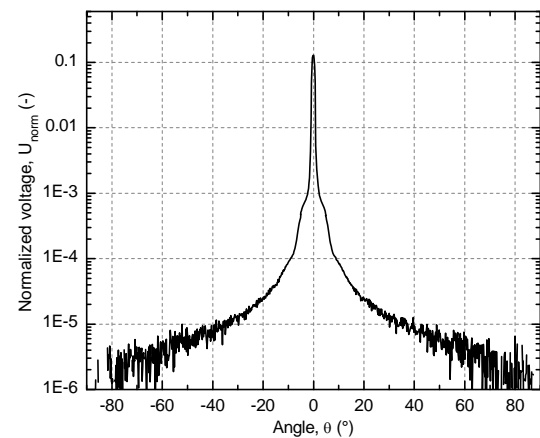
(d) 1230UD-H-90, measurement 1



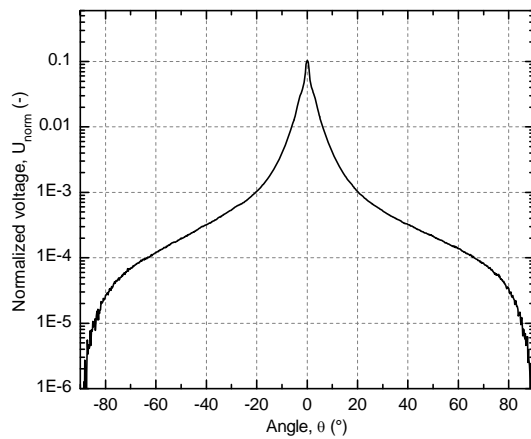
(b) 1230UD-H-0, measurement 2



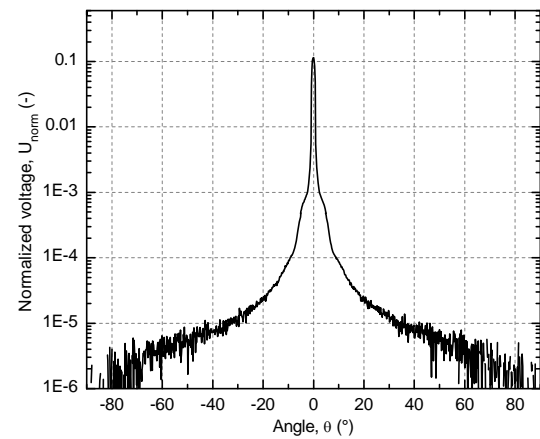
(e) 1230UD-H-90, measurement 2



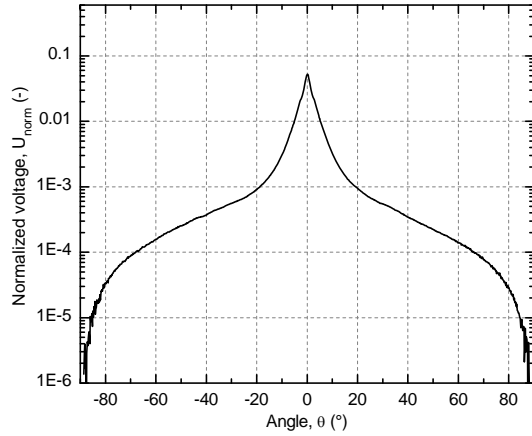
(c) 1230UD-H-0, measurement 3



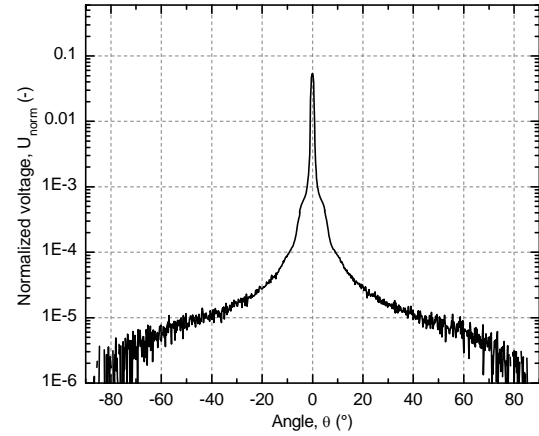
(f) 1230UD-H-90, measurement 3

**Figure F.8.** Scattering diagrams of specimens 1230UD-H in (a-c) 0°-direction and (d-f) 90°-direction.

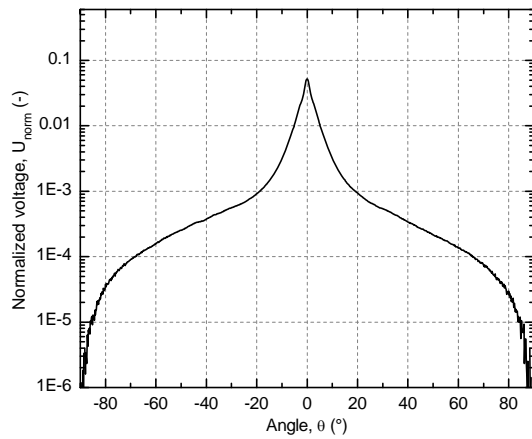
(a) 1640UD-H-0, measurement 1



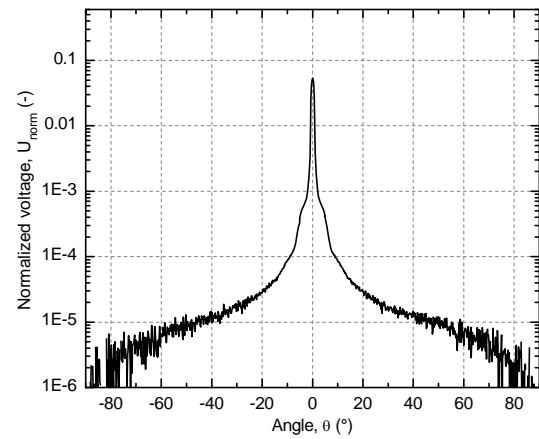
(d) 1640UD-H-90, measurement 1



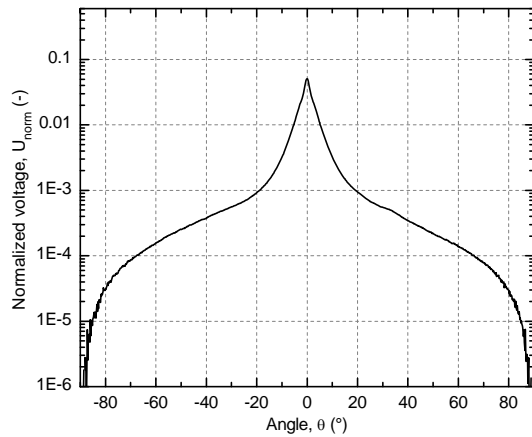
(b) 1640UD-H-0, measurement 2



(e) 1640UD-H-90, measurement 2



(c) 1640UD-H-0, measurement 3



(f) 1640UD-H-90, measurement 3

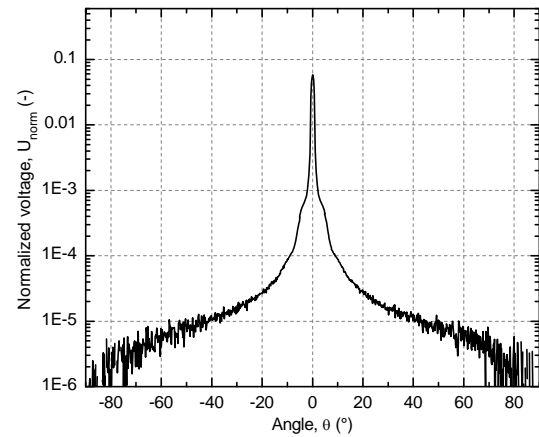
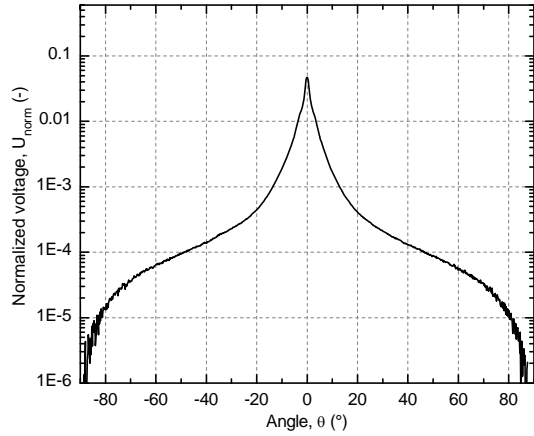
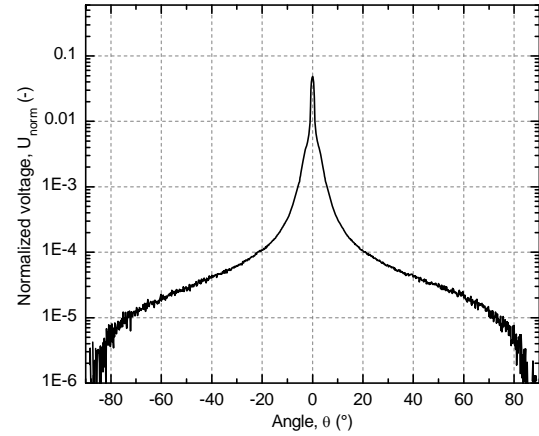


Figure F.9. Scattering diagrams of specimens 1640UD-H in (a-c) 0°-direction and (d-f) 90°-direction.

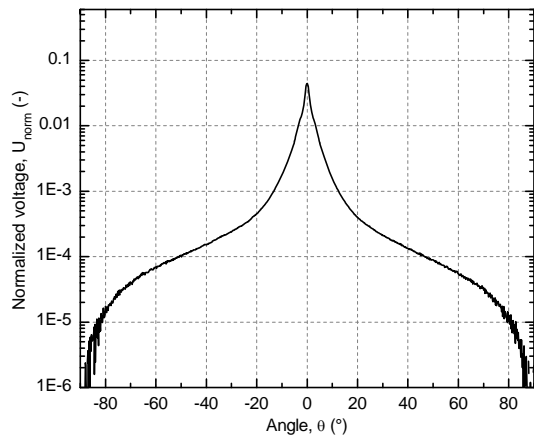
(a) 1230CP-H-0, measurement 1



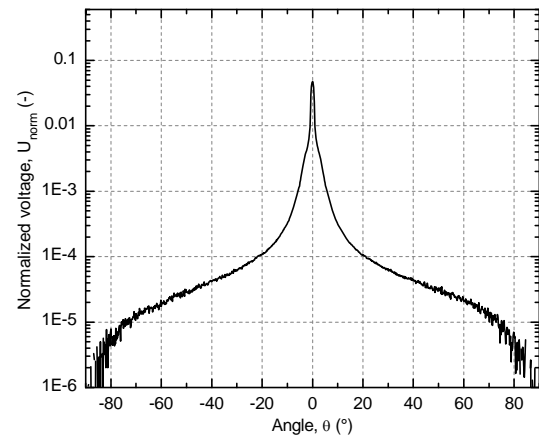
(d) 1230CP-H-90, measurement 1



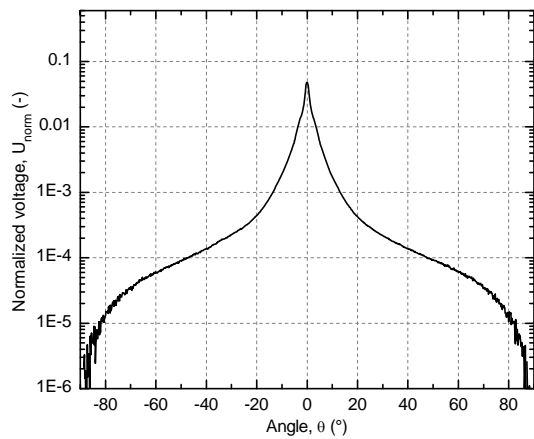
(b) 1230CP-H-0, measurement 2



(e) 1230CP-H-90, measurement 2



(c) 1230CP-H-0, measurement 3



(f) 1230CP-H-90, measurement 3

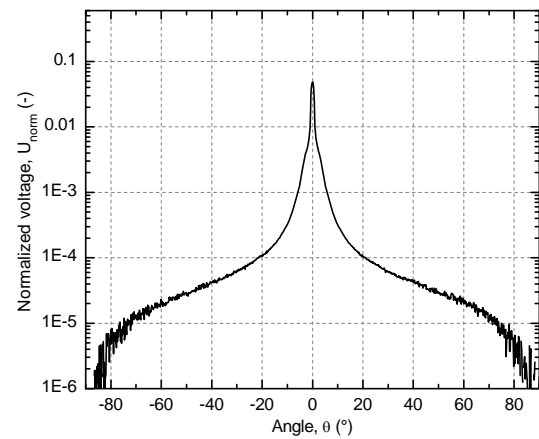
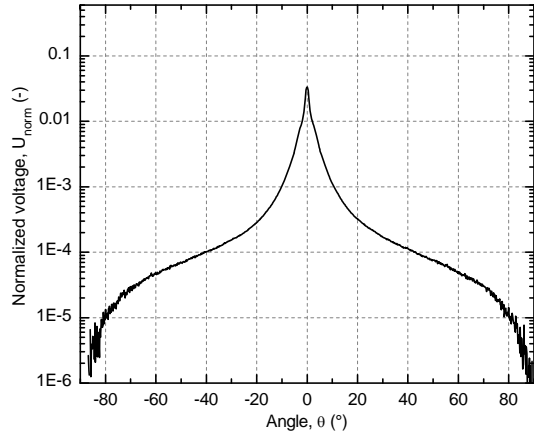
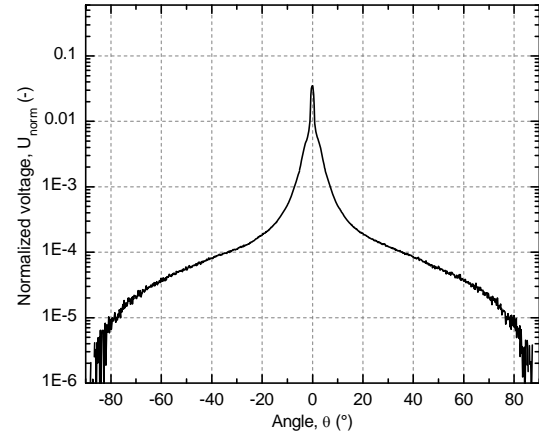


Figure F.10. Scattering diagrams of specimens 1230CP-H in (a-c) 0°-direction and (d-f) 90°-direction.

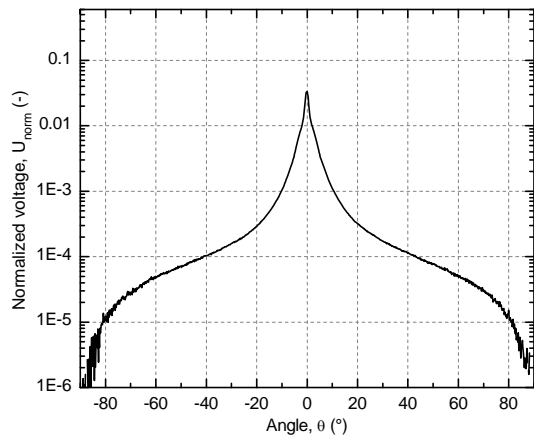
(a) 1640CP-H-0, measurement 1



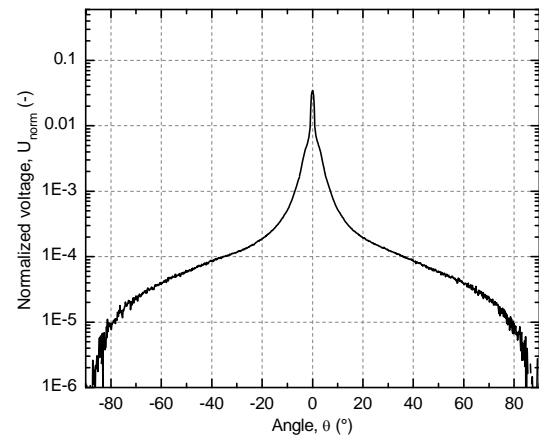
(d) 1640CP-H-90, measurement 1



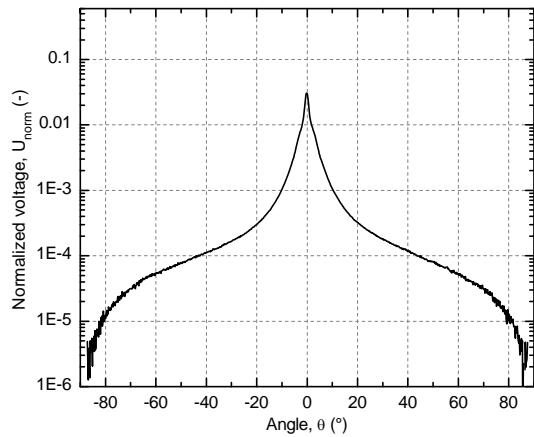
(b) 1640CP-H-0, measurement 2



(e) 1640CP-H-90, measurement 2



(c) 1640CP-H-0, measurement 3



(f) 1640CP-H-90, measurement 3

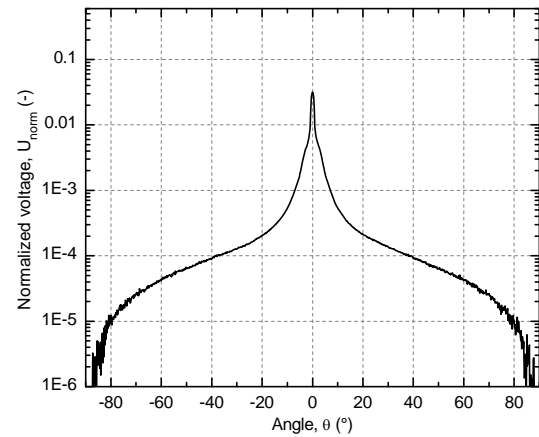


Figure F.11. Scattering diagrams of specimens 1640CP-H in (a-c) 0°-direction and (d-f) 90°-direction.

G Results of tensile experiments

G.1. Introduction

The results of the tensile experiments are presented below. The specimens are shown in Appendix A and were cut from laminates fabricated with PolyLite 420-181 unsaturated polyester resin manufactured by Reichhold Inc. (Durham, United States) and unidirectional E-glass fabrics from Tissa (Oberkulfm, Switzerland). The specimens had the dimensional specifications given by ASTM D3039/D3039M-08¹, with the exception of two 820UD-L specimens loaded in the 90°-direction which were two centimeters shorter than the specified values due to dimensional limitations of the original laminate.

Three strain-measuring systems were used in these experiments (see Figure G.1):

1. MTS clip gage
2. 0°/90° stacked T rosette HBM strain gage 1-XY91-6/350
3. linear HBM strain gage 1-LY11-6/120

and the results for the three measuring systems are presented in Figures G.2 to G.13.

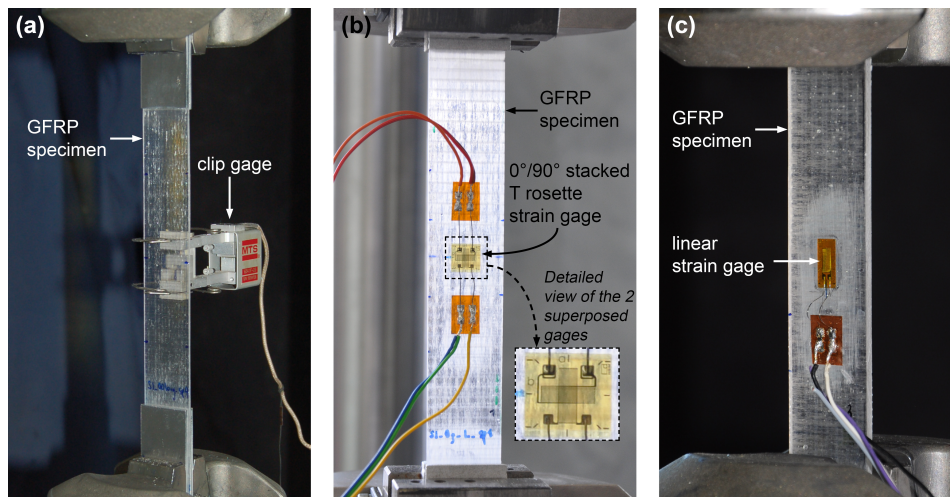


Figure G.1. GFRP tensile specimens equipped with (a) clip gage, (b) 0°/90° stacked T rosette strain gage and (c) linear strain gage.

The clip gage was used in three 820UD-L specimens. However as slippage problems were observed this measuring system was discarded for the following experiments.

The 0°/90° stacked T rosette gages were used in unidirectional (UD) and cross-ply (CP) specimens with reinforcement weights of $w \geq 1230 \text{ g/m}^2$ in order to investigate their Poisson ratios and the obtained

values are reported in Figures G.6 to G.13. However the measured ultimate strains were frequently lower than the expected values – especially for some CP specimens and also for some UD specimens loaded in the 90°-direction. The HBM technical support confirmed that inaccuracy of this type of stacked gages had already been reported for fiber-reinforced materials and recommended discarding the results and equipping the specimens with linear gages.

Figures G.2 to G.13 show the load-strain curves for the tensile experiments and the strain-measuring system is indicated for each curve, i.e. clip gage, 0°/90° stacked gage and linear gage. Only results obtained with linear gages were considered for the evaluation of the E-modulus of the specimens – load-strain curves presented in Chapter 4 also correspond to results obtained with this type of gage.

At least three tensile experiments were performed for each reinforcement weight, fiber architecture, fiber volume fraction series and loading (0°- or 90°-) direction. For laminate 410UD-L, five specimens were evaluated in the 0°-direction. These specimens tended to buckle when they were gripped in the servohydraulic MTS machine due to their great slenderness – the machine introduced a very small compression load when the grips were closed. This phenomenon was specially observed in specimens 4 and 5 and their results were disregarded. For laminate 820UD-L, five experiments were performed in the 0°-direction and four in the 90°-direction. Results for specimens 4 and 5 (0°-direction) and specimen 4 (90°-direction) were not considered in the analyses in Chapter 4 in order to present the same number of experimental results, i.e. three per loading direction, as for the other laminates.

G.2. Tensile results

G.2.1. Series L

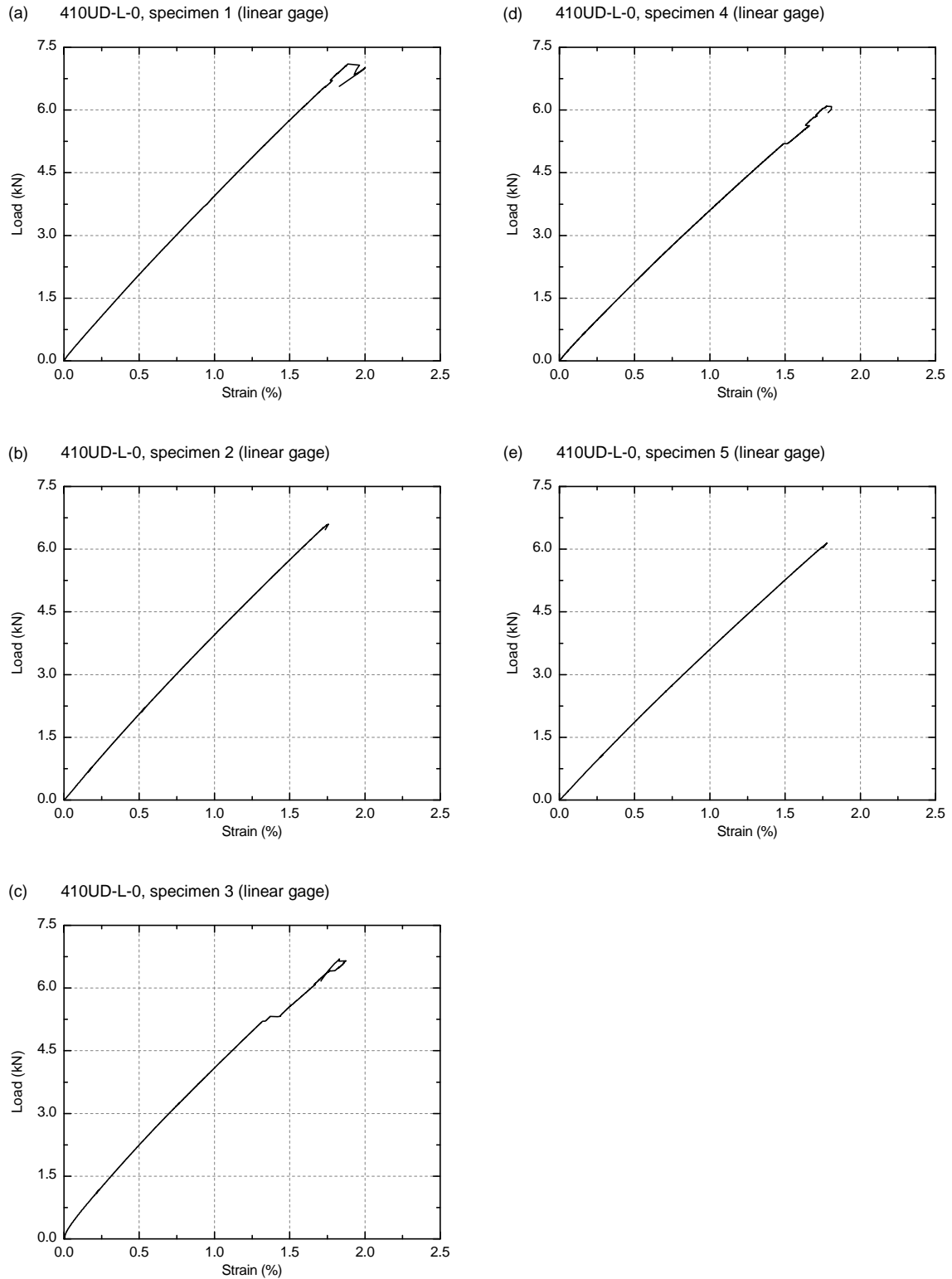


Figure G.2. Load-strain curves for 410UD-L specimens loaded in 0° -direction.

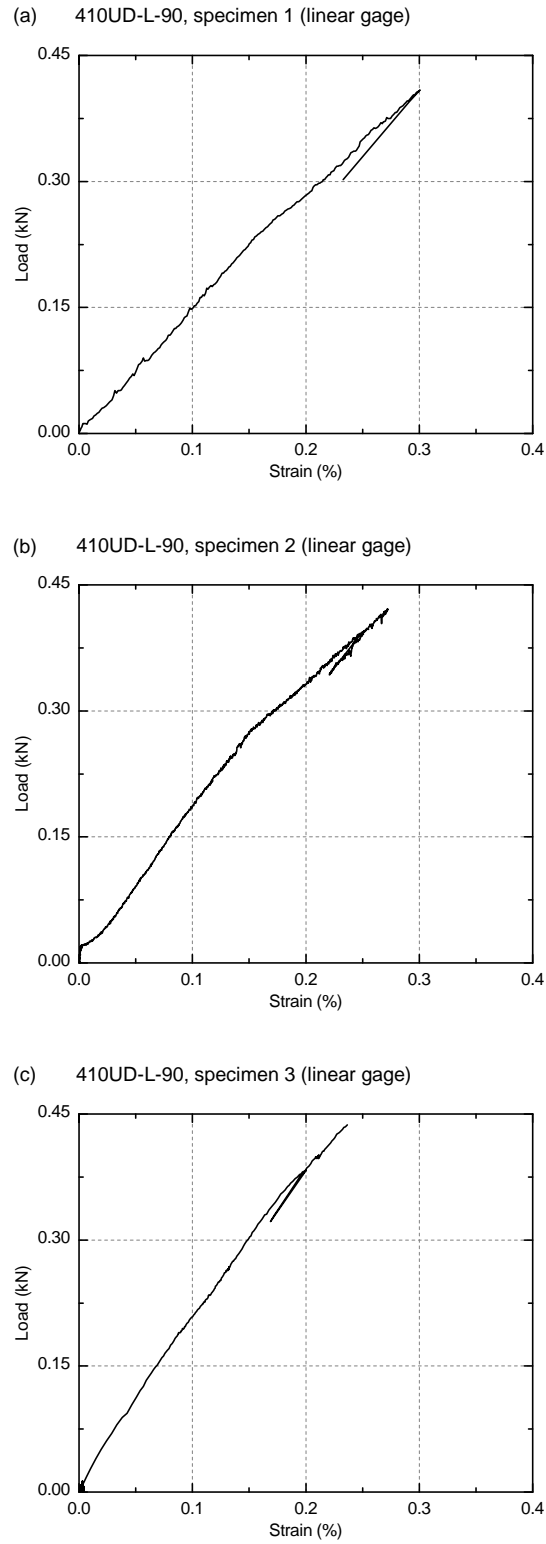
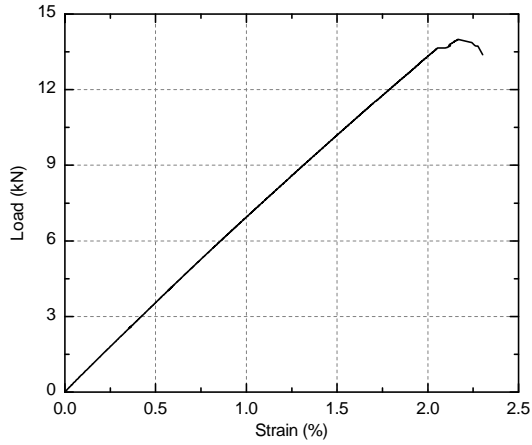
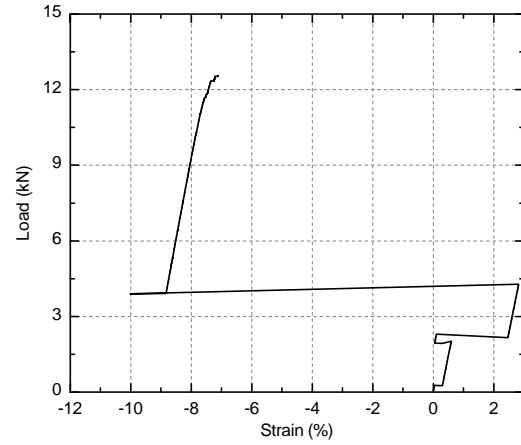


Figure G.3. Load-strain curves for 410UD-L specimens loaded in 90°-direction.

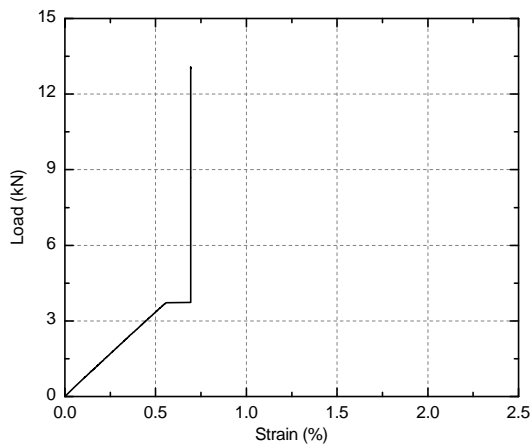
(a) 820UD-L-0, specimen 1 (linear gage)



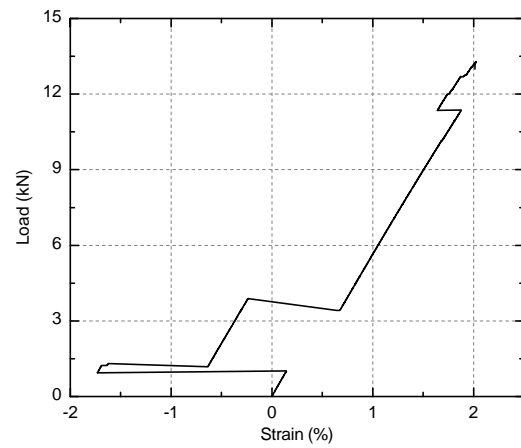
(d) 820UD-L-0, specimen 4 (clip gage)



(b) 820UD-L-0, specimen 2 (linear gage)



(e) 820UD-L-0, specimen 5 (clip gage)



(c) 820UD-L-0, specimen 3 (clip gage)

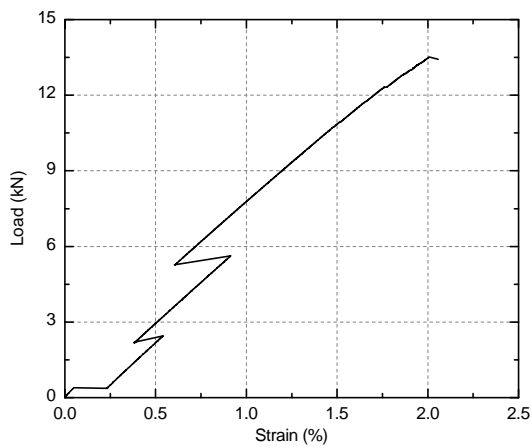


Figure G.4. Load-strain curves for 820UD-L specimens loaded in 0°-direction.

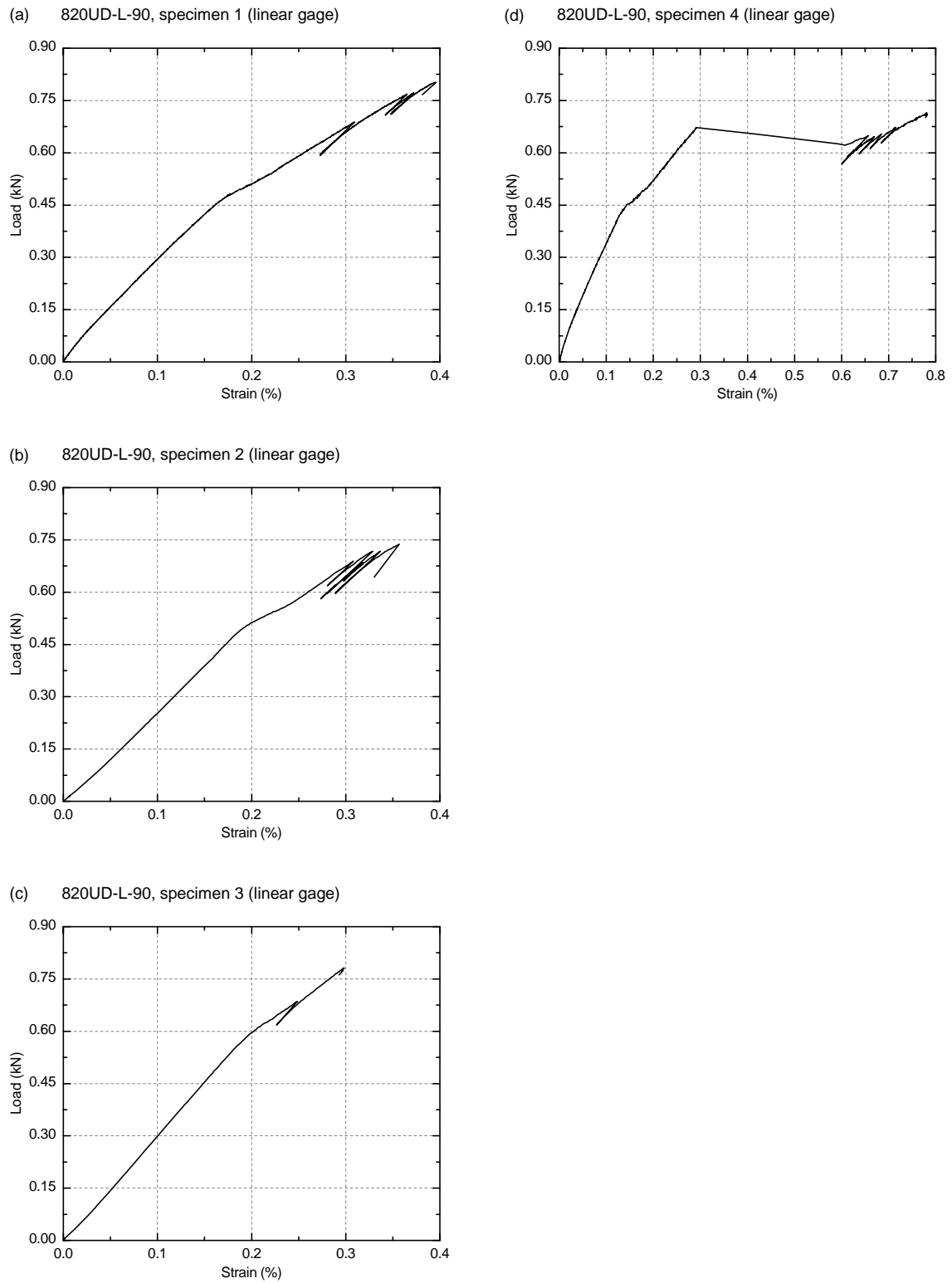


Figure G.5. Load-strain curves for 820UD-L specimens loaded in 90°-direction.

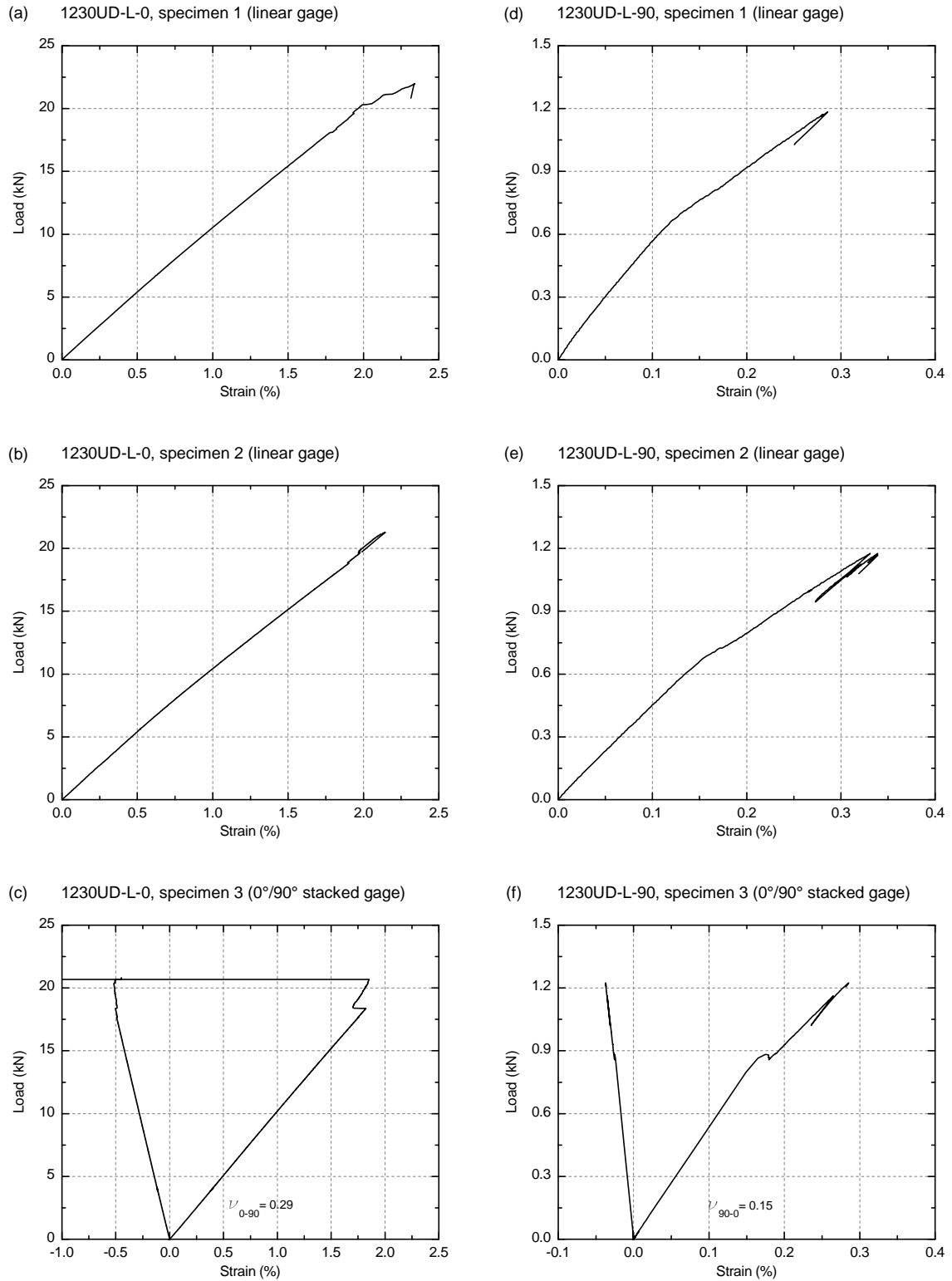
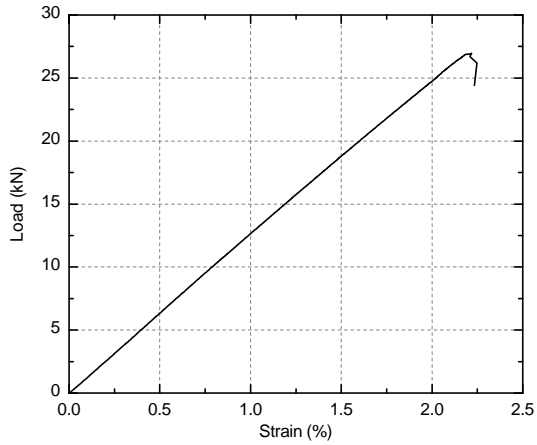
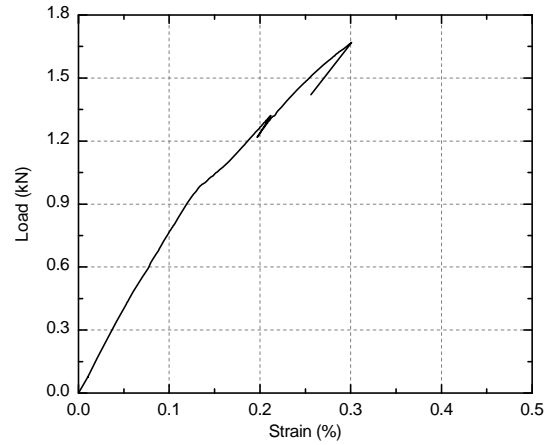


Figure G.6. Load-strain curves for 1230UD-L specimens loaded in (a-c) 0°-direction and (d-f) 90°-direction.

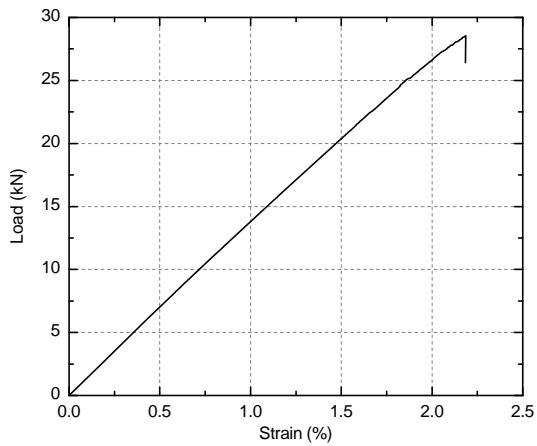
(a) 1640UD-L-0, specimen 1 (linear gage)



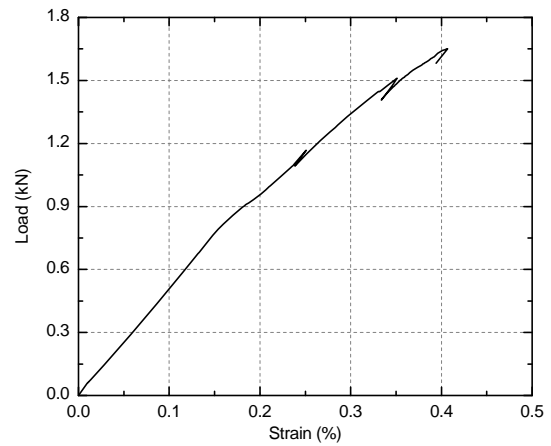
(d) 1640UD-L-90, specimen 1 (linear gage)



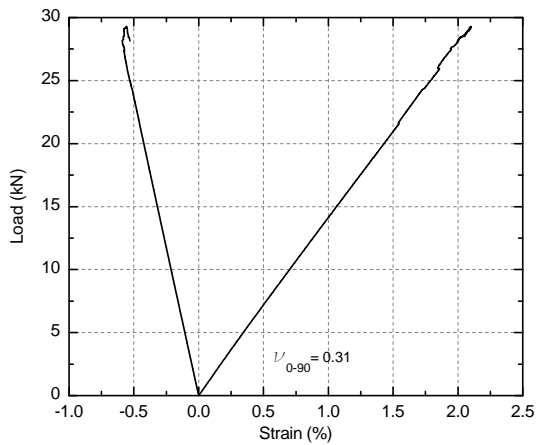
(b) 1640UD-L-0, specimen 2 (linear gage)



(e) 1640UD-L-90, specimen 2 (linear gage)



(c) 1640UD-L-0, specimen 3 (0°/90° stacked gage)



(f) 1640UD-L-90, specimen 3 (0°/90° stacked gage)

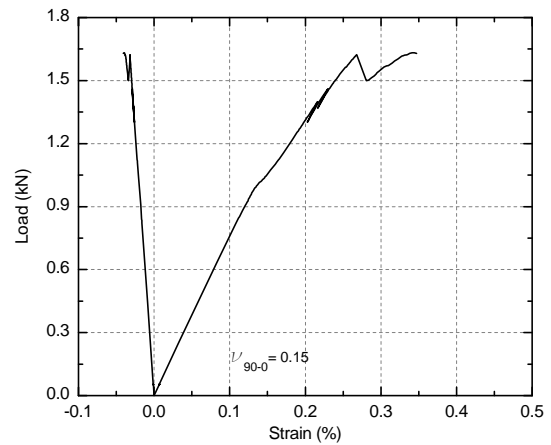


Figure G.7. Load-strain curves for 1640UD-L specimens loaded in (a-c) 0°-direction and (d-f) 90°-direction.

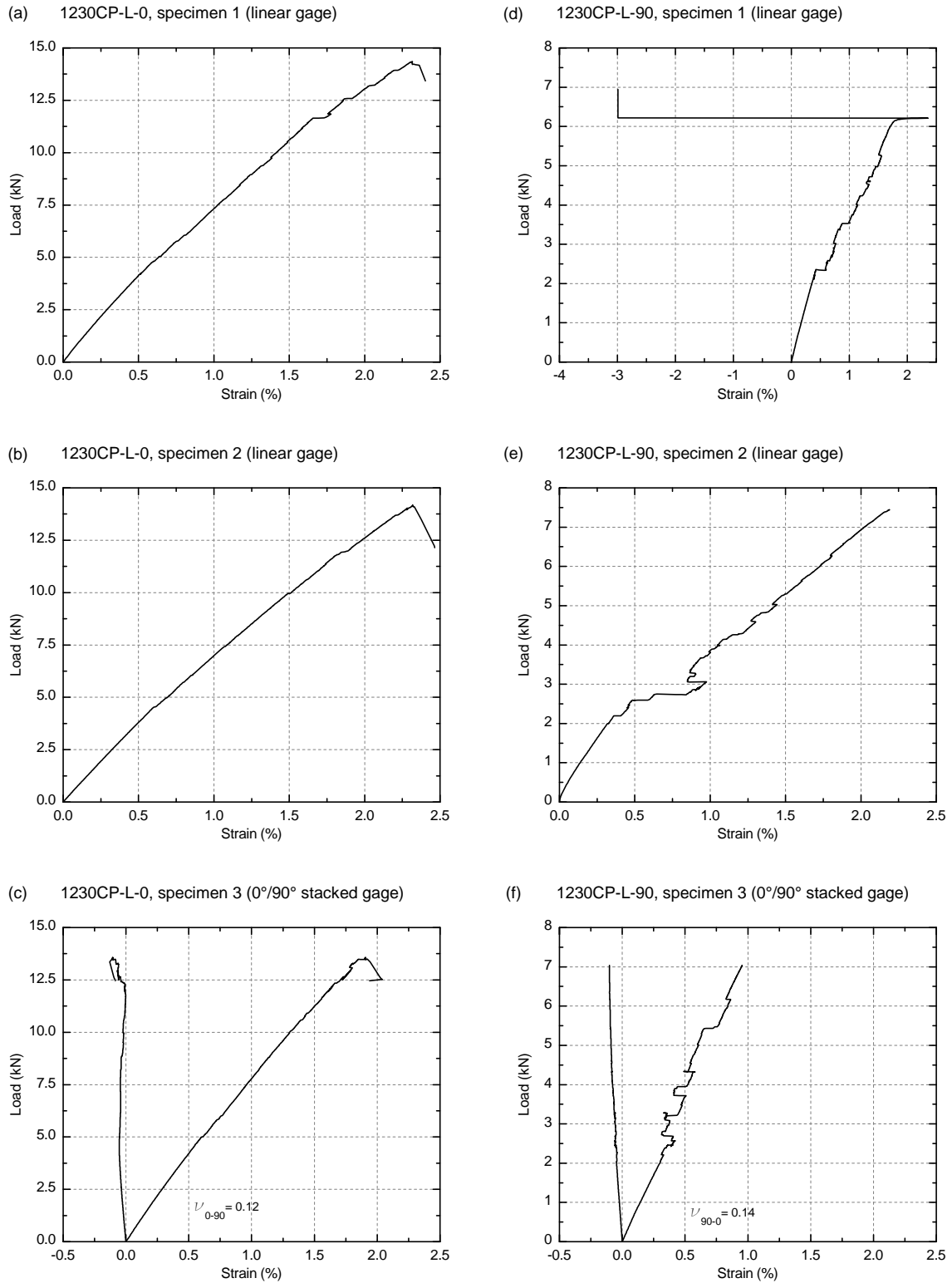


Figure G.8. Load-strain curves for 1230CP-L specimens loaded in (a-c) 0°-direction and (d-f) 90°-direction.

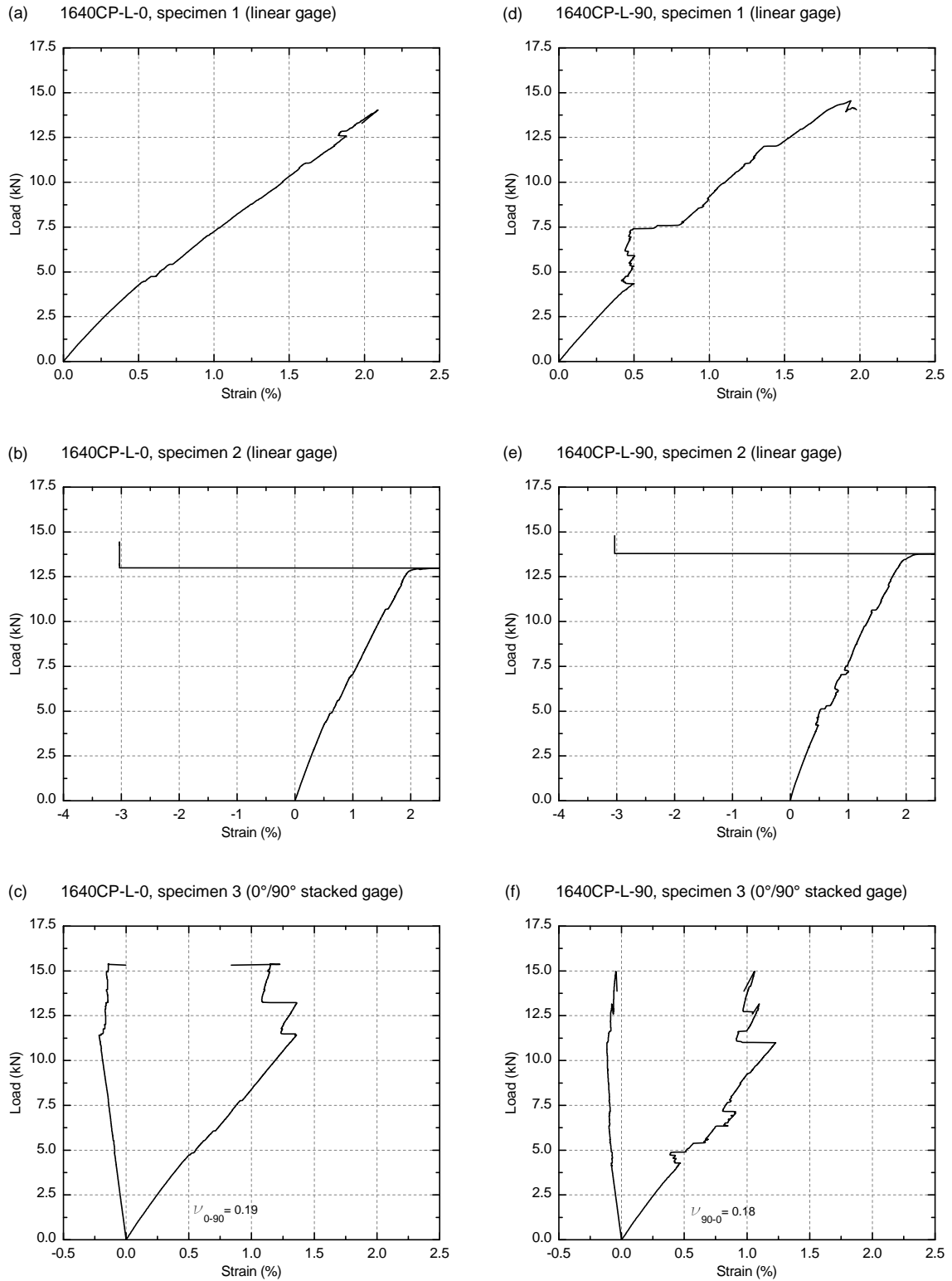


Figure G.9. Load-strain curves for 1640CP-L specimens loaded in (a-c) 0°-direction and (d-f) 90°-direction.

G.2.2. Series H

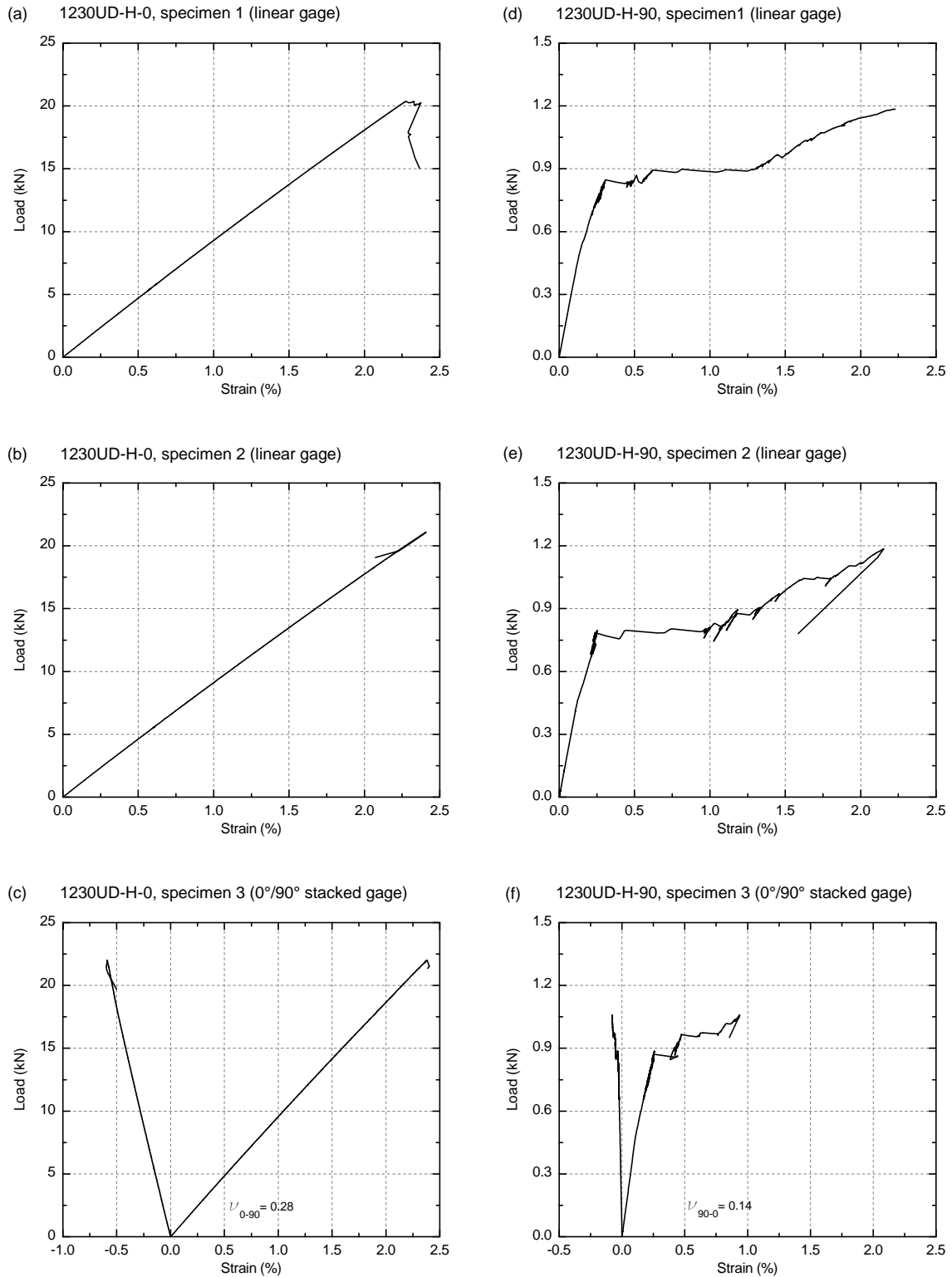


Figure G.10. Load-strain curves for 1230UD-H specimens loaded in (a-c) 0°-direction and (d-f) 90°-direction.

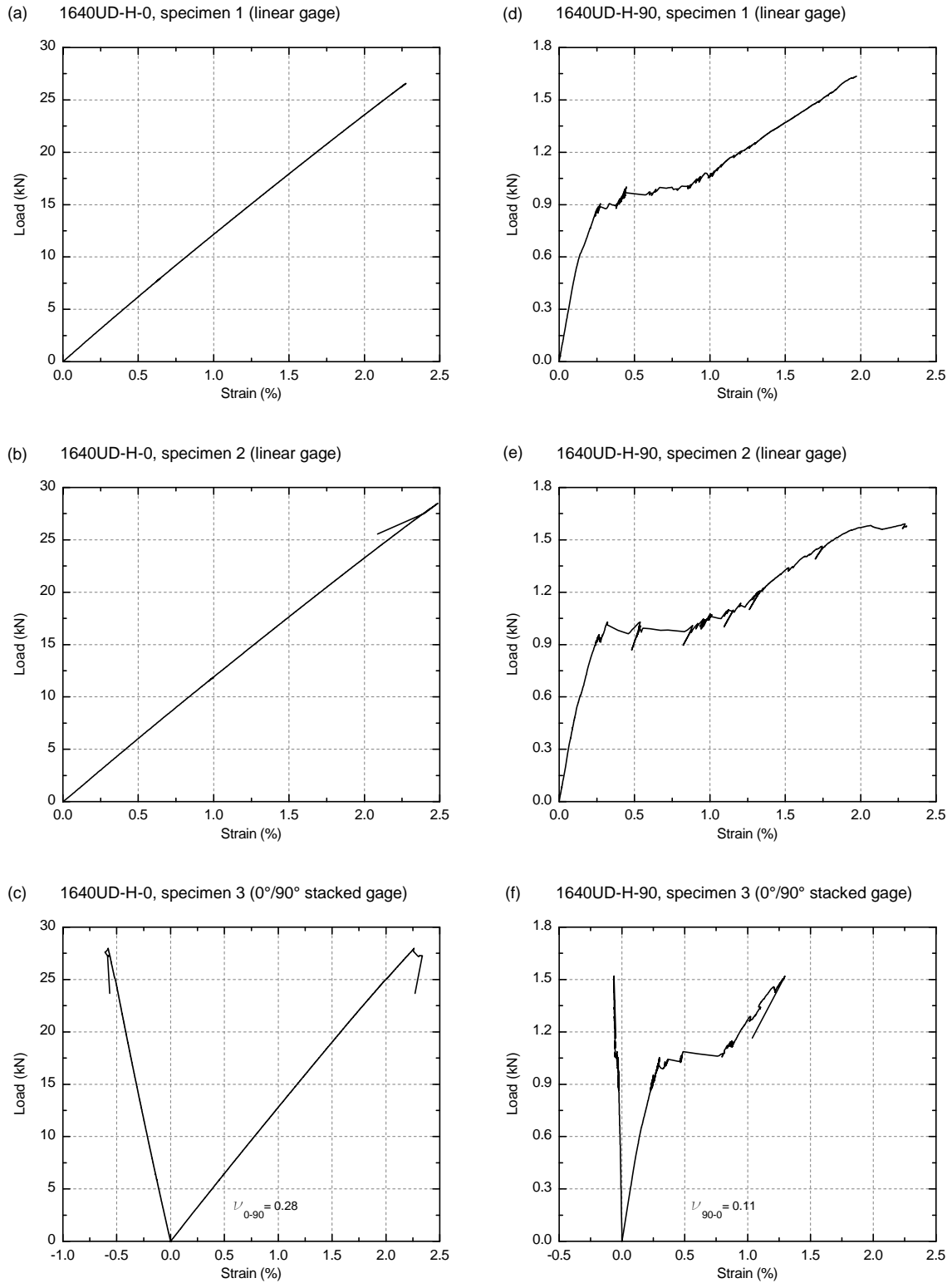


Figure G.11. Load-strain curves for 1640UD-H specimens loaded in (a-c) 0°-direction and (d-f) 90°-direction.

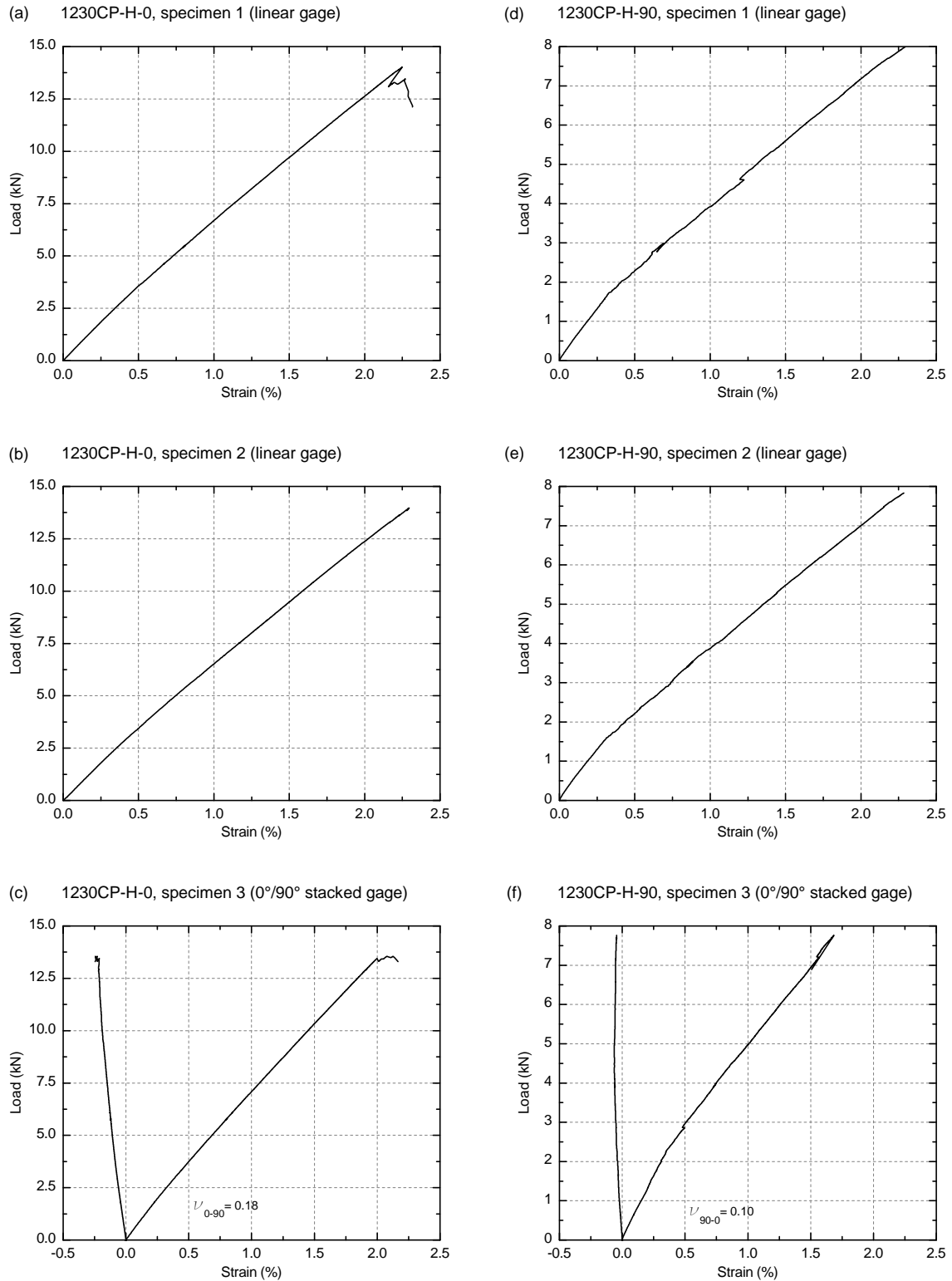


Figure G.12. Load-strain curves for 1230CP-H specimens loaded in (a-c) 0°-direction and (d-f) 90°-direction.

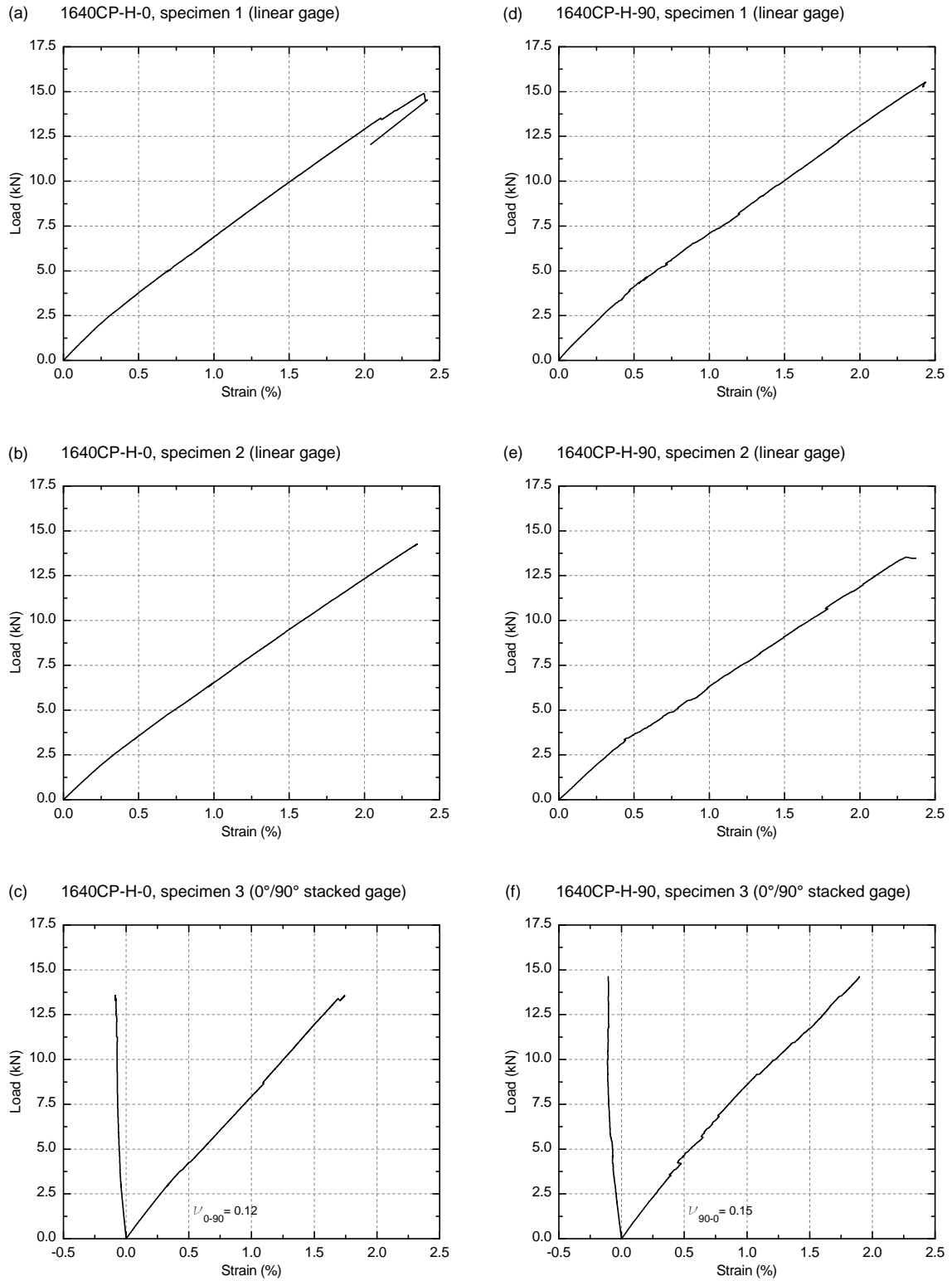


Figure G.13. Load-strain curves for 1640CP-H specimens loaded in (a-c) 0°-direction and (d-f) 90°-direction.

G.6. References

1. ASTM Standard D3039/D3039M-08. *Standard Test Method for Tensile Properties of Polymer Matrix Composite Materials*. West Conshohocken, PA: American Society for Testing Materials, October 2008.

Curriculum Vitae

Carlos Pascual Agulló

Born: 1983

Nationality: Spanish

✉ carlospascualagullo@hotmail.com

EDUCATION

2010-2014: Ecole Polytechnique Fédérale de Lausanne, EPFL, Lausanne, Switzerland.

PhD student at the Composite Construction Laboratory (CCLAB).

2001-2008: Universidad Politécnica de Valencia, UPV, Valencia, Spain.

Msc in Civil Engineering.

WORK EXPERIENCE

2010-2014: Ecole Polytechnique Fédérale de Lausanne, EPFL, Lausanne, Switzerland.

Research and teaching assistant at the Composite Construction Laboratory (CCLAB).

2009-2010: Ecole Polytechnique Fédérale de Lausanne, EPFL, Lausanne, Switzerland.

Research and teaching assistant at the Structural Concrete Laboratory (IBETON).

2008-2009: Fibrotec Materiales Compuestos S.L., Valencia, Spain.

Engineer (lightweight composite structures for building and bridge construction).

LIST OF PUBLICATIONS

Journal papers

1. Pascual C, de Castro J, Schueler A, Vassilopoulos AP and Keller T. Total light transmittance of glass fiber-reinforced polymer laminates for multifunctional load-bearing structures. Accepted for publication in *J Compos Mater* 2013; DOI: 10.1177/0021998313511653.
2. Pascual C, de Castro J, Kostro A, Schueler A, Vassilopoulos AP and Keller T. Diffuse light transmittance of glass fiber-reinforced polymer laminates for multifunctional load-bearing structures. Accepted for publication in *J Compos Mater* 2013; DOI: 10.1177/0021998313511655.
3. Pascual C, de Castro J, Kostro A, Schueler A, Vassilopoulos AP and Keller T. Optomechanical investigation of glass fiber-reinforced polymer laminates for multifunctional load-bearing structures. Submitted to *J Compos Mater* in June 2014.

Conference proceedings

1. Pascual C, de Castro J, Schueler A, Vassilopoulos AP and Keller T. Total light transmittance of glass fiber-reinforced polymer laminates for multifunctional load-bearing structures. In: *Proceedings of CISBAT International Conference*, Lausanne, Switzerland, 4-6 September 2013, pp.73-78. Lausanne: LESO-PB.
2. Pascual C, de Castro J, Schueler A, Vassilopoulos AP and Keller T. Total light transmittance of GFRP laminates for building construction. In: *Proceedings of CICE Conference*, Vancouver, Canada, 20-22 August 2014.
3. Pascual C, de Castro J, Kostro A, Schueler A, Vassilopoulos AP and Keller T. Light diffusion in GFRP laminates for building construction. In: *Proceedings of CICE Conference*, Vancouver, Canada, 20-22 August 2014.

